# MICROMECHANICAL TUNABLE VERTICAL CAVITY SURFACE EMITTING LASERS

A DISSERTATION

SUBMITTED TO THE DEPARTMENT OF ELECTRICAL ENGINEERING

AND THE COMMITTTEE ON GRADUATE STUDIES

OF STANFORD UNIVERSITY

IN PARTIAL FULFILLMENT OF THE REQUIREMENTS

FOR THE DEGREE OF

DOCTOR OF PHILOSOPHY

IN

ELECTRICAL ENGINEERING

Edward C. Vail

March 1997

UMI Number: 9723428



UMI
300 North Zeeb Road
Ann Arbor, MI 48103

I certify that I have read this dissertation and that in my opinion it is fully adequate, in scope and quality, as a dissertation for the degree of Doctor of Philosophy.

Prof. Chang-Hasnain, Principal Advisor

I certify that I have read this dissertation and that in my opinion it is fully adequate, in scope and quality, as a dissertation for the degree of Doctor of Philosophy.

Prof. Yamamoto, Associate Advisor

I certify that I have read this dissertation and that in my opinion it is fully adequate, in scope and quality, as a dissertation for the degree of Doctor of Philosophy.

Prof. Nishimura

Approved for the University Committee on Graduate Studies:

# Abstract

Tunable lasers, filters, and detectors are useful in many applications including communications, spectroscopy, and beam steering. Typical tunable devices are constructed with bulk optics, making them expensive. To address this problem, integrated devices which tune with either carrier injection or temperature have received considerable attention in recent years. Although wide tuning ($\Delta\lambda$>>1%) has been achieved, there have been several drawbacks to these devices. All methods to tune lasers have had to mode hop (i.e. they must discretely jump between wavelengths) to tune more than a few nanometers. Widley tunable filters and detectors with high extinction ratios have also proved difficult to build.

This thesis discuss a new tuning mechanism: micromechanical tuning of vertical cavities. Vertical cavities have several nice features, including circular modes, wide mode spacing, no cleaved facets, compact size, wafer scale testing, and integrability into 2-D arrays. When coupled with micromechanical movement, wide ($\Delta\lambda/\lambda$ >>1%) continuous tuning can be achieved with just a single electrical contact. Micromechanical movement is voltage-controlled and requires only $\mu$W of tuning power compared to mW for other mechanisms.

Tunable filters, tunable detectors, and the first micromechanical tunable vertical cavity surface emitting laser (VCSEL) were fabricated. The optical and mechanical performance of these devices closely agrees with calculations. In all three cases record tuning ranges were achieved. New fabrication techniques, including the use of wet oxidation of AlAs, resulted in a dramatic improvement

in device performance. With these improvements, VCSELs were obtained with 19.1 nm of tuning. To the best of our knowledge, this is the widest, continuous tuning range ever achieved with a monolithic semiconductor laser. We also achieved threshold currents of 460 μA and peak powers of 0.9 mW. This represents the best device performance of micromechanical tunable VCSELs and the first demonstration of performance comparable to the best VCSELs.

# Preface

I first began working on this project in early 1994. My advisor, Professor Chang-Hasnain, had previously worked on making arrays of VCSELs each at different wavelengths. Her technique was to deposit layers of different thicknesses during fabrication inside the cavity to create devices of different wavelengths. The next logical step seemed to be a device with a layer whose thickness could be adjusted after fabrication, allowing tuning after the device was completed.

Another member of our group, Marianne Wu, was beginning to work on tunable VCSELs starting with temperature tuning, but had also been thinking of using mechanical tuning. We decided to work on the project together.

We both contributed equally to the work covered in Chapters 2-4 of this thesis. It was not uncommon for one person to work during the day and the other person to take over at night, when deadlines approached. When Marianne writes up her thesis, it is likely the work of these chapters will be repeated, although the focus will be somewhat different.

After demonstrating the first micromechanical tunable VCSEL, Marianne and I decided to split our efforts. I focused on improving the laser while Marianne worked on the filter, detector, and (perhaps) a system demonstration. My work on the laser is described in Chapter 5. In this chapter I discuss an oxidized VCSEL with record tuning of 19.1 nm. That particular device had a threshold around 3 mA and powers of tenths of mW. I also reported another device with only 8 nm of tuning, but with thresholds of 460 $\mu$A and powers as high as 0.9 mW. At the time this was the widest tuning range, lowest threshold, and highest power ever achieved for a micromechanical tunable VCSEL.

A couple months after starting this project, we discovered other groups were working or had worked on a similar ideas, notably Professor Harris's group, also at Stanford. Their approach was fairly different than ours, as they were using metal mirrors and we were planning on using semiconductor DBR's. They also feltd structures with multiple supports were necessary to keep the tilt of the end mirror low, while we felt the it was possible, as well as simpler, to use cantilevers. After discussions with them, we decided to attack the problem with our different approaches. As it turns out, both approaches worked, although with different results[1-10].

Improved results should be possible in the future. Using my advisor's technique, fixed wavelength lasers spanning 40 nm have been generated. This much tuning should be possible for micromechanical lasers. For fixed wavelength VCSELs, threshold currents as low as 50 μA and single mode powers of a few mW have been reported and should be obtainable with tunable devices as well. Tunable VCSELs should be expandable to other wavelengths from the red to the communication wavelengths in the IR. Tunable detectors and filters have even greater potential. Using the techniques described in this thesis and novel oxidized AlAs materials, filters and detectors from the visible to the mid-IR should be possible with tuning ranges of 100's of nm.

In performing this work I was helped by many people. My advisor, Prof. Chang-Hasnain, taught and inspired a clueless first year grad student. My fellow group members, Dan Francis, Giorgio Giaretta, Gabriel Li, Melissa Li, Sui Lim, Marianne Wu, Yongan Wu, and Wu-Pen Yuen, did me so many favors I lost count. Lars Eng gave me the benefit of his frank advice and experience. Rashid Nabiev always knew the theory behind any subject and gave me numerous suggestions. It is impossible to accomplish anything in the cleanroom without the help of excellent staff: Tom Carver at Ginzton was always friendly, helpful and knowledgeable; Karl Brandt, Robin King, and Jim McVittie helped me with my processing in CIS at Stanford; Charlie Williams, Katalin Voros, Bob Hamilton, and Phil at the Berkeley microfab did excellent jobs getting the equipment up and running at Berkeley. Donna Hudson kept the group running at Stanford and always brightened my day. Jay Ento has helped to make the transformation to Berkeley a pleasant one. I would like to thank the members of my Orals Committee, Prof. Yamamoto, Prof. Fejer, and Prof. Zebker for taking

time out of their busy schedules to thoroughly test me. I would also like to thank Prof. Yamamoto and Prof. Nishimura for taking the time to read what has turned into a lengthy thesis. I would like to thank my Mom, Dad, sister and friends Mark and Lydia for their support over the last 5 years.

## References


[1] E. C. Vail, M. S. Wu, G. S. Li, L. Eng, and C. J. Chang-Hasnain, "GaAs micromachined widely tunable Fabry-Perot filters," *Electron. Lett.*, vol. 31, p. 228-229, 1995.

[2] M. S. Wu, E. C. Vail, G. S. Li, W. P. Yuen, and C. J. Chang-Hasnain, "Widely and continually tunable micromachined resonant cavity detector with wavelength tracking," *IEEE Photon. Technol. Lett.*, vol. 8, no. 1, p. 98-100, 1996.

[3] M. S. Wu, E. C. Vail, G. S. Li, L. Eng, and C. J. Chang-Hasnain, "Speed and polarization characteristics of widely tunable micromachined GaAs Fabry-Perot filters," CLEO '95, Baltimore, MD, Paper CThL4, 1995.

[4] M. C. Larson, B. Pezeshki, and J. S. Harris, "Vertical coupled-cavity microinterferometer on GaAs with deformable-membrane top mirror," *IEEE Photon. Technol. Lett.*, vol. 7, no. 4, p. 382-384, 1995.

[5] M. C. Larson, and J. S. Harris, "Broadly-tunable resonant-cavity light-emitting diode," *IEEE Photon. Technol. Lett.*, vol. 7, no. 11, p. 1267-1269, 1995.

[6] M. C. Larson, and J. S. Harris, Jr., "Broadly tunable resonant-cavity light emission." *Applied Phys. Lett.*, vol. 67, no. 5, p. 590-592, 1995.

[7] M. S. Wu, E. C. Vail, G. S. Li, W. Yuen, and C. J. Chang-Hasnain, "Tunable micromachined vertical cavity surface emitting laser," *Electron. Lett.*, vol. 31, no. 4, p. 1671-1672, 1995.

[8] M. C. Larson, A. R. Massengale, and J. S. Harris, "Continuously tunable micromachined vertical cavity surface emitting laser with 18 nm wavelength range," *Electron. Lett.*, vol. 32 no. 19, p. 330-332, 1996.

[9] E. C. Vail, G. S. Li, W. Yuen, and C. J. Chang-Hasnain, "High performance micromechanical tunable vertical cavity surface emitting lasers," *Electron. Lett.*, vol. 32, no. 20, p. 1888-1889, 1996.

[10] M. C. Larson, and J. S. Harris, Jr., "Wide and continuous wavelength tuning in a vertical-cavity surface-emitting laser using a micromachined deformable-membrane mirror," *Appl. Phys. Lett.*, vol. 68, no. 7, p. 891-893, 1996.

## Table of Contents

## List of Tables

## List of Figures

# 1. Introduction

Most lasers are like musical instruments that play only one note. The frequency of the light is fixed, and only the power can be changed. This is sufficient for many applications, but a laser whose frequency can be controllably tuned opens up many new possibilities. Indeed, many demonstrations of tunable lasers have already been shown.

However, tunable lasers have had trouble keeping up with the advances of traditional lasers. Using semiconductors, lasers have a shrunk from large, table top instruments to the size of a transistor costing a few dollars. This advance enabled lasers to become commonplace. Laser printers, CD players, supermarket checkout stands, computer networks, and telephone calls all use semiconductor lasers. Often, semiconductor lasers performed better than the larger lasers they replaced. Tunable lasers have yet to undergo this transformation. Today, a tunable laser still costs around $10,000 and takes up at least a cubic foot.

This thesis will discuss transistor sized tunable laser based on micromechanical motion that could potentially cost $10. For some applications, it outperforms the large, bulk tunable lasers available today. Such a device would enhance existing applications and make new ones cost-effective. In addition, the same technology can be used to fabricate other useful components such as tunable filters and tunable detectors.

Although there are several competing methods of integrated tuning, the unique features of micromechanical tuning (wide continuous tuning of a single mode with only one tuning contact) make it the ideal choice for certain applications. Several records have already been set by the devices of this thesis, and there is still plenty of room for improvement.

## 1.1 Applications of Tunable Devices

This section will describe some tunable device applications, showing the general usefulness of tunable devices and how the devices of this thesis could be used.

### 1.1.1 WDM networks

Current fiber optic networks work by shining laser light on one end of an optical fiber and detecting the light at the other end. Information is sent by turning the laser on and off*. However, there is a limit to how fast the laser can be turned on and off. To increase the amount of information that can be sent, light of different wavelengths could all be sent down the same fiber and detected separately. Each wavelength would be generated by its own laser, which could be individually modulated to send its own stream of information. This technique is called wavelength division multiplexing(WDM) [1].

Besides the increased transmission capacity, there are several other advantages of WDM links. First of all, existing fiber links could be upgraded using WDM without laying new cables. Since a large fraction of a network's cost stems from actually laying down the fiber cable, this could provide an economical way to upgrade existing links.

WDM also has the advantage of being a simple way to multiplex different format signals. For example, a digital phone signal and an analog cable TV signal can be sent along the same fiber, simply by using different wavelengths for each signal.

---

* In reality, the laser is never turned completely off, because it takes a long time to turn back on. A wide variety of methods for sending information exist. Telephone networks are usually digital, sending 1's and 0's as high and low light levels. Cable television networks are usually analog, sending signals by continuously varying the light level.

A third advantage of WDM is that the wavelength of the signal can be used to route signals. For example, it is common for a central office to send information over a distance to a cluster of different users. With WDM, all the information could be sent on one fiber to a splitter. This splitter could send each wavelength to a different destination. The splitter can be completely passive, requiring no power supply. This makes the splitter easy to install, reliable, and robust.

WDM is also advantageous because it requires only one amplifier to amplify many signals. Typically, amplifiers are required every 20 km or so[2] in a long haul fiber link to make up for the losses of the fiber. Recently, optical amplifiers which directly amplify light have widely been implemented. Optical amplifiers provide gain over a broad range of wavelengths (~10 nm). This means that just one optical amplifier can amplify an entire WDM signal. This is very advantageous over laying multiple fibers, with each one carrying its own signal and requiring its own amplifier.

To date, WDM has been used only in high performance links due to the cost of the components. If low-cost WDM components are developed the advantages of WDM could be extended to more commonplace systems such as local area networks. The micromechanical tunable devices discussed in this thesis are ideally suited for this application. In the following sections, we discuss how micromechanical tunable devices could be used in WDM systems.

#### *1.1.1.1 Receivers*

In many WDM systems, such as broadcast networks, a single wavelength needs to be detected from a multiwavelength signal. Micromechanical tunable devices are useful in these applications in two ways. First, the tunable filters and tunable detectors of Chapters 2 and 3 of this thesis can be used to directly detect the wavelength signal of interest. These devices are advantageous since they are cheap, polarization insensitive, widely and continuously tunable, easy to design with a wide variety of extinction ratios and bandwidths, surface normal, and voltage controlled.

Alternatively, the tunable lasers of Chapter 5 can be used for coherent detection[3]. The received signal is combined with a local signal generated by a tunable VCSEL. The tunable VCSEL wavelength is adjusted so the beat signal of the desired wavelength channel and the tunable VCSEL is in a particular RF range. The power in this RF range is directly proportional to the desired signal to be detected. Although this method is more complicated, it has the advantage of a narrow, electronically controlled bandwidth.

#### *1.1.1.2 Transmitters*

Another key component for WDM systems is a transmitter. The tunable laser of Chapter 5 is ideal for this application. Tuning the laser can be used to switch between the various WDM channels, or simply to keep the wavelength of the laser constant despite errors introduced by processing, temperature variations, driving currents, aging, and so forth.

#### *1.1.1.3 Add/Drop*

When combined with an optical circulator[46] (a device that directs light depending on the direction it is traveling), micromechanical devices can perform an add/drop function on a WDM signal. This means a single wavelength channel can be detected or added without disturbing the other wavelengths of a WDM signal. Figure 1.1 shows how this add/drop function would work. To remove a particular frequency, an optical circulator would direct a signal on to a tunable detector or filter. A filter (or detector) would transmit the wavelength of interest and reflect all the others. The reflected wavelengths would be directed to the next device by the optical circulator. This is called a "drop" since one wavelength channel has been removed. The add function works similarly, only a tunable VCSEL is used. When this device is turned on, it adds a signal to all the other wavelengths, which are reflected.

This add/drop function could be used in a network like the one depicted in Figure 1.2. The topology would basically be a ring. Each node in the network would consist of a receiver/transmitter pair shown in Figure 1.1. Each

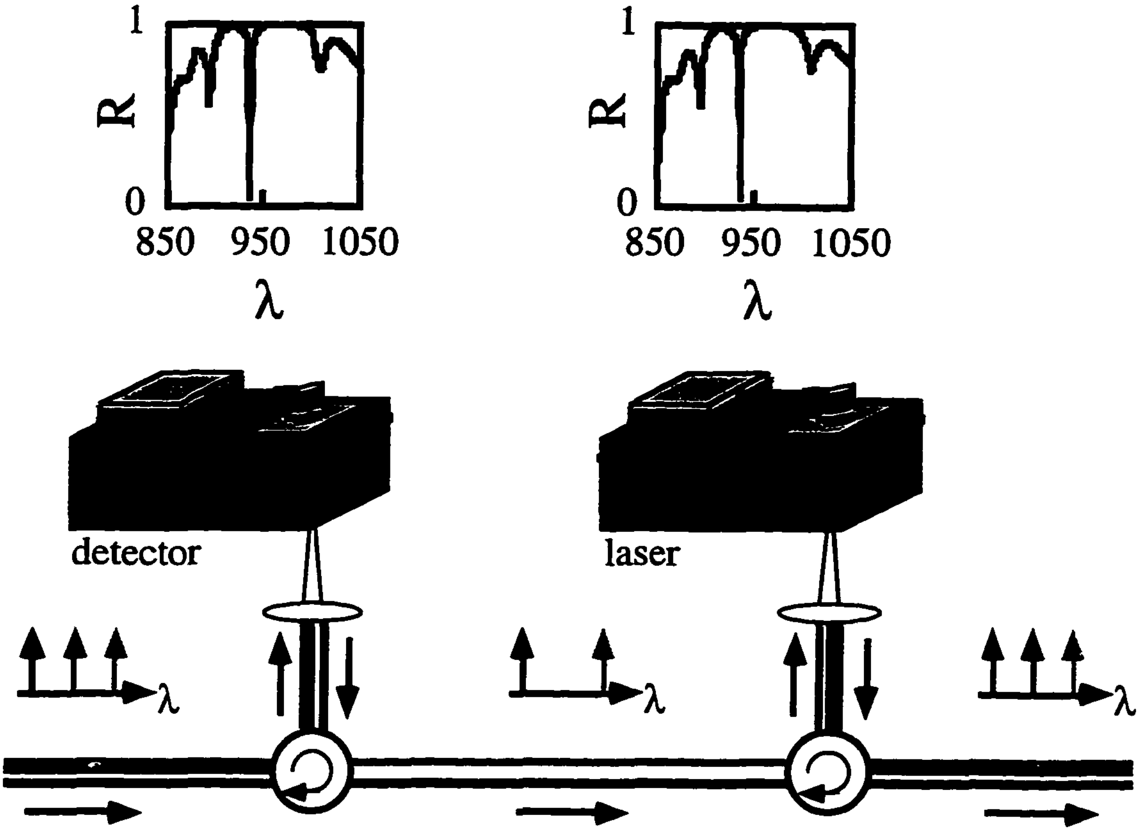


*Figure 1.1 - Demonstration of the Add/Drop feature of vertical cavity structures when used in conjunction with an optical circulator. All wavelengths of light are reflected except for the resonance wavelength of the tunable detector or laser. This allows a single wavelength to be removed (left side) or added (right side).*

wavelength could then act as a reconfigurable ring, containing as many or as few of the nodes as desired.

### 1.1.2 Board to Board Interconnects

Increasingly, the interconnects between chip limit the performance of today's computers. Electrical interconnects have limited speed due to RC time constants and suffer from electrical interference. Both of these problems worsen as the length of the interconnect increases. On the other hand, the capacitance of optical interconnects does not increase with length and interference between optical signals is insignificant. Thus, optical interconnects are used for long distances. Recently, they have also been implemented for shorter and shorter links which could eventually reach the board to board or chip to chip level inside

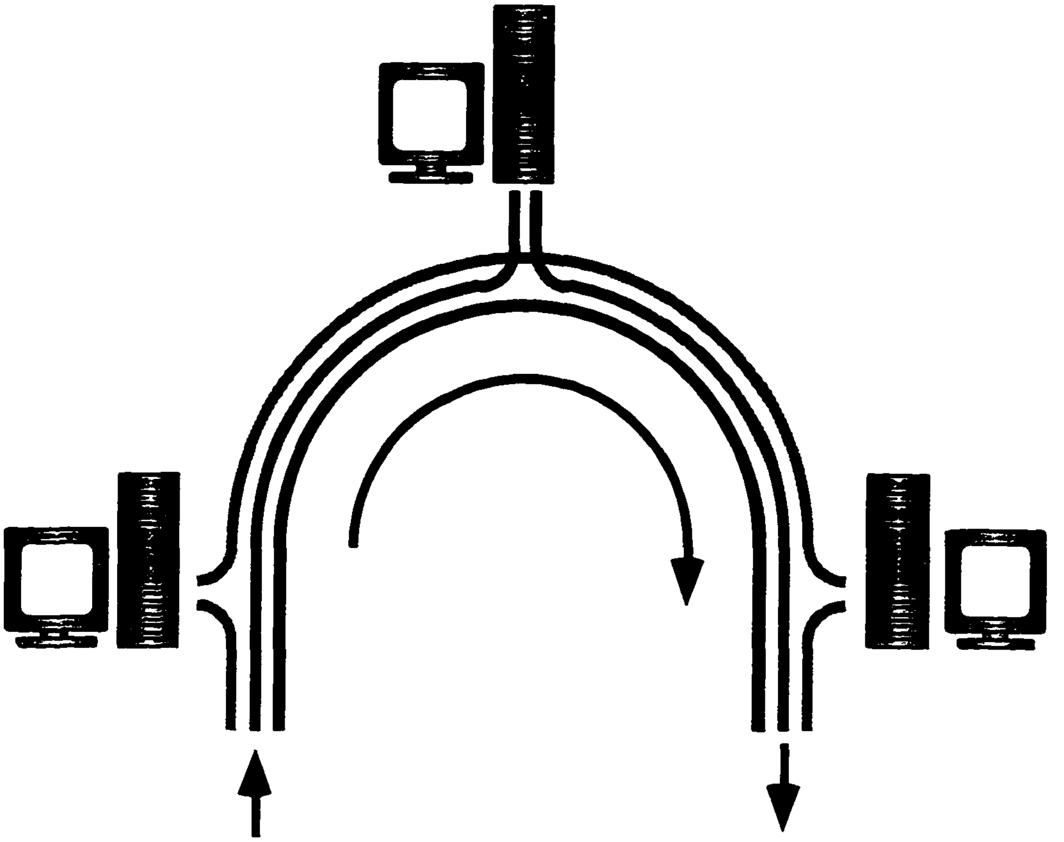

*Figure 1.2 - Schematic of a simple WDM network using the scheme of Figure 1.1.*

computers. Optical interconnects are also advantageous because a large number of interconnections can be completed using a single lens.

Figure 1.3 shows optical interconnects where chips are stacked one on top of another[7]. Each chip detects certain wavelengths while passing others. In this way, different boards can be addressed by changing the wavelength. By using the tunable laser of Chapter 5, such a system would be reconfigurable. The devices are ideally suited to the task, since it is surface normal and compact.

### 1.1.3 Spectroscopy

Spectroscopy is a tool that is often used in the laboratory. However, the number of everyday applications has been limited by the large cost of spectrometers. The tunable filters discussed in Chapter 2 could be used to make low-cost, hand-held, battery-operated spectrometers useful in a variety applications: color matching and quality control for paint, textiles, displays, and

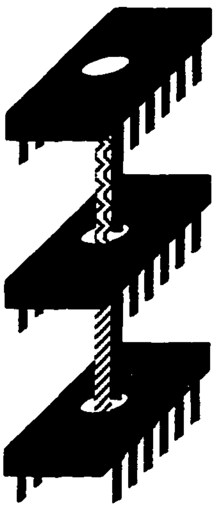

*Figure 1.3 - Schematic of chip to chip optical interconnects. Different wavelengths are used to address different boards in the system.*

printers; field instruments for biological and geological applications; and test instruments for the WDM networks described above. The tunable filters would represent a tiny fraction (probably only a few dollars) of the overall instrument cost.

The tunable laser of Chapter 5 could be used to measure narrow linewidth resonances. This could be useful in measuring emissions in automotive or industrial applications. The narrow linewidth of lasers allows very precise spectroscopy to be performed. The measurements could be performed by shining the output beam through the medium to be probed, or by allowing the gas to be probed into the tunable air gap and placing a detector on board. The latter method would increase the sensitivity of the measurement by the Q of the cavity (~200), although the interaction length would also be limited (2 μm). The intracavity technique could be implemented in a very compact device by integrating the detector on the same chip as the laser.

### 1.1.4 Beam steering

A long standing goal in optics is beam steering, the ability to control the direction of a beam of light. This would be useful for many existing applications such as laser printers, CD players, and supermarket checkouts. It would also enable new applications for lasers, such as displays. Presently beam steering is achieved with a spinning mirror or a galvanometer. These macroscopic systems have potential reliability problems, high cost, limited speeds, and high tuning power.

Beam steering can also be achieved using a tunable source and a dispersive element, such as a diffraction grating or a prism. By tuning the wavelength of the source, the direction of propagation can be changed. For many applications, the changing wavelength of the source has no undesirable effects.

In theory, the number of resolvable spots is limited by the linewidth of the source and the tuning range. For the tunable laser in Chapter 5 with 19.1 nm of tuning and a line width on the order of 1 GHz, that means approximately 6000 resolvable spots. This is enough to print a 20" line at 300 dots per inch. In practice, the number of resolvable spots will be limited by the resolution of the dispersive element. Assuming a typical resolution of 1 Å, the number of resolvable spots becomes 191. This is still enough to print a 1/2" line at 300 dpi and could be useful in some printing applications. As the tuning range is increased with improved devices, the number of resolvable spots will increase.

### 1.1.5 Broad bandwidth applications

A number of applications, such as fiber gyros and optical low coherence reflectometry (OLCR), require a broad bandwidth source in a single spatial mode. A rapidly tunable source can be used in place of a true broad bandwidth source in many cases. The micromechanical tunable VCSEL of Chapter 5 has the potential to be a highly efficient source for these applications.

## 1.2 Existing tunable devices

The usefulness of tunable lasers has made them the target of much research. This section discusses past devices to put this thesis in context.

### 1.2.1 Bulk optics

Commercial tunable lasers are made using bulk optics. In these lasers, a tunable element (such as a grating or a etalon) is used to select one wavelength for lasing from a broad range of possible lasing wavelengths. These systems are sensitive to alignment and also to vibrations. They are also expensive, costing approximately $10,000. Since tuning is achieved by moving a macroscopic element, the speed is slow and the required tuning power substantial. These systems are typically also large, on the order of a cubic foot.

An additional problem with these systems is that they do not naturally continuously tune, but hop between the wavelengths of the cavity modes. This problem is corrected through more complicated designs. If a diffraction grating is used as one of the end mirrors, it can be made to move while it also changes angle. With the right ratios of movement, the Fabry-Perot mode can be made to tune at the same rate as the reflected wavelength. However, this imposes severe alignment tolerances, and it is not unusual for one or two mode hops to still take place.

### 1.2.2 Semiconductor - simple tuning

Because of these problems with bulk tunable devices, the need for an integrated tunable laser was realized early on. In addition to the dramatic reductions in size and cost, vibration sensitiviey would be reduced becuase of the solid, compact design, and tuning could potentially be electronically controlled.

Most tuning applications require a narrow, single mode spectrum. As a result, wavelength filters such as those used in DFB or DBR lasers must be used. These fix the wavelength using periodic structures. To tune the wavelength, it is necessary to change the effective periodicity of these structures. This is accomplished by changing the refractive index of the material.

There are three mechanisms that change the refractive index and have been used to tune monolithic semiconductor lasers: the electro-optic effect, temperature, and carrier injection. The electro-optic effect has produced 1 % tuning of refractive index[8], but with high losses. It is theoretically capable of very high speeds, since the RC time constant is ~100 GHz. Temperature changs the refractive index approximately 1%, but is slow and causes large changes in the threshold current and the output power. Carrier injection tuning is theoretically fast (ns) and can induce a 1% shift in refractive index without the deleterious effects of temperature tuning. It is the most popular mechanism used for tuning.

However, the 1% change in refractive index for carrier injection limits the amount of tuning. Simple structures tune proportional to the change in refractive index and are limited to 1% tuning[9]. If larger refractive index changes could be made, there is no reason semiconductor lasers could not tune over the entire gain bandwidth (~10%).

Carrier injection also requires a fair amount of power to tune. Since the tuning is current controlled, mW's of power is required to maintain a fixed wavelength. This power consumption can also limit tuning time due to slow thermal effects. Unless excellent heat sinking is provided, the device tunes quickly at first due to carrier injection, but then drifts slowly due to thermal effects.

### 1.2.3 Widely tunable structures

Several novel structures which leverage the carrier injection refractive index change to tuning beyond 1% have been developed. The three most popular are the Y-junction[10-], the sampled grating, and the vertical coupled filter[12]. These clever structures have achieved tuning limited only by the semiconductor gain bandwidth (~10%), but none of these techniques can provide continuous tuning of lasers. Instead, the lasers must hop from mode to mode. The modes are often closely spaced, so this hopping is not always apparent, but it can nonetheless seriously effect the stability and noise properties of the device. For example, mode partition noise is a common problem, in which the total power of a laser is constant but the proportion in each mode changes. This problem may not be apparent from the output with a power meter, but can cause large fluctuations in power after propagating through a system. In addition, many of the problems are absent at a certain DC bias but reappear under modulation, different environmental conditions, or a different DC bias.

Another problem with these widely tunable structures is they have multiple tuning contacts. A tuning contact is required to tune the Fabry-Perot modes to reach all possible wavelengths. A vertical coupled filter requires an additional contact to select the Fabry-Perot mode, while the sampled grating and Y-junction lasers require two additional contacts to tune. With all these different contacts, biasing the devices is complicated and can change with temperature, aging, bias point, and modulation.

In addition, the fabrication of the two structures that work the best, the sampled grating and the vertical coupled filter, is also complicated. Typically, e-beam lithography and at least one regrowth are required.

Since all widely tunable devices are edge-emitting, they do not naturally have symmetric beams for easy fiber coupling. Precise cleaving and high reflectivity coating are also commonly required, increasing costs. The finished device is also usually at least 1 mm long, taking up valuable space on a sample.

Finally, none of these techniques transfers very well to tunable filters and detectors. The sampled grating device cannot be used as a filter at all. The Y-junction has not yet been implemented as a tunable filter. The vertical coupled filter has problems achieving high extinction ratios and narrow bandwidths. Inside a laser, these effects are less noticeable, since the laser automatically selects out the mode with the lowest loss and suppresses all the others. However, in a tunable filter extinction ratio directly determines the crosstalk of the system. Twenty or thirty dB side mode suppression ratios are typically required and the 10 dB achievable[13] with these devices is insufficient. Finally, these devices are polarization sensitive. This can greatly increase system complexity since it necessitates the use of polarization maintaining fiber.

## 1.3 Micromechanical tunable devices

This thesis will discuss a radically different method of achieving wide tuning based on vertical cavities and micromechanical movement. This method has wide, continuous tuning with a host of other advantages discussed in this section.

### 1.3.1 Vertical cavities

Commercial semiconductor lasers are edge-emitting. In an edge emitter the light propagates parallel to the surface of the chip. The chip is cleaved on two sides which act as mirrors to form a cavity. About a decade ago, a new structure, a vertical cavity laser, was successfully fabricated[14]. In this structure, the light propagates normal to the surface of the chip. High reflectivity mirrors are formed by growing many layers to form a distributed bragg reflector (DBR). Since then, performance has steadily improved, with threshold currents now as low as 38 μA[15], wall plug efficiencies as high as 59%[16], and single mode powers of several mW, albeit not all within the same device.

Vertical cavity structures have several advantages over edge-emitting structures. Because the cavity length in vertical cavities is so much shorter (~μm), they have only a single longitudinal mode which can lase. Due to their symmetry, vertical cavities have a circular mode which is easy to couple into fibers. This also makes them polarization-insensitive as filters or detectors. Because vertical cavities do not require cleaved facets, they have the potential for reducing packaging costs. The devices also have a small size, making higher throughput per wafer possible. Their surface normal operation makes fabrication into 2-D arrays easy and makes them attractive for optoelectronic applications.

Several groups have already attempted to tune vertical cavity surface emitting lasers (VCSELs) using temperature[17–19], carrier injection[20], or external cavities. Since only a single mode exists in a vertical cavity, continuous tuning is easily achieved simply by directly tuning this mode's wavelength. Carrier injection tuning has been limited to 0.5 Å of tuning. This is much lower than 1%, because not all the layers of a VCSEL structure can be injected with carriers and unintentional heating counteracts carrier injection tuning. Temperature has been used to tune VCSELs 10.1 nm (1%), but with severe changes in the LI curve for the device and slow speeds.

### 1.3.2 Micromechanical tuning

To increase the tuning of vertical cavity structures, the devices described in this thesis will use a new mechanism, micromechanical tuning. That is, the spacing between the two mirrors is physically changed using flexible micromechanical structures. This method is not limited by material properties, since, in theory, there is no limit to the mirror's movement.

Recently, micromachining and micromechanical systems have received considerable attention[21,22]. Micromachining has primarily been performed on silicon substrates using films of silicon nitride, silicon dioxide, and polysilicon. A wide variety of devices have been fabricated including optical modulators[23,24], motors, flow meters, resonators for clocks, mirrors, lenses, beam steering elements, accelerometers, atomic force microscope heads[25], pressure sensors, voltage sensors[26], and displays[27-29]. However, the optical use of silicon micromachines is limited by two factors. First, silicon is an indirect bandgap semiconductor. This means it is unsuitable for devices that give off light, such as lasers or LEDs. Second, no lattice-matched semiconductor which can be grown on silicon exists. As the GaAs and InP material systems have shown, the ability to grow different materials is useful for fabricating mirrors and waveguides, for selective etchants, for selective oxidations, and for bandgap engineering. In this thesis, we use GaAs based devices to bring the innovations of micromachining to active optical devices and the benefits of heteroepitaxy to micromachining.

Micromechanical tuning has none of the disadvantages of mechanical tuning with bulk optics. Because electrostatic attraction is used to move the mirrors, tuning is achieved simply by applying a voltage. Only μW of tuning power is required. Since the device is integrated, the cost is low and no alignment is required. The tuning time is quite rapid (~μs) because of the high frequency of the mechanical resonances of the device. Since single crystalline material is used to tune, and it is strained well below the yield point, the lifetime of the device is long. The devices are also insensitive to vibration due to their low mass and high stiffness.

The devices discussed in this thesis are all in the 900-1000 nm wavelength range, where it is easiest to make VCSELs and vertical cavity structures. However, VCSELs have been made with wavelengths as short as 640 nm[30] on GaAs substrates and at the important communication wavelengths of 1.3 μm[31] and 1.55 μm[32,33] using diffusion bonding of InP substrates to GaAs. It should be possible to take the techniques of this thesis and make tunable VCSELs at these wavelengths as well. Tunable filters and detectors can go even further; using different materials, filters from the visible to the mid-infrared should be possible.

## 1.4 Summary

This thesis will demonstrate tunable filters, detectors, and lasers based on the micromechanical tuning of vertical cavity structures. Even though this is the first demonstration for many of these devices, they demonstrate larger continuous tuning than existing technologies. We show that the results match predictions for calculations and show how these devices can be designed. Lifetime, polarization, tuning speed, near field, tuning range, and LI measurements are recorded to confirm the expected benefits of micromechanical tuning. This thesis demonstrates micromechanical tuning is a viable technology, and shows its potential for much improved performance in the future.

## 1.5 References

[1] C. A. Brackett, "Dense wavelength division multiplexing networks: principles and applications," *IEEE J. Sel. Areas Commun.*, vol. 8, no. 6, p. 948-964, 1990.

[2] B. P. Lathi, *Modern Digital and Analog Communication Systems*, Holt, Rinhart and Winston, Inc, p. 345, 1989.

[3] L. G. Kazovsky, *Optical Fiber Communication Systems*, Artech House, Boston, 1996.

[4] M. Koga, "Compact quartzless optical quasi-circulator," *Electron. Lett.*, vol. 30, no. 17, p. 1438-40, 1994.

[5] G. W. Pearson, and J. S. Krasinski, "Design for a low-loss polarization independent all-fiber optical circulator for bid-directional fiber communications," *SPIE Vol. 1792, Components for Fiber Optic Applications VII*, p. 37-42, 1992.

[6] M. Koga, and T. Matsumoto, "High-isolation polarization-insensitive optical circulator for advanced optical communication systems," *J. of Lightwave Tech.*, vol. 10, no. 9, p. 1210-7, 1992.

[7] G. Giaretta, G. S. Li, W. Yuen, C.J. Chang-Hasnain, "Novel wavelength-selective single-mirror resonant detector", Conference on laser and elecro-optics(CLEO96) technical digest series, Vol. 9.

[8] Z. M. Chuang, and L. A. Coldren., "Enhanced Wavelength Tuning in Grating-Assisted Codirectional Coupler Filter," *IEEE Photon. Technol. Lett.*, vol. 5, no. 10, p. 1219-1221, 1993.

[9] T. L. Koch, and U. Koren, "Semiconductor Lasers for Coherent Optical Fiber Communications," *J. of Lightwave Technol.*, vol. 8, no. 3, p. 274-293, 1990.

[10] M. Kuznetsov, P. Verlangieri, A. G. Dentai, C. H. Joyner, and C. A. Burrus, "Widely tunable (45 nm, 5.6 Thz) Multi-Quantum-Well Three-Branch Y3-Lasers for WDM Networks," *IEEE Photon. Technol. Lett.*, vol. 5, no. 8, p. 879-882, 1993.

[11] Y. Tohmori, Y. Yoshikuni, H. Ishii, F. Kano, T. Tamamura, Y. Kondo, and M. Yamamoto, "Broad-Range Wavelength-Tunable Superstructure Grating (SSG) DBR Lasers," *IEEE J. of Quantum. Electron.*, vol. 29, no. 6, p. 1817-1823, 1993.

[12] R. C. Alferness, U. Koren, L. L. Buhl, B. I. Miller, M. G. Young, T. L. Koch, G. Raybon, and C. A. Burrus, "Broadly tunable InGaAsP/InP laser based on a vertical coupler filter with 57-nm tuning range," *Appl. Phys. Lett.*, vol. 60, no. 26, p. 3209-3211, 1992.

[13] G. Griffel, and A. Yariv, "Frequency Response and Tunability of Grating-Assisted Directional Couplers," *IEEE J. of Quantum Electron.*, vol. 27, no. 5, p. 1115-1118, 1991.

[14] K. Iga, F. Koyama, and S. Kinoshita, "Surface Emitting Semiconductor Lasers," *IEEE J. of Quantum Electron.*, vol. 24, no. 9, p. 1845–55, 1988.

[15] D. L. Huffaker, L. A. Graham, H. Deng, and D. G. Deppe, "Sub-40 μA Continuous-Wave Lasing in an Oxidized Vertical-Cavity Surface-Emitting Laser with Dielectric Mirrors," *IEEE Photon. Tech. Lett.*, vol. 8, no. 8., p. 974-6, 1996.

[16] B. Weigl, G. Reiner, M. Grabherr, and K. J. Ebeling, "Oxidised GaAs QW vertical-cavity lasers with 40% power conversion efficiency," *Electron Lett.*, vol. 32, no. 19, p. 1784-6, 1996. This paper only describes 40% wall plug efficiency, obviously. However, this same group reported 59% wall plug efficiency as a post-deadline paper at ISLC 96 in Haifa, Isreal.

[17] C. J. Chang-Hasnain, J. P. Harbison, C. E. Zah, L. T. Florez, and N. C. Andreadakis, "Continuous wavelength tuning of two-electrode vertical cavity surface emitting lasers," *Electron. Lett.*, vol. 27, no. 11, p. 1002-1003, 1991.

[18] P. R. Berger, N. K. Dutta, K. D. Choquette, G. Hasnain, and N. Chand, "Monolithically Peltier-cooled vertical-cavity surface-emitting lasers," *Appl. Phys. Lett.*, vol. 59, no. 1, p. 117-119, 1991.

[19] L. Fan, M. C. Wu, H. C. Lee, and P. Grodzinski, "10.1 nm range continuous wavelength-tunable vertical-cavity surface-emitting lasers," *Electron. Lett.*, vol. 30, no. 17, pp. 1409-1410, 1994.

[20] C. Gmachi, A. Kock, M. Rosenberger, E. Gornik, M. Micovic, and J. F. Walker, "Frequency tuning of a double-heterojunction AlGaAs/GaAs-vertical-cavity surface-emitting laser by a serial integrated in-cavity modulator diode," *Appl. Phys. Lett.*, vol. 63, no. 3, p. 219-221, 1993.

[21] P. D. Deimel, "Micromachining Processes and Structures in micro-optics and optoelectronics," *J. Micromech. Microeng.*, vol. 1, p. 199-222, 1991.

[22] C. Linder, L. Paratte, M.-A. Grétillat, V. P. Jaecklin, and N. F. de Rooij, "Surface Micromachining," *J. Micromech. Microeng.*, vol. 2, p. 122-32, 1992.

[23] W. R. Wiszniewski, R. E. Collins, and B. E. Pailthorpe, "Mechanical Light Modulator Fabricated on a Silicon Chip Using SIMOX Technology," The 7th International Conference on Solid-State Sensors and Actuators, p. 1027-30.

[24] O. Solgaard, F. S. A. Sandejas, and D. M. Bloom, "Deformable Grating Optical Modulator," *Optics Letters*, vol. 17, no. 9, p. 688-90, 1992.

[25] J. Brugger, N. Blanc, Ph. Renaud, and N. F. de Rooij, "Capacitive AFM Microlever with Combined Integrated Sensor/Actuator Functions," The 7th International Conference on Solid-State Sensors and Actuators, p. 1044-7.

[26] Z, Xiao, S. Norman, and O. Engström, "A Novel Microstructure Sensor For Voltages on High Potentials or Low Pressures," The 7th International Conference on Solid-State Sensors and Actuators, p. 1023-1026.

[27] J. M. Younse, "Mirrors on a Chip," *IEEE Spectrum*, p. 27-31, Nov. 1993.

[28] K. E. Peterson, "Micromechanical Light Modulator Array Fabricated on Silicon," vol. 31, no. 8, p. 521-23, 1977.

[29] L. J. Hornbeck, "Deformable-Mirror Spatial Light Modulators," SPIE vol. 1150, Spatial Light Modulators and Applications III, p. 86-102, 1989.

[30] K. D. Choquette, R. P. Scheider, Jr., M. Hagerott Crawford, K. M Geib, and J. J. Fiegel, "Continuous wave operation of 640-660nm selective oxidized AlGaInP vertical-cavity lasers," *Electron. Lett.*, vol. 31, p. 1145-6, 1995.

[31] Y. Qian, Z. H. Zhu, Y. H. Lo, H. Q. Hou, M. C. Wang, and W. Lin, "1.3 μm Vertical Cavity Surface-Emitting Lasers with Double-Bonded GaAs-AlAs Bragg Mirrors," *IEEE Photon. Tech. Lett.*, vol. 9, no. 1, p. 8-10, 1997.

[32] Y. Ohiso, C. Amano, Y. Itoh, K. Tateno, T. Tadokoro, H. takenouchi, and T. Kurokawa, "1.55 μm vertical-cavity surface-emitting lasers with wafer-fused InGaAsP/InP-GaAs/AlAs DBRs," *Electron. Lett.*, vol. 32, no. 16, p. 1483-1484, 1996.

[33] N. M. Margalit, D. I Babic, K. Streubel, R. P. Mirin, R. L. Naone, J. E. Bowers, and E. L. Hu, "Submilliamp long wavelength vertical cavity lasers," *Electron. Lett.*, vol. 32, no. 18, p. 1675-7, 1996.

# 2. Micromechanical Tunable Filters

As we saw in the previous chapter, many applications require a tunable filter including, WDM communications [1], optical interconnects, and low cost spectroscopy. Simple tunable filters have limited tuning range[2]. Ironically, there are fewer semiconductor widely tunable filters available than widely tunable lasers. Many techniques for increasing the tuning of lasers do not work for filters. For example, the sampled grating tunable laser cannot function as a tunable filter. Tunable lasers which do use tunable filters have less stringent requirements on the filter compared to WDM communication requirements. This is because the nonlinearity of the laser enhances the changes in loss between various modes. For example, the grating coupled waveguide tunable laser uses a tunable filter[3,4] inside of it, but it has been difficult to demonstrate extinction ratios higher than 10 dB and bandwidths narrower than a few nm with this filter.

Alternative monolithic tunable technologies have other disadvantages. Acousto-optic tunable filters[5,6] require watts of power, are typically polarization sensitive, and would probably be expensive to manufacture due to the large chip size. Continuously tunable Liquid crystal[7,8] filters are slow, temperature sensitive, and polarization sensitive. Mach-Zender tunable filters[9]. are not continuously tunable, are polarization sensitive, and require a large chip area.

This chapter presents a micromechanical tunable filter[10] which is compact, widely and continuously tunable, surface normal, cost-effective, demonstrates high extinction ratios, and narrow bandwidths. The filter has 70 nm of continuous tuning using 4.9 V and 50 pA of tuning voltage and current, respectively. To the best of our knowledge, this is the widest continuous tuning range of a semiconductor tunable filter using a single tuning mechanism.

Furthermore, the device is polarization insensitive and suitable for use with multi-mode fibers. The surface-normal structure is naturally fabricated as a 2-D array and is optimal for fiber coupling. The device fabrication process is simple and high yield, requiring only two non-critical lithography steps.

In addition to being useful in their own right, tunable filters are a stepping stone towards more complicated micromechanical tunable Fabry-Perot devices. The tunable detectors and lasers of later chapters build off the work of this chapter. For this reason, this chapter covers a wide range of topics: tuning speed, polarization properties, lifetime, tuning voltage, and tuning properties.

## 2.1 Principle of Operation

A schematic of the device is shown in Figure 2.1. A Fabry-Perot cavity is formed between two AlGaAs distributed bragg reflector (DBR) mirrors with the upper DBR, mirror freely suspended 1.2 μm above the substrate by a cantilever. *Modern Optics* by Hecht and Zajak provides a good review of Fabry-Perots and DBRs if these are unfamiliar. Put simply, the DBRs can be thought of as partially reflecting mirrors. These are spaced a few microns apart, facing each other to form what is called a Fabry-Perot cavity. Most light is reflected from such a structure. However, if an integral number of half wavelengths fit into the cavity and the mirrors are equally reflecting, all the light is transmitted. In this way a Fabry-Perot can act as a filter, transmitting one wavelength of light but reflecting all others.

The upper DBR mirror and substrate are doped to form a *pn* junction. This is reverse biased by applying a voltage to the Au contact pad and the substrate. As a voltage is applied, electrostatic attraction causes deflection of the cantilever towards the substrate. Deflection of only 0.33 μm causes the Fabry-Perot resonance wavelength to tune from 970 nm to 900 nm. Consequently, during normal operation, the cantilevers do not contact the substrate; sticking problems which have been observed in other micro-machines are thus avoided.

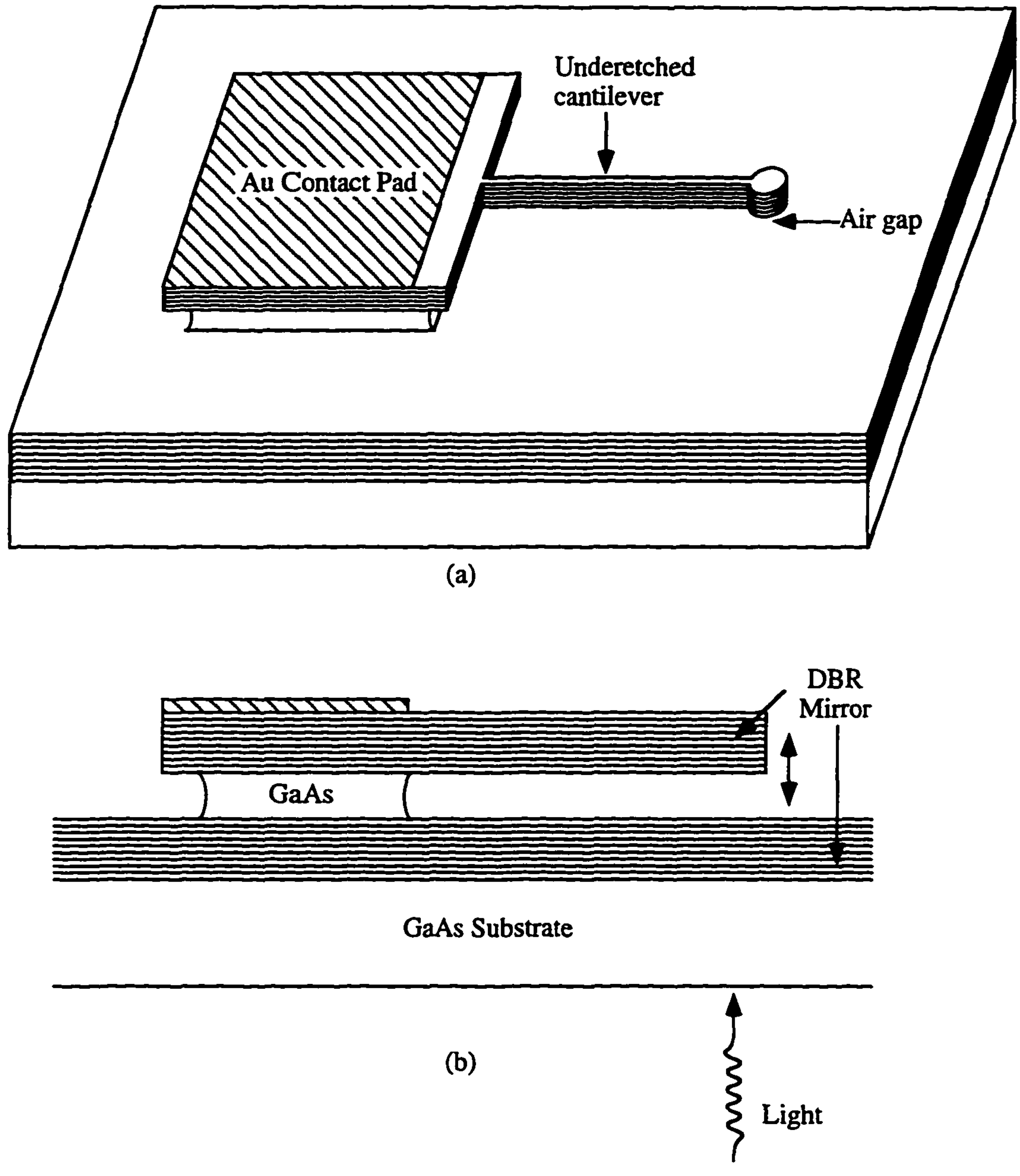


*Figure 2.1 - Schematic of the micromechanical tunable filter. (a) 3-d view (b) side view.*

## 2.2 Layer Structure and Growth

The first step in designing the filter is to determine the layer compositions and thicknesses for the mirrors and cavity. To do this, we used a reflectivity calculation program written by a member of our group[11]. This program generates the reflectivity spectrum for a set of layers. Each layer's thickness, composition, and loss are specified. The program then calculates the refractive index at each wavelength.

Using this program, we modeled the final layer design of the filter. The structure consists of a *p*-doped 12.5 mirror pair $Al_{0.09}Ga_{0.91}As/Al_{0.58}Ga_{0.42}As$ DBR with the top pair of layers $p^+$-doped for good contacts, an undoped 1.2 μm GaAs sacrificial layer, an *n*-doped $Al_{0.09}Ga_{0.9}As$/AlAs mirror pair, and a 9 pair *n*-doped AlAs/GaAs distributed bragg reflector (DBR). The GaAs layer is etched away during fabrication and tuning is achieved by changing the length of the remaining air gap.

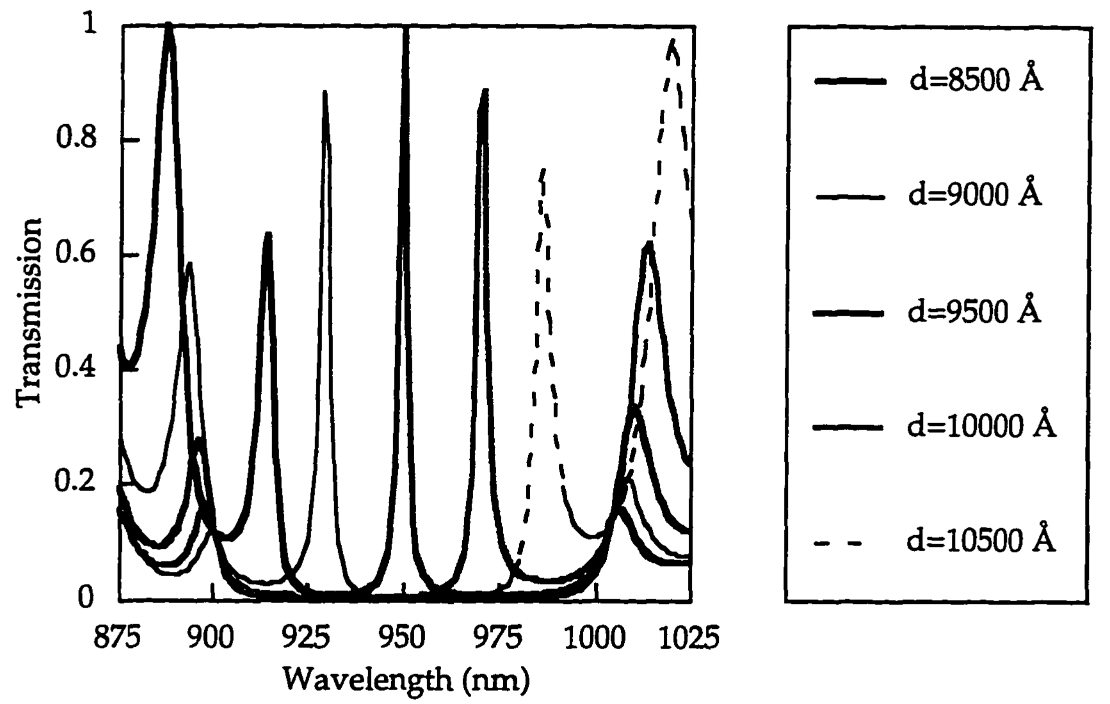


*Figure 2.2 - Calculated filter response (substrate absorption not taken into account).*

Figure 2.2 shows the transmission calculated for the tunable filter. The Fabry-Perot peak shifts from 986 nm to 915 nm, as the air gap is changed from 1.05 μm to 0.85 μm, achieving ~70 nm of tuning with a 2 nm FWHM bandwidth. Figure 2.2 also shows the finite reflectivity band of the DBR mirrors. For wavelengths larger than 1000 nm or smaller than 900 nm, the DBRs are not highly reflective and light is transmitted.

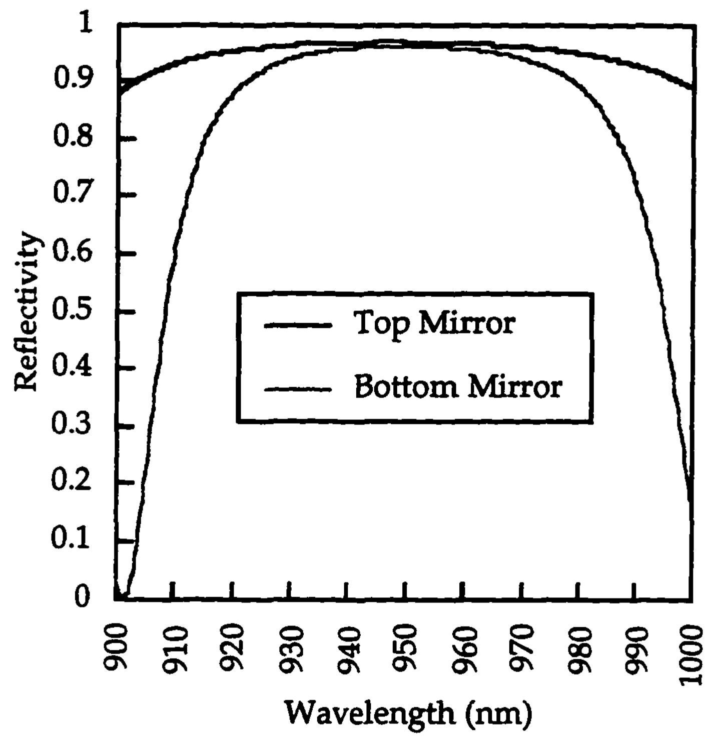


*Figure 2.3 - Top and bottom mirror reflectivity for the tunable filter.*

In Figure 2.2, not all of the Fabry-Perot peaks have 100% transmission. To get perfect transmission, the top and bottom mirror reflectivities must be matched. However, Figure 2.3 shows these reflectivities have different curvatures with wavelength. The reflectivities can only be matched at discrete

*Table 2.1 - Table of various tunable air gap thicknesses and their corresponding Fabry-Perot wavelengths and mirror reflectivities.*

| $d$(Å) | $d/d_0$ | $\lambda$ (nm) | $R_{top}$ | $R_{bottom}$ |
|---|---|---|---|---|
| 11000 | 0.92 | 995 | 0.911 | 0.501 |
| 10500 | 0.88 | 986 | 0.938 | 0.813 |
| 10000 | 0.83 | 971 | 0.959 | 0.936 |
| 9500 | 0.79 | 950 | 0.968 | 0.962 |
| 9000 | 0.75 | 929 | 0.963 | 0.937 |
| 8500 | 0.71 | 915 | 0.945 | 0.803 |
| 8000 | 0.67 | 907 | 0.920 | 0.391 |

wavelengths (in this case at the center wavelength of 950 nm). Table 2.1 summarizes the tuning and reflectivities for the tunable filter.

This problem could be corrected by matching the curvature of the reflectivities. Unfortunately, we cannot simply use the same structure for the top and bottom mirrors because the top mirror exits into air while the bottom mirror exits into GaAs. The refractive index difference of the layers determines the curvature of the DBR reflectivity. Because the refractive index difference of the top air/AlGaAs interface is so large ($n_{air}$=1, $n_{GaAs}$=3.5), it greatly reduces the curvature of the top mirror reflectivity. This is partly (but not completely) compensated by the smaller composition difference of the top DBR mirror pairs ($Al_{0.09}Ga_{0.91}As$/$Al_{0.58}Ga_{0.42}As$) compared to the bottom pairs (AlAs/GaAs). In the future, an even smaller composition difference or a mixture of 1/4 and 31/4 layers in the top mirror pairs could be used to match the curvature.

The layer structure was grown by MBE on an *n*-doped substrate. The resulting single crystalline material is excellent for micromachining since it is reproducible and has excellent mechanical properties[12].

## 2.3 Fabrication

Figure 2.4 summarizes the fabrication steps of the tunable filter. First photoresist is patterned into cantilevers of a variety of different widths(2 μm, 4 μm, and 6 μm), lengths(25 μm, 50 μm, 75 μm, and 100 μm ), and end circle diameters(10 μm, 15 μm, and 20 μm). A $SiCl_4$ anisotropic dry etch is used to etch down to the sacrificial GaAs layer. An isotropic selective dry etch then etches the sacrificial layer[13]. This etch adds $SF_6$ to $SiCl_4$ to passivate AlGaAs surfaces and reduce the DC bias of the plasma from 180 Volts to 30 Volts. Figure 2.5 shows a scanning electron microscope (SEM) image of a test structure after going through this etch. The etching selectivity is excellent, with no detectable etching of the AlGaAs. Furthermore, the use of dry etching eliminates surface tension collapse observed with wet etching[14]. Using a wire mesh of 100 μm wires with 254 μm spacing as a shadow mask, gold squares are evaporated on the contact pads.

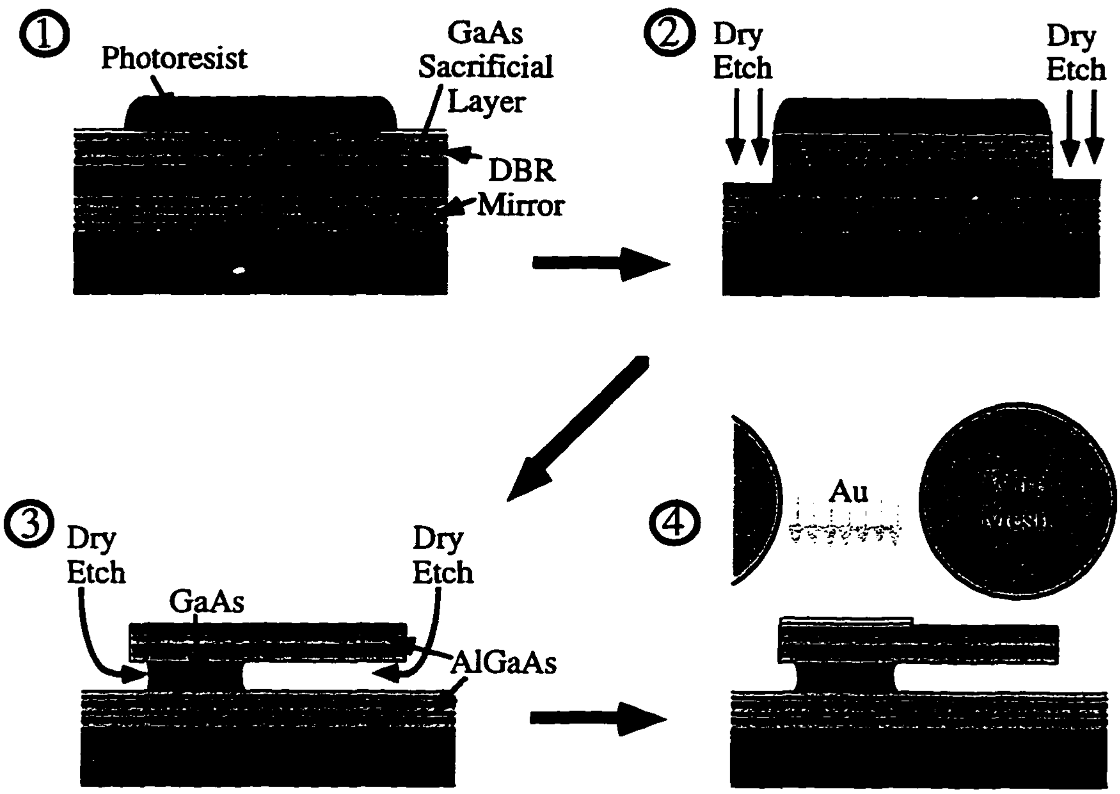


*Figure 2.4 - Summary of the major fabrication steps for the micromechanical tunable filter.*

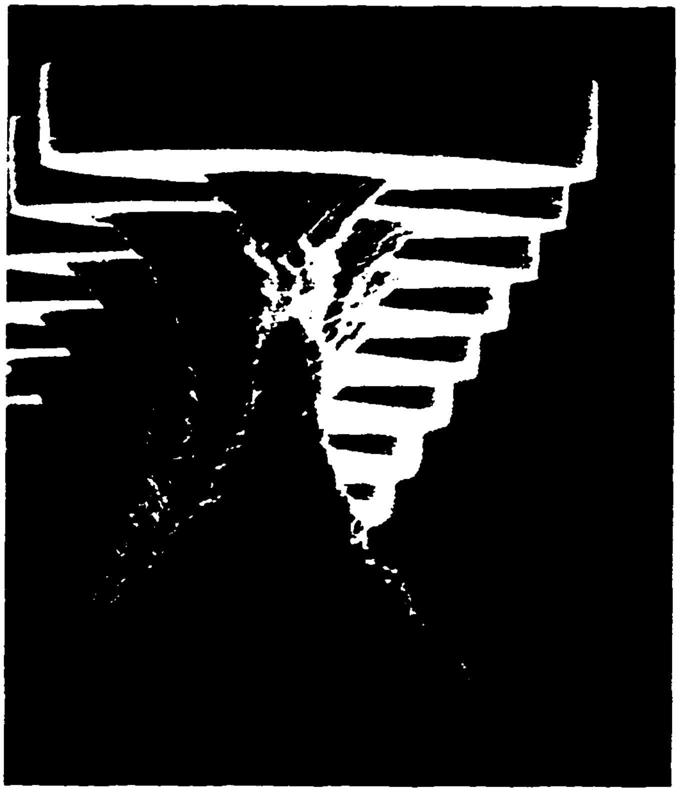

*Figure 2.5 - 20 μm diameter $Al_{0.3}Ga_{0.7}As$ disks which have been undercut by the selective dry etch.*

Figure 2.6 shows an early problem that had to be overcome. This structure used pure AlAs in the cantilever. When the etches were first completed the structure looked fine. However, after a couple weeks the structure looked like the figure. AlAs slowly oxidizes in air, which causes it to expand and crack. By lowering the Al concentration to $Al_{0.6}Ga_{0.4}As$ in the cantilever this problem is avoided.

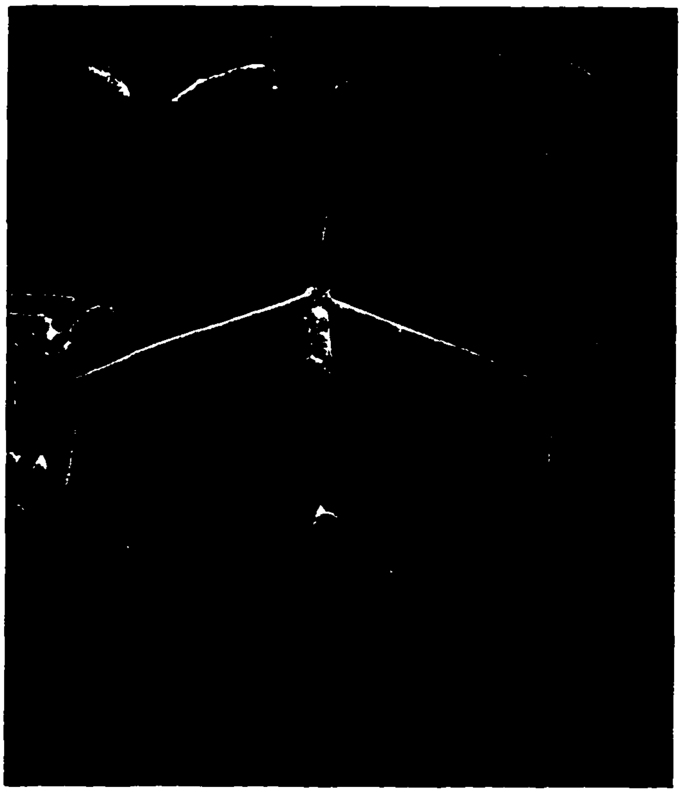

*Figure 2.6 - An AlAs structure after a few days in air. This problem is corrected by not using high Al concentration AlGaAs (Al <0.6).*

Figure 2.7 shows an SEM photograph of some completed devices. The large squares on the left are the contact pad used to apply the tuning voltage. Because the contact pad is much larger than the end circle, it is not completely underetched and holds the cantilevers up. The array of circles to the right is a test structure for measuring etch undercut. Each circle's diameter is 1 μm different from its neighbors. When a circle is completely undercut, it falls to the substrate. This can be observed under a optical microscope or a SEM. The completely undercut circles appear dark because they are in poor contact to the substrate. In Figure 2.7, only the largest three circles have not fallen. This provides an easy way to tell when the cantilevers have been completely undercut.

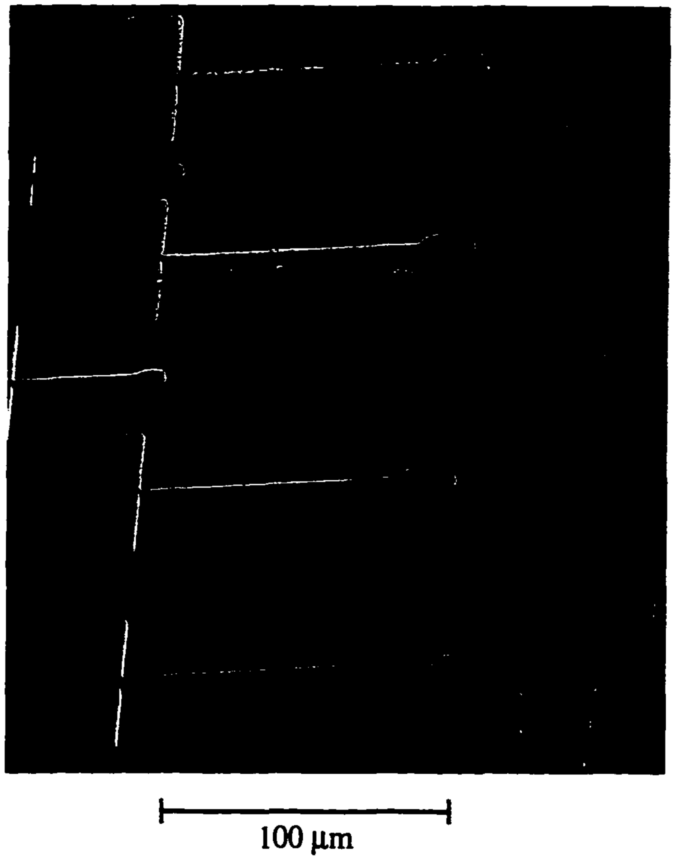


*Figure 2.7 - Completed micromechanical tunable filters. The large squares at the left support the cantilever and act as the tuning contact. There are several devices shown here, all 100 μm long. The cantilever widths vary from 2 to 6 μm and the end circles have 20 μm diameter, except for the device at the bottom, which has a 15 μm diameter.*

The fallen circles are easier to see in Figure 2.8. This shows an undercut cantilever looking end on. As can be seen, it is held over the substrate by the cantilever. In the foreground, some test circles are visible. The ones on the right are slightly larger and have not completely been undercut. The circles on the left have been completely undercut and have fallen to the substrate.

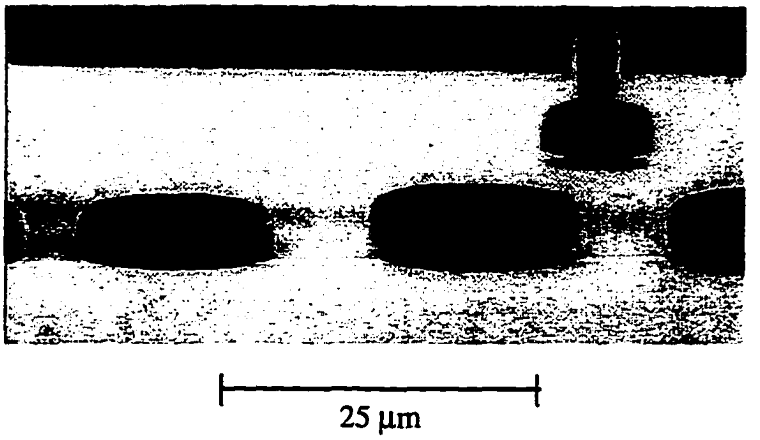


*Figure 2.8 - End on view of an undercut cantilever with some test circles in the foreground. Note that the right, slightly larger, test circles are still supported while the left, slightly smaller, test circles have fallen.*

Figure 2.9 shows a finished device from the side. The cantilever has been undercut, and despite the long length, is still completely straight. This suggests that no net strain gradient exists across the device.

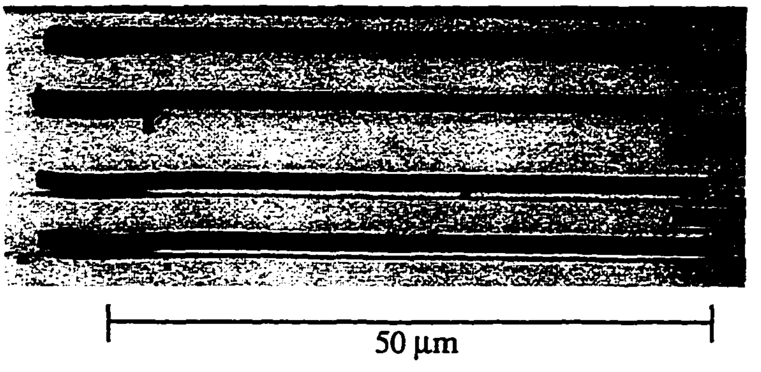


*Figure 2.9 - Undercut cantilevers looking from the side of the device at high angle of incidence. Despite the long cantilevers, they appear completely straight.*

Another completed device is shown in Figure 2.10 at a high enough angle to be able to see underneath the cantilever. As can be seen, it is completely free from the substrate. In the close up, it is possible to make out the DBR mirror pairs in the cantilever.

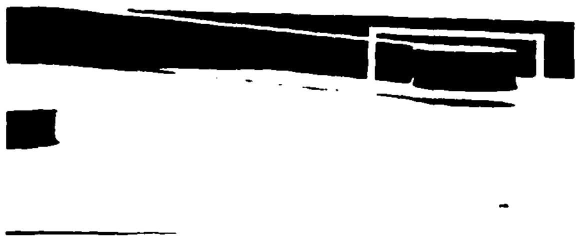

(a)

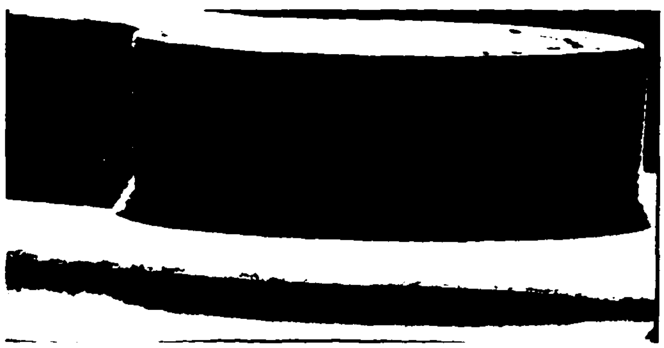

(b)

*Figure 2.10 - Completed device looking end on. The outlined white box in (a) is shown blown up as (b). Note the DBR mirror layers which can just barely be made out in the cantilever.*

## 2.4 Performance

### 2.4.1 Tuning

The tuning performance of these devices is shown in Figure 2.11, which plots the transmission versus wavelengths at various bias voltages. As the applied voltage is changed from 0 to 4.9 V, the Fabry-Perot resonance continuously shifts 70 nm towards shorter wavelengths. This agrees with the 70 nm of tuning range predicted by the calculations in Section 2.2. The FWHM resolution bandwidth is 6 nm. The DBR mirror bandwidth is between 890 nm and 980 nm. This results in the rise of transmission for wavelengths longer than 980 nm. The current necessary to reverse bias the junction is roughly 50 pA, making the total tuning power less than 250 pW. The contrast of the device is

20.3 dB, compared to the 26 dB predicted. The loss of the device is 5.5 dB, of which 1.5 dB is due to reflection from the substrate air interface and 1.7 dB is due to absorption in the heavily *n*-doped substrate. The remaining 2.3 dB excess loss is attributed to the device's imperfect transmission at resonance, either due to scattering loss or mismatched reflectivity of the mirrors. All of the aforementioned loss mechanisms can be reduced. By increasing the mirror reflectivities, resolution and extinction ratio can also be increased. Figure 2.12 shows the transmission for fixed wavelengths as the voltage is swept. This figure is less noisy than Figure 2.11 because the tunable laser is more stable at fixed wavelengths*. The deflection of the cantilever is dependent on the square of the voltage, making peaks at lower voltages appear wider. Figure 2.12 also illustrates how this device could be used as a modulator.

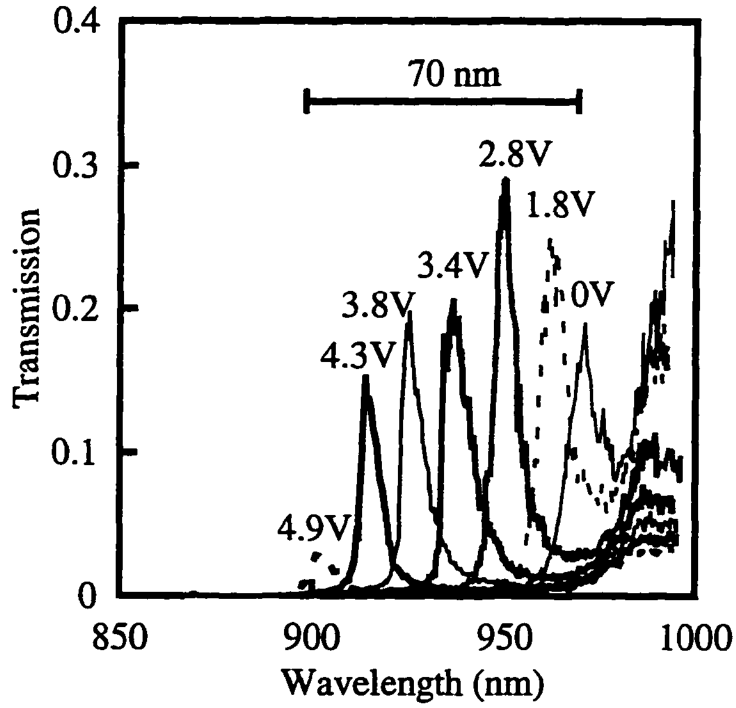


* Incidentally, the noise of Figure 2.11 is an excellent example of the poor performance of currently available tunable lasers.

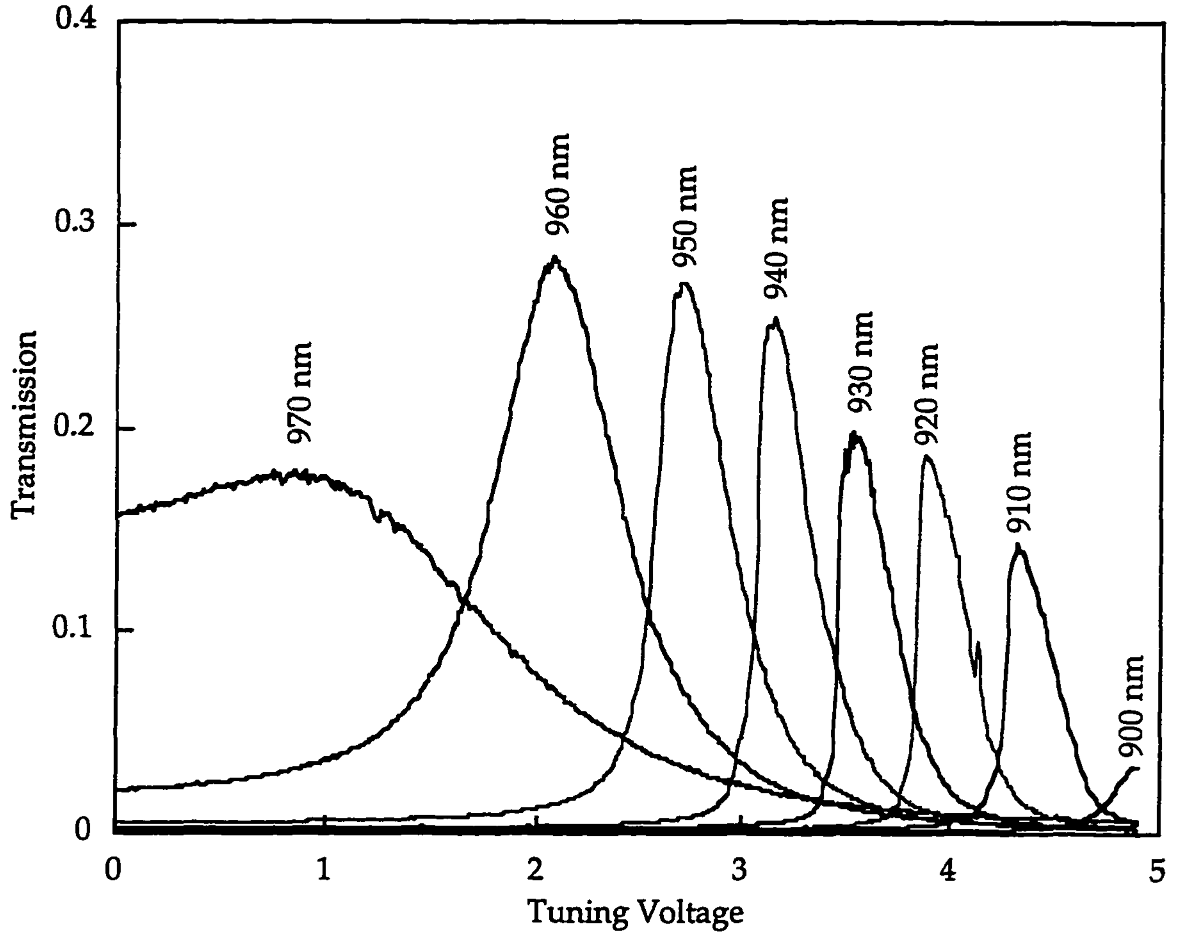


*Figure 2.12 - Transmission as a function of tuning voltages for various fixed input wavelengths. This is essentially the same information in Figure 2.11 but less noisy because the tunable source can be kept a fixed wavelength.*

Comparing the results in Figure 2.11 to the calculated filter response in Figure 2.2, some differences are apparent. For instance the curves are shifted towards shorter wavelengths and the peak heights are not as even. This is because the growth wavelength was shifted 20 nm to shorter wavelengths from the design and the absorption of the substrate increases greatly for wavelengths less than 910 nm. If substrate losses and growth errors are taken into account, we get Figure 2.13 which agrees closely with the experimental results in Figure 2.11. By using a lower doped substrate, an antireflection coating on the substrate, and staying at longer wavelengths, results like those in Figure 2.11 should be possible.

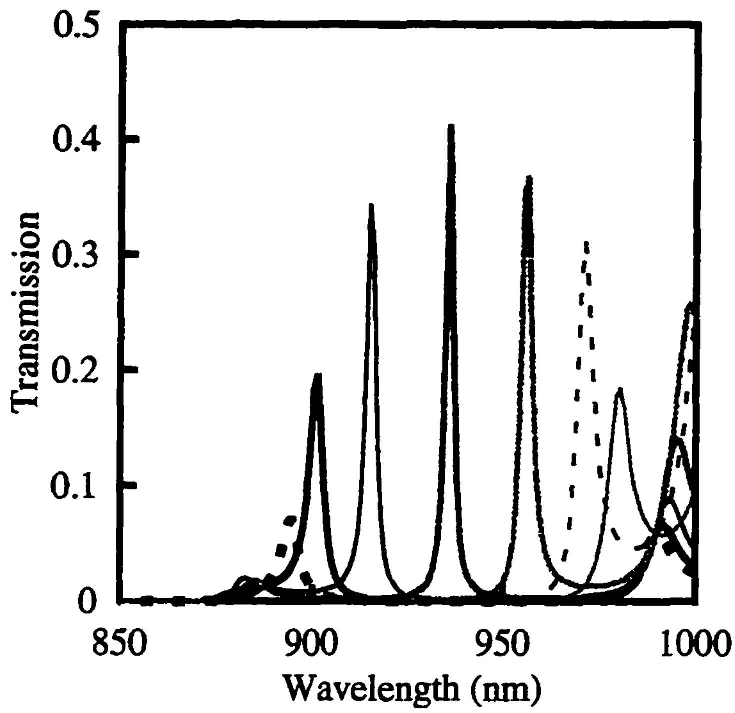


### 2.4.2 Polarization Properties

The surface normal operation of the device suggests that it is polarization insensitive. However, the small deviations from circular symmetry could conceivably introduce some polarization dependence. To verify there is no polarization dependence, Figure 2.14 shows the filter response for orthogonal polarizations with the incident light held at 920 nm while the control voltage is scanned. The tuning, insertion loss, and extinction ratio were all verified to have no polarization dependence. Intermediate polarization angles were checked and no polarization effects were observed. Thus the device eliminates the need for costly polarization maintaining optics or polarization scrambling.

## 2.5 Cantilever Mechanical Properties and Calculations

The mechanical properties of the cantilever are important in determining the tuning voltage and speed of these devices. The mechanical properties of AlGaAs are well known, so device performance can be calculated prior to

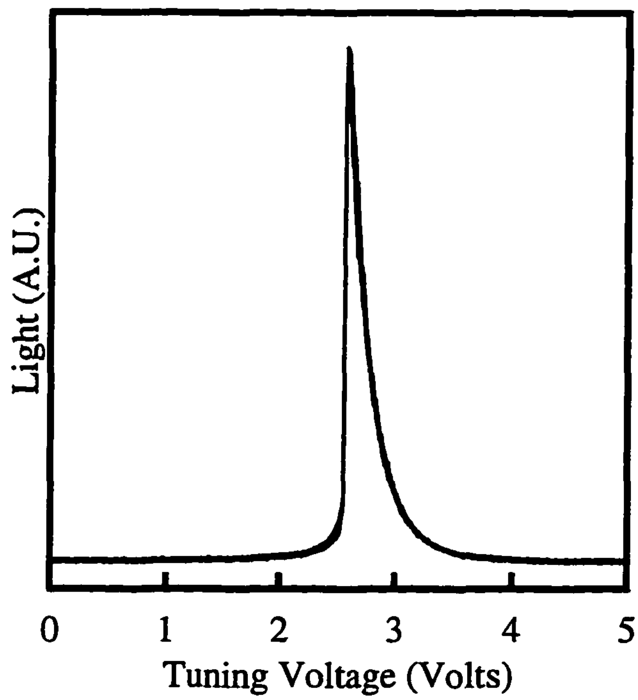


fabrication. In this section, these calculations are performed and compared to measured results.

Although this section discusses a straightforward application of well-known laws[15], some fascinating results are obtained. Because the dimensions involved in these devices are thousands of times smaller than in everyday life, they often perform in unexpected ways. For example, this chapter shows how forces not normally observed macroscopically, such as electrostatic attraction and surface tension, dominate gravitational forces. At these small scales, single crystalline GaAs also behaves very differently from bulk GaAs, becoming as pliant as rubber. The mechanical resonance frequencies of the cantilevers also is quite high (up to ~Mhz), allowing tuning times in the sub-μS range.

### 2.5.1 DC Characteristics

#### *2.5.1.1 Derivation of Equations*

To derive the differential equations that govern the bending, the cantilever is first broken into small parts, as shown in Figure 2.15. The equations are derived by examining how the forces and displacements change across each $dx$ part. Using the boundary conditions at the ends of the cantilever, the deflection for a certain applied force can then be computed.

There are basically four important quantities in the calculation: the downward pressure on the cantilever ($P$), the cumulative downward force on the cantilever ($F$), the torque on the cantilever ($\tau$), and the displacement of the cantilever ($z$). All four of these change along the length of the cantilever (i.e., are functions of $x$).

The downward pressure on the cantilever can be determined by modeling the device as a parallel plate capacitor with the cantilever and the substrate as the two plates. The angle of the cantilever is small (<0.5°) and can be ignored over a small area, $dA$. Since the cantilever is as little as 2 μm across, yet over 1 μm from the substrate, fringe fields are significant. Nevertheless, the parallel plate capacitor model provides a good starting point. The electrostatic pressure can be derived by looking at the energy stored in a parallel plate capacitor

$$dU = \frac{dCV^2}{2} = \frac{\varepsilon(dA)V^2}{2d} \tag{2-1}$$

where $dC$ is the capacitance of the differential element, $\varepsilon$ is the dielectric constant of the intervening material, $dA$ is the area of the differential element, $V$ is the applied voltage, and $d$ is the distance between the parallel plates. Taking the derivative of this stored energy versus distance $d$ gives the downward force of the cantilever. By moving $dA$ to the other side, the downward pressure on the cantilever is obtained:

$$P = \frac{dU/dd}{dA} = -\frac{\varepsilon V^2}{2d^2} \tag{2-2}$$

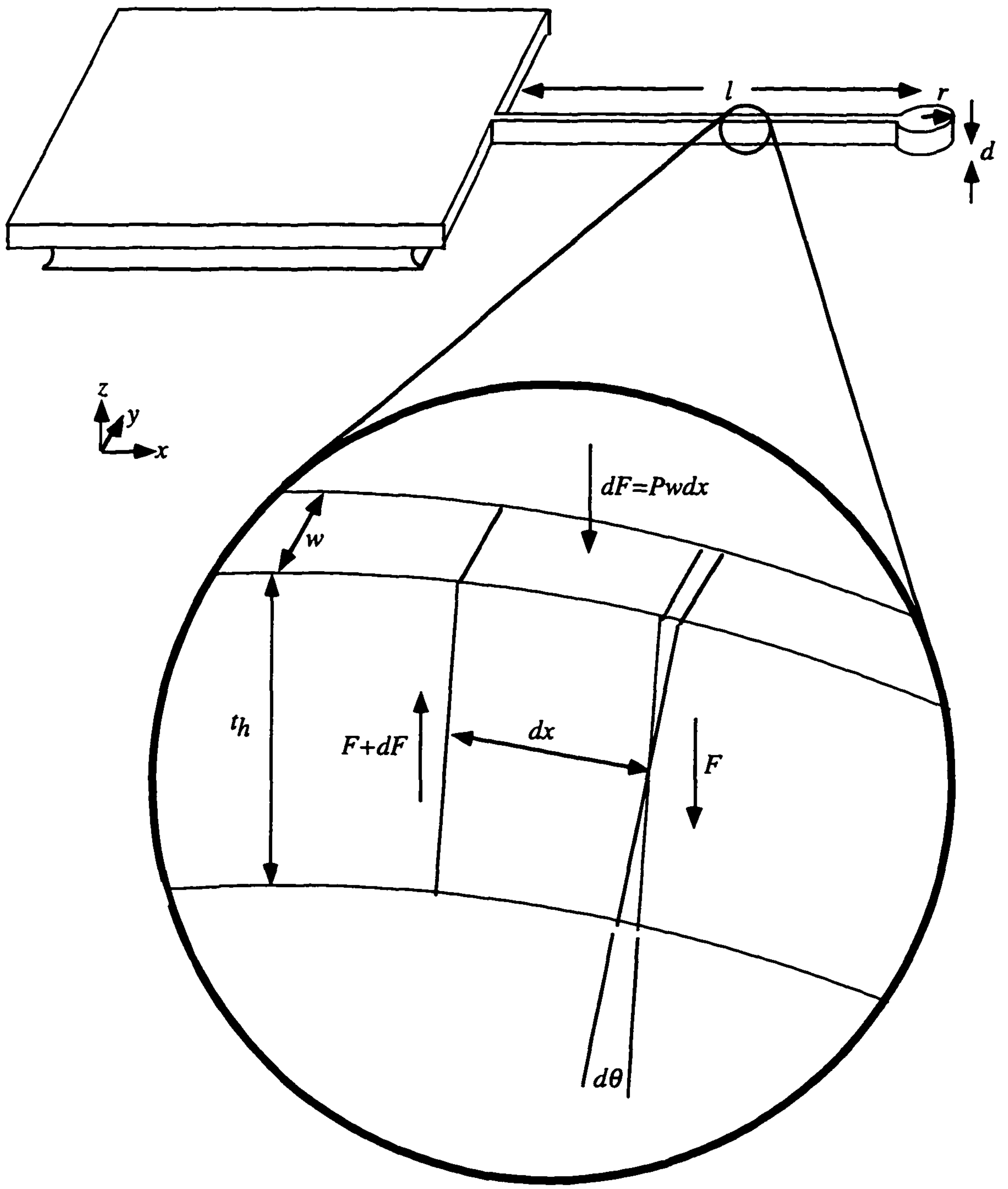


*Figure 2.15 - Schematic of the cantilever and the various parameters used in the mechanical calculations.*

Perhaps a more intuitive way of deriving this same equation is to realize the force per unit area is simply the charge per unit area $\left(\frac{\varepsilon V}{2d}\right)$ times the electric field $\left(\frac{V}{d}\right)$.

Since the cantilever bends down, $d$ is a function of $x$. So we should rewrite (2-2) as

$$P(x) = -\frac{\varepsilon V^2}{2d^2(x)} \tag{2-3}$$

where

$$d(x) = d_0 - z(x) \qquad (2\text{-}4),$$

$d_0$ being the unperturbed distance between the cantilever and the substrate.

Now the equation for the cumulative downward force can be derived. This is the downward force felt by the cantilever at a particular point $x$. For a straight cantilever with no end circle, it is zero at the tip and gradually builds up towards the base from the electrostatic pressure on the cantilever. For a cantilever with an end circle, the force starts as the force due to the end circle and increases towards the base. It is tempting to approximate the entire force as the force from the end circle, ignoring the distributed force along the cantilever. However, this introduces considerable error since the area of the cantilever is comparable to the area at the tip. For example, the thinnest cantilevers are 2 μm wide and the largest end circle diameter is 20 μm. Assuming a reasonable length of 100 μm, the area of the end circle is approximately 300 μm$^2$ while the area of the cantilever length is 200 μm$^2$. Since keeping this term is not difficult, the distributed force is kept in the cantilever model. The rate of change of cumulative downward force ($F$) is simply the pressure times the width or

$$\frac{dF(x)}{dx} = P(x)w \qquad (2\text{-}5).$$

Essentially, the force on the left of a $dx$ element is larger than the force to the right of a $dx$ element by an amount $dF$ equal to the pressure times the area, or $P(x)wdx$, as shown in Figure 2.15.

Once the force along the cantilever length is known, the differential equation for the torque can be derived. This is the torque that bends the cantilever. Zooming in on a small element, $dx$, there exists a certain torque acting on the right of the element $dx$. As we move to the left of the element, the torque increases by the force $F$ times the lever arm length $dx$. In other words,

$$\frac{d\tau(x)}{dx} = F(x) \qquad (2\text{-}6).$$

The torque starts at zero at the end of the cantilever and then builds up as we move towards the base.

Finally, given the torque, the curvature can calculated. In Figure 2.15, a wedge-shaped $dx$ element is assumed to result from the application of a torque. This shape is chosen because it is the only shape where bending stops strain from building up, as shown in Figure 2.16. Let's break this $dx$ wedge element into many tiny $dz$ elements as shown in Figure 2.17. In general, the shear strains are a couple orders of magnitude less than the compressive and tensile forces, so they can be ignored.

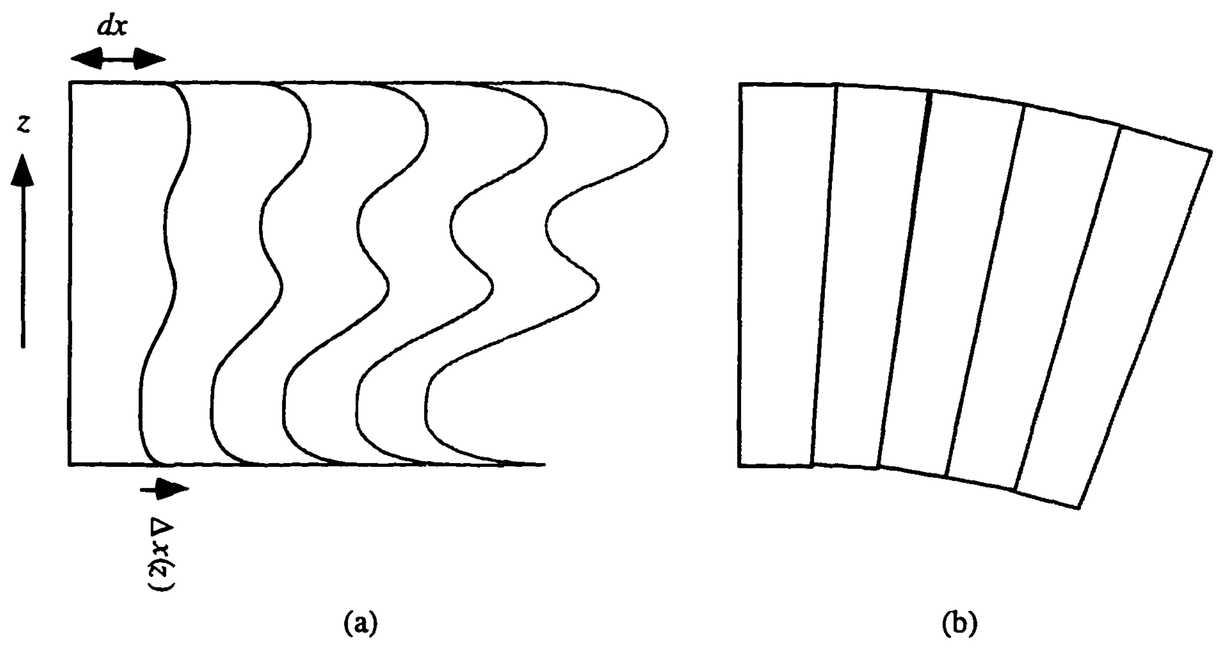


*Figure 2.16 - Figure showing why dx elements must be wedge shaped. (a) When dx elements are deformed by an arbitrary function sheer strain increases without limit as elements are added unless (b) the function is linear (a wedge). Then sheer strain can be relieved by expansion and deflection.*

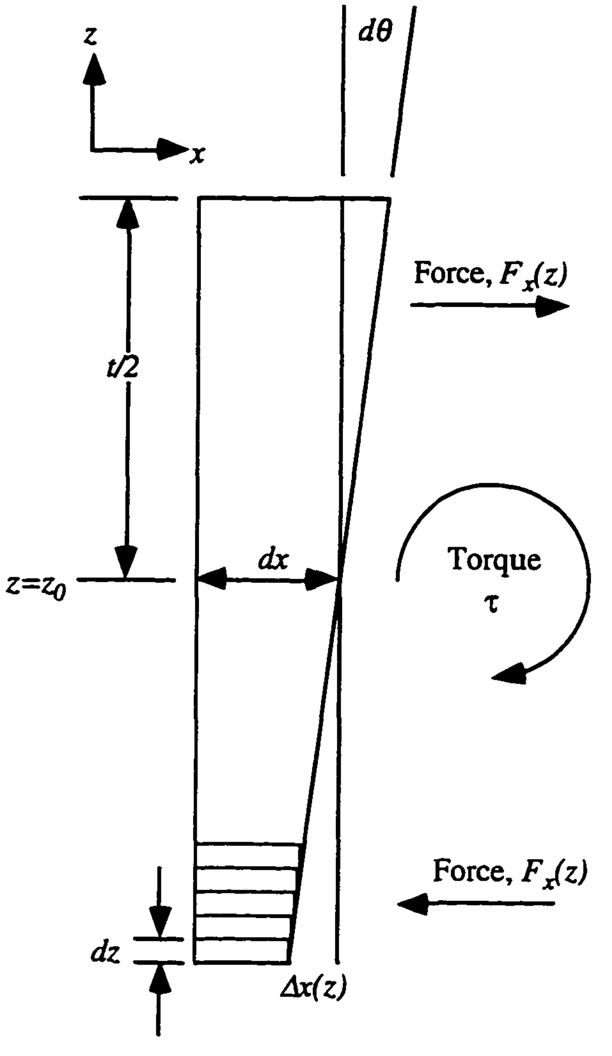


*Figure 2.17 - Close up of individual wedge used to calculate the relationship between the torque applied to the cantilever ($\tau$) and the curvature of the cantilever $d\theta$/dx.*

Because we are dealing with a cantilever, there is no net force pulling or pushing along the length of the cantilever. If such a force existed, the cantilever would shrink or expand to alleviate it. So the compressive force on the bottom of the cantilever and a tensile force on the top must balance out to zero. The force, $dF_x(z)$, on any $dz$ element is equal to the strain,

$$\varepsilon(z) = \frac{\Delta x(z)}{dx} \qquad (2\text{-}7),$$

times the Elastic Modulus of the material, $E$, times the area of the element which is just $dz$ times the width $w$. In other words,

$$dF_x(z) = E\frac{\Delta x(z)}{dx}wdz \tag{2-8}$$

Since the total force must cancel out and the function $\Delta x(z)$ is linear, the deviation must be odd about $z_0$ so

$$\Delta x(z) = d\theta(z - z_0) \tag{2-9}$$

where $d\theta$ represents the change in angle over a $dx$ element and $z_0$ is the midway point on the cantilever. For small angles, this approximately equals the change in slope and is related to the curvature of $z(x)$ by

$$\frac{d\theta}{dx} = \frac{d^2z}{dx^2} \tag{2-10}$$

By performing these substitutions into equation (2-8) we get

$$dF_x(z) = E\frac{d^2z}{dx^2}(z - z_0)wdz \tag{2-11}$$

All of these $dF_x(z)$ add up with their corresponding lever arms $(z - z_0)$ to determine the total torque on the wedge,

$$\begin{aligned}\tau(x) &= \int_{z_0-t/2}^{z_0+t/2}(z - z_0)dF_x(z)\\ &= \int_{z_0-t/2}^{z_0+t/2}(z - z_0)^2E\frac{d^2z}{dx^2}wdz\\ &= \frac{t^3wE}{12}\frac{d^2z}{dx^2}\end{aligned} \tag{2-12}$$

and we have a formula linking the torque applied to the cantilever to the curvature.

### 2.5.1.2 *Calculation of Deflection*

With equations (2-3), (2-4), (2-5), (2-6) and (2-12), a differential equation for $z$ can be derived. Unfortunately, it turns out to be nonlinear in the form of

$$\frac{d^4z}{dx^4} = \frac{a}{z^2} \tag{2-13}$$

where $a$ is a constant and $z$ has been shifted by an amount $d$ through substitution. Even if a solution to this differential equation could be obtained, since it is nonlinear it would likely have to be resolved from scratch for each new applied voltage in order to match the boundary conditions.

There are a number of ways to attack this problem. This simplest is just to assume that the gap size does not change much and so the force applied to the cantilever is constant. Then equation (2-3) becomes

$$P(x) = -\frac{\varepsilon V^2}{2d^2} \tag{2-14}$$

Now the problem is easily solved since (2-5) can be integrated to get $F(x)$. Then, (2-6) can be integrated to get $\tau(x)$. Finally, (2-12) can be integrated to yield $z(x)$. The deflection versus applied voltage is given by $z(l)$.

Following this method, let's look at the boundary conditions on $F(x)$. At the tip of the cantilever

$$F(l) = AP = \pi r^2 \frac{\varepsilon V^2}{2d^2} \qquad (2\text{-}15).$$

assuming the end circle force can be approximated as a point force in the center of the end circle. If we now integrate (2-5) from $l$ to $x$, we get

$$F(x) = F(l) + \frac{\varepsilon V^2}{2d^2} w(l-x) \qquad (2\text{-}16).$$

The net torque at the end of the cantilever must be zero so

$$\tau(l) = 0 \qquad (2\text{-}17).$$

Integrating (2-6) from $l$ to $x$ we get

$$\tau(x) = F(l)(l-x) + \frac{\varepsilon V^2}{2d^2} w \frac{(l-x)^2}{2} \qquad (2\text{-}18).$$

Finally, using $z(0)=0$ and $dz(0)/dx=0$, equation (2-12) can be integrated from 0 to $x$ twice to yield

$$z(x) = \frac{12}{t^3 wE}\left[F(l)\left(l\frac{x^2}{2} - \frac{x^3}{6}\right) + \frac{\varepsilon V^2}{2d^2} w\left(l^2\frac{x^2}{4} - l\frac{x^3}{6}\right)\right] \tag{2-19}$$

This means $z(l)$, the total deflection of the end mirror, is

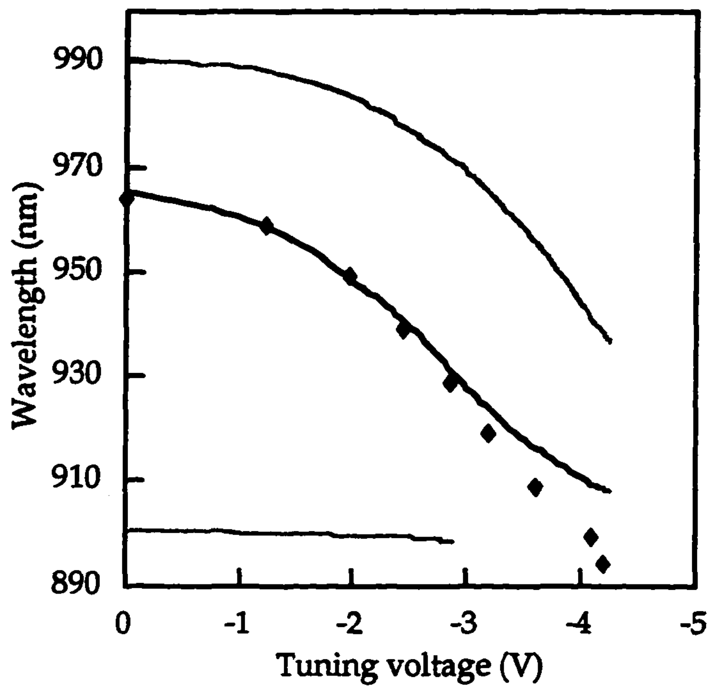


*Figure 2.18 - Tuning wavelength versus tuning voltage, both measured (diamonds) and calculated (gray lines). The 25 nm discrepancy is due to growth error. The black line shows the calculated tuning taking this growth error into account.*

$$z(l) = \frac{4l^3}{t^3wE}\left[F(l) + \frac{\varepsilon V^2}{2d^2}wl\left(\frac{1}{4}\right)\right] \qquad (2\text{-}20)$$

Using this result, the Fabry-Perot resonance wavelength can now be calculated using the reflectivity program in section 2.2. The results are shown in Figure 2.18. The theoretical and experimental values are about 25 nm offset from each other, due to errors in the growth of the structure. If the growth error is taken into account, good agreement between experimental and theoretical tuning are obtained over most of the tuning range. At the shorter wavelengths, however, the calculations underpredict the amount of tuning which occurs due to the approximation of the air gap as a constant thickness $d$ when calculating the electrostatic force. In fact, at the end of the tuning range the true air gap is only $2d/3$. This introduces an error of approximately 50 % into the maximum tuning voltage. In the future, this could be corrected by performing numerical calculations which include the dependence of the cantilever pressure on air gap thickness. For the moment, the agreement of Figure 2.18 shows the calculations can be used to estimate the tuning voltage of structures.

### 2.5.1.3 *Approximate Scaling Laws*

To estimate how the tuning voltage changes with cantilever dimensions, it is often useful to neglect the distributed force along the cantilever. Although this introduces significant errors (%50) in the absolute calculations, it is accurate in predicting the change in voltage as dimensions are changed. With this approximation equation (2-20) becomes

$$z(l) = \frac{4l^3}{t^3 wE}\left(\pi r^2 \frac{\varepsilon V^2}{2d^2}\right) \qquad (2\text{-}21).$$

For example, this equation says that if the thickness of a cantilever is to be doubled, the length should also be doubled to have roughly the same tuning voltages.

It is interesting to investigate the physical reasons behind the dependencies of (2-21). Of course, it makes sense that the displacement is inversely proportion to the bulk modulus, $E$, and proportional to the area, $\pi r^2$. The displacement is inversely proportional to the width of the cantilever, $w$. One can just think of two cantilevers side by side, to see a cantilever which is twice as wide must be twice as stiff. The voltage, $V$, and the air gap thickness, $d$, have a square dependence because they effect both the charge on a surface and the field applied to the charge. The cube dependence of the length, $l$, is the result of it affecting calculation in three ways: it increases the lever arm of the force, it amplifies the angle of deflection, and it increases the length of the flexible material. Doubling the length doubles the torque at the base of the cantilever, doubling the bending angle. The angle is amplified by the (2 times longer) cantilever. Finally, the cantilever is bending not only at the base, but along its whole length. By doubling a cantilever's length, we double its flexibility. Putting these factors together results in a displacement that is increased by a factor of eight. Similar logic can be used to derive the thickness' cube dependence. A thicker cantilever has a larger lever arm to counteract any applied torque, must be strained a greater amount for the same angular displacement , and has more material to resist the deflection.

#### *2.5.1.4 Maximum Tuning Deflection*

Using the approximations of the previous section, the maximum tuning of the device can also be estimated[14]. First, we need to undo a previous approximation. If we make the force dependent on the air gap thickness, as it really is, equation (2-21) becomes

$$z(l) = \frac{4l^3}{t^3 wE}\left(\pi r^2 \frac{\varepsilon V^2}{2(d-z(l))^2}\right) \tag{2-22}$$

Rearranging this equation we get

$$z(l)[d-z(l)]^2 = \frac{4l^3}{t^3 wE}\left(\pi r^2 \frac{\varepsilon V^2}{2}\right) \tag{2-23}$$

Only the left side of this equation depends on $z(l)$. Figure 2.19 plots both sides of (2-23) versus $z(l)$. The intersection points between the curves show where equation (2-23) is satisfied and a possible value for $z(l)$ for a given tuning voltage. The circled left-most intersection point is normally used. As the voltage changes, the $z(l)$ corresponding to the left-most intersection point moves. The middle intersection point is unstable. The right-most intersection point has $z(l)>d$, which is unphysical. This corresponds to a stable solution, where the cantilever is stuck to the substrate. The left side of (2-23) has a local maxima at $d/3$ which limits the maximum tuning in the air gap thickness to $d/3$. If greater tuning is attempted, the cantilever jumps all the way down to the substrate. If the voltage is removed the cantilever either returns to its original position, or remains stuck due to Van Der Walls forces.

The above calculation assumes the cantilever can be modeled as a spring with all the force applied at the tip. This is an approximation, since the cantilever actually has a distributed force along its whole length. Therefore, the true maximum tuning varies somewhat from the $d/3$ predicted above. Straight cantilevers can tune more than $d/3$ while doubled-back cantilevers tune less. To see why, look at a straight cantilever. In this case, it is more accurate to model the center of force as somewhat towards the base, rather than at the tip. This point is where the $d/3$ rule really applies. But when this point is at $d/3$, the tuning head has been deflected down more than $d/3$ because it is further out on the cantilever. Therefore, more than a $d/3$ tuning in the air gap can occur.

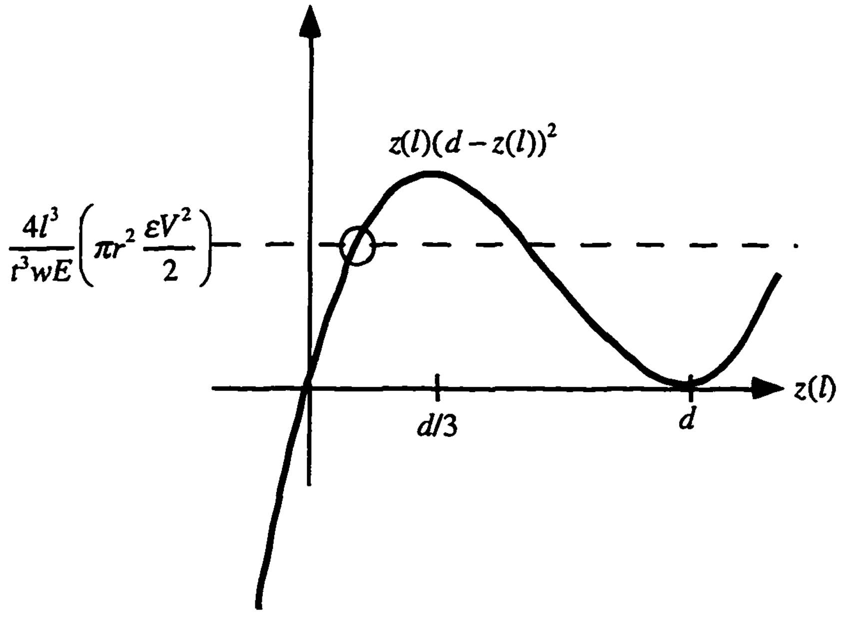


*Figure 2.19 - Plots of left side (black) and right side (dashed) of equation (2-23). Intersection point shows the* z(l) *for a given voltage.*

These calculations were verified experimentally using the tuning data for devices. Straight cantilevers with a $3\lambda/2$ air gap layer were found to be able to tune slightly more than $\lambda/2$. This is easy to measure because these devices were able to tune through the entire tuning range back to the starting wavelength and then a bit more. Double-backed cantilevers were found not to tune over the entire tuning range. The $d/3$ limit was also observed directly using a special SEM setup. An SEM with a feed-through was used to bias a packaged device while under observation. Figure 2.20 shows photos taken of a straight cantilever with no end circle under different biasing conditions. The cantilever w continuously tunes over $d/3$ and then to abruptly snaps to the substrate.

(a)

(b)

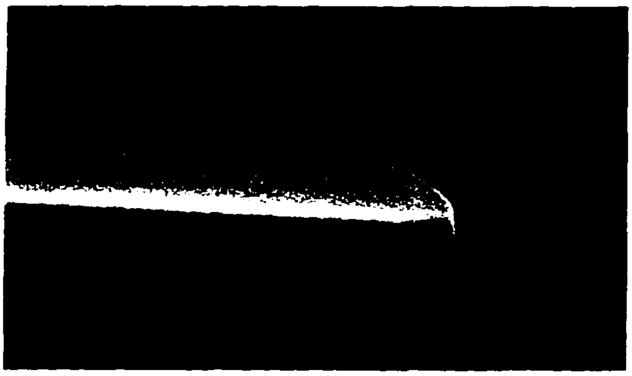

(c)

(d)

*Figure 2.20 - 2 μm wide cantilever under various bias conditions. (a) View of whole device with contact pad off to the left. These devices had no end circle. (b) Close up of the end. (c) DC bias enough to make cantilever touch the substrate. (d) AC bias with the cantilever hitting the substrate.*

### 2.5.1.5 *Maximum Strain*

With the equations derived in section 2.5.1.2, the maximum strain in the cantilever can be estimated and compared to the yield strain (at which GaAs breaks). The maximum strain in the device occurs at the base of the cantilever at the top and bottom edges. Using equations (2-7), (2-9), (2-10), (2-12), and (2-18), the maximum strain is derived to be

$$\varepsilon_{max} = \frac{6}{t^2 w E}\left( F(l)l + \frac{\varepsilon V^2}{2d^2} w \frac{l^2}{2} \right) \qquad (2\text{-}24).$$

For the tunable filter the maximum strain is 0.0026%. Table 2.2 shows the yield strain for a variety of materials[16,18]. As shown, they are all larger than the maximum strain in the cantilevers. Yield strain depends a great deal on material preparation. For example, a 99% Al alloy can have 5 times the yield strain of straight Aluminum. Single crystalline AlGaAs has 100 times the yield strain of bulk AlGaAs, because yield strain is highly dependent on defects. Using MBE, we are able to grow single crystalline AlGaAs as the cantilever material. This single crystalline material has a high yield strain value, ~3%, and is very pliant. Cantilevers can be deflected 30° to one side with the probe and still bounce back into place, as if made of rubber. The maximum strain is 1000 times less than the yield strain of the material.

*Table 2.2 - Table of yield strains for various materials. Single crystalline material is usually at the top end of the range while bulk material is usually at the low end of the range.*

| Material | Yield Strain |
|---|---|
| Si | 6.8%-0.08% |
| AlGaAs | 3.4%-0.047% |
| Steel | 2%-0.4% |
| Mg | 0.40% |
| Al | 0.24%-0.014% |
| Au | 0.16% |
| $SiO_2$ | 0.15% |

*2.5.1.6 Surface Tension Collapse*

One of the advantages of the dry etching process is that it does not suffer from the surface tension problems of wet etching processes. In wet etching, the surface tension during drying can pull the cantilever to the substrate. Once pulled to the substrate, the levers may bond to the surface and stick there.

This point was shown experimentally using a sample created with dry etching. All of the levers were free and suspended over the substrate. Photoresist was spun on it, followed by acetone and methanol to wash it off. After the photoresist and rinse, some of the longer levers were stuck to the substrate. Figure 2.21 shows which levers stuck and some simple calculations predicting the observed behavior.

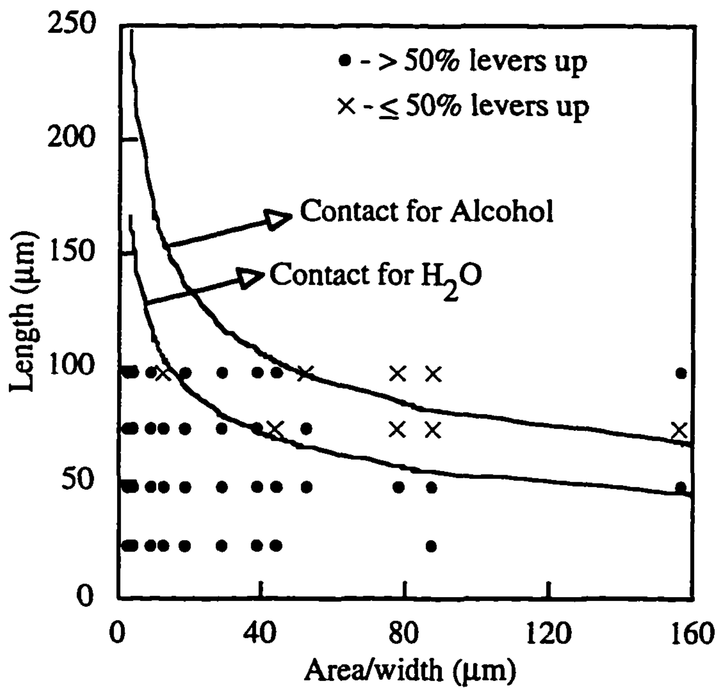


*Figure 2.21 - Levers sticking to the substrate after spinning of photoresist and rinsing off. Circles show levers where more than 50% were stuck to the substrate. X's show where more than 50% of the levers were still up. Solid lines show approximate calculated borders above which surface tension is strong enough to bring the lever in contact with substrate.*

These calculations were performed by substituting the forces of surface tension for the electrostatic forces. The force was again approximated as just the contribution from the circular end of the cantilever. Surface tension can roughly be modeled as a membrane under tension on the surface of a liquid. For example, the air/water interface exerts a tiny force pulling the walls of a glass of water towards the center. To approximate the force on a cantilever due to surface tension, it is tempting just to multiply the perimeter of the cantilever by the surface tension parameter, $\gamma$ (usually in units of dynes/cm), giving

$$F = 2\pi r\gamma \sin(\theta) \qquad (2\text{-}25)$$

However, this force is much smaller than another force caused by surface tension. Liquids are attracted and repulsed by various solids. For example, water is attracted to glass, giving rise to a meniscus. Usually liquids are attracted to solids. This causes effects like capillary action and wicking of liquids. For micromechanical devices, liquids accumulate in narrow gaps, if they are dipped in water. As the sample dries, the volume of the liquid under the cantilever goes down and it begins to contract. However, due to the attraction it feel towards solids it is also attracted outwards. This causes the whole liquid to be under a slight vacuum. This vacuum acts on the cantilever, pulling it downwards.

To calculate the force, we first need to characterize the liquid's attraction to the solid. This can be summarized in one parameter, $\theta$. This is the angle the liquid/air interface makes against the solid's surface at equilibrium. At this angle, the attractive force the liquid feels to the surface is exactly canceled by the surface tension pulling it back. This effect is shown in Figure 2.22. As the sample dries, the remaining water underneath the cantilever tries to pull itself out to the edges through the capillary force. However, this increases the volume of the liquid. To counteract this outward expansion, the liquid is under a vacuum. The steady state is shown in Figure 2.22, with the capillary action pulling the liquid out and the vacuum pulling the liquid back. The pressure of this vacuum is

$$P = \frac{2\gamma \cos(\theta)}{d} \qquad (2\text{-}26).$$

This pressure can be substituted for the electrostatic pressure in the equations of section 2.5.1.1 to calculate whether a device sticks when dried. This capillary force is much larger than the straight surface tension force, because the relatively large area of the cantilever leverages the capillary force up. This can be seen by looking at the force on the end circle

$$F = \frac{2\pi r^2 \gamma \cos(\theta)}{d} \qquad (2\text{-}27).$$

Comparing this to the straight surface tension force of (2-25), we can see the capillary force is bigger by a factor of $\cot(\theta) r / d$. Since $r$ is much bigger than $d$ and $\cot(\theta)$ is usually on the order of one, the capillary force is considerably larger than the straight surface tension force.

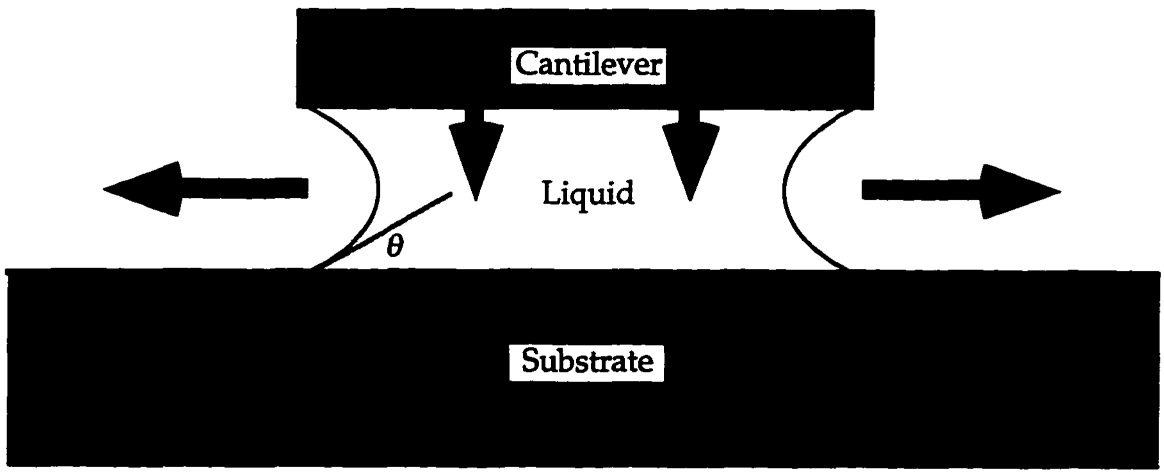


*Figure 2.22 - Schematic showing how the capillary force arises when drying a sample.*

*2.5.1.7 Weight of the Cantilever and Vibration Sensitivity*

One term we have neglected to mention throughout the calculations is the weight of the cantilever. It turns out that at this scale this term is so much smaller than the electrostatic force, it is essentially insignificant.

The equivalent pressure of the gravitational force is given by

$$P = \rho g t \qquad (2\text{-}28)$$

where $\rho$ is the density of the cantilever, $t$ is the thickness of the cantilever, and g is the gravitational acceleration constant (9.8 m/s$^2$). Plugging typical values for the filter ($t$=1.78 μm, $\rho$=4 g/cm$^3$) into this formula gives a pressure of 8.7 X $10^{-2}$ N/m$^2$. If we do the same thing for the electrostatic force given by equation (2-2) using a voltage of 5 V, we get 7.6 X $10^1$ N/m$^2$. So the gravitational force is a factor of 1000 less than the electrostatic force. It would take an acceleration of 100 g's to get the filter to detune an amount equal to its resolution bandwidth.

Further insensitivity to acceleration can be achieved in future designs. If a higher tuning voltage (say 50 V) device is used, the gravitational force becomes $10^5$ less than the electrostatic force. This would be useful for a narrow linewidth device, such as the tunable lasers discussed in later chapters. In this case, 1 g of acceleration would cause only 60 MHz of detuning, which is less than the best VCSEL linewidths ever reported.

### 2.5.2 Modulation Characteristics

In this section, we discuss the tuning speed characteristics for micromechanical tunable devices. We demonstrate a critically damped rise time of 7.5 μs in air. Furthermore, we demonstrate devices with resonant frequencies of 1.16 MHz, which could lead to 300 ns tuning speeds using a critically damped structure. These results closely match the predictions from calculations, with no fitting parameters.

#### *2.5.2.1 Measurements*

The tuning speed of the filter is limited by the mechanical response of the cantilever. The cantilever system is a damped mechanical oscillator. The modulation response in air is illustrated in Figure 2.23 for 6 μm wide cantilevers of varying lengths with 10 μm end-circles. Shorter cantilevers are stiffer and have less mass, causing them to have higher resonance frequencies. Shorter cantilevers also have a higher Q due to increased stiffness and lower cross-sectional area, since the primary damping term is drag in air. Despite the fact that the tuning is done mechanically the highest resonant frequency is quite fast—1.16 MHz.

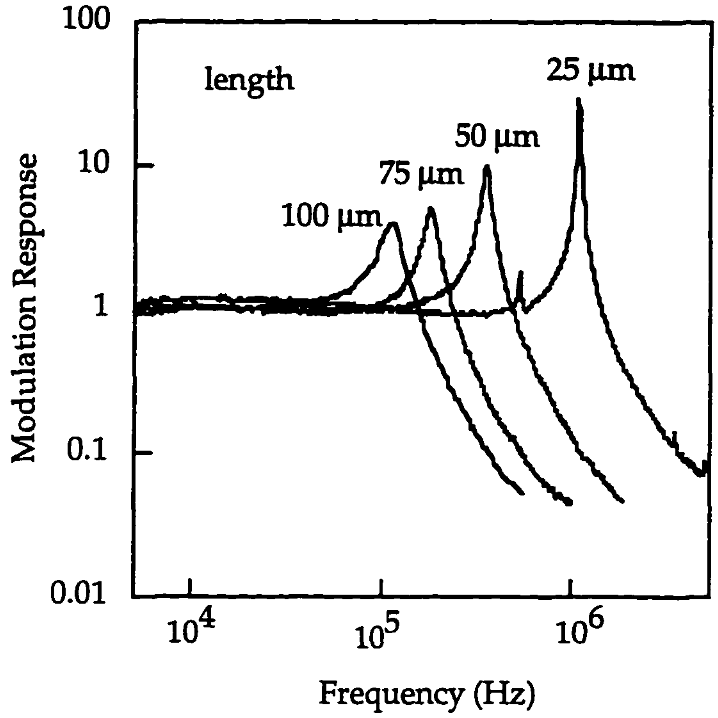


*Figure 2.23 - The filter modulation response for tuning of 6 µm wide cantilevers with 10 µm end circles with various lengths.*

These measurements were performed using a digital oscilloscope, a Ti-sapphire laser, a function generator, a probing station, and a computer. Figure 2.24 illustrates the measurement method. The filter is biased halfway off its point of maximum transmission. A small AC voltage is applied to the cantilever and the amplitude and phase of the transmitted AC optical signal is measured. The computer automates the setup by changing the frequency of the applied input signal and recording the amplitude and phase. The computer adjusts the strength of the input ac signal to keep the measured optical signal constant. Since the amplitude of the optical signal, and hence the displacement, is kept constant, the measurement is not affected by nonlinearities in the transmission's dependence on displacement.

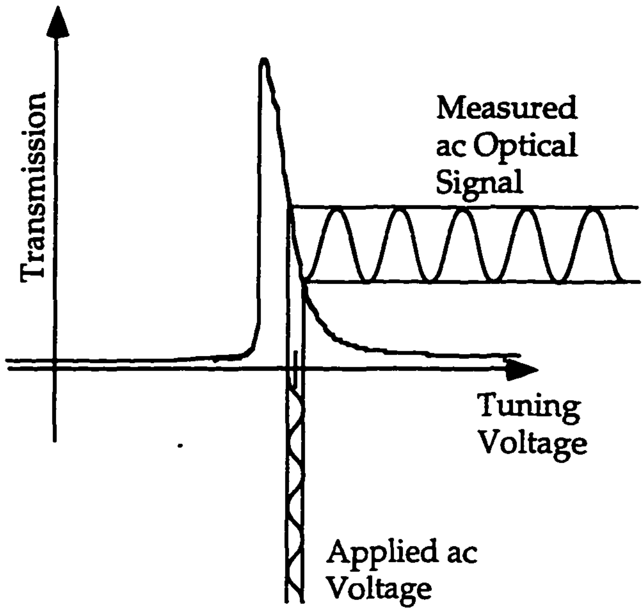


*Figure 2.24 - Technique for measuring modulation response of tuning. The filter is biased to one side of maximum transmission. As an AC voltage is applied, the transmitted light is correspondingly modulated.*

We can also measure the large signal response of these devices by tuning the cavity from off to on resonance while observing the transmitted light. The step response for a device with a 1.16 MHz resonant frequency is shown in Figure 2.25. Because this structure is underdamped, there is significant ringing. The 450 ns period of the optical oscillation corresponds to double the frequency of mechanical oscillation resulting from the curved Fabry-Perot transmission function. The inset to Figure 2.25 shows the 14 μs switching time for the transient response to a step input applied at time t = 0 s. For a critically damped system, the rise time can be 0.3 times the resonance period. For this structure, this would imply a tuning time of 300 ns. There are several ways the damping on this system could be increased. First, it could be packaged under higher pressure. The air would then exert greater damping forces. Second, the flow of air could be restricted so that it could not quickly enter or exit the region under the cantilever. For example, if only a narrow crack around the cantilever was left for air to flow in and out, damping would be increased. Third, the cantilever could be packaged in a liquid.

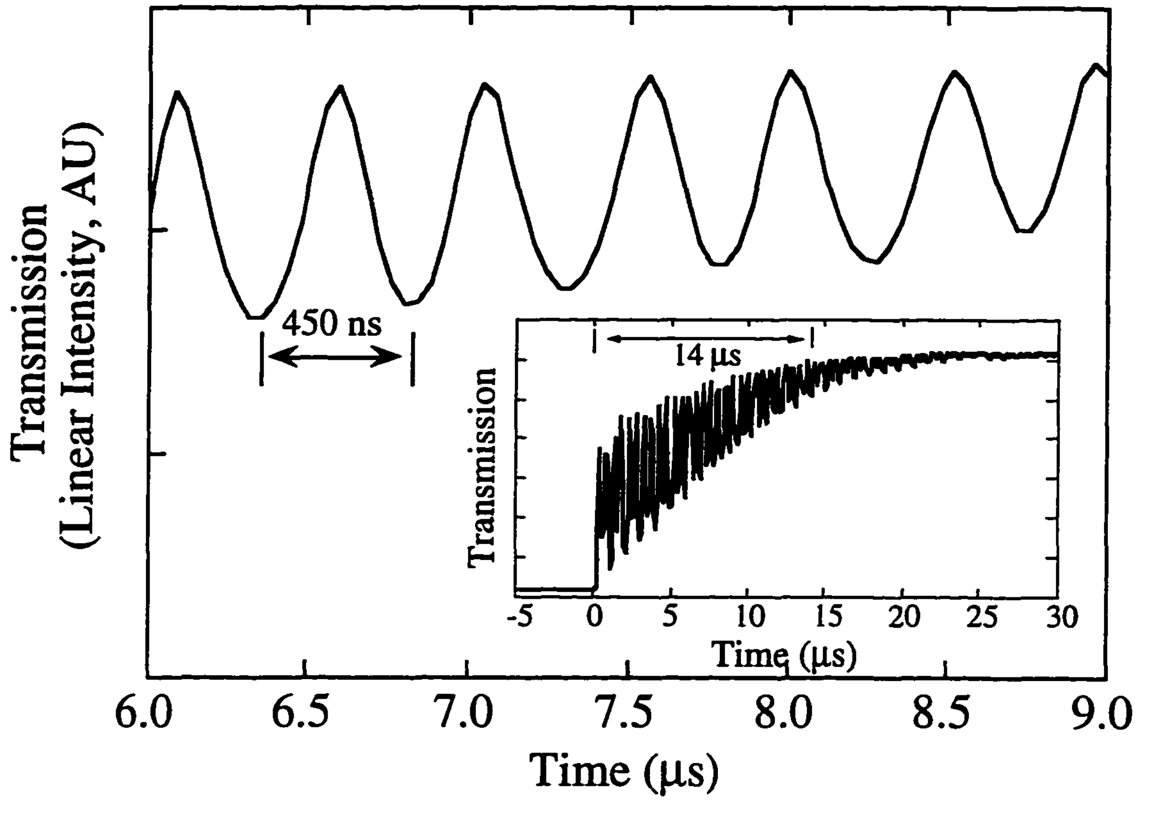


*Figure 2.25 - Transmission versus time for a cantilever with a 1.16 MHz resonant frequency with a step function of applied voltage. Even though the cantilever moves quite quickly the settling time is long due to ringing (inset).*

For the moment, the easiest way to get critical damping is to change the geometry of the device. A larger tuning head and a longer, narrower, and hence less stiff cantilever can be critically damped. The disadvantage to this approach is a decrease in the resonance frequency. Nevertheless, the overall tuning time does improve. The step response for a critically damped, 2 μm wide, 100 μm long cantilever with a 20 μm end-circle and a resonance frequency of 76 kHz is shown in Figure 2.26. A critically damped rise time of 7.5 μs was measured. Figure 2.27 shows the small signal response for this device.

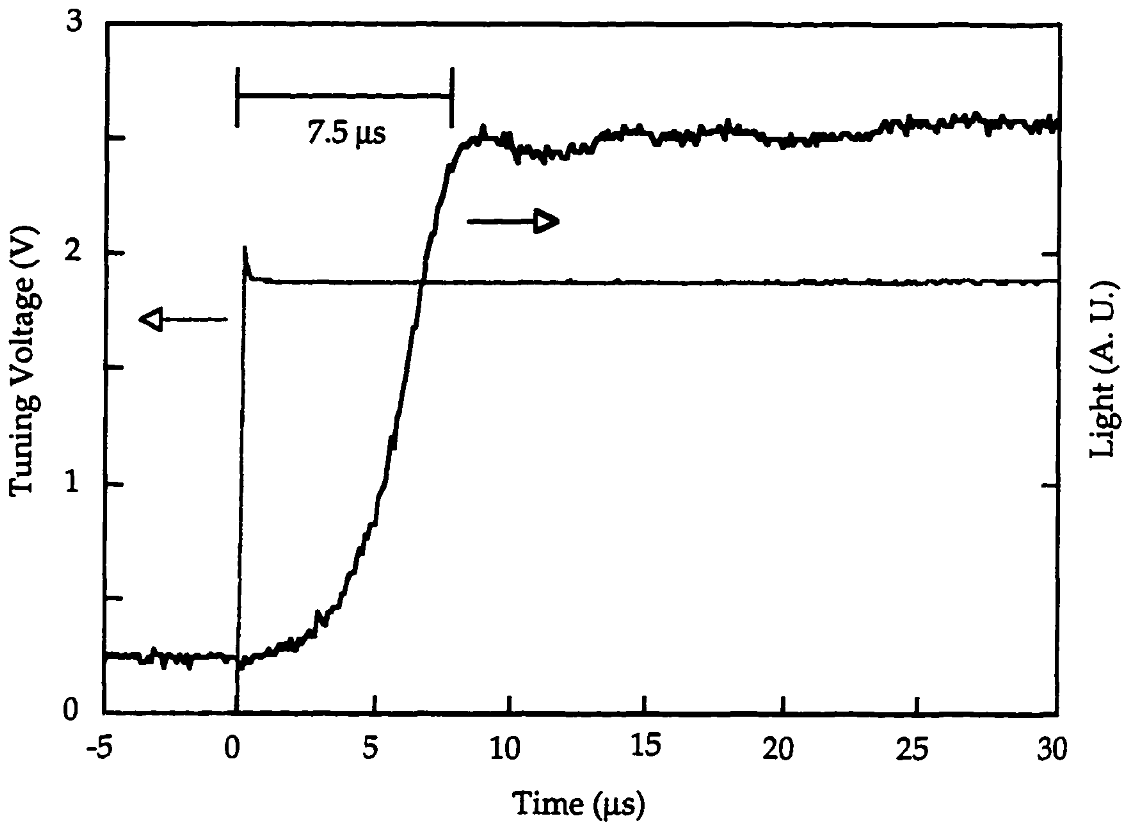


*Figure 2.26 - Large signal tuning of a critically damped structure. The black line shows transmitted light of the filter. The gray line shows the applied voltage step.*

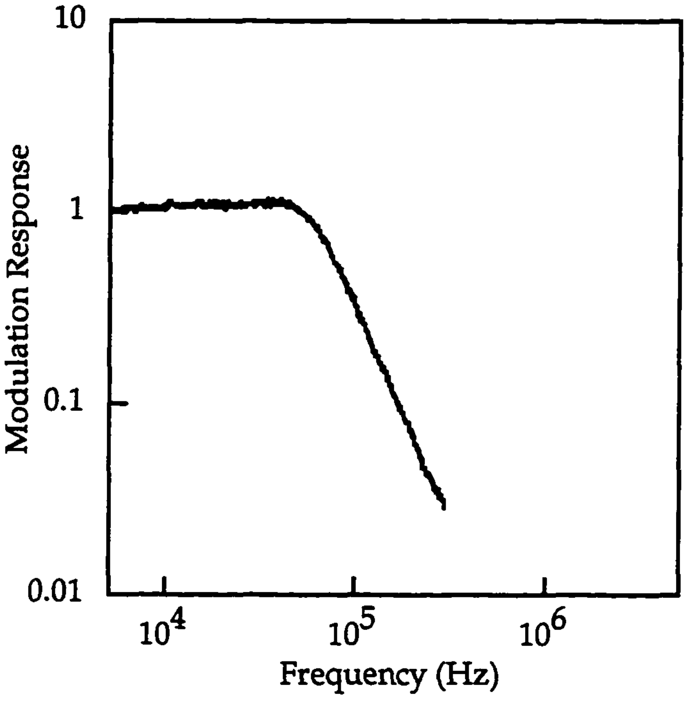


*Figure 2.27 - Small signal modulation response for the critically damped structure.*

#### 2.5.2.2 *Calculation*

We can calculate the resonance frequencies of the cantilevers by modifying the equations in section 2.5.1, replacing the electrostatic force on the cantilever with the inertia of the cantilever. So equation (2-14) becomes

$$P(x) = -\rho \ddot{z}(x) t \qquad (2\text{-}29)$$

where $\rho$ is the density of the material, $\ddot{z}(x)$ is the second derivative with respect to time of the vertical displacement, and $t$ is the thickness. Using this differential equation and the differential equations for force, torque, and curvature (equations (2-5), (2-6), and (2-12)) a differential equation in terms of displacement can be derived:

$$\frac{\partial^4 z(x)}{\partial x^4} = \frac{-12\rho}{Et^2} \ddot{z}(x) \qquad (2\text{-}30)$$

The solution to this differential equation is

$$z(x) = [A \sin kx + B \cos kx + C \sinh kx + D \cosh kx] \sin(\omega t + \phi) \qquad (2\text{-}31)$$

where $A$, $B$, $C$, and $D$ are constants set by the boundary conditions; $\omega$ is the frequency of oscillation; $\phi$ is the phase of the oscillations; and $k$ is the given by

$$k^4 = \frac{12\rho}{Et^2} \omega^2 \qquad (2\text{-}32).$$

By applying the boundary conditions we can get the relationship between $A$, $B$, $C$, and $D$, and find the values of $k$. Let's starts with some simple approximations for the boundary conditions and gradually add complexity. First, assume the left edge is rigidly held so that

$$z(0) = 0 \qquad (2\text{-}33)$$

and

$$\left. \frac{dz}{dx} \right|_{x=0} = 0 \qquad (2\text{-}34).$$

Also, let's assume the end of the cantilever has no end circle and is totally free so

$$\tau(l) = 0 \qquad (2\text{-}35)$$

and

$$F(l) = 0 \qquad (2\text{-}36).$$

Using these four equations the relationship between $A$, $B$, $C$, and $D$ and the characteristic equation for $k$,

$$\cos kl = \frac{-1}{\cosh kl} \qquad (2\text{-}37),$$

can be determined. If the right and left sides of this characteristic equation are plotted, one finds an infinite number of intersection points where (2-37) is solved. Each intersection point and its $k$ value correspond to a mode of the cantilever. Plugging these values for $k$ into the equations, the shape and frequency of each mode can be determined.

For the cantilever shapes used in this thesis, only the fundamental mode is significantly excited for three distinct reasons. First, higher order modes have poor modal overlap with the applied pressure. Higher order modes have sections moving up and down at the same time. Only the lowest order mode has the entire cantilever moving in phase with the electrostatic pressure, so this mode is excited much more than the other modes. Second, the higher order modes are effectively stiffer. They require more bending of the cantilever to achieve the same vertical displacement. This means the same voltage does not excite a higher order mode as much as the fundamental mode. Third, the damping in air is dependent on the velocity squared. Higher order modes oscillate faster and therefore have increased damping. For these reasons, we do not see any higher order mode peaks in Figure 2.23.

The boundary conditions used above are only approximations. Correcting the boundary conditions makes the equations messier, although still solvable. For example, if we add in the force the end circle contributes, equation (2-36) becomes

$$F(l) = \rho \ddot{z}(l) \pi r^2 t \qquad (2\text{-}38).$$

The characteristic equation becomes

$$\frac{\pi r^2 k}{w} = \frac{1 + \cos(kl)\cosh(kl)}{\sin(kl)\cosh(kl) - \sinh(kl)\cos(kl)} \qquad (2\text{-}39).$$

At this point, a program like Mathematica is useful for keeping track of the various terms solving for roots of the characteristic equation. The calculation can be further refined by taking into account the mass of the various alloys, the crystallographic dependence of the elastic modulus, the rigidness of the end circle preventing bending for *r* of the cantilever length, and the exact area of the cantilever where the circle and cantilever match. At most, these corrections change the calculated frequency approximately 15%.

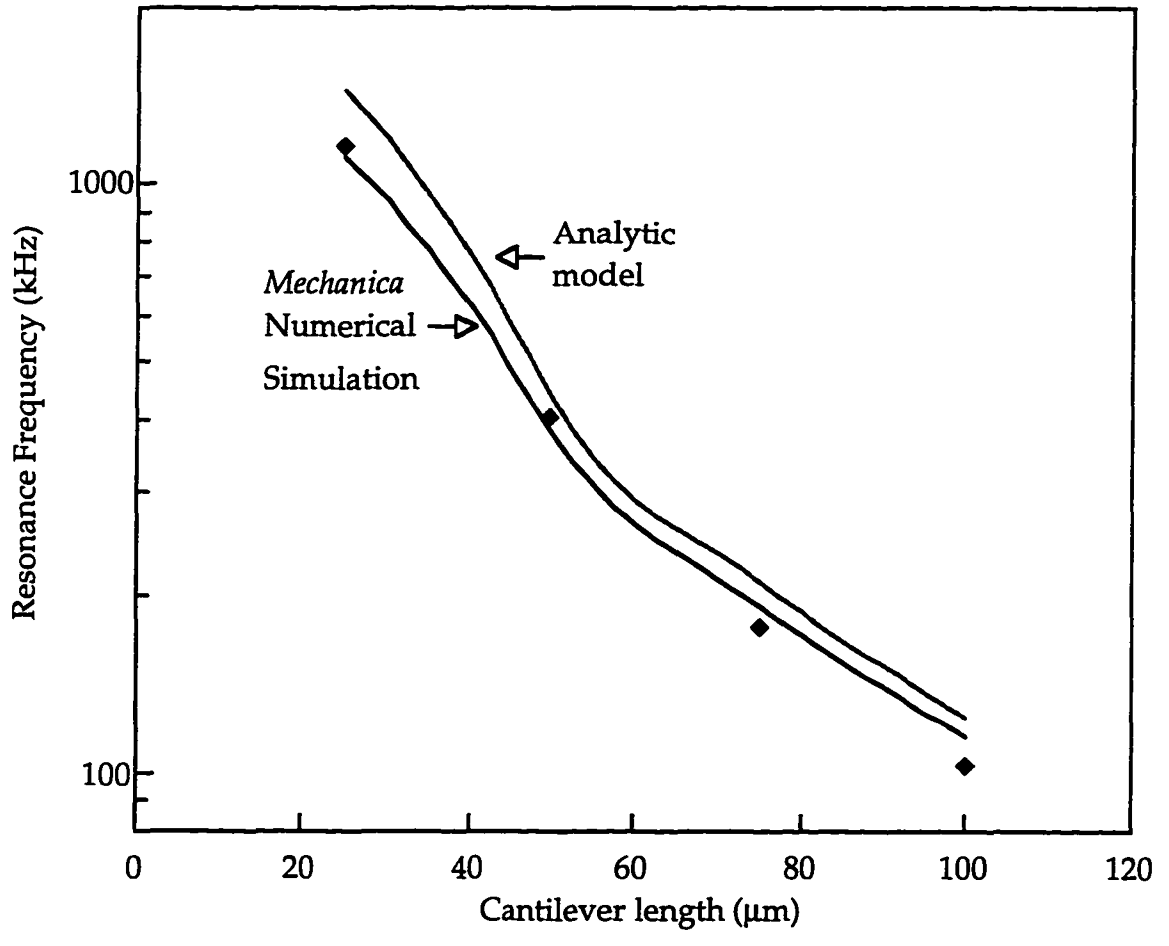


*Figure 2.28 - Experimental measurements (diamonds), analytical calculation (gray line), and numerical computation (black line) of the resonant frequency for various lengths of a 6 μm wide cantilever with a 10 μm diameter end circle.*

Figure 2.28 shows the experimental and calculated resonance frequencies versus length for the cantilevers of Figure 2.23. With out any fitting parameters the analytical model presented above matches the experimental data fairly closely. However, it is still 10% high in its predictions of the resonant frequency.

This is because the model does not take into account that the base of the cantilever has been undercut and is not rigid. The device can also be modeled using a full numerical simulator called *Mechanica*. Without taking the flexible base into account, it matches the analytical results to 3%. When the flexible base is included, the calculated resonant frequency changes as much as 30% for the short cantilevers. For example, the 25 μm cantilever has a predicted resonant frequency of 1.4 MHz without taking the flexible base into account, but this drops to 1.12 MHz with the flexible base. Comparing this to the measured frequency of 1.16 MHz, we see that good agreement is obtained. In general, the accuracy is approximately +/-5%. This is within the error of the prediction, since the cantilever width is only known to within +/-10%.

#### 2.5.2.3 *Tradeoff: Speed and Voltage*

There is a trade-off between high tuning speed and low tuning voltage. For example, a resonance of 1.16 MHz was measured for a 25 μm long, 6 μm wide cantilever, but this device required 54 V to tune the first 10 nm. In comparison, the 100 μm long, 2 μm wide cantilever required only 4.3 V to tune over 70 nm and 1.7 V to tune the first 10 nm, but had a resonance frequency of 76 kHz.

The resonant frequency of a device can be described by

$$f_0 = \frac{1}{2\pi}\sqrt{\frac{k}{m}} \tag{2-40}$$

where $k$ is an effective spring constant and $m$ is an effective mass. So clearly there are two ways we can increase the resonant frequency: increase $k$ or decrease $m$. However, if $k$ is increased, the tuning voltage goes up due to the increased stiffness of the cantilever. If we decrease $m$, we must not do it by decreasing the area of the device, since this also increases the required tuning voltage. To see this more quantitatively, we need the equations for the mass

$$m = \rho A t \qquad (2\text{-}41),$$

and for $k$. $k$ can be expressed in terms of $l, w, A, t$, etc., but the real parameters of interest are the tuning voltage and range. If we specify a certain tuning voltage and a certain tuning distance, we have in effect already specified $k$. This follows from the equation defining $k$,

$$F = k\Delta d \tag{2-42}$$

where $F$ is the force applied by the tuning voltage and $\Delta d$ is the tuning distance required to get a given tuning range. Plugging in the formula

$$F = \frac{\varepsilon_0 A V^2}{2d^2} \tag{2-43}$$

into (2-42) and solving for $k$ gives

$$k = \frac{\varepsilon_0 A V^2}{2d^2 \Delta d} \quad (2\text{-}44).$$

If we plug this and (2-41) into (2-40) we get

$$f_0 = \frac{1}{2\pi}\sqrt{\frac{\varepsilon_0}{\rho t 2d^2 \Delta d}}V \quad (2\text{-}45).$$

So the resonant frequency of the device is directly proportional to the tuning voltage required by the device.

This is not to say that the tuning speed cannot be improved while keeping the tuning voltage to reasonable levels. Just looking at equation (2-45), we can see that a lighter material, a thinner cantilever, a smaller tuning distance, and a smaller air gap would all improve the resonant frequency without increasing the tuning voltage. Recent new processing capabilities have allowed very thin, highly reflective oxidized mirrors to be made. These devices would have higher resonant frequencies for the same tuning voltage. The above calculations also make numerous assumptions, which clever devices may be able to circumvent. But the point is most of these changes improve things by only so much. After that point, there are necessarily trade-offs between trade off tuning voltage and resonant frequency.

This trade-off is shown for the current generation of filters in Figure 2.29. This plots the tuning voltage to tune 10 nm versus resonant frequency for a variety of tunable filters ranging in widths from 2 to 6 μm, lengths from 25 to 100 μm, and end circle diameters of 0 μm to 20 μm. Despite these different shapes, the points fit closely along a proportional line.

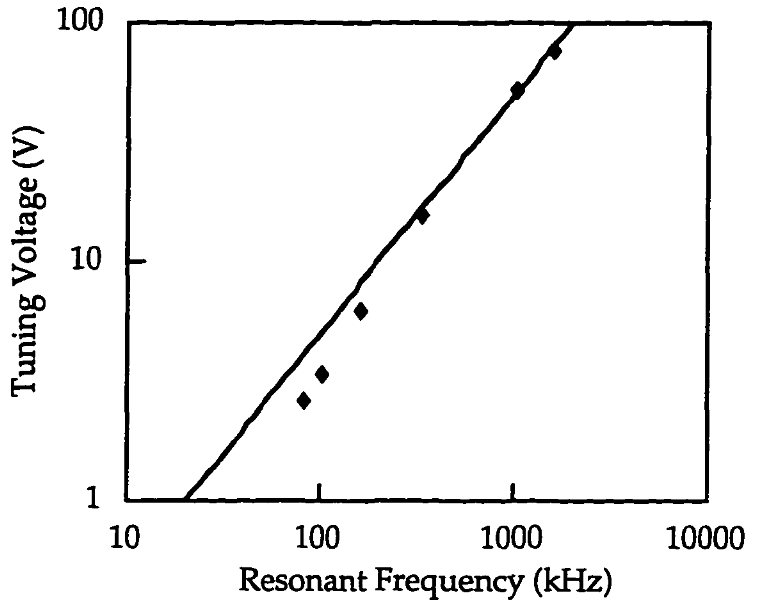


*Figure 2.29 - Tuning voltage versus resonant frequency for a variety of cantilever widths, lengths, and end circle areas. They fit closely to a proportional curve.*

## 2.6 Lifetime Measurements

One concern for a mechanical tunable device is its lifetime. In the macroscopic world, we are used to mechanical things wearing out. However, things are different with microscopic single crystalline material. The micromechanical devices described here should have a long lifetime. Of course, comprehensive testing must be done before this can be definitively established. In this chapter, we discuss why long lifetime is expected and show some promising preliminary results.

Materials generally have two to three regions in their "stress-strain curve", the plot of their expansion or contraction as a function of pressure. For low forces materials elastically deform. That is, they bend, but when the force is removed, they return to their original shape. When a high enough force is applied, two things can happen. The material could start to inelastically bend and then break. In this domain, if the force is removed the material does not return to its original shape. The other possibility is the material just breaks. The pressure above which elastic bending no longer occurs is called the yield strength.

Most materials have a temperature below which they cannot be bent permanently[19]. Above that temperature, there is a region at high strain where they can be bent permanently. For example, below -160°C, iron cannot be bent permanently. Of course, if you apply a force it bends, but when the force is released it returns to its original position. If you apply more force in an effort to permanently bend it, it eventually just breaks. However, at room temperature, it is possible to bend iron permanently (for example, a coat hanger). The temperature where this transition takes place is called the Brittle-to-Ductile Transition (BDT) temperature. It is usually ~0.6 of the melting point temperature.

The Brittle-to-Ductile Transition temperature for most semiconductors is several hundred degrees C. So, except during certain processing steps, semiconductors are in the brittle regime*. Hence, they break instead of bend. What this boils down to is that at room temperature GaAs cannot be bent permanently. Therefore, there is no need to worry about hysteresis or permanent bending when moving GaAs levers: they break first.

What causes the BDT and why is it seen in so many materials? The answer lies in the movement of defects. Above the BDT, defects can move around and form to alleviate strain. When they do this they cause the material to permanently bend. Below the BDT defects cannot move, and if we break a bond the defect stays in the same place. This favors the creation of cracks and breaking. Fortunately, as we saw in section 2.5.1.5, the strain required to break single crystalline GaAs is quite large and the maximum strain in typical devices is 1000 less than the yield strain.

* However, if you were to look at the mechanical properties of GaAs at 500°C it could bend permanently. In fact, this is precisely why so much research has been done in this area. When a material is bent permanently it introduces defects, which degrade electronic devices. So during high temperature processes with semiconductors, it is very important that no bending from thermal stresses occurs.

Preliminary experimental data partially confirming the lifetime claims is shown in Figure 2.30. After nine thousand cycles, no change was observed in the tunable filter. Much longer lifetimes should be possible. The current measurement was limited by the measurement equipment, which was designed for DC measurements. Longer lifetimes, up to billions of cycles, are shown in section 5.9.

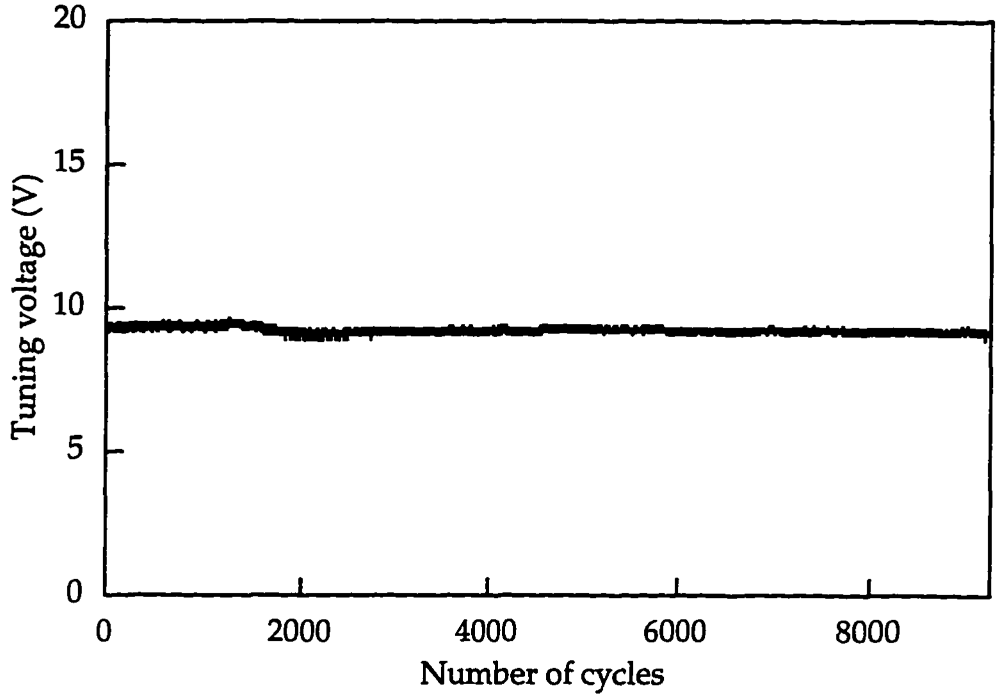


*Figure 2.30 - Preliminary lifetime measurement. A tunable filter was swept through its entire tuning range while illuminated with a fixed wavelength source. The voltage of peak transmission was recorded and is shown versus the number of cycles.*

## 2.7 Conclusion

In conclusion, we have demonstrated a surface normal filter with 70 nm of continuous tuning by applying a 4.9 volt tuning voltage. Resolution bandwidths of 6 nm, extinction ratios of 20.3 dB, and tuning speeds of 7.5 μs were also obtained. The fabrication is simple, high yield, and requires only two noncritical masking steps. The filters are polarization insensitive throughout the entire tuning range. Experimental results for tuning voltage, range, and speed are in good agreement with theoretical calculations. The lifetime of these devices is expected to be long. With the theory and tests of this chapter, we are now able to continue on to tunable detectors and tunable VCSELs.

## 2.8 References

[1] C. A. Brackett, "Dense Wavelength Division Multiplexing Networks: Principles and Applications," *IEEE J. Select. Areas Commun.*, vol. 8, no. 6, p. 948-64, 1990.

[2] T. L. Koch, F. S. Choa, F. Heismann, and U. Koren, "Tunable Multiple-Quantum-Well Distributed-Bragg-Reflector Lasers as Tunable Narrowband Receivers," *Electron. Lett.*, vol. 25, no. 14, p. 890-2, 1989.

[3] L. L. Buhl, R. C. Alferness, U. Koren, B. I. Miller, M. G. Young, T. L. Koch, C. A. Burrus, and G. Raybon, "Grating Assisted Vertical Coupler/Filter for Extended Tuning Range," *Electron. Lett.*, vol. 29, no. 1, p. 81-2, 1993.

[4] C. Wu, C. Rolland, F. Shepherd, C. Lorocque, N. Puetz, K. D. Chik, and J. M. Xu, "InGaAsP/InP Vertical Directional Coupler Filter with Optimally Designed Wavelength Tenability," *IEEE Photon. Technol. Lett.*, vol. 4, no. 4, p. 457-9, 1993.

[5] A. D'Alessandro, D. A. Smith, and J. E. Baran, "Multichannel Operation of an Integrated Acousto-Optic Wavelength Routing Switch for WDM Systems," *IEEE Photon. Technol. Lett.*, vol. 6, no. 3, p. 390-2, 1994.

[6] K. W. Cheung, M. M. Choy, and H. Kobrinski, "Electronic Wavelength Tuning Using Acousto-optic Tunable Filter with Broad Continuous Tuning Range and Narrow Channel Spacing," *IEEE Photon. Technol. Lett.*, vol. 1, no. 2, p. 38-40, 1989.

[7] K. Hirabayashi, H. Tsuda, and T. Kurokawa, "Tunable Liquid-Crystal Fabrey-Perot Interferometer Filter for Wavelength-Division Multiplexing Communication Systems," *J. Lightwave Technol.*, vol. 11, no. 12, p. 2033-43, 1993.

[8] J. S. Patel, "Electrically Tunable Ferroelectric Liquid-Crystal Fabry-Perot Filter," *Optics Lett.*, vol. 17, no. 6, p. 456-8, 1992.

[9] N. Tokato, T. Kominato, A. Sugita, K. Jinguji, H. Toba, and M. Kawachi, "Silica-Based Integrated Optic Mach-Zehnder Multi/Demultiplexer Family with Channel Spacing of .01-250 nm," *IEEE J. Select. Areas. Commun.*, vol. 8, no. 6, p. 1120-7, 1990.

[10] S. R. Mallinson, J. H. Jerman, "Minature Micromachined Fabry-Perot Interferometers in Silicon," *Electron. Lett.*, vol. 23, no. 20, p. 1041-3, 1987.

[11] The program was written by G. S. Li and S. F. Lim. It uses the transfer matrix method to calculate the reflectivity. The layer thicknesses and compositions are specified by an input file, and the program calculates the refractive index for each wavelength.

[12] H. Ukita, Y. Uenishi, H. Tanaka, "A Photomicrodynamic System with a Mechanical Resonator Monolithically Integrated with Laser Diodes on Gallium Arsenide," *Science*, vol. 260, p. 786-9, 1993.

[13] S. Salimian, C. B. Cooper, III, "Selective dry etching of GaAs over AlGaAs in $SF_6/SiCl_4$ mixtures," *J. Vac. Sci. Technol.*, vol. 6, no. 6, p. 1641-4, 1988.

[14] C. H. Mastrangelo, and C. H. Hsu "Mechanical Stability and Adhesion of Microstructures Under Capillary Forces--Part I: Basic Theory," *J. Microelectromechanical Sys.*, vol. 2, no. 1, p. 33-43, 1993.

[15] B. Hök, and K. Gustafsson, "Vibration Analysis of Micromechanical Elements," *Sensors and Actuators*, vol. 8, p. 235-43, 1985.

[16] Wynant, R. and Ediger, M.,*Electrooptics Handbook*, McGraw-Hill, Inc., 1994.

[17] Peterson, K. E., "Silicon as a Mechanical Material," *Proceedings of the IEEE*, vol. 70, no. 5, p. 420-57.

[18] Ukita, H., Uenishi, Y., and Tanaka, H., "A Photomicrodynamic System with a Mechanical Resonator Monilithically Integrated with Laser Diodes on Gallium Arsenide," *Science*, vol. 260, p. 786-9, (1993).

[19] K. T. Faber, and K. Mallow, Editors, *The Mechanical Properties of Semiconductors*, Vol. 37 of *Semiconductors and Semimetals*, Academic Press, Inc., San Diego, (1992).

# 3. Micromechanical Tunable Detectors

## 3.1 Introduction

In the previous chapter, a wide tuning low-cost filter useful for WDM systems and handheld spectroscopy was demonstrated. In most of these applications, immediately after filtering the light a detector would be needed. This chapter discusses a tunable filter integrated with a detector, eliminating a bulky external detector. There are several additional advantages to this approach: built-in shielding against ambient light, resonant cavity detection for high speeds, and several wavelength tracking possibilities.

The tunable detector requires several of the same design changes needed by the tunable VCSEL: a third contact, a tunable air gap layer inside the top mirror, and an *npn* structure. Getting these design changes to work is a step along the way to a tunable VCSEL.

The detector fabricated for this chapter has a QW absorption region inside the Fabry-Perot cavity, making it a resonant cavity detector[1,2]. The wavelength is again continuously tuned by applying a voltage to electrostatically attract the two mirrors. The tunable detector exhibited a wide tuning range of 30 nm, 17 dB extinction ratio, 11% quantum efficiency, using a 7 volt tuning voltage and 50 μA tuning current. To the best of our knowledge, this is the widest tuning range ever demonstrated for a tunable detector[3,4]. Like the filter, the tunable detector is polarization insensitive, easy to couple, compact, and simple to process. Also like the filter, the devices are naturally fabricated as 2-D arrays with no cleaved facets, allowing for wafer scale processing and possible integration with other electronic and optical devices.

In addition, using certain biasing schemes, this detector can function as two novel devices: (1) A tunable detector with signal tracking and (2) a wavelength meter. Using a feedback path internal to the device, the FP cavity can be locked close to an input signal wavelength. Thus, this detector can tune to different wavelength channels and lock onto them, allowing a large tolerance for environmental and aging wavelength shifts, while maintaining the maximum possible extinction of neighboring channels.

## 3.2 Design and Principles of Operation

To turn the tunable filter of the previous section into a tunable detector a quantum well is added to the center of the cavity. This quantum well absorbs light resonating inside the cavity and converts it to electrical current[5]. A number of changes are made to the device design to add this absorber. The tunable air gap is moved from the center of the cavity to inside one of the mirrors, to make room for the absorber. An additional pn junction is added to the device to bias the quantum well absorber. Finally, the processing of the device is changed to make contact to this additional pn junction.

Figure 3.1 shows a schematic of the tunable resonant cavity detector. The tunable air gap is placed inside the top mirror, splitting it into two parts. Most of the top mirror is suspended above a tunable air gap by a 100 μm long, 2 μm wide cantilever, but a few mirror pairs are beneath the gap. The part of the top mirror hovering over the substrate is a 20 μm diameter, 2.71 μm thick disk. The upper and lower parts of the top mirror are doped n and p, respectively, and are reverse-biased to apply the tuning voltage. Beneath the p-layers is a l-cavity of GaAs, containing three strained InGaAs quantum wells to absorb the light. Below this layer is the bottom DBR which is doped *n* like the substrate. This forms a *pn* junction to bias the quantum well.

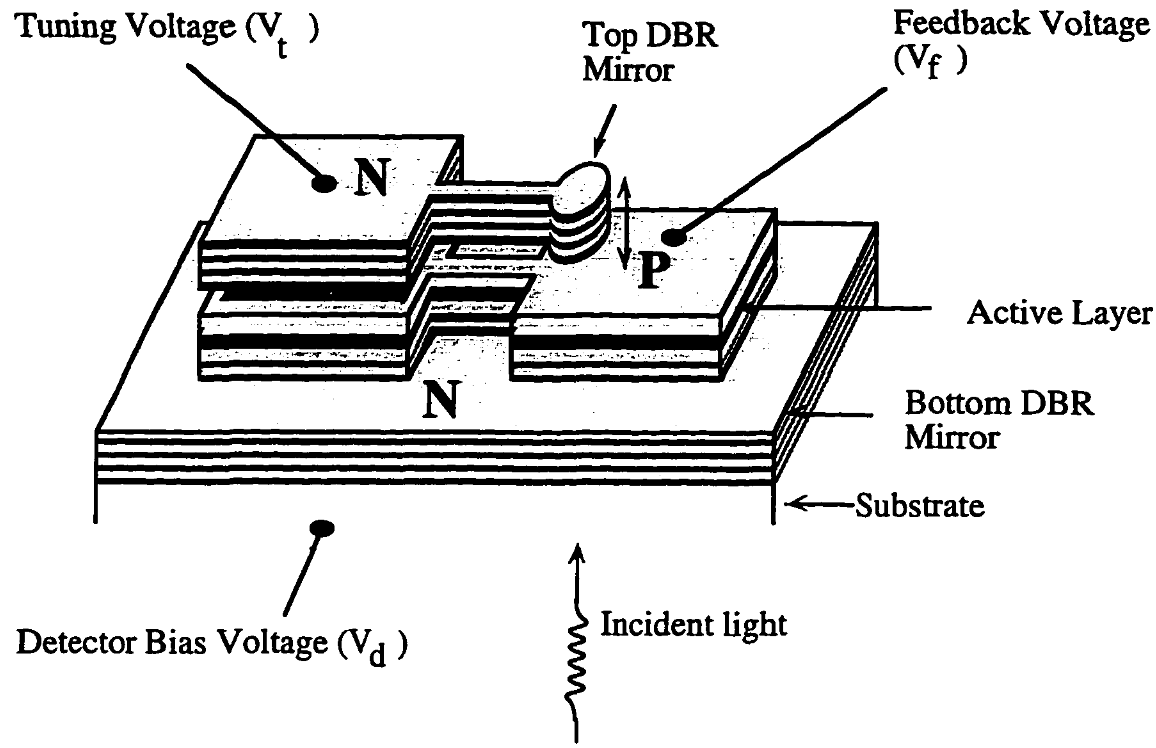


*Figure 3.1 - Schematic of the micromechanical tunable detector.*

By applying a voltage to the top cantilever, it is electrostatically attracted to the substrate, causing the Fabry-Perot resonance of the cavity to shift. Moving the top mirror a mere 0.4 μm causes the Fabry-Perot peak to continuously tune 30 nm. Since the top mirror is moved over only 29% of the gap, no sticking or hysterisis is observed.

### 3.2.1 Design of tunable detector - reflectivities and absorption

For the tunable filter, 100% transmission occurs when reflectivity of the two mirrors is equal. This section investigates which combinations of reflectivities and absorptions make the detector 100% absorbent.

We start with a simple model for the Fabry-Perot cavity shown in Figure 3.2. This consists of two reflectors with an absorbing layer between them. Such a structure is 100% absorbing if it does not transmit or reflect any light. If the back mirror (R2) is 100% reflecting, no light is transmitted. Suppose we mentally lump the absorbing layer in with the 100% R2 reflector to create a mirror with an effective reflectivity of R'2. The cavity does not "know" whether absorption or transmission causes $R_2'$ to be less than 100%. The problem has now been reduced to that of the tunable filter: if $R_1$ and the absorption are adjusted so $R_1=R_2'$, no light is reflected from the device, and therefore all the light is absorbed.

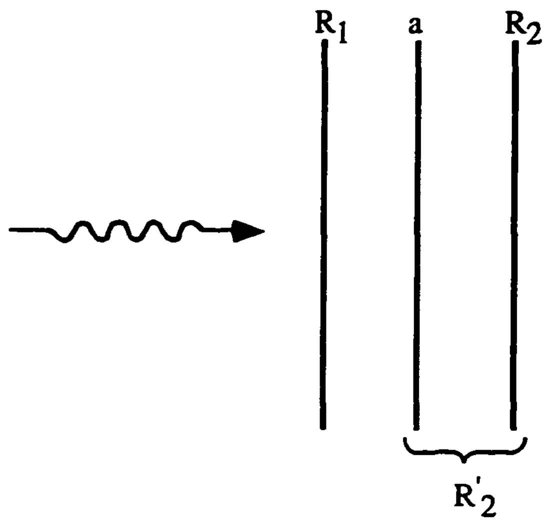


*Figure 3.2 - Simple model for the tunable detector to determine the best absorption and mirror reflectivities. One helpful way to look at the tunable detector is to lump the absorption and $R_2$ into an effective $R_2'$. Then the problem is reduced to that of the filter.*

Calculating the round trip absorption is straightforward, except for one tricky point: *it is very important to take into account reflections from the absorbing layer*. Without these reflections, effects due to standing waves are not properly accounted for. For example, if the absorbing layer is placed at a node in the standing wave pattern, no absorption should occur, because there is no field there. This seems to contradict what one would expect by superimposing two counter-propagating traveling plane waves. In that case, it appears light absorbed from the left traveling and right traveling wave, and hence from the standing wave made by the superposition of these two waves. These two views can be reconciled by including the reflections which occur at an abrupt change to a absorbing or amplifying medium. In the case of an absorbing medium placed at a null, these reflections add constructively to the transmitted beams, making up for the "absorbed" light.

This effect is shown in Figure 3.3 for an 80 Å QW with 6000 cm-1 of absorption placed in two counter-propagating waves. The reflected field (Er) of the right traveling wave adds constructively to the transmitted field ($E_t$) of the left traveling wave if the left and right traveling waves are exactly out of phase (i.e,. null in the standing wave pattern) at the middle of the quantum well. In this way, absorption is compensated by the reflected light. The opposite happens if the right and left traveling waves are in phase; $E_r$ and $E_t$ destructively interfere, doubling the effective absorption.

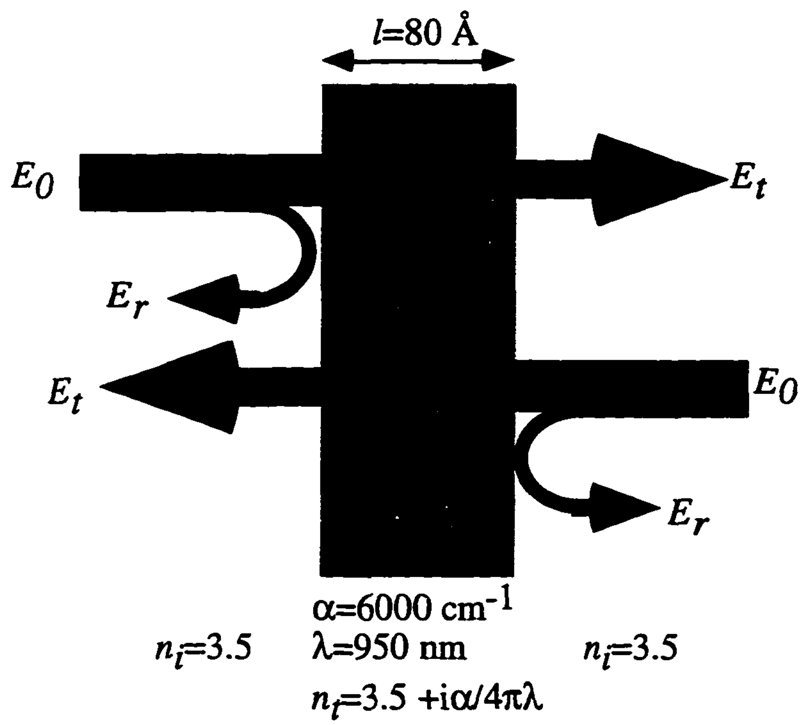


*Figure 3.3 - Even two mediums with the same real part of the refractive index produce a reflection if their imaginary parts are different (i.e., different loss or gain). In a standing wave, these reflections add coherently to the transmitted wave causing zero absorption at a null and extra absorption at an antinode.*

This effect can be calculated. Figure 34 shows the simple case of an 80 Å layer (the same thickness as the quantum wells) with the same real part of the refractive index as the surrounding material (Re(ni))=Re(nt))=3.5) but a different imaginary part. The imaginary part of the refractive index for the quantum well layer is

$$\mathrm{Im}(n_t) = \frac{i\alpha}{4\pi\lambda} \tag{3-1}$$

where $\lambda$ is the wavelength (950 nm) and $\alpha$ is the absorption of 6000 $cm^{-1}$. The layer is a Fabry-Perot cavity with transmission

$$\frac{E_t}{E_0}=\frac{(1-r^2)e^{-i\delta/2}}{1-r^2e^{-i\delta}} \tag{3-2}$$

where $\delta$ is the round-trip propagation factor

$$\delta=\frac{2\pi n_t(2l)}{\lambda} \tag{3-3}$$

and $r$ is the reflectivity of the outside to inside interface

$$r=\frac{n_i-n_t}{n_i+n_t} \tag{3-4}.$$

With the above parameters, the single pass transmission comes out to 0.99522, which matches the transmission ignoring reflections, 0.99521. This single pass absorption is plotted in Figure 3.4 as the thin black line. However, the counter propagating wave is reflected by the absorption layer by

$$\frac{E_r}{E_0}=\frac{r\left(1-e^{-i\delta}\right)}{1-r^2e^{-i\delta}} \tag{3-5}.$$

Figure 3.4 shows the total "transmitted" wave when this reflected wave is added in. When the two counter-propagating waves are out of phase at the center of the quantum well, the reflected wave exactly compensates for the "absorbed light". When the counter-propagating waves are in phase, the effective absorption becomes twice as high, because the reflected wave adds out of phase.

This is important for matching $R_1$ and $R_2'$. For example, suppose bandwidth requirements dictate $R_1$ (and therefore $R_2'$) should be equal to 99%. At first glance, it appears a 0.5% single pass absorber is necessary to get a round trip absorption of 1% and an effective reflectivity $R_2'$ of 99%. However, if the absorber is placed at the antinode, only a 0.25% absorber is actually needed, and if the absorber is placed at a node, infinite absorption is needed. This point is equally important for the gain of VCSELs, discussed in the next two chapters.

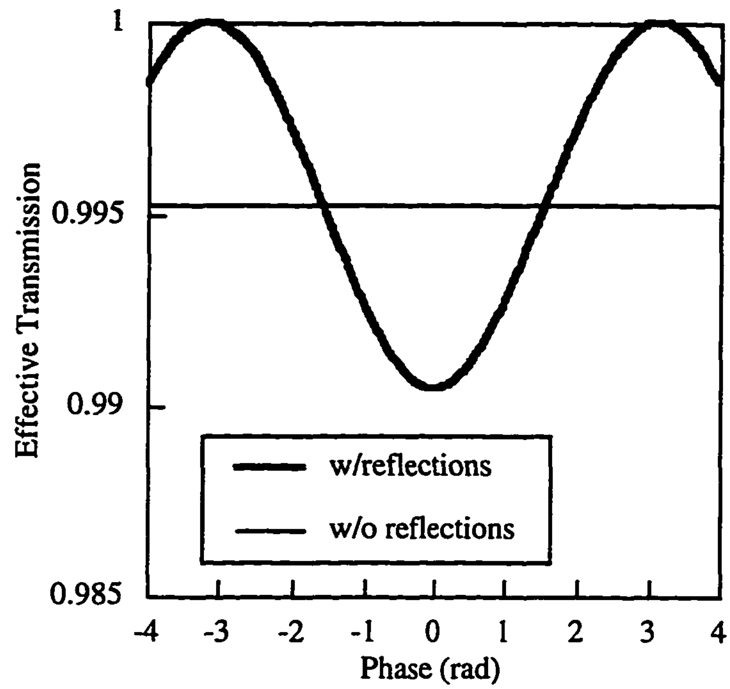


*Figure 3.4 - The effective transmission of a quantum well first looking at the transmitted light for a plane wave heading in one direction (thin line), then adding up the transmitted wave for one plane wave with the reflected wave from an opposite traveling plane wave (thick line). This causes changes in the effective absorption of the quantum well with respect to the phase difference between the two counter-propagating plane waves which can also be understood as standing wave effects.*

### 3.2.2 Effect of Moving Tunable Air Gap into the Top Mirror

Moving the tunable air gap into the top mirror complicates the cavity somewhat. The optical performance of the detector can be calculated with the same program used for the filter. However, before performing calculations, this section tries to give an intuitive grasp of how these devices tune by reducing the full layer structure to simple models.

Figure 3.5 shows the true layer structure for the tunable detector and also a three-mirror model. The device is modeled as a high reflectivity top mirror (rt), a high reflectivity bottom mirror (rb), and a medium reflectivity intracavity mirror (r). The fields penetrate into the DBR, mirrors making them appear to be past the first surface by about 0.9 μm. This penetration is taken into account by placing the idealized hard (i.e., no penetration depth) mirrors at this position. Tuning is simulated by moving the top mirror ($r_t$).

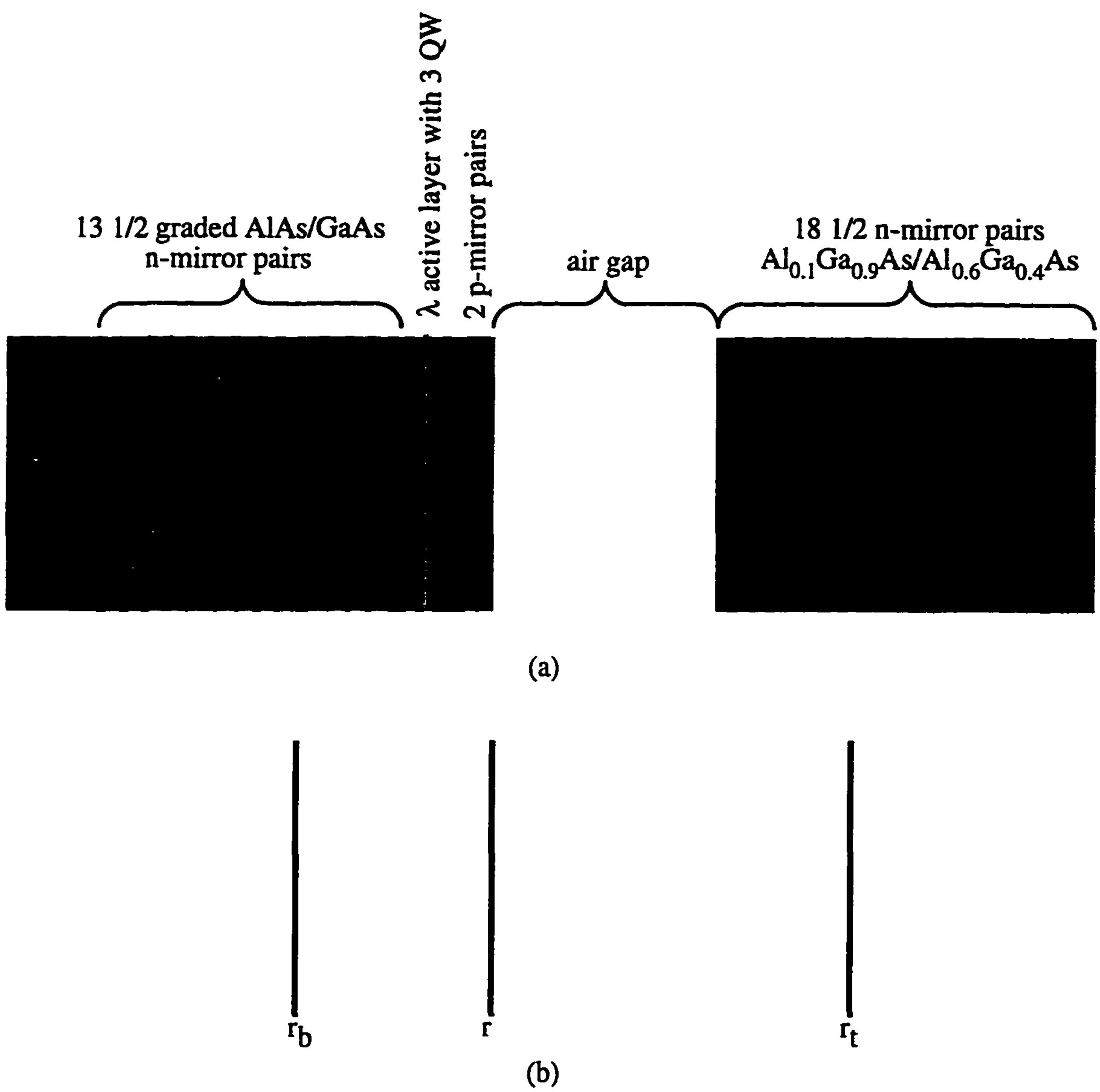


*Figure 3.5 - (a) The real layer structure of the tunable detector. The 2* p*-mirror pairs consist of a* $Al_{0.6}Ga_{0.4}As/GaAs$ *mirror pair next to the active region and a* $Al_{0.6}Ga_{0.4}As/Al_{0.1}Ga_{0.9}As$ *next to the tunable air gap. The active region consists of 3 80 Å* $In_{0.16}Ga_{0.84}As$ *QW. (b) An idealized model of the real tunable detector which takes into account the effective penetration depths of the mirrors.*

Figure 3.6 shows the calculated reflectivity using this model for various air gap thicknesses. The reflectivity is calculated using the Fabry-Perot reflectivity formula

$$\frac{E_r}{E_0} = r_b + \frac{r_t(1 - r_b^2)e^{-i\delta}}{1 + r_b r_t e^{-i\delta}} \qquad (3\text{-}6)$$

where $r_t$ is the top mirror reflectivity from inside the cavity and $r_b$ is the bottom mirror reflectivity from outside the cavity. As the air gap thickness changes, the Fabry-Perot resonances tunes. The tuning is not quite as much as if the air gap is inside the cavity. In that case, an air gap change by $\lambda/2$ causes 100 nm of tuning. Here, an air gap change of $\lambda/2$ causes only 40 nm of tuning.

The two top reflectors can be thought of as an effective mirror which moves an effective distance for a given real movement of the top reflector. The

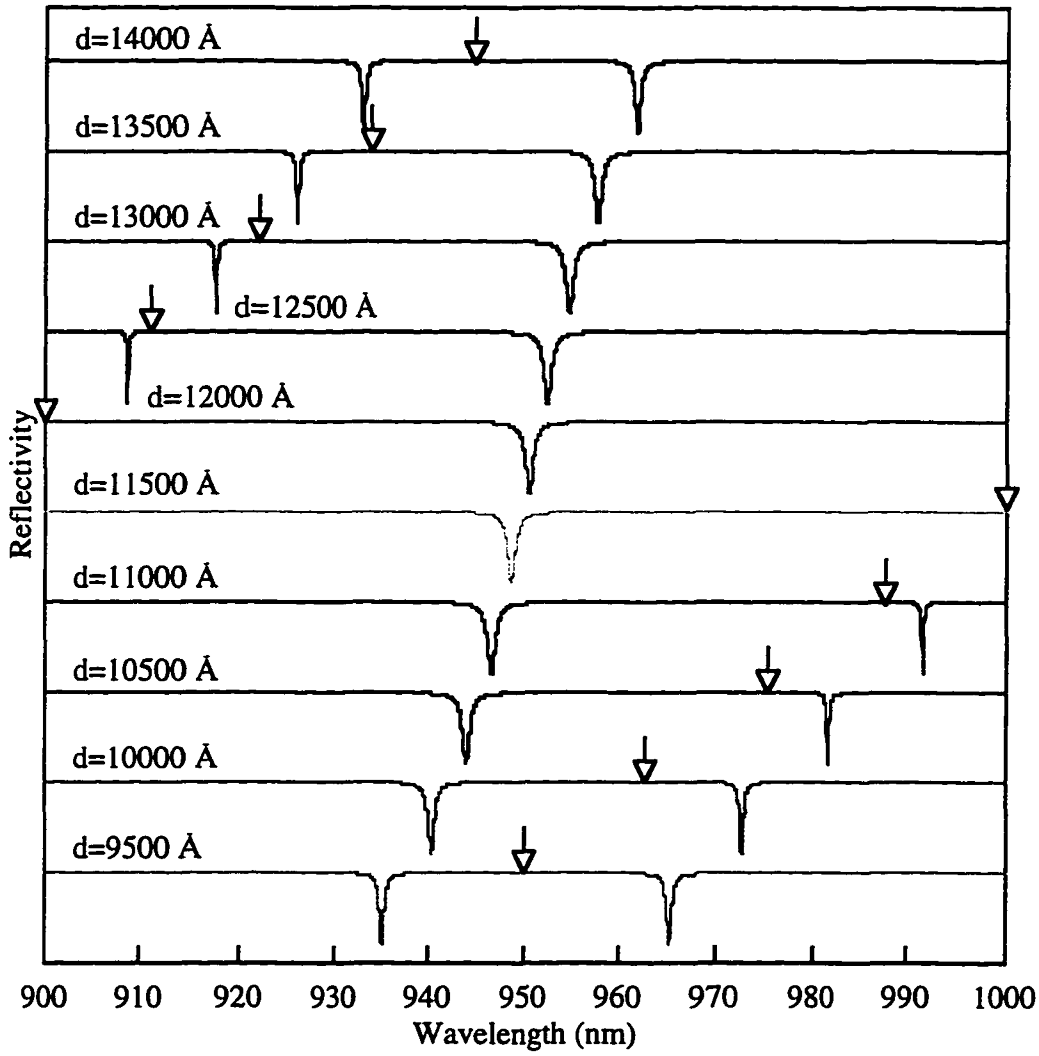


*Figure 3.6 - Calculated reflectivity versus wavelength for various air gaps using the ideal model. The arrows point to the wavelength of the tunable air gap resonance. The tuning of the λ-cavity occurs at a slower rate than the air gap. Also note the tuning speeds up when the air gap resonance approaches the λ-cavity resonance, giving rise to an s-shaped curve.*

ratio of effective movement to real movement depends on r. A higher r lowers this ratio. This simple way of considering the problem works for low values of r when the air gap resonance and the λ-cavity resonance are far apart.

However, this model does not completely explain device behavior. For example, it does not explain the reduction in free spectral range down to 40 nm or the faster tuning when the airgap resonance is close to the λ-cavity resonance. The problem is that the penetration of the top mirror and the ratio of effective movement are not constant. No position and effective movement for the effective top mirror is correct for all wavelengths and air gap thicknesses. Only approximate values which roughly predict device performance over a finite range can be chosen.

The higher the value of $r$, the more the penetration depth changes with air gap position and wavelength, and the less accurately performance can be modeled using an effective top mirror. For example, suppose the middle p layer consists of 6 mirror pairs. Then the penetration depth can vary from about 5 mirror pairs when the air gap is out of resonance (a typical penetration depth for a DBR) to about 16 mirror pairs (6+6 for the symmetric air gap cavity, +5 for the normal penetration depth) when the air gap is in resonance. This effect is shown in Figure 3.7, using the simple model and a higher $r$ of 0.95. Most of the tuning of the air gap does not tune the λ–cavity. Almost all the tuning occurs over a small range where the air gap resonance and λ–cavity resonance are close. This makes it impossible to find a effective position of the top mirror that gives either the correct tuning or Fabry-Perot order for the device.

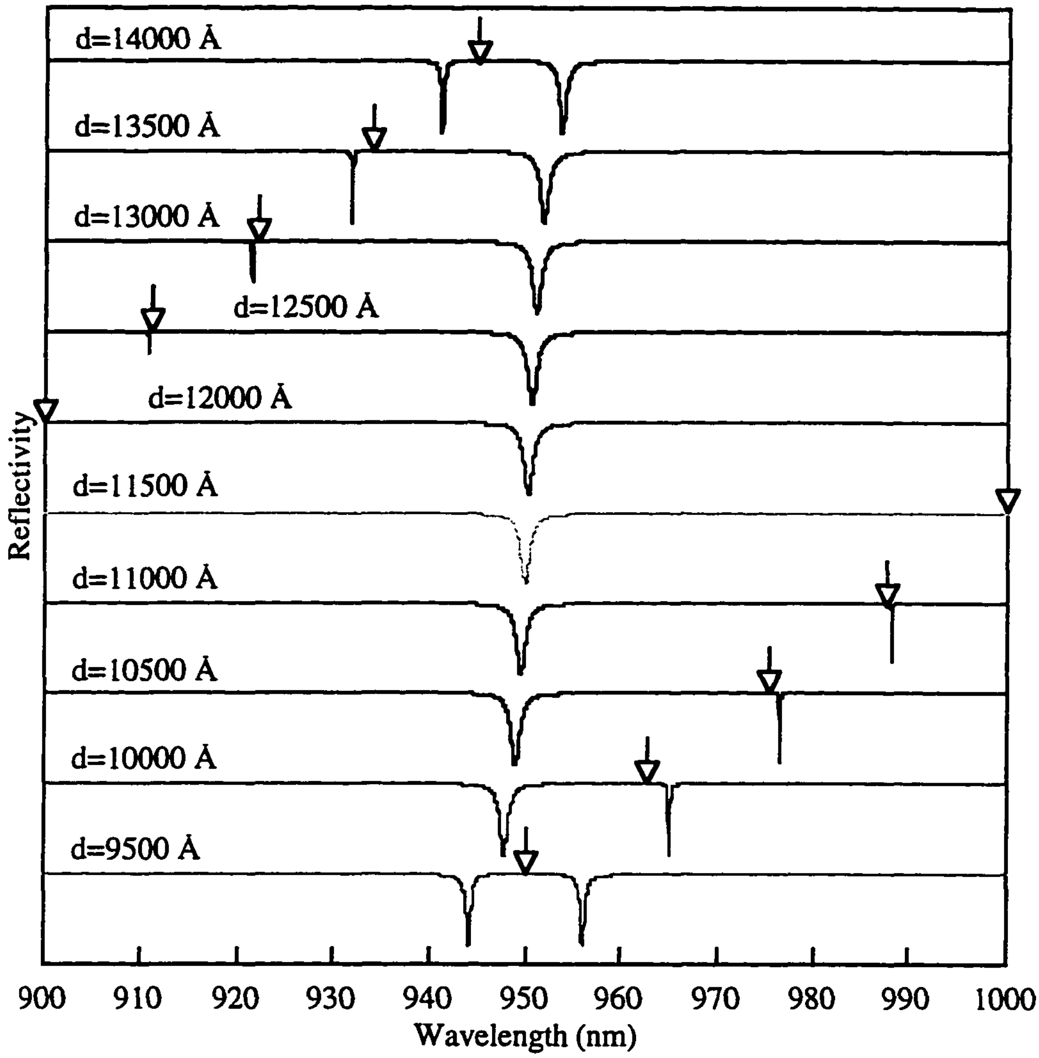


*Figure 3.7 - Calculated reflectivity versus wavelength using the ideal model for a higher reflectivity (r=0.95). The arrows represent the position of the tunable air gap resonance. Note that tuning only occurs mostly when the tunable air gap is resonating at the same wavelength as the λ–cavity (λ=950 nm). This effect is not very well explained by an effective top mirror theory.*

A more complete way of looking at the device is to considerate as a coupled cavity. This is more complicated, but works well for all values of $r$ and explains all the phenomena. The λ–spacer layer and the tunable air gap each form cavities, which are coupled through the middle $p$-layers. The performance is similar to other coupled resonators, such as two pendulums coupled by a weak spring. When the resonators are weakly coupled, either due to a large mismatch in the resonance frequencies or weak coupling, each resonator is, in essence, excited independent of the other. However, when the resonant frequency of the individual cavities are close (how close depends on how strongly they are coupled), the resonances of combined system behave differently than the resonances of the individual systems. If the resonances of the uncoupled systems are the same, the combined system resonates at two frequencies equally spaced around the uncoupled resonant frequency. The stronger the coupling between the systems, the larger the spacing or splitting of these two frequencies. It's as if the resonant frequencies of the two cavities were repulsed by each other.

This effect can explain the operation of the tunable detector. The resonance of the air gap can be thought of as pushing around the resonance of the l-spacer cavity. The amount of "pushing" and "splitting" can be increased by increasing the coupling between the two cavities (i.e,. removing p-layers to lower r). The tuning range is determined by the "splitting" when the uncoupled resonant frequencies are equal, as shown in Figure 3.8. This shows the reflectivity spectra when the l-spacer cavity and the air gap have the same

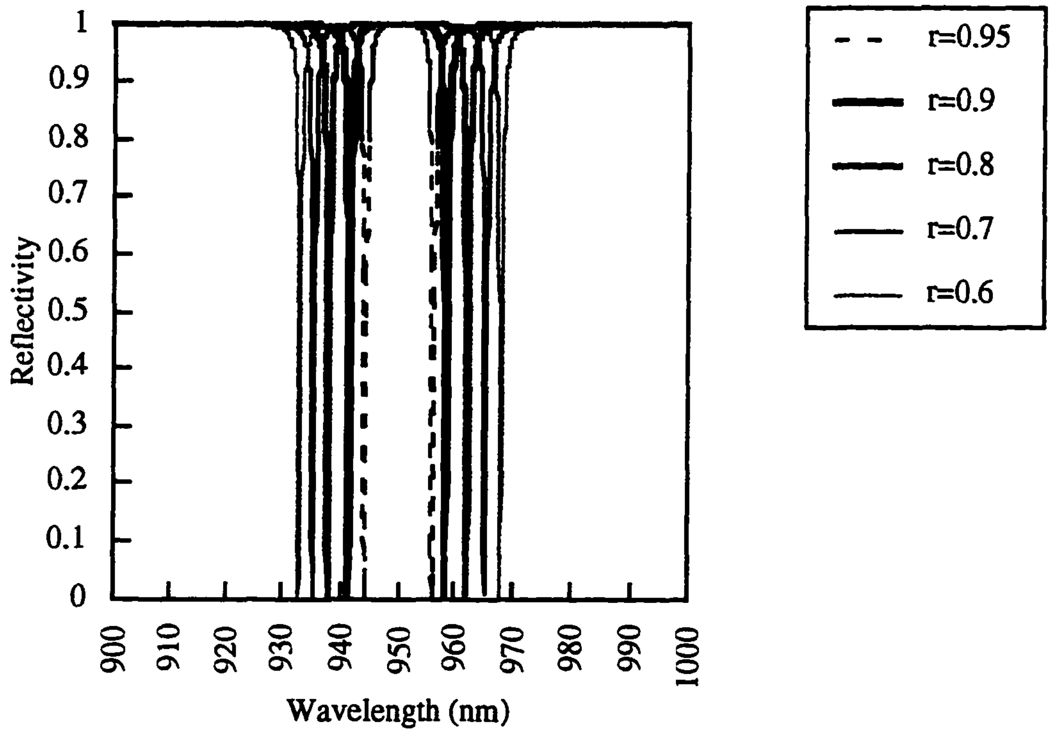


*Figure 3.8 - Reflectivity of the ideal device for different values of the intracavity coupling mirror r. Note that as the coupling increases (r decreases) the splitting of the coupled cavity mode increases.*

resonance wavelength of 950 nm. The resonance does not occur at 950 nm but is split into two resonances on either side of 950 nm. The amount of splitting depends on the amount of coupling between the two cavities. More coupling (lower $r$) leads to greater splitting, or greater wavelength spacing between the two modes.

Although this idea of one resonance pushing the other resonance around is useful for guessing how a structure behaves, it is useful to take a more in depth look at the causes of this repulsion. Figure 3.9 shows the phase of the reflected light from top mirror ($r+r_t$) from inside the cavity with a calculated air gap thickness of 950 nm. As the wavelength approaches the resonance wavelength of the air gap, a $2\pi$ change in the phase takes place. The swiftness of this change depends upon the reflectivity of the middle mirror, r. A higher reflectivity r causes a narrower resonance and hence a quicker change in the phase. This phase affects the resonance of the total cavity through the round-trip phase condition. To be a steady-state mode, light must come back in phase with itself after one round trip so

$$\phi_{bot} + 2\phi_{cav} + \phi_{top} = 2n\pi \tag{3-7}$$

where $\phi_{bot}$ is the phase from the bottom mirror, $\phi_{cav}$ is the single pass phase from the cavity, $\phi_{top}$ is the phase from the top mirror, and $n$ is any integer. We can plot $-(\phi_{bot} + 2\phi_{cav})$ on the same graph as the top mirror phase, $\phi_{top}$, in Figure 3.9. Where the curves cross, the whole structure resonates. This happens in two places, resulting in the two modes of Figure 3.7. This also shows the splitting gets bigger with a lower reflectivity, $r$, because the phase shift occurs over a larger wavelength span.

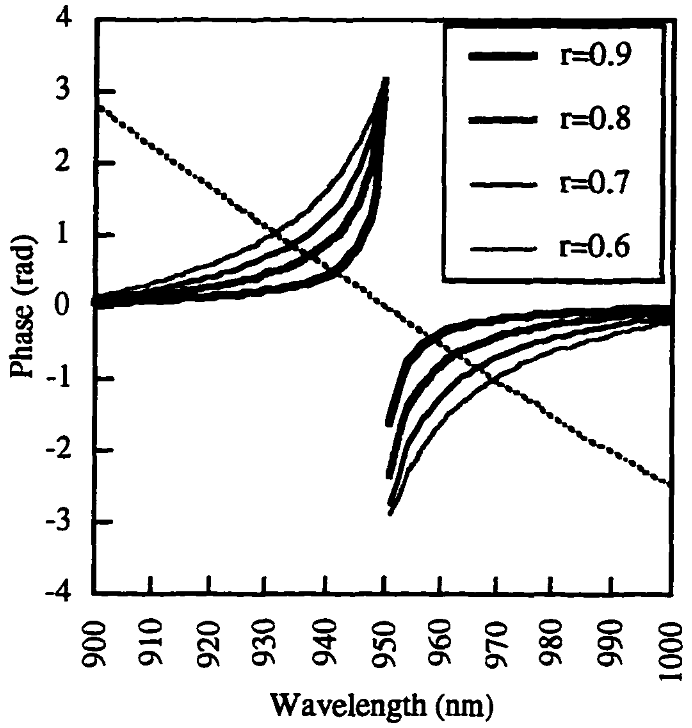


*Figure 3.9 - Phase of the top mirror versus wavelength for an air gap spacing of 9500 Å and different coupling mirror values (r). The dashed curve shows the negative phase of the bottom mirror plus the cavity. Where the two intersect, the phase condition is satisfied and a resonance exists. Note the splitting increases with increased coupling (lower r) between the two cavities.*

Now we see how the coupled cavity model correctly predicts the tuning performance. Figure 3.10 shows the phase of the top mirror versus wavelength for different tuning gap thicknesses in the high reflectivity case. The negative of the phase due to the bottom mirror and the cavity is again also plotted so the resonances are shown by the intersections. This model shows significant tuning only over the region where the air gap and λ–cavity resonances are close to each other (the thick black curve in the Figure). For most of the air gap spacings the λ–cavity, resonance stays at its natural resonance at 950 nm.

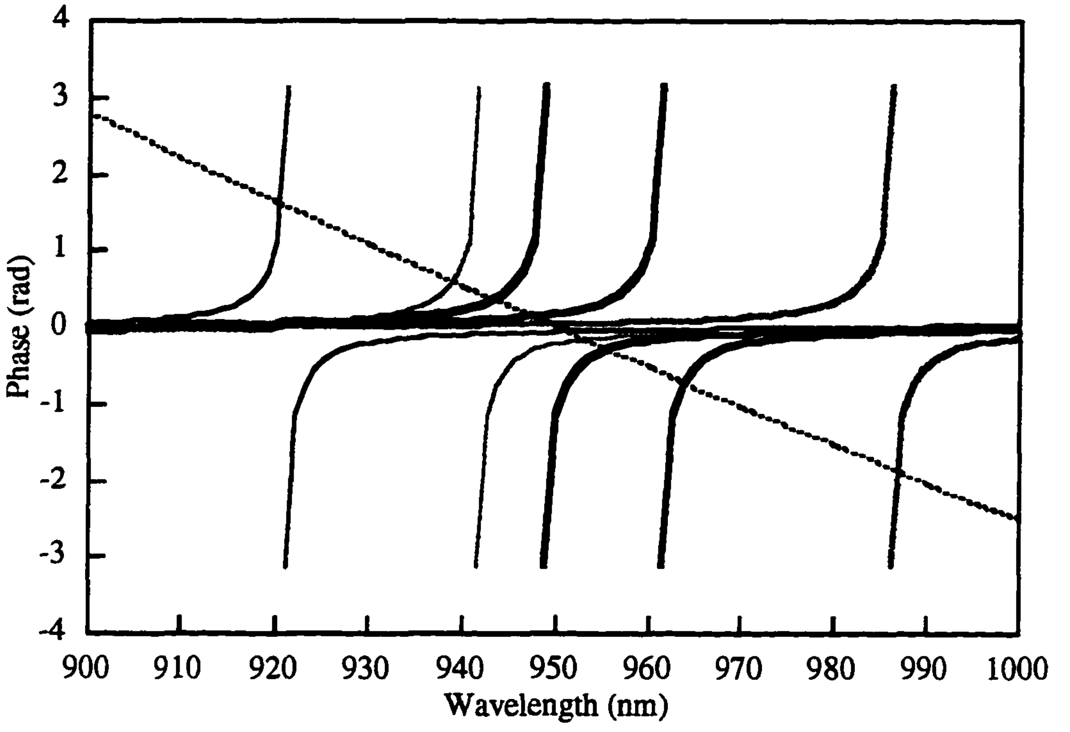


*Figure 3.10 - Using the simple model, the phase of the top mirror versus wavelength for the high reflectivity case is plotted at various air gap thicknesses: 13926 Å (thin gray line), 13000 Å (thin black line), 11000 Å (thick light gray line), 10000 Å (thick dark gray line), 9500 Å (thick black line). The dashed curve shows the negative phase for the bottom mirror plus spacer layer. The intersection points show the resonances. Note how most of the tuning occurs when the air gap cavity is matched to the lambda spacer cavity at 950 nm.*

For the tunable detector, a higher coupling (r=0.7) was used to achieve higher tuning. Then the phase diagram looks like Figure 3.11. Here, we have not plotted all the different air gap spacings of Figure 3.9, but have omitted air gap thicknesses where not much tuning is happening. Using this simple model, a maximum tuning range of ~35 nm is predicted.

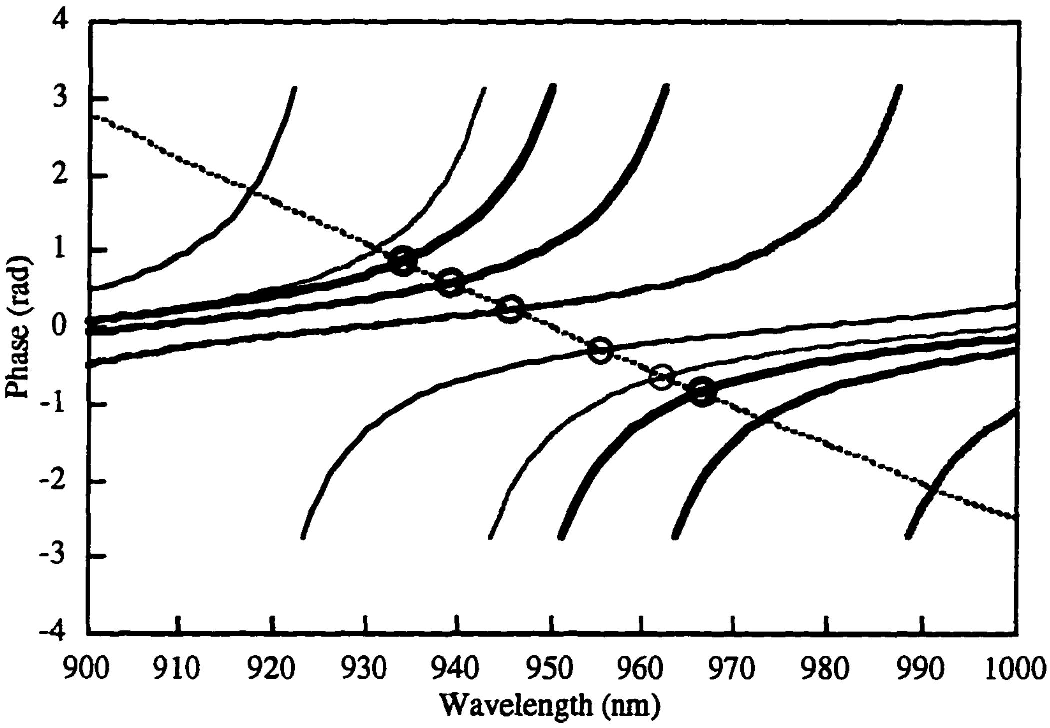


*Figure 3.11 - Using the simple model, the phase of the top mirror versus wavelength at various air gap thicknesses: 13926 Å (thin gray line), 13000 Å (thin black line), 11000 Å (thick light gray line), 10000 Å (thick dark gray line), 9500 Å (thick black line). The dashed curve shows the negative phase for the bottom mirror plus spacer layer. The intersection points show the resonances. Note how these move to short wavelengths as the mirror moves.*

In Figure 3.7, only λ–cavity resonance does not tune much, while the air gap resonance tunes quite a bit. Could the air gap mode be used for tuning? In many cases, the answer is no. The reason is that of the two modes, the mode closer to the λ–spacer cavity has the greatest excitation inside the λ–spacer cavity. The mode closer to the tunable air gap resonant wavelength mostly excites the air gap. For the tunable laser discussed in the next couple chapters, high field excitation in the λ–spacer cavity is needed to have enough gain to overcome the losses of the device. However, with a low loss device or a tunable detector, it may be possible use a structure similar to the tunable filter, and just put the QW active regions inside the mirror. Such a device would be able to tune over a range as wide as the DBR band.

### 3.2.3 Exact mirror design and reflectivity calculations

After roughly designing a structure using the idealized model, the exact properties of the detector can be calculated, as was done for the filter in section 2.2. Most of the curves are similar to the simple model curves where the DBRs are high reflectors.

The real structure is grown on a *n*+ GaAs wafer and consists of a *n*-doped 13 1/2 pair graded AlAs/GaAs DBR mirror, a lambda cavity with three 80 Å $In_{0.16}Ga_{0.84}As$ strained quantum wells, a *p*-doped $Al_{0.6}Ga_{0.4}As$/GaAs DBR pair, a *p*-doped $Al_{0.6}Ga_{0.4}As$/ $Al_{0.1}Ga_{0.9}As$ DBR pair, a 1.39 μm i-GaAs sacrificial layer, and finally a 18 1/2 pair *n*-doped $Al_{0.6}Ga_{0.4}As$/$Al_{0.1}Ga_{0.9}As$ DBR mirror stack. This top *pin* junction is the one that is reverse-biased to apply a tuning voltage, while the bottom *pn* junction is used to bias the QW absorber.

Figure 3.12 shows the phase of the reflected light from the top mirror for different numbers of *p* layers. It looks similar to the simple model case of Figure 3.9. The differences show up at around $\lambda$=995 nm and $\lambda$=905 nm. These arise because at these wavelengths the DBR is no longer a high reflector. The negative phase due to the bottom DBR mirror and cavity are also shown in Figure 3.12 and behaves almost exactly the same as in Figure 3.9. The intersection points that indicate resonances also behave similarly. For the detector, 2 mirror pairs were used to get 40 nm of tuning.

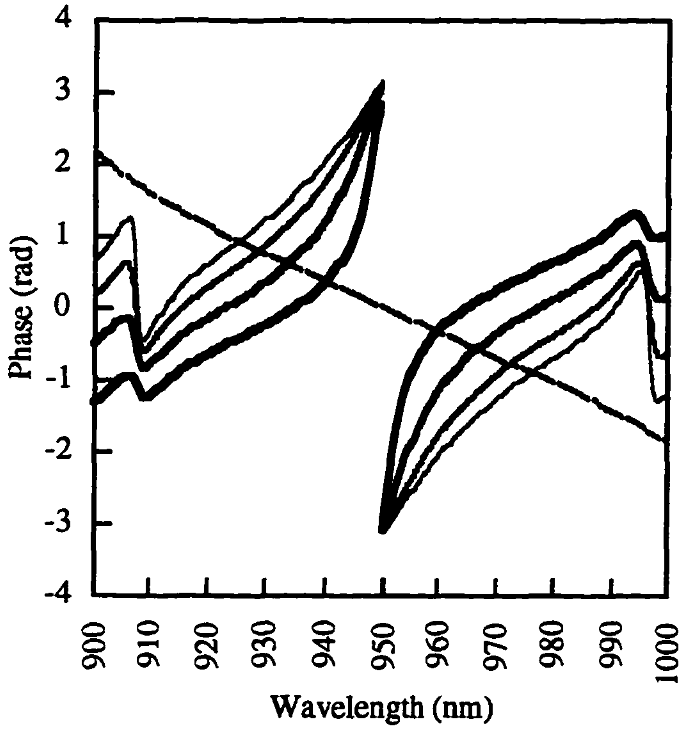


*Figure 3.12 - Plot of top mirror phase versus wavelength with a 9500 Å air gap and different numbers of p mirror pairs: 1 mirror pair (thin gray line), 2 mirror pairs (thin black line), 4 mirror pairs (thick gray line), and 8 mirror pairs (thick black line). The dashed line shows the negative phase of the bottom mirror and spacer. The intersections of these curves show the modes of the device. Note that the splitting of the two modes goes down as the number of mirror pairs goes up (and coupling goes down).*

The tuning of the full structure can be investigated by looking at Figure 3.13, which is analogous to Figure 3.11. This shows the top mirrors phase versus wavelength as the length of the tunable air gap layer is changed. Over the region of interest, the performance is similar to the idealized case. The major differences are at the edges of the plot, where the DBR starts to look less like a mirror.

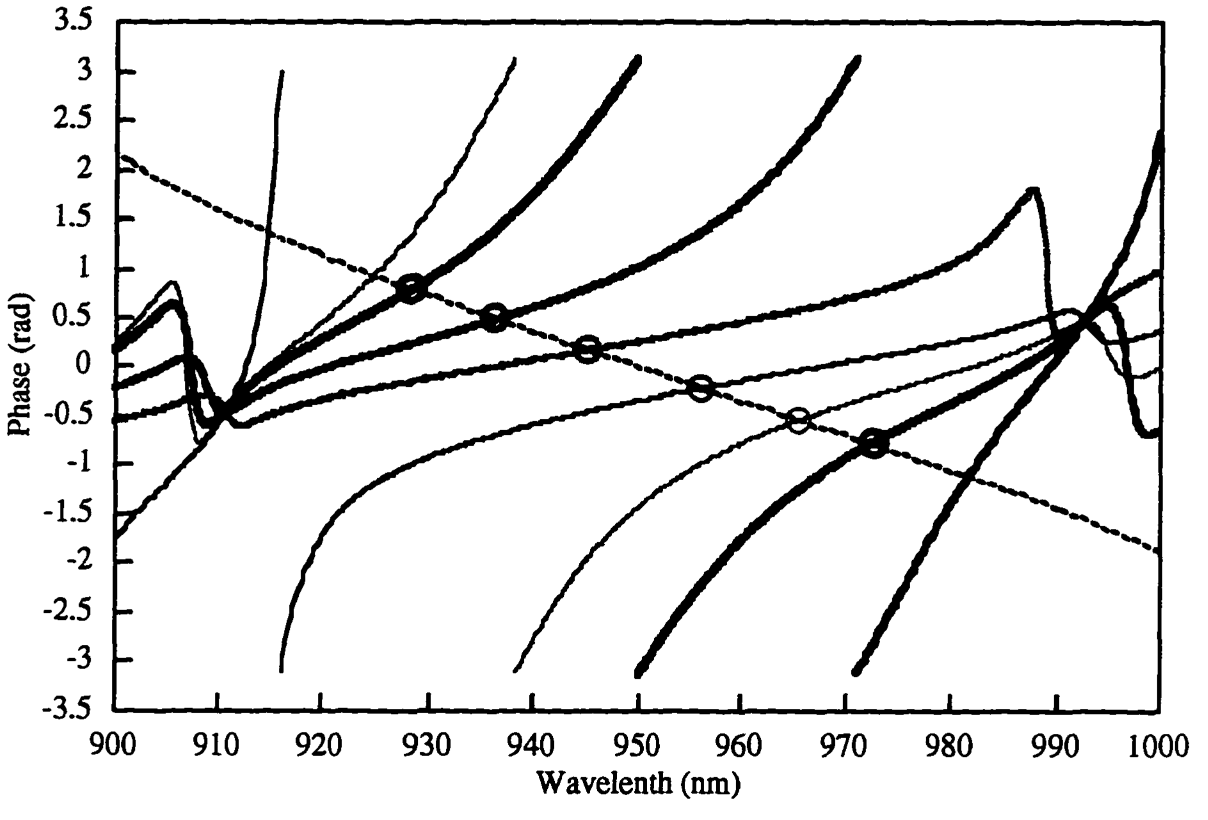


*Figure 3.13 - Plots of the phase of the top mirror versus wavelength for tuning gap thicknesses 13926 Å (thin gray line), 13000 Å (thin black line), 11000 Å (thick light gray line), 10000 Å (thick dark gray line), and 9500 Å (thick black line). The dashed line shows the negative phase of the bottom mirror and spacer cavity. Where these curves intersect (circles) is where the phase condition is met and the device resonates.*

Finally, the reflectivity of the whole device can be calculated, and is shown in Figure 3.14. By comparing it to Figure 3.13, it can be seen that the resonances indeed occur at the points where the phase of the top mirror crosses the negative phase of the bottom mirror and the cavity. This full calculation predicts a "free-spectral range" of 44 nm.

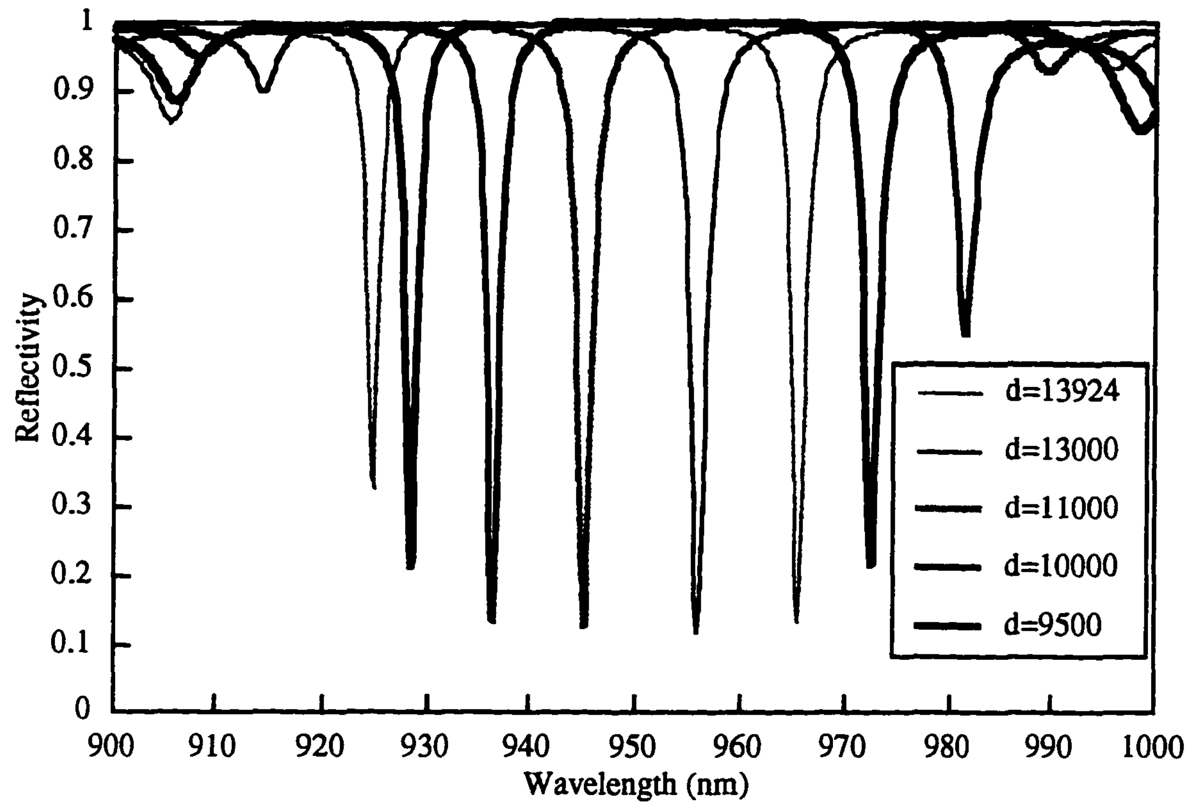


*Figure 3.14 - Plot of reflectivity vs. wavelength showing the Fabry-Perot resonances of the tunable detector for various air gap thicknesses(d). As the air gap shrinks from 13924 Å, the device tunes over almost 40 nm.*

To determine the optimum quantum well absorption, it is necessary to calculate the losses of the mirrors. The calculated bottom mirror reflectivity is shown in Figure 3.15. The top mirror reflectivity depends on air gap spacing as well as the wavelength, which is shown in Figure 3.16. Basically, the bottom reflector is about 2% less reflective than the top reflector. So ideally the quantum wells should have a round-trip absorption of 2%. The quantum well active region of a laser, which has an absorption of about 6%, is used. This provides protection against bleaching of the QW and does not seriously degrade the performance, as seen in Figure 3.14. Despite the mismatch, the minimum calculated reflectivity is 0.15; i.e., there is only a 15% penalty in responsivity for this excess loss.

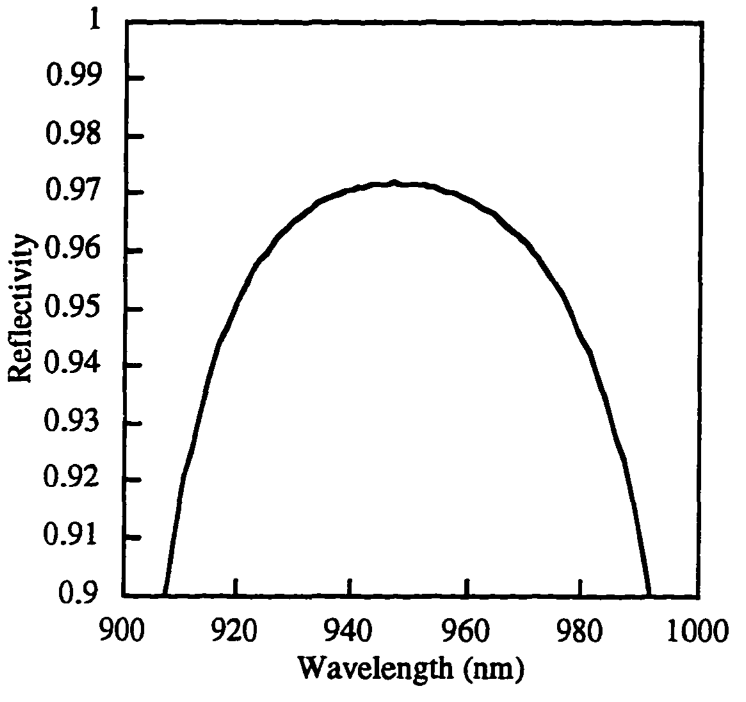


*Figure 3.15 - Bottom mirror reflectivity versus wavelength.*

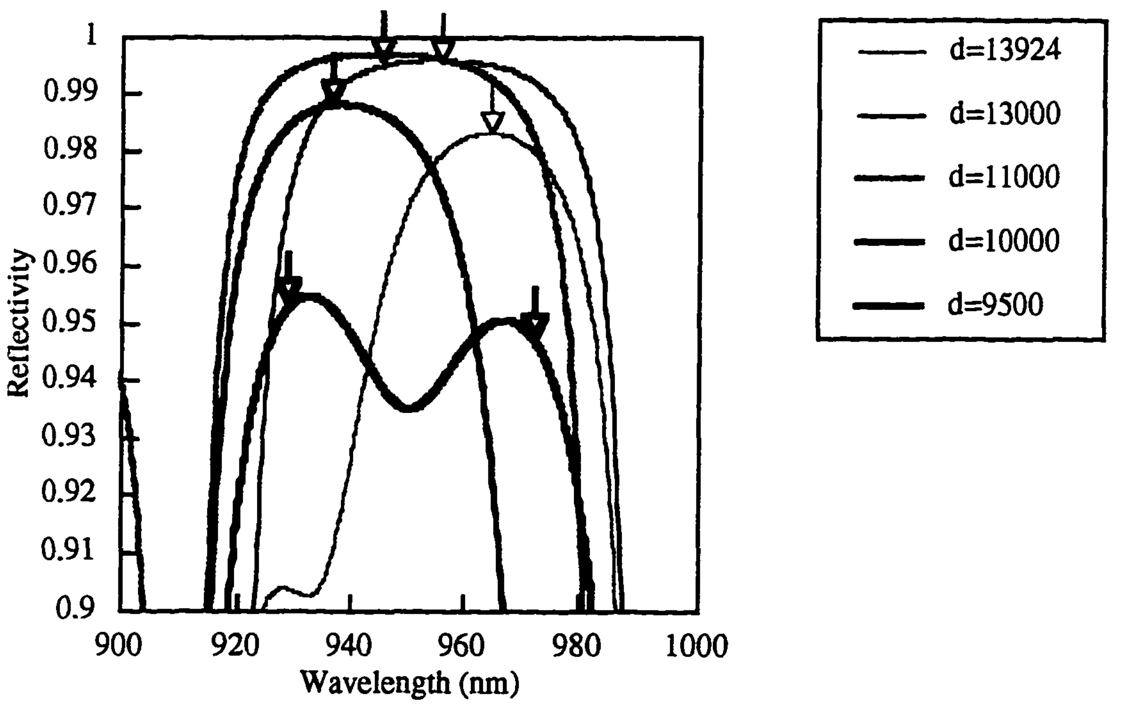


*Figure 3.16 - Top mirror reflectivity versus wavelength for various tunable air gap thicknesses. The arrows show the position of the Fabry-Perot mode for the given air gap.*

## 3.3 Fabrication

The main difference in the fabrication of the micromechanical tunable detector from the tunable filter are the steps to generate the middle *p*-contact. The layers were again grown using MBE, ensuring stable, high-quality, single crystalline mechanical material. The fabrication steps are summarized in Figure 3.17. The first step is to wet etch a large mesa which defines the middle *p*-contact. Then the cantilever lithography is performed, with the tip of the cantilever positioned inside the *p*-contact mesa. This alignment is non-critical, since the 20 μm tuning head can be anywhere inside the *p*-contact. Because wet etching is used for the *p*-contact mesa, the edges are sloped and the 1.4 μm thick cantilever photoresist can easily "climb" the walls of the mesa. The sample is then anisotropically dry etched to define the cantilever. The etch depth is controlled so that the areas that will form the middle *p*-contact are etched down the GaAs sacrificial layer. Note that areas not protected by the mask of step 1 or

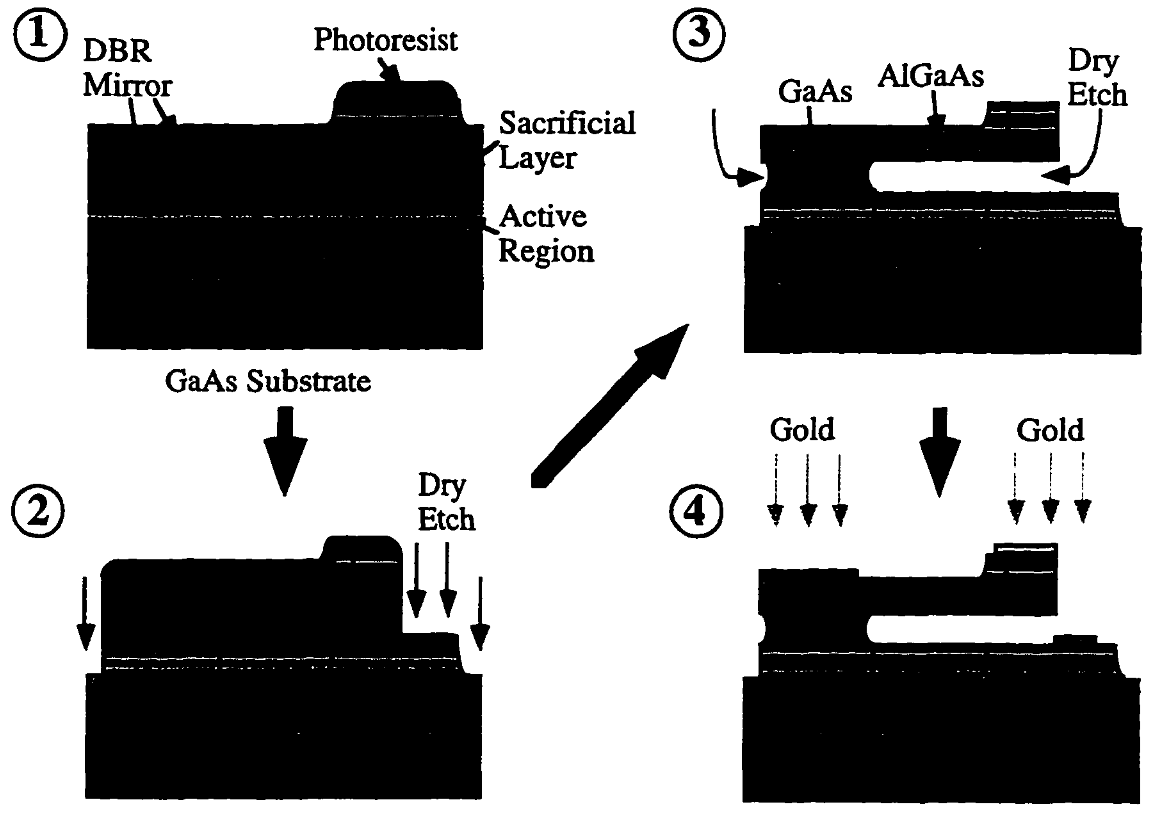


*Figure 3.17 - The major fabrication steps for the micromechanical tunable detector.*

2 are etched down past the active region, providing isolation between devices. Note also that the cantilever is thinner than the tuning head, lowering the tuning voltage. As shown in Section 0, a thinner cantilever is one way to get around the speed/tuning voltage trade-off. Finally, the isotropic selective dry etch is used to free the cantilever and gold is evaporated using a shadow mask.

## 3.4 Performance

The responsivity versus wavelength of the tunable detector for various tuning voltages, $V_T$, is shown in Figure 3.18 with the middle *p*-contact grounded ($V_F = 0$) and the detector biased at 5 volts ($V_{DET} = 5$ V). As we increase the top contact voltage from 0 to 7 V, the Fabry-Perot wavelength shifts 30 nm from 948 nm to 918 nm. A tuning current of 50 μA is required. The resolution bandwidth is 4 nm and the extinction ratio is 17 dB. These are design parameters, which can be improved by increasing the finesse of the Fabry-Perot

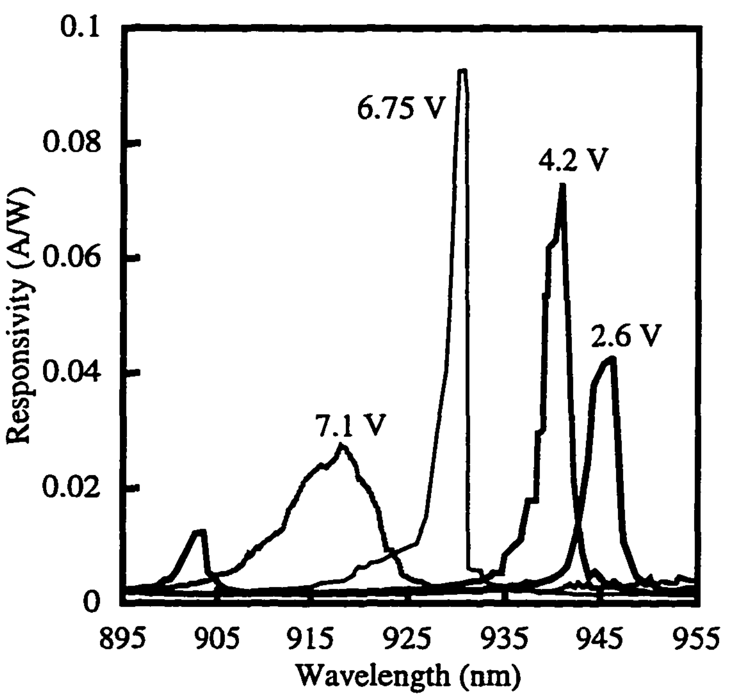

cavity. The responsivity of the detector is 0.091 A/W at the peak, corresponding to a 11% quantum efficiency.

Figure 3.19 shows the calculated tuning of the detector. The tuning range and free spectral range agree quite well with the measured data of Figure 3.18, but the responsivity does not. The variation and maximum amplitude of the responsivity (11%) are not as good as the calculated results. Approximately 3.2 dB of the efficiency loss is due to the lack of an anti-reflection coating at the substrate interface and the substrate absorption. The latter increases greatly at shorter wavelengths. However, this still does not explain the remaining factor of 3 lower responsivity. We posit that it is due to free carrier absorption in the mirrors or poor extraction of carriers from the quantum well. Layers designed to allow the carriers to tunnel out of the device should alleviate this problem in the future. Additionally, the excitonic peak of the quantum well absorption causes large changes in the absorption with wavelength, although the bias voltage of the detector should minimize this effect[6]. Measurements on the quantum well absorption versus bias voltage would help to ensure that this is not a problem.

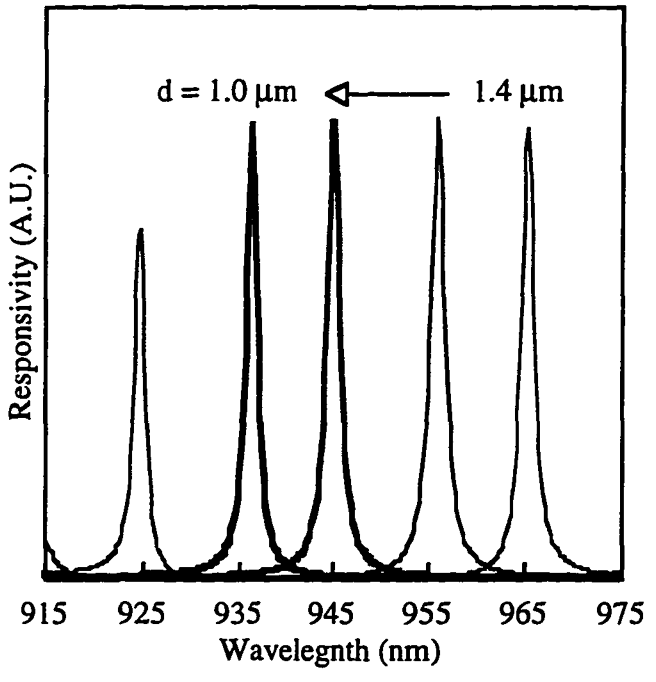


*Figure 3.19 - Calculated responsivity versus wavelength for the tunable detector.*

Another problem was a fabrication error in the gold top layer so that it did not cover the DBR. This reduced the top mirror reflectivity allowing the light to leak out the top mirror and throwing off the balance of the QW absorption to mirror loss.

Although the problems listed in the previous paragraph can be corrected, there is a simpler way to improve the device. Instead of making a resonant cavity detector, the tunable filter could be integrated with a bulk detector. This has all the advantages of the current device (compact, no coupling, wavelength tracking, and so forth) and sufficient speeds for most applications. This device is easier to build as well, since the top and bottom mirror reflectivities can be matched over a range of wavelengths, which is impossible with the quantum well absorption and the mirror reflectivities. A tunable filter can also have much wider tuning ranges (~100 nm with AlAs/GaAs, 100's of nm with other materials). Thick bulk detectors can also easily detect light over 100's of nm. A tunable detector designed this way should be simple to grow and have a constant high responsivity over a wide tuning range.

## 3.5 Wavelength Tracking Operation

In addition to functioning as a narrowband tunable detector, the device can be biased differently to track signals of varying wavelength. Figure 3.20 shows an electrical equivalent circuit for the device, superimposed on a side view schematic. The tuning contact (and cantilever) is isolated from the rest of the device by the two back-to-back diodes at the left of the schematic. The wavelength tracking effects discussed in this section are enabled by adding a load in between the ground and the middle *p*-contact, also called the feedback contact. Figure 3.21 shows how the equivalent circuit is biased for normal operation and for wavelength tracking. If the feedback contact is grounded, no tracking effects are observed.

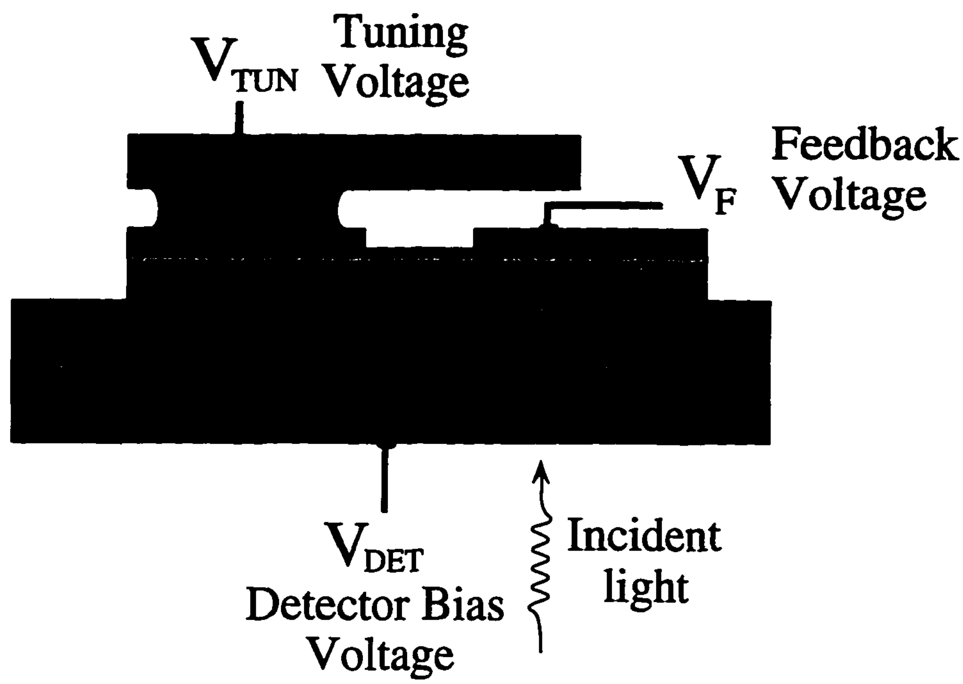


*Figure 3.20 - Side view of the micromechanical tunable detector with the electrical equivalent circuit superimposed.*

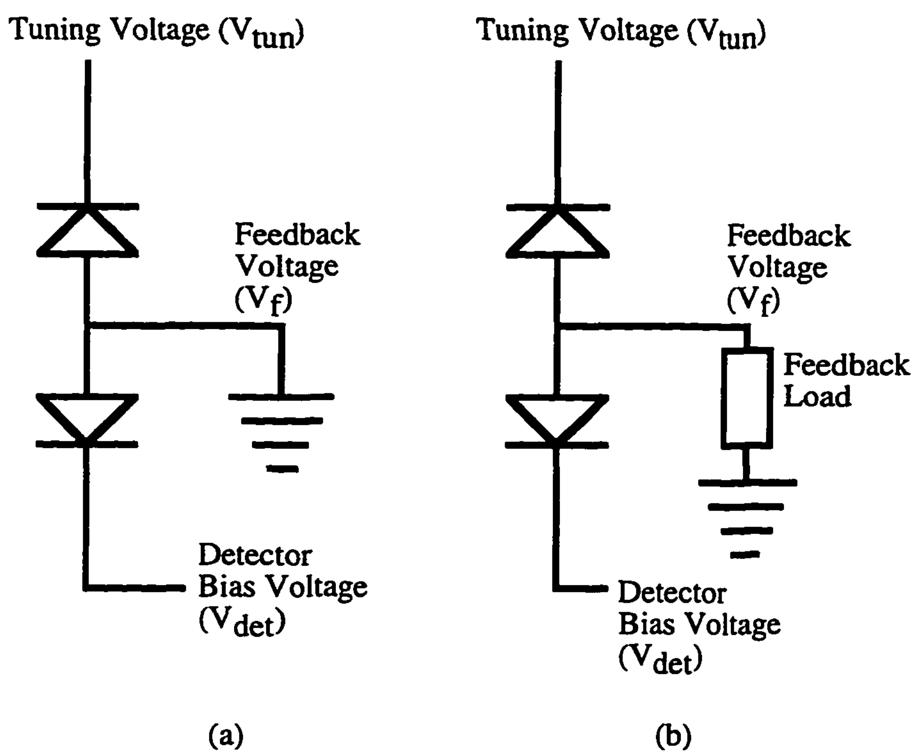


*Figure 3.21 - Equivalent circuits and biasing methods for (a) normal operation (i.e,. no tracking) and (b) tracking enabled.*

Adding a feedback load leads to wavelength tracking, because the cantilever position is determined by the difference between the feedback voltage and the tuning voltage ($V_T$ - $V_F$). Normally, the feedback voltage, $V_F$, is grounded, so the cantilever position is determined solely by the tuning voltage. However, Figure 3.22 shows the changed photocurrent dependence, the $V_F$ dependence is taken into account. By setting $V_F$=0, this becomes just the detector equivalent of the tunable filter shown in **Figure 2.12.**

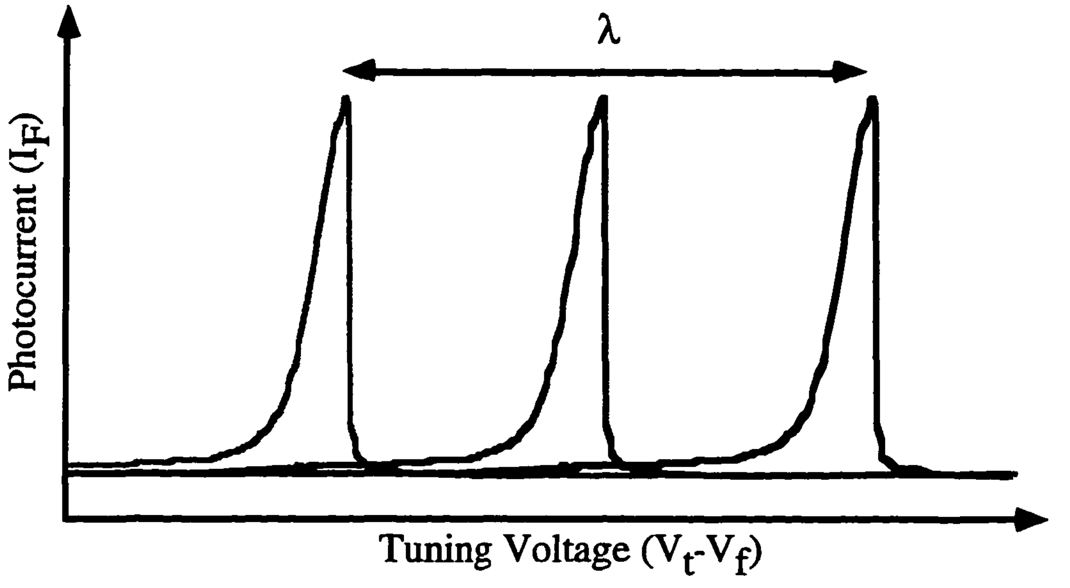


*Figure 3.22 - Schematic plot of photocurrent versus tuning voltage. Different wavelengths from long wavelengths (light gray) to short wavelengths (black) shift into resonance for different values of $V_f$. Letting $V_f$≠0 frees the resonance wavelengths to shift instead of being determined solely by the applied tuning voltage ($V_t$).*

For tracking operation, we add a high impedance load, for example a large resistor, in between $V_F$ and ground. When light is detected, current flows across the load, making $V_F$ depend on the detected light. This makes the attractive voltage ($V_T$ - $V_F$), and hence the Fabry-Perot wavelength, dependent on the detected light. But the detected light is also a function of $V_T$ - $V_F$, closing a feedback loop which allows the resonance wavelength to track the incident wavelength. All of this is accomplished with a constant detector and tuning voltage applied to the device.

For example, suppose a current source is used as the feedback load. Figure 3.23 replots the voltage-current relationships of Figure 3.22, but with the voltage-current curve for the current source. The circled intersection points show stable operating points of the device. (The uncircled intersection points are unstable.) As the peak position shifts with wavelength, the operating point also changes. Essentially, $V_f$ automatically adjusts to keep the resonant wavelength close to the wavelength of the incident light (i.e., tracking the incident light).

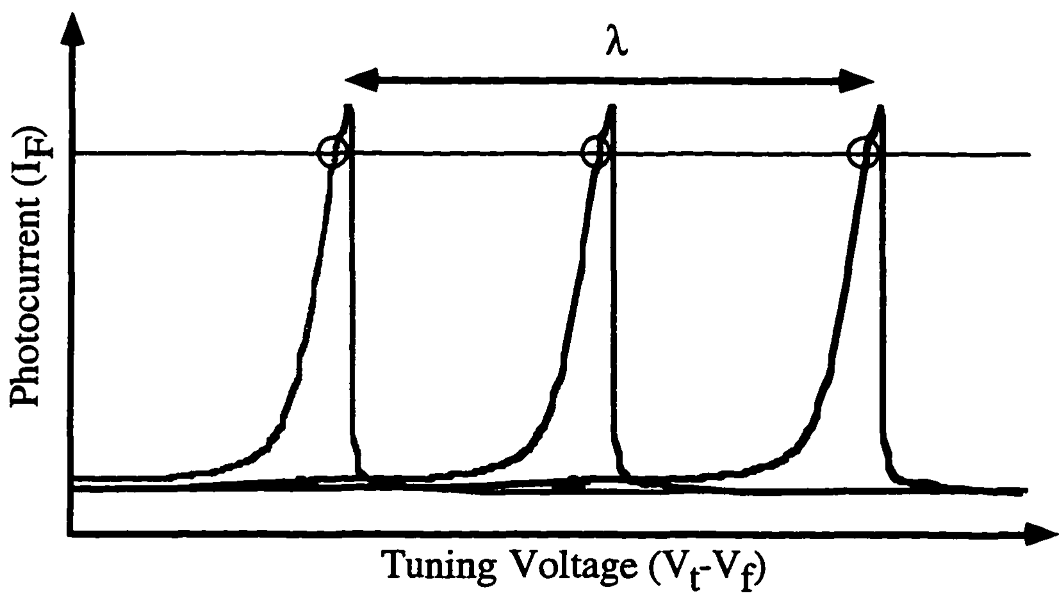


*Figure 3.23 - The case where the feedback contact is connected to a current source. Now $I_f$ is constrained to a fixed level (thin line) and operating points are shown by circles. $V_f$ adjusts itself to keep the device in resonance. If $V_f$ is monitored, it has a one-to-one correspondence to the wavelength.*

To see how this works, suppose the incident light shifts to shorter wavelengths. The amount of detected light decreases as the device shifts out of resonance. This decreases the photocurrent. However, the current source tries to keep the same current level flowing by making $V_F$ increasingly negative. This brings the device back into resonance, since the higher $V_T$ - $V_F$ causes the cantilever to bend down and the Fabry-Perot resonance to shift to shorter wavelengths.

Tracking using a current source feedback load can be seen experimentally in Figure 3.24. This figure shows the feedback voltage as a function of wavelength of the incident light. The detector tracks the input light over 25 nm of tuning, and could be used to measure the wavelength of incident light. Although the curve is somewhat jagged, we do not believe this is due to the device, but rather to the tunable Ti-sapphire source that was used for testing. Bulk tunable sources have tendency to mode hop, causing their wavelength to tune in jumps rather than continuously*. Figure 3.24 plots the measured wavelength of the Ti-sapphire versus the nominal wavelength read from the tuning knob. As can be seen, the wavelength does not tune smoothly. We believe the jaggedness of the wavelength meter in Figure 3.24 is simply the tunable detector measuring these wavelength hops.

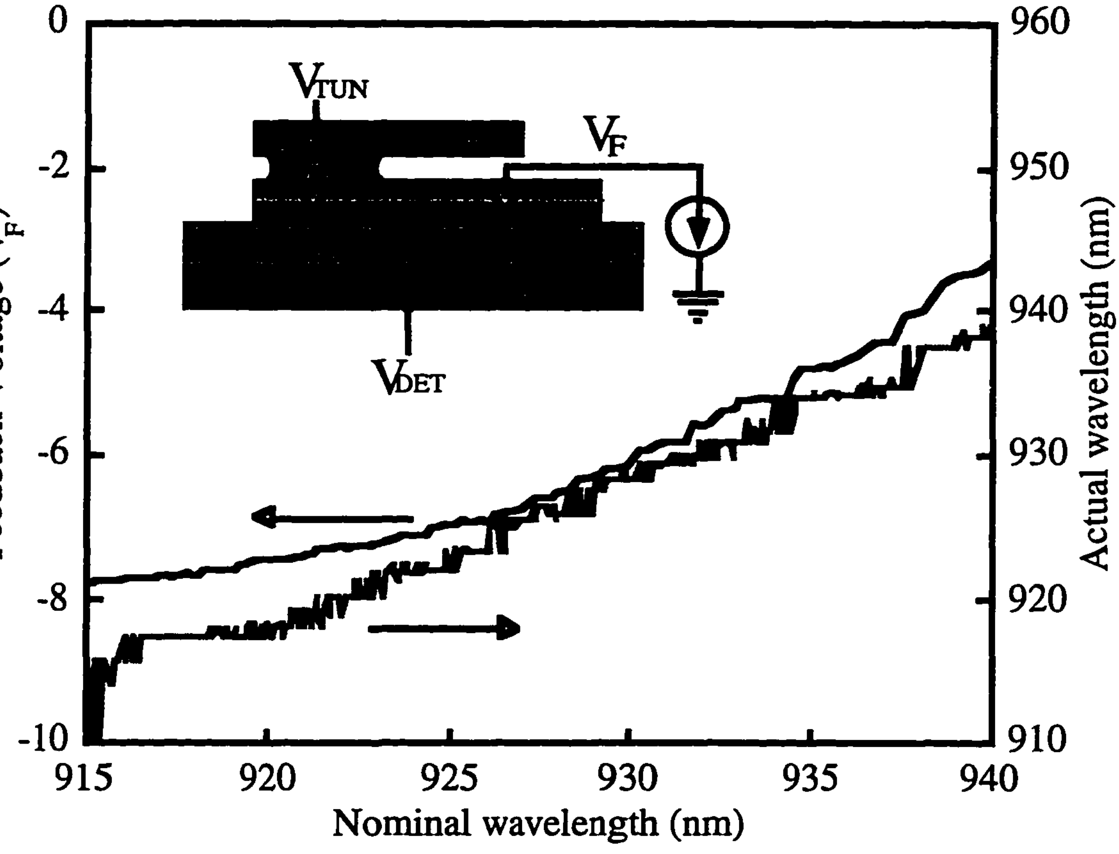


*Figure 3.24 - Demonstration of the tunable detector acting as a wavelength meter with a current source as the feedback load (inset). By measuring the feedback voltage (black line) the wavelength of the incident light can be determined. The steps in the curve are attributed to the tunable Ti-sapphire laser used to probe the device. The gray line shows the actual wavelength vs. the set wavelength on the Ti-sapphire laser.*

* Incidentally, this is an excellent example of the need for better tunable lasers, something this thesis will address in the next two chapters.

Another application for wavelength tracking is providing increased wavelength tolerances in wavelength division multiplexed (WDM) systems. Wavelength stability is a notorious problem for these systems, because almost everything affects the wavelengths of WDM components, including temperature, aging, and strain. One way around this problem is to increase the wavelength spacing between channels to relax the wavelength constraints. However this is not as easy as it might seem. A wider bandwidth filter or detector made by lowering the reflectivities of a Fabry-Perot has not only a larger bandwidth ($\approx 1/\pi\,(1\text{-}R_1R_2)\lambda/n$) but also decreased extinction ratio ($\approx \left(1-\sqrt{R_1R_2}\right)^2/2$). Multicavity structures can be designed to give a top hat like response[7]. Another possibility, is to let the narrow response tunable detector of this chapter track incoming wavelengths over a finite range. This gives an effective top hat response for single wavelength signals. One advantage of this technique is the crosstalk and noise are always the smallest possible, because the tunable detector is always a narrow bandwidth filter. It merely appears to be broader bandwidth due to its tracking properties.

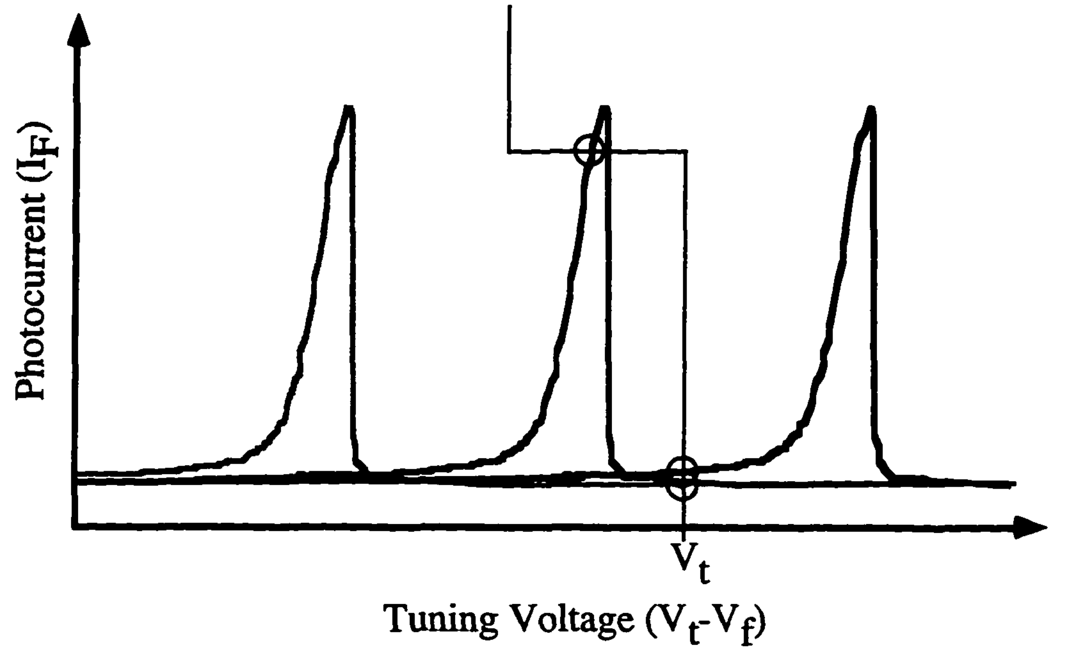


*Figure 3.25 - With more complicated feedback loads, more sophisticated wavelength tracking can be accomplished. In this case the feedback load is 0 V until a current limit is reached. The current then stays clamped until a certain voltage is reached, at which point the voltage is clamped from rising further. This allows the resonance to track incident light in a designated band.*

The tunable detector tracks over a limited range if a voltage limited current source is used as the feedback load. Figure 3.25 shows the load curves with this feedback load. The tuning voltage determines which channel the tunable detector locks onto. The range over which the tunable detector tracks is determined by the voltage limits on the current source.

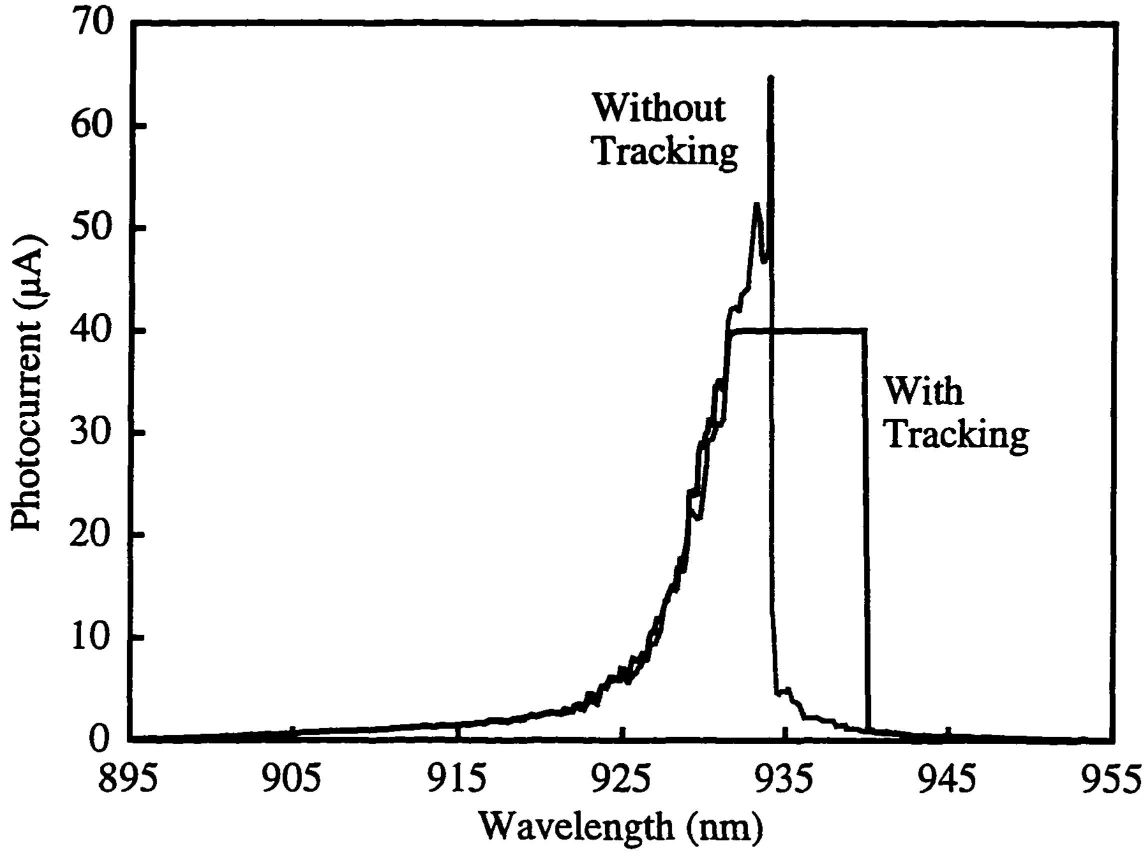


Figure 3.26 shows an experimental demonstration of limited range wavelength tracking. Without tracking (i.e., with the feedback contact grounded), the detector continues to exhibit the narrow peaks. With tracking, the effective response is broad and flat, resembling a top hat. In a WDM system, the received wavelength for this channel could shift around within this flat response region with no adverse effect on the system performance. Figure 3.27 shows how the feedback voltage compensates for the shifting wavelength to keep the device in resonance within this tracking range.

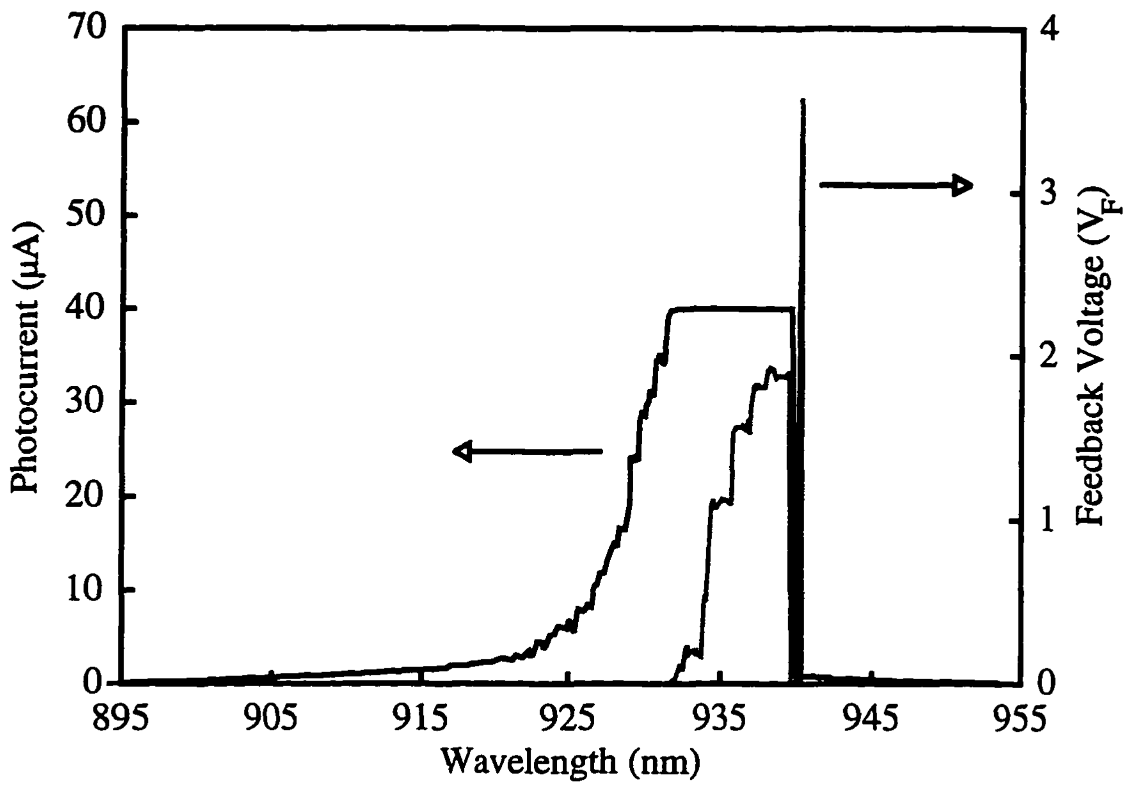


## 3.6 Conclusion

We have demonstrated the first micromechanical tunable detector along with the concepts to design it. The detector is potentially low cost with a wide continuous tuning range of 30 nm, using a low 7 V tuning voltage. The detector can optionally be biased to track single wavelength signals over a designable part of the tuning range, relaxing the strict component tolerances currently required for WDM systems. Furthermore, the detector may also be used as a low-cost spectrometer or wavelength meter through a novel tracking effect.

## 3.7 References

[1] K. Lai, and J. C. Campbell, "Design of a Tunable GaAs/AlGaAs Multiple-Quantum-Well Resonant-Cavity Photodetector," *IEEE J. of Quantum Electronics*, vol. 30, no. 1, p. 108-14, 1994.

[2] S. L. Daryanani, G. W. Taylor, S. K. Sargood, T. Vang, and B. Tell, "The inversion channel resonant-cavity enhanced photodetector for two-dimensional optoelectronic array applications," *IEEE Photon. Technol. Lett.*, vol. 5, no. 6, p. 677-9, 1993.

[3] F. S. Choa, W. T. Tsang, R. A. Logan, R. P. Gnall, T. L. Koch, C. A. Burrus, M. C. Wu, Y. K. Chen, and R. Kapre, "InGaAs/InGaAsP integrated tunable detector grown by chemical beam epitaxy," *Appl. Phys. Lett.*, vol. 63, no. 13, p. 1836-8, 1993.

[4] T. L. Koch, F. S. Choa, F. Heismann, and U. Koren, "Tunable Multiple-Quantum-Well Distributed-Bragg-Reflector Lasers as Tunable Narrowband Receivers," *Electron. Lett.*, vol. 25, no. 14, p. 890-2, 1989.

[5] T. E. Van Eck, P. Chu, W. S. C. Chang, and H. H. Wieder, "Electroabsorption in an InGaAs/GaAs strained-layer multiple quantum well structure," *Appl. Phys. Lett.*, vol. 49, no. 3, p. 135-6, 1986.

[6] P. W. Yu, G. D. Sanders, K. R. Evans, D. C. Reynolds, K. K. Bajaj, C. E. Stutz, and R. L. Jones, "Photocurrent spectroscopy of InxGa1-xAs/GaAs Multiple quantum wells," *Appl. Phys. Lett.*, vol. 54, no. 22, p. 2230-2, 1989.

[7] S. F. Lim and C. J. Chang-Hasnain, "A Proposal of Broad Bandwidth Vertical-Cavity Laser Amplifier," *IEEE Photon. Technol. Lett.*, vol. 7, no. 11, p. 1240-2, 1995.

# 4. Proton Implanted Micromechanical Tunable VCSELs

## 4.1 Introduction

Prior to the work in this chapter, all monolithic tuning of VCSELs was done either with temperature or carrier injection. Temperature tuning[1-4] is slow, has limited tuning range (<10.1 nm), and causes severe changes in the light-current characteristics of VCSELs. Carrier injection[5] has even smaller tuning ranges of 15 GHz. Moreover, neither of these methods are likely to increase tuning beyond 10 nm due to material limitations.

In this chapter, we discuss the first ever micromechanical tunable VCSEL[6]. This nonoptimized device was able to increase the record for tuning of VCSELs by 50% to 15 nm. At the time of publication, it was also the widest continuous tuning ever achieved with a monolithic device. This chapter discusses the design, development and performance of these devices.

## 4.2 Principle of Operation

A tunable VCSEL is like a tunable detector in reverse. In a tunable detector, light is focused on the Fabry-Perot, resonates inside the cavity, and is absorbed by the quantum well. In a tunable VCSEL, the quantum wells are forward-biased, causing them to amplify light resonating in the cavity. The laser output then leaks out of the partially reflecting mirrors. In fact, a tunable VCSEL can be used as a poor tunable detector, simply by changing the bias polarity of the bottom *pn* junction.

For optimal performance, the mirror reflectivities and quantum well properties are different for the detector and the laser. In the detector, the quantum well absorption should be as close as possible to the mirror loss, for maximum absorption. In a VCSEL, the maximum possible gain (which is equal to the unpumped quantum well absorption) is designed to be significantly higher than the mirror loss, so that pumping requirements on the quantum well are not excessive.

There is one extra requirement for the tunable VCSEL which is optional for the tunable detector: the pump current must be confined to the Fabry-Perot cavity. In the tunable detector, light is naturally absorbed only inside the cavity. Incident light away from the cavity (i.e., where there is no cantilever) hits only a mirror and is reflected. The entire middle contact can be reverse biased but only inside the cavity are significant amounts of light present. For the VCSEL, the quantum wells are forward-biased to provide gain. Since this requires large current densities, the forward biased region needs to be as small as possible. This was accomplished just underneath the top mirror. A device without current confinement operates so inefficiently and generates so much heat, it often does not lase no matter how hard it is pumped.

The tunable VCSELs discussed in this chapter used proton implant for current confinement. Proton implant makes semiconductors electrically insulating by causing damage. Protons are accelerated up to several hundred keV and directed at the semiconductor. The protons knock atoms out of place causing damage to the crystal. This causes mid-level states which trap electrons and holes making the semiconductor non-conductive. Areas of the semiconductor can be protected so they remain conductive. In this case, the cantilever provides protection of the critical areas, forcing current to flow only inside the Fabry-Perot cavity.

Using this method, we were able to demonstrate the first micromechanical tunable VCSEL with its record tuning range. This success proved the soundness of the micromechanical tuning technique, spurring the development of the improved devices detailed in the next chapter.

## 4.3 Design

Figure 4.1 shows a schematic of the proton implanted tunable VCSEL. It is similar to the tunable detector discussed in the previous chapter. The tuning voltage is still applied to the top contact and the middle contact is still grounded. The difference in operation is the bottom *pn* junction is now forward biased. The proton implant, shown by the cross-hatched region, is used to create a buried insulator layer in the *p*-region everywhere except underneath the cantilever. As shown in Figure 4.2, this forces the pumping current to flow underneath the circular tuning head, pumping only that region.

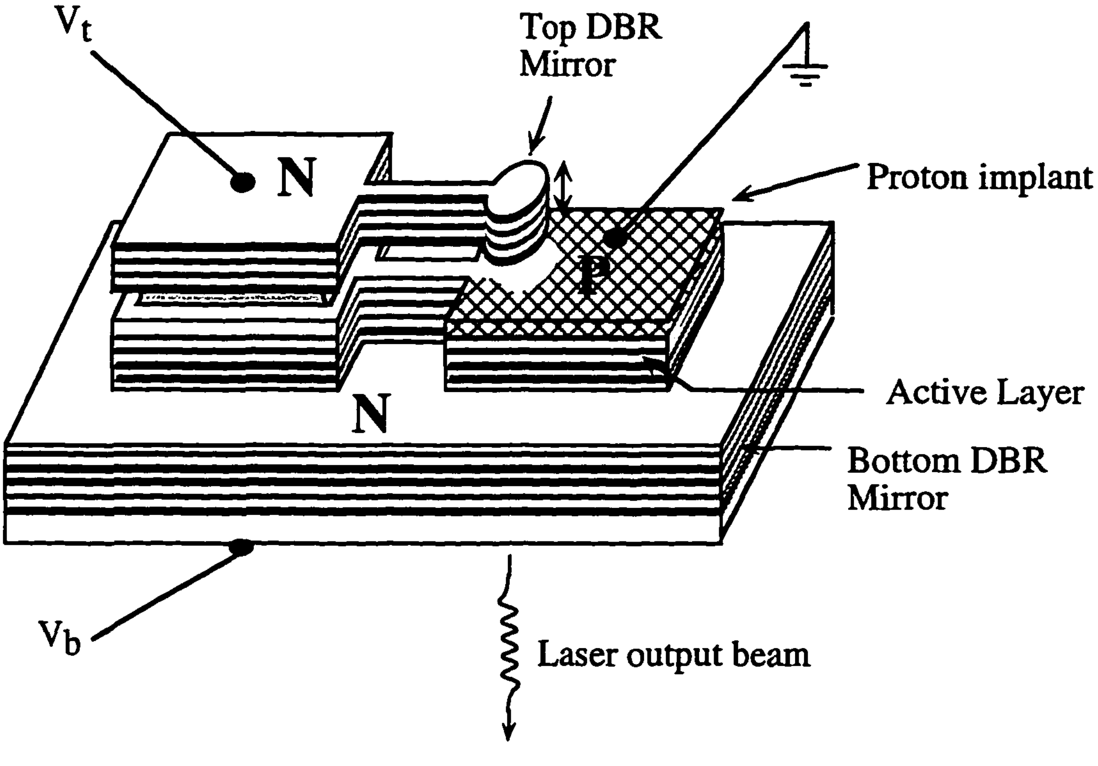


*Figure 4.1 - Schematic of the proton implanted micromechanical tunable VCSEL*

### 4.3.1 Epitaxial design

The epitaxial design differs in two main ways from the tunable detector: the reflectivity of both mirrors is increased by adding mirror pairs and the number of mirror pairs in between the tunable air gap and the substrate is increased to six. Increasing these *p*-DBR mirror pairs increases the light reflected before the tunable air gap reducing cavity losses due to top mirror tilt or roughness of the air-semiconductor interface. (In Chapter 5, we fabricate a device where these losses are insignificant.) A thicker *p*-layer is also required to keep the proton implant far away from the QW active region and *p*+ contacting layer.

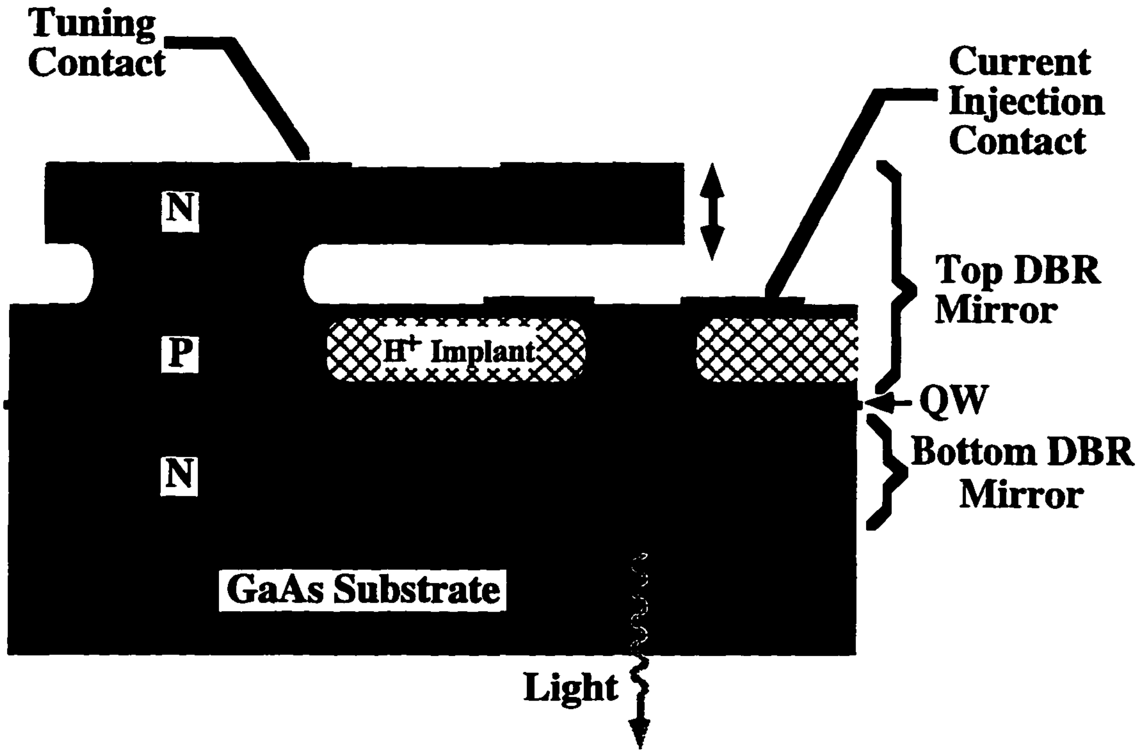


*Figure 4.2 - Side view schematic of the proton implanted micromechanical tunable VCSEL to illustrate device operation*

The growth program is summarized here. To form the bottom mirror, 23.5 *n*-doped graded AlAs/GaAs mirror pairs followed by 4 graded *n*-doped $Al_{0.6}Ga_{0.4}As$/GaAs mirror pairs were grown on a *n*-substrate. This was followed by the quantum well active region which consisted of a one lambda spacer layer of $Al_{0.1}Ga_{0.9}As$ with three 80 Å $In_{0.14}Ga_{0.86}As$ quantum wells separated by 100 Å GaAs barriers . This was followed by a graded quarter lambda *p*-doped $Al_{0.6}Ga_{0.4}As$ layer and a 3/4 λ GaAs layer. This layer should undercut during the selective dry etch and break the middle *p*-contact gold for isolation. This is followed by the rest of the *p*-layer: 4 graded $Al_{0.6}Ga_{0.4}As$/GaAs DBR mirror pairs and a final $Al_{0.6}Ga_{0.4}As/Al_{0.1}Ga_{0.9}As$ mirror pair where the $Al_{0.1}Ga_{0.9}As$ layer has been *p*+ doped for better contacting. This was followed by the sacrificial layer 12740 Å of *i*-GaAs. This thickness was used since it is 19/4 λ in GaAs and only slightly bigger than 5/4 λ in air. This way the top mirror is high reflecting both with and without the GaAs layer in place. Finally, the top mirror was completed with 22.5 lightly *n*-doped top $Al_{0.1}Ga_{0.9}As/Al_{0.6}Ga_{0.4}As$ DBRs. The last $Al_{0.1}Ga_{0.9}As$ layer was increased in thickness to 1150 Å in order to phase match the reflection from the gold.

### 4.3.2 Reflectivity calculation

As with the filter in section 2.2 and the detector in section 3.2.3, a program which calculates the reflectivity of the dielectric stack was used to ensure the desired device tuning and mirror reflectivities. Using this program, the Fabry-

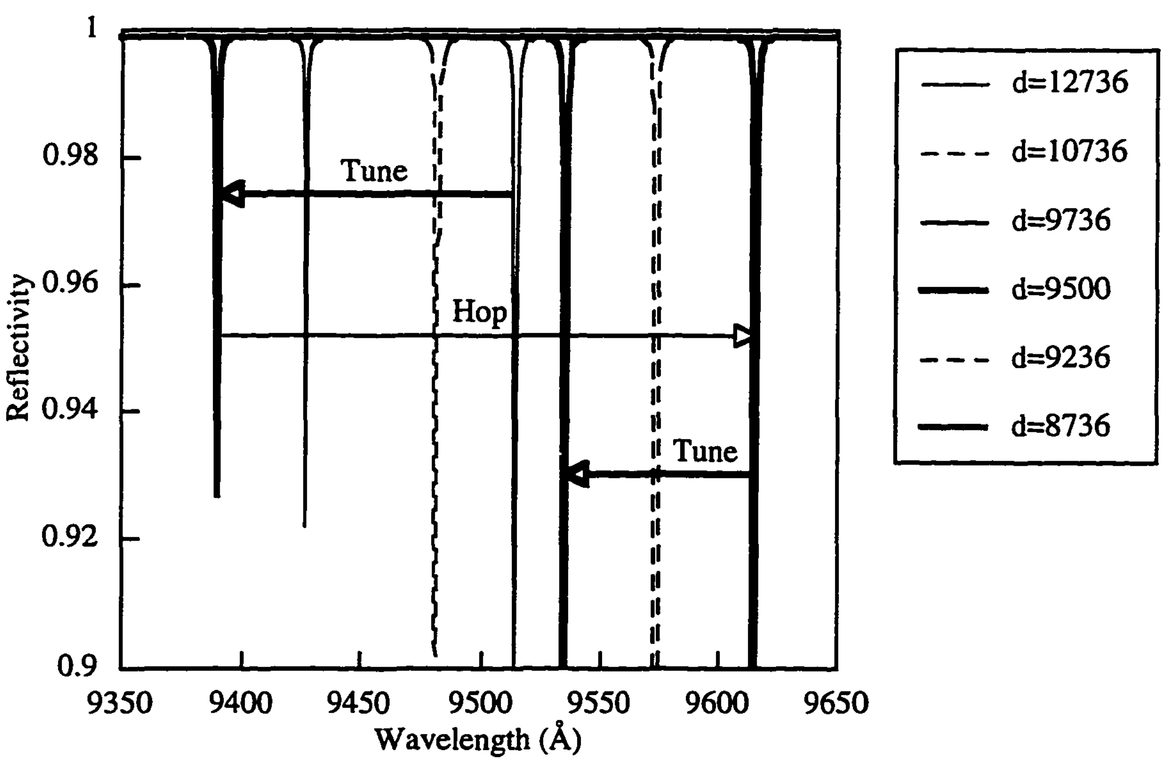


*Figure 4.3 - Calculated reflectivity of the structure for different air gap thicknesses (d). The Fabry-Perot dip starts at 951 nm, tunes to 939 nm, hops to 962 nm, and then tunes to 953 nm as the air gap is reduced from 12736 Å to 8736 Å.*

Perot resonance wavelengths ($\lambda_{fp}$) versus air gap size (d), and hence the tuning range, can be determined as shown in Figure 4.3. The top and bottom mirror reflectivities can then be calculated for each wavelength. If the reflectivities are too low or too high, they can be adjusted by adding or subtracting mirror pairs, respectively. The top mirror reflectivity spectrum depends on the air gap thickness and is shown for various air gap thicknesses in Figure 4.4. The bottom mirror reflectivity spectrum, shown in Figure 4.5, does not depend on the air gap thickness and only needs to be calculated once.

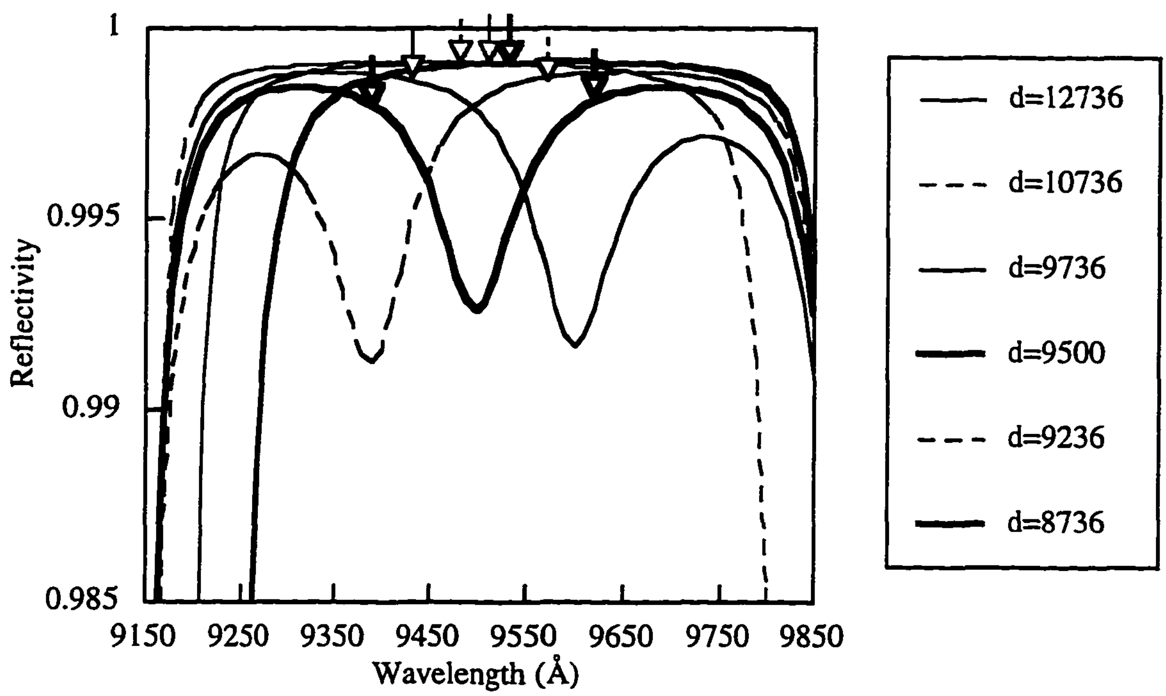


*Figure 4.4 - Calculated top mirror reflectivities for different air gap thicknesses. Note the dip caused by the top air gap which acts like a coupled cavity. Fortunately this dip does not occur at the same wavelength as the Fabry-Perot resonances which are indicated by the arrows.*

Figure 4.6 shows the losses versus wavelength. The loss is approximately 0.3% over most of the tuning range, a number typical for traditional VCSELs. The bottom mirror losses are approximately twice those of the top mirror, since this is a bottom emitting device. For test structures where the GaAs is left in place the top and bottom mirror reflectivity are 99.88% and 99.79%, respectively. This leads to a total loss of 0.33% which is small enough to allow the test structures to lase.

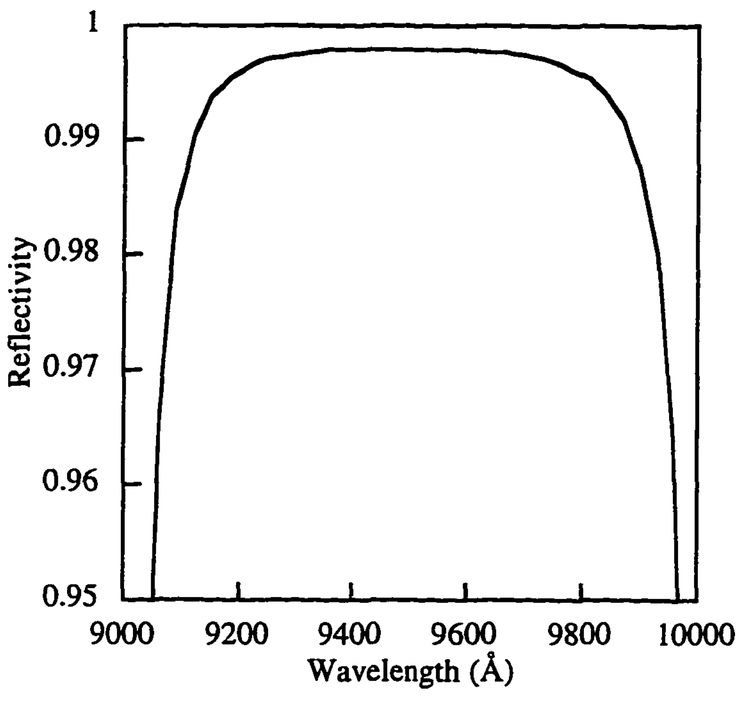


*Figure 4.5 - Calculated bottom mirror reflectivity for the proton implanted VCSEL*

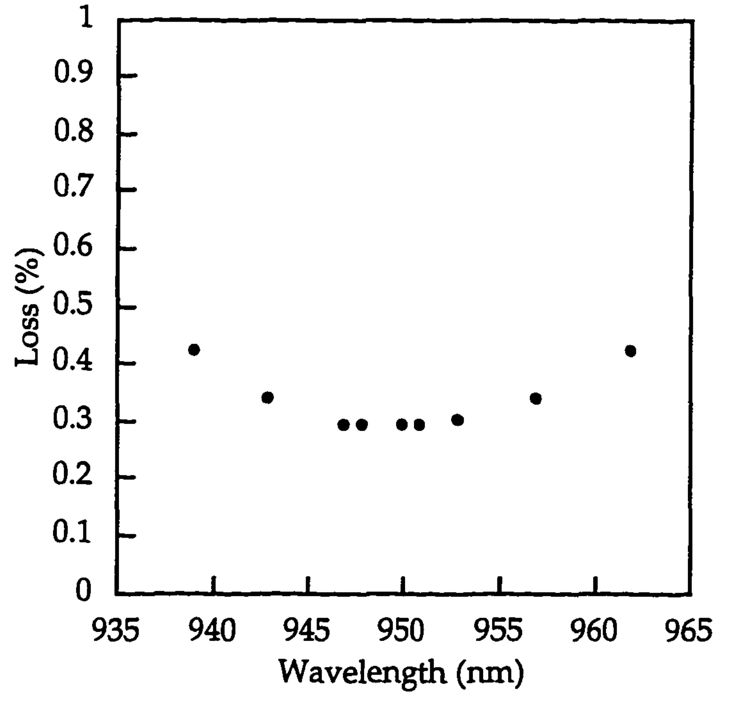


*Figure 4.6 - Loss of the tunable VCSEL over its tuning range.*

Ideally, the reflectivity of the top mirror would be 100% so no light is wasted in the top mirror. Figure 4.4 shows the top mirror reflectivity is actually only 99.9%, a significant amount of loss for a VCSEL, but it is difficult to reduce this loss without encountering other difficulties. Since free carrier absorption already dominates the top mirror losses, increasing the number of mirror pairs in the top mirror does not improve the mirror reflectivity. The absorption can be reduced by lowering the doping level near the active region. However, this increases the resistance and hence the power dissipation in the *p*-layers. Another possibility is to increase the reflectivity of the interfaces by increasing the refractive index differences of the layers, for example by using AlAs/GaAs DBRs or moving the air interface closer to the active region. However, since AlAs oxidizes, it is undesirable to have it exposed, and reducing the number of mirror pairs increases the losses due to air/GaAs interface roughness and top mirror tilt. In addition, since this device is proton implanted, a certain minimum thickness of the *p* layer is required. Since lower top mirror reflectivity only lowers the efficiency of the device, the top mirror reflectivity was kept at this level to avoid these other problems.

### 4.3.3 Material Check - Edge Emitting and Surface Emitting Lasers

#### *4.3.3.1 Introduction*

Achieving a working tunable laser is more difficult than achieving tunable detectors or filters. For a laser, the loss requirements are tighter, the Fabry-Perot cavity must be aligned to the gain peak, the growth is more complicated, and there is the added complexity of current confinement. A misalignment of 20 nm (2%) between the quantum well gain peak and the Fabry-Perot peak makes it hard for conventional VCSELs to lase CW. However, a tunable filter has no gain peak to align; a tunable detector would still function even with a 50 nm (5%) misalignment.

This difficulty was borne out in practice. For example, the tunable detector and tunable filter only required a single growth and processing run.

On the other hand, the tunable VCSEL took four growths and three processing runs to achieve.

This section discusses test structures which allow us to characterize laser material and processing steps. The test structures are broad-area edge-emitting lasers and test VCSELs. Using these structures, we were able to identify problems with several wafers and proton implant process steps, before going through the whole processing run.

#### 4.3.3.2 *Broad Area Edge Emitting Lasers*

The first test structures were broad-area edge-emitting lasers. The threshold current density of these broad area lasers is a gauge of the quality of the quantum wells. Their lasing wavelength is the wavelength of peak gain of the quantum wells. This wavelength can be compared the Fabry-Perot wavelength measured using test VCSELs.

These devices were made for all four lasing wafers (wafers 16, 86, 136, 139). Because the tunable VCSELs are three-terminal devices they have an *npn* structure. It was necessary to etch off the top *n*-doped portion, consisting of the top DBR mirrors and the GaAs sacrificial region[7]. Gold stripes 100 μm wide were evaporated, and then the whole sample was etched through the active region to provide isolation.

When this was performed, wafer 86 was found not to lase at all. A few devices acted as LEDs with peak emission at 950 nm as designed, but none of the devices could be made to lase with current densities less than 1 kA/cm$^2$ (pulsed) at which point the devices were destroyed. This is a fairly low current density for failure to occur. No further work was performed on wafer 86.

The other wafers, 16, 136, and 139, all did lase as broad area lasers. Wafer 16, lased at a wavelength of 1050 nm, 100 nm from the design wavelength. Threshold current densities of 500 A/cm$^2$, or 170 A/cm$^2$ per quantum well, were measured. This wafer was one of the first wafers grown by our machine. So it is not surprising the wavelength was misaligned. We continued to process wafer

16 since it was grown without substrate rotation and had matching Fabry-Perot peaks over a small region, but it never did function correctly.

Wafers 136 and 139 were fairly close to the design wavelength of 950 nm, lasing at ~940 nm. These bars had excellent threshold current densities of approximately 360 A/cm$^2$, or 120 A/cm$^2$ per quantum well. These samples could be driven over the full range of the pulser without failing (2 A, or 2.9 kA/cm$^2$).

Wafer 136 differed from wafer 139 in having an AlAs stop etch layer with a GaAs contact layer underneath. Wafer 139 simply had an $Al_{0.1}Ga_{0.9}As$ stop etch layer which also functioned as the contact layer. Wafer 136 was grown because there was some worry that it would be difficult to make electrical contact to a $Al_{0.1}Ga_{0.9}As$. However, the very similar performance of Wafer 136 and 139 suggest that this worry was unfounded.

It was later discovered that Wafer 136 had an error in its growth. Its GaAs sacrificial layer was grown as $Al_{0.1}Ga_{0.9}As$, making it useless. This was discovered when this layer would not etch in the dry etch. In addition, both wafers' isolation layer, a 3/4 λ GaAs layer designed to be undercut to break the contact gold, was also $Al_{0.1}Ga_{0.9}As$. This was because one of the aluminum furnaces was not closed properly. For the sake of brevity, the rest of this section focuses on wafer 139, the wafer that eventually worked.

#### 4.3.3.3 *Test VCSELs*

In the test VCSEL structure, small squares (10 µm to 40 µm on a side) of the top *n* mirror and GaAs region are left in place. Proton implant is used to confine the current to the region underneath the top *n*-mirror. If these structures lase, it proves that the lateral injection works and that the gain peak is properly aligned to the DBR bands. Then, the only possible problem with a tunable VCSEL would have to do with the air/GaAs interface, such as scattering loss or tilt loss.

The first technique we used to fabricate proton implanted test VCSEL lasers was similar to that for broad area lasers. Broad 100 µm by 100 µm mesas were etched to provide isolation between neighboring devices. Then smaller mesas varying in size form 10 µm to 40 µm squares were wet etched inside the 100 µm by 100 µm mesas. These smaller mesas functioned as the top mirror for the VCSEL. Gold was then evaporated, using a shadow mask to isolate the various devices. A blanket proton implant of the samples was done. This proton implant damaged all the areas which were not protected by the top mirror (i.e. everywhere except under the smaller mesa). It was hoped this would cause the current to flow underneath this smaller mesa. Two samples with different proton implant energies were tried: 15 keV and 50 keV.

Unfortunately, these first test VCSELs did not function. The 15 keV implanted sample acted like no implant had been performed. Current simply flowed over the entire sample. Apparently the 3000 Å of gold on the sample was enough to stop this low energy implant. The 50 keV sample stopped all current from flowing and the devices functioned as an open circuit. At around 20 volts the devices broke down and became short circuits..

The 50 keV samples because of a problem with the lateral injection. Normally, proton implanted VCSELs are fabricated using very deep implants, because the top DBR is so thick. As shown in Figure 4.7, this leaves a undamaged layer above the proton implant which can conduct the current

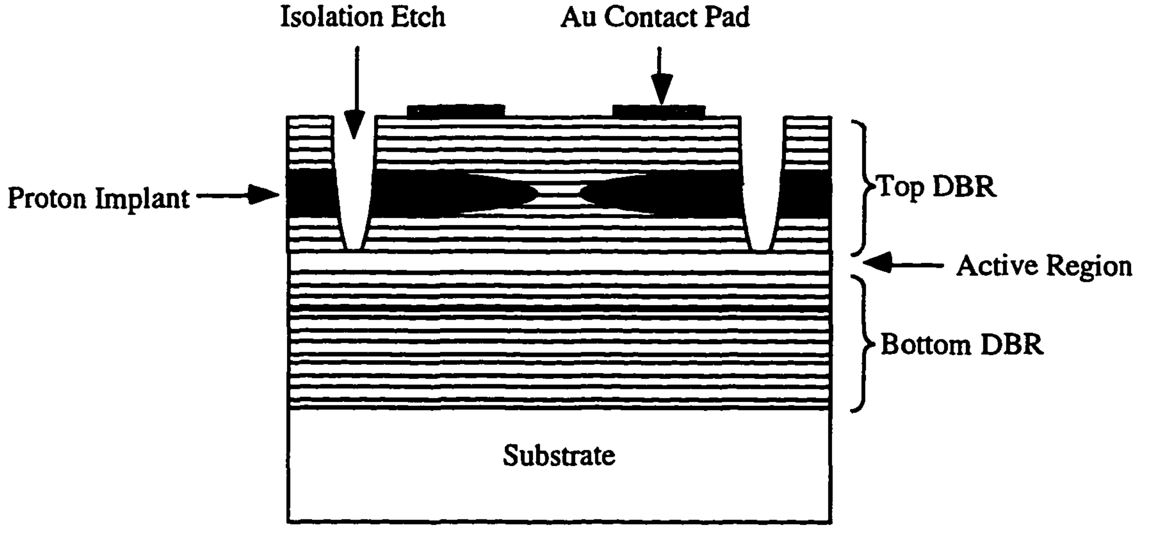


*Figure 4.7 - Typical top emitting proton implanted VCSEL. Note the layers underneath the contact are still conducting.*

sideways. Unfortunately, the *p*-layer we implanted is much thinner, so the damage is much closer to the surface (as shown in Figure 4.8). This makes contacting and lateral conduction of current more difficult. In addition, the sidewalls of the inner mesa were wet-etched, making them sloped. This can cause a upward slope on the proton implant at the *n* mirror, cutting off the active region from the middle gold contacts.

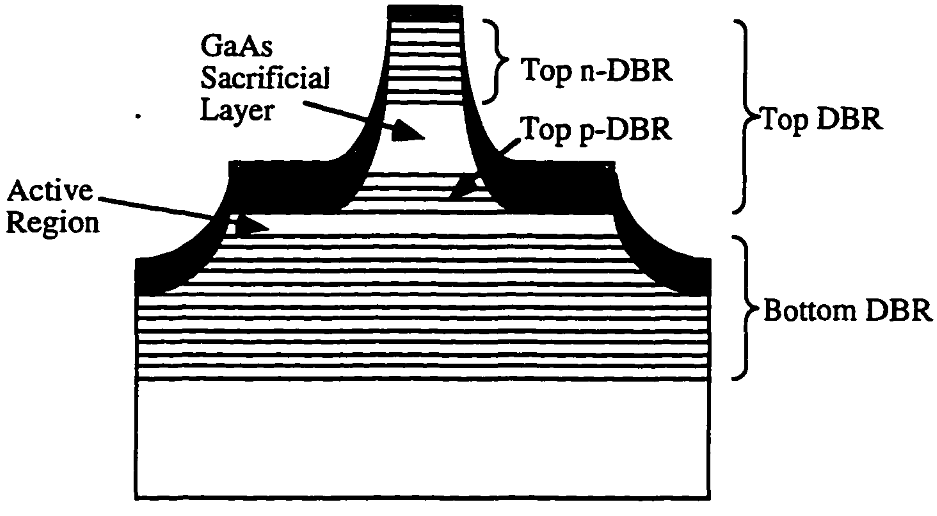


*Figure 4.8 - First attempt at a test VCSEL for the tunable material. These lasers did not function since current could not be conducted laterally.*

*4.3.3.4 Proton Implant Improvement*

In order to overcome the problem with lateral injection, three new proton implanting techniques were tried and are shown in Figure 4.9. In the deep implant technique shown in Figure 4.9(a), the smaller mesa is now etched using RIE. This creates vertical sidewalls, providing a better break in the proton implant. The implant energy for this technique was also increased so that most of the damage occurred in the bottom DBR. It was hoped that this would leave the *p* layer conductive but confine the injected electrons underneath the top mirror. However, these devices did not work and behaved similarly to the first test VCSELs. At first the junction appeared to be an open circuit. If enough voltage was applied, current would eventually flow, but this seemed to be due to the device breaking down. At no point was any light seen from these devices.

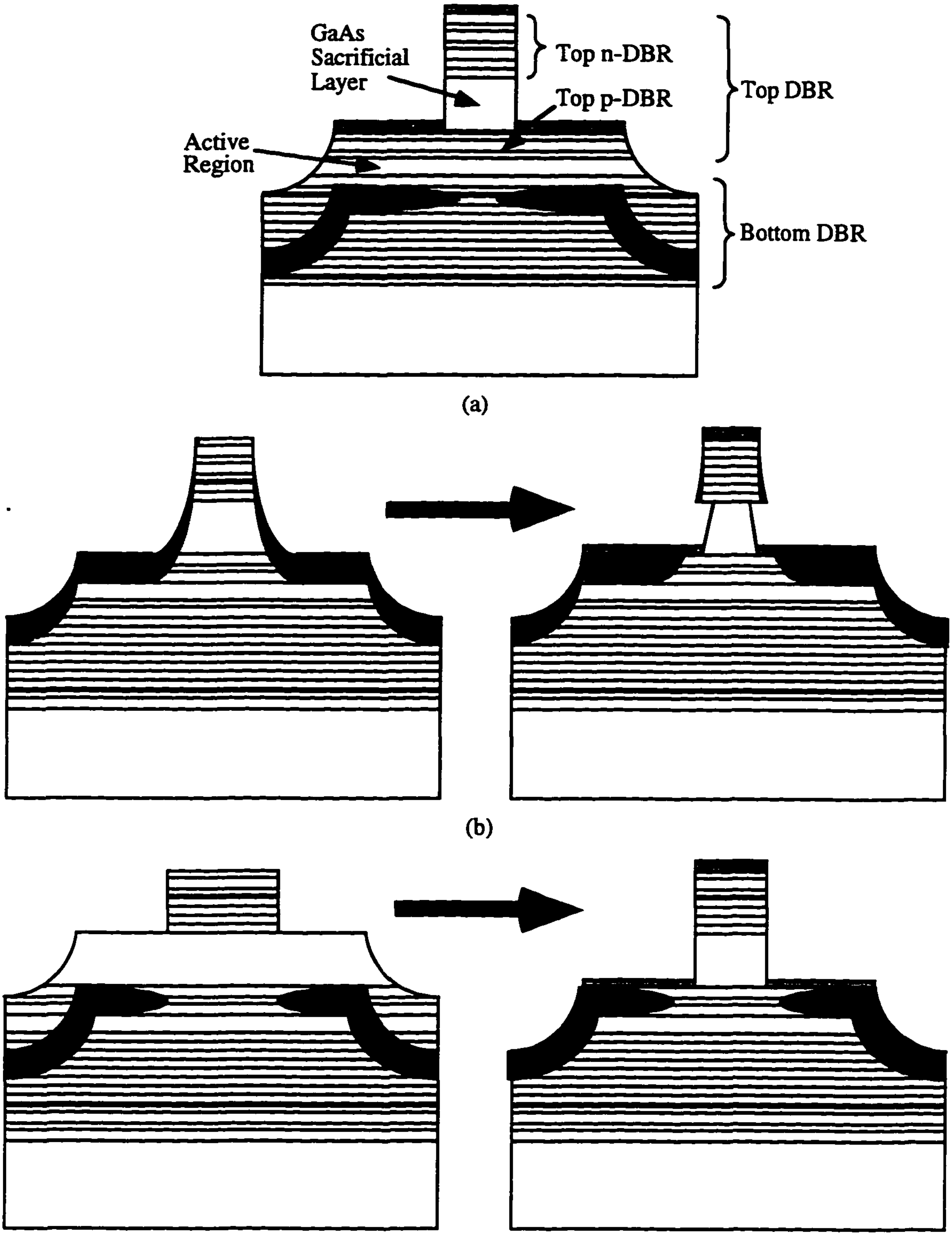


*Figure 4.9 - Three improved techniques for lateral injection proton implant. (a) Deep implant so current confinement is performed in the n-layer (b) Sample is implanted, then some implanted material is selectively etched away (c) Sample is implanted and then laterally nonselectively etched.*

The next technique, the wet etch technique, is shown in Figure 4.9(b). This method is very similar to the first method; in both, the mesas are wet etched and then proton implanted. Then, they are selectively etched again by citric acid which only etches low Al concentration material, removing some of the proton implanted material to expose unimplanted parts of the contact layer. When gold is evaporated, it now "overhangs" the proton implant. Thus, even if the implanted parts of the *p*-layer are not conductive, current is still be laterally injected from the gold into the unimplanted parts of the *p* layer.

These VCSELs lased with a lasing wavelength of 940 nm, closely matching the gain peak measured with the broad area lasers. The threshold current density was ~1-2 kA/cm$^2$. Approximately 20 devices were tested with roughly the same performance. The wavelength changed about 5 nm across the sample and the threshold current varied by a factor of 2. The change in the threshold current density was due to change in the size of the lasing mode.

A third proton implant technique used a nonselective etch, instead of citric acid, to etch laterally. This limited the amount of lateral etching to the thickness of the sacrificial layer (~1μm), but did not result in the selective etching of the top DBR mirror as with the previous technique. Test VCSELs fabricated using this technique also lased with results comparable to those etched with citric acid. This was the technique that we decided to use for the real structures.

There are a number of challenges with VCSEL growths (e.g., matching the gain peak to the Fabry-Perot peak, getting good quality quantum wells, keeping track of thousands of shutter operations), and achieving a lateral injection proton implanted process is difficult. By making test broad area edge emitters, narrow stripe edge emitters, and test VCSELs, we identified the potential problems without going through the time-consuming process of fabricating tunable VCSELs.

### 4.3.4 Tilt Loss Calculation and Double Back Structure

Because the loss requirements for VCSELs are so rigorous (~0.1%), there was some worry about the tilt of the mirror causing excess loss. There are basically two simple ways of calculating the losses from a tilted mirror: ray tracing and coupled tilted waveguides. In this case, the ray tracing technique predicted the tilt would cause huge losses, while the coupled waveguide technique predicted the tilt would cause small losses. To be on the safe side we tried to minimize the tilt. One way to do this is by having the cantilever double-backed. If the dimensions are just right, it is possible to get the tilt to be zero at the tip. In this section, we show how to calculate these dimensions.

#### 4.3.4.1 *Tilt Loss Calculation*

But first, it is interesting to estimate the losses from a tilted end mirror using the two different methods. For the ray tracing method, the cavity is approximated as two hard (i.e., metal) mirrors a few microns apart, as shown in Figure 4.10. This spacing, d~4 μm, is bigger than the air gap since the field penetrates into the mirror cavity. We approximate the round-trip loss

$$\alpha = 1/N \tag{4-1}$$

where $\alpha$ is the round-trip loss and $N$ is the number of round-trips before a ray escapes starting at the center of the cavity. The lateral displacement of the beam on the $n$th bounce is just $2d\theta_{n'}$. The cumulative lateral displacement of the ray on the $n$th bounce, $x_n$, is the sum of the lateral displacements for each round trip

$$x_n = \sum_{n'=1}^{n} 2d\theta_{n'} \tag{4-2}$$

where $\theta_{n'}$ is the angle on the $n'$th bounce given by the equation

$$\theta_{n'} = 2\theta_0 n' \tag{4-3}$$

where $\theta_0$ is the angle between the two mirrors. Basically the beam is deflected by twice the mirror angle for each round trip. Substituting this into (4-2) yields

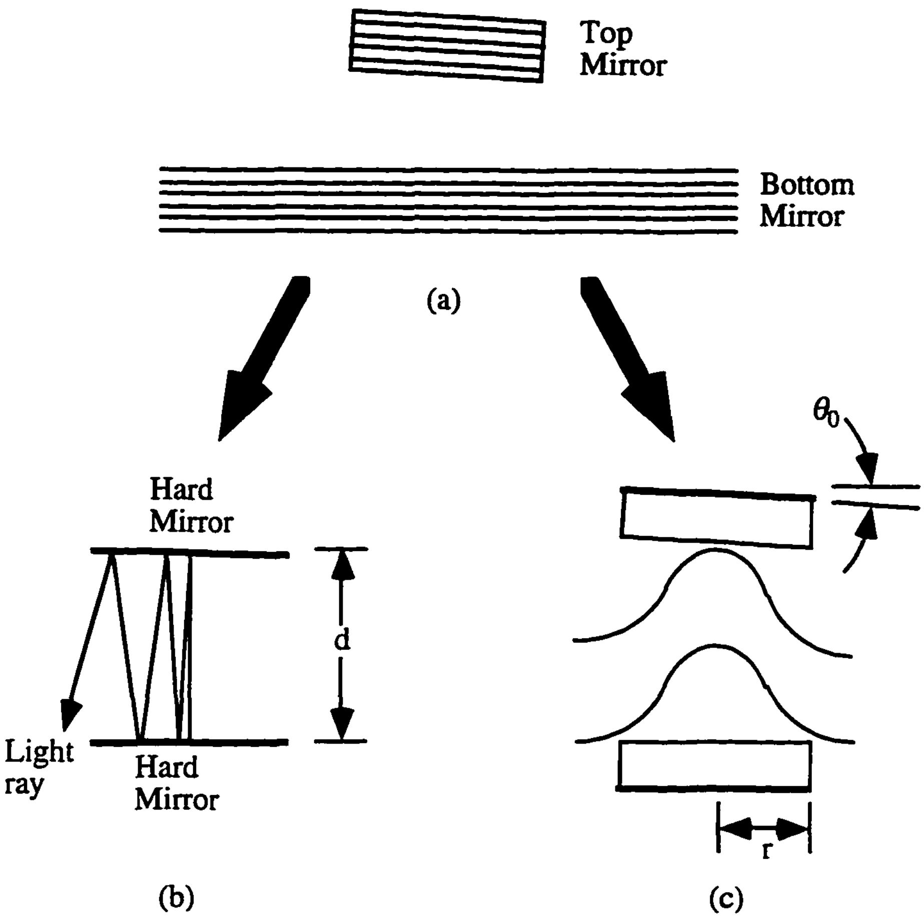


*Figure 4.10 - Schematics of the models used to calculate tilt losses. (a) The air gap is taken as the whole cavity. The system can be approximated as either (b) a ray reflecting between two mirrors or (c) two coupled tilted waveguides with hard mirrors on the end.*

$$\begin{aligned} x_n &= \sum_{n'=1}^{n} 2d\theta_{n'} \\ &= \sum_{n'=1}^{n} 4d\theta_0 n' \\ &= 4d\theta_0 \frac{n(n+1)}{2} \\ &\approx 2d\theta_0 n^2 \end{aligned} \tag{4-4}$$

If we substitute in the radius of the end circle $r$ for $x_n$, and hence $N$ for $n$, we can rearrange the equation to solve for the N, the number of round-trips before the light is lost,

$$N = \sqrt{\frac{r}{2d\theta_0}} \tag{4-5}$$

So the approximate round trip loss is

$$\alpha = \sqrt{\frac{2d\theta_0}{r}} \tag{4-6}$$

Due to its simplicity the ray tracing technique is often used to calculate the tilt loss, but it tends to grossly overestimate the cavity losses for the small dimensions of the device. According to this model, a typical fully deflected 100 μm long cantilever would have a loss of 3%. If this level of loss was correct, neither the devices detailed in this chapter nor the next chapter would have lased.

The other method for calculating the loss is to consider the problem as the loss between two tilted waveguides, with the top mirror and the base functioning as the tilted waveguides. The round-trip loss is obtained from the modal overlap between the tilted modes. Suppose the electric field profile of the mode, $E(x)$, has been normalized so

$$\int_{-\infty}^{+\infty} E(x)E^*(x)dx = 1 \tag{4-7}.$$

The round trip loss is approximately equal to

$$\alpha = 2\left(1 - \int_{-\infty}^{+\infty} E(x)E^*(x)e^{-i\theta_0 x}dx\right) \tag{4-8}$$

where the two is for the two couplings, one into and one out of the top curved mirror, and the $e^{-i\theta_0 x}$ term is because of the angular difference $\theta_0$ between the two modes. Let's assume a Gaussian functional form for E(x)

$$E(x) = \frac{e^{-ax^2/2}}{\sqrt[4]{\pi/a}} \tag{4-8}$$

which should be a reasonable approximation for the fundamental mode. Then evaluating equation (4-8) we get

$$\begin{aligned}\alpha &= 2\left(1-\int_{-\infty}^{\infty}\frac{e^{-ax^2-i\theta_0 x/\lambda}}{\sqrt{\pi/a}}dx\right)\\ &= 2\left(1-e^{-\frac{\theta_0^2}{2a\lambda^2}}\int_{-\infty}^{\infty}\frac{e^{-a\left(x+\frac{i\theta_0}{2a\lambda}\right)^2}}{\sqrt{\pi/a}}dx\right)\\ &= 2\left(1-e^{-\frac{\theta_0^2}{2a\lambda^2}}\right)\\ &\approx \frac{\theta_0^2}{a\lambda^2}\end{aligned} \tag{4-9}$$

We can approximate the size of the mode as basically the size of the end circle so

$$a \approx 1/r^2 \tag{4-10}$$

and therefore

$$\alpha \approx \frac{\theta_0 r^2}{\lambda^2} \tag{4-11}$$

If we plug in some typical numbers into these equations, $r$=10μm, λ=1 μm, and$d$=4μm, and plot them over the operating angle of a device, we get a different set of results.. As can be seen in Figure 4.11, there is a big discrepancy between the two calculations. The waveguiding model is more accurate, since the ray tracing method ignores the substantial waveguiding effects at these small dimensions. However, the waveguiding model has its faults, too. It assumes all higher order modes dissipate away, when in reality they are recoupled as well. Whether these higher order modes help or hinder the round-trip loss is difficult to say without full beam propagation simulations.

Figure 4.11 also overstates the loss, because the calculations assume the air gap is the main cavity of the device, when in reality only half the light makes it to the air gap. The other half of the light is reflected by the $p$ layers. Taking these effects into account, the worst case round-trip loss should be less than 0.1%. This number is equal to half the top mirror losses and a quarter of the bottom mirror losses. These calculations show the tilt loss can not prevent the device from lasing. However, it is significant enough to affect the differential efficiency of the device by ~20% so it is useful to investigate ways to minimize it.

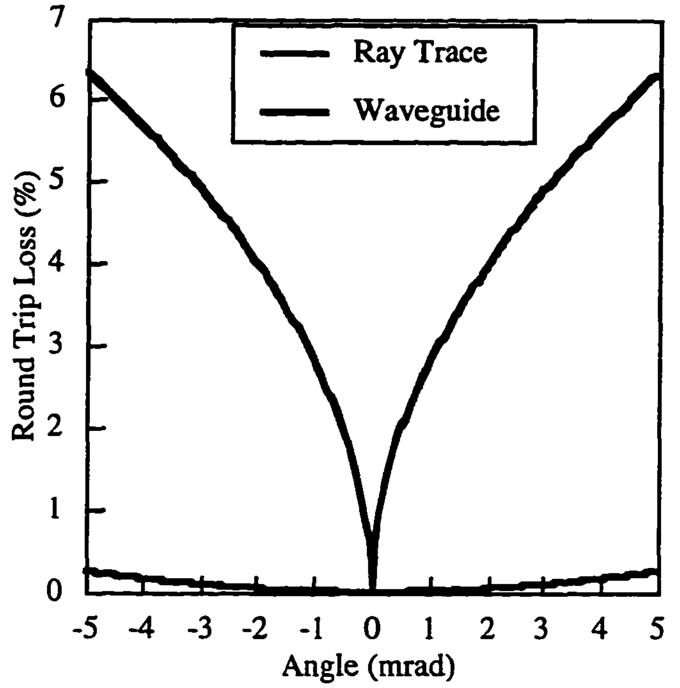


*Figure 4.11 Plot of calculated round-trip loss using two different techniques: ray tracing (gray line) and waveguiding (black line).*

### *4.3.4.2 Double Back Structure*

One way to minimize the tilt is to double back the cantilever as shown in Figure 4.12. By getting the lengths just right, the tilt can be made to go to zero at the cantilever tip. To calculate the dimensions that do this, we need to use the differential equations developed for calculating cantilever displacement in section 2.5.1. Because the cantilevers now twist as well as bend, a few extra differential equations are needed. To differentiate between the variables for twist and bending, the subscripts $x$ and $y$ are used, respectively. The variables of interest with the new subscripts are shown in Figure 4.13.

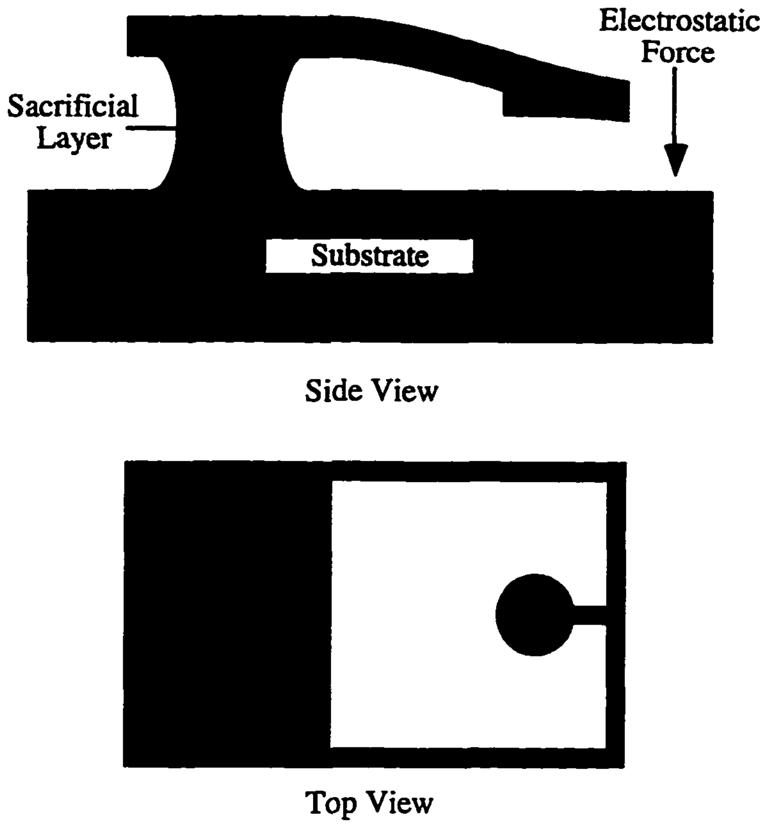


*Figure 4.12 - Side view and top view of doubled back structure designed to cancel out end mirror tilt*

The equations derived in section 2.5.1 can now be rewritten with their new subscripts:

$$\frac{dF(x)}{dx} = Pw \tag{4-12}$$

$$\frac{d\tau_y(x)}{dx} = F(x) \tag{4-13}$$

$$\frac{d\theta_y(x)}{dx} = \frac{12}{Et^3w}\tau_y \tag{4-14}$$

where $F(x)$ is the downward force along the cantilever, $x$ is the position measured along the length of the cantilever, $P$ is the downward electrostatic pressure on the cantilever surface, $\tau_y(x)$ is the bending torque, $\theta_y(x)$ is the angle of the cantilever, $t$ is the cantilever thickness, $w$ is the cantilever width, and $E$ is the elastic modulus. For these equations the pressure is once again assumed to be a constant, even though it depends on spacing between the cantilever and the substrate and hence on $x$. The structure has zero tilt only within this approximation, but this should eliminate a large fraction of the tilt.

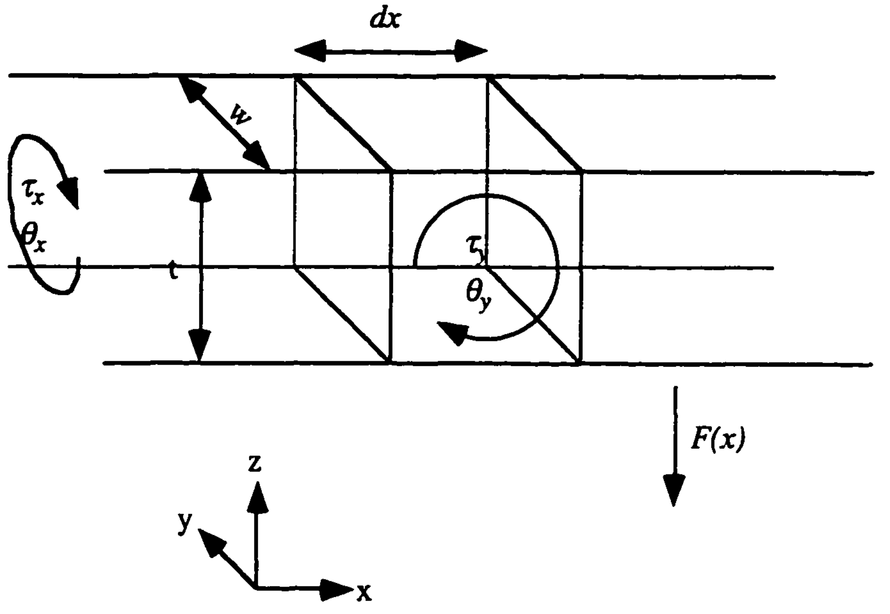


*Figure 4.13 - Schematic of the parameters used in the differential equations used to calculate the tilt of the doubled back structure.*

Because the double back structures turn corners, the twist of the cantilevers also has to be considered. In particular, the twist of the crossbeams which connect the outgoing cantilever with the doubled back section directly contributes to end mirror tilt. A set of differential equations are needed to calculate this twisting, similar to the ones above. The twisting torque does not change with length so

$$\frac{d\tau_x(x)}{dx} = 0. \tag{4-15}$$

In other words, the twisting torque $\tau_x(x)$ is a constant along the length of the cantilever. The twisting as a function of this twisting torque can be derived using the approach illustrated in Figure 4.14, which shows a small $dx$ length element looking down the axis of the twisting (i.e., down the axis inside the cantilever). Let's break the $dx$ slice into little $dydz$ pieces and look at the contribution of each piece. The force of each $dydz$ element, $dF$, is just the shear strain constant, $E_s$, times the shear strain, times the area $dydz$. So

$$dF = E_s \frac{\sqrt{y^2+z^2}\,d\theta_x}{dx} dydz \tag{4-16}$$

where $dx$ is the thickness of the element, and $d\theta_x$ is the change in twist angle over the $dx$ element. Torque just equals this $dF$ force times the lever arm, $\sqrt{y^2+z^2}$, so

$$\begin{aligned} d\tau_x &= dF\sqrt{y^2+z^2} \\ &= E_s(y^2+z^2)\frac{d\theta_x}{dx} dydz \end{aligned} \tag{4-17}$$

By integrating over the entire surface of the $dx$ element, the total torque required to achieve a twist of $d\theta_x$ over the element $dx$ is found to be

$$\begin{aligned} \tau_x &= \int_{-t/2}^{t/2}\int_{-w/2}^{w/2} E_s(y^2+z^2)\frac{d\theta_x}{dx} dydz \\ &= E_s \frac{wt(w^2+t^2)}{12}\frac{d\theta_x}{dx} \end{aligned} \tag{4-18}$$

Rearranging this we get

$$\frac{d\theta_x}{dx} = \frac{12}{E_s wt(w^2+t^2)}\tau_x \tag{4-19}$$

Now we have all the differential equations we need to solve for the cantilever tilt: (4-12), (4-13), (4-14), (4-17), and (4-19).

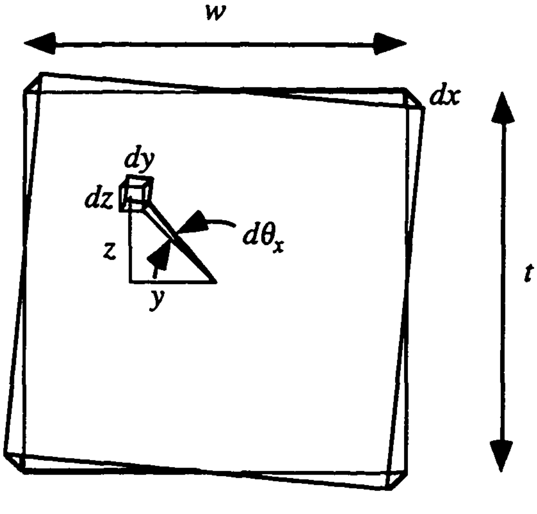


*Figure 4.14 - Diagram for calculating the twist of the cantilevers. A small dx length element of the cantilever is shown, looking down the length of the cantilever. The top square is twisted relative to the bottom one due to the applied torque ($\tau_y$) on the cantilever.*

Before solving the differential equations, we need to figure out what their boundary conditions are. Figure 4.15 summarizes the boundary conditions. They are fairly intuitive, with the most complications coming from the sign changes at the turns. We have not shown the sign changes here, as it is easier to figure out sign changes on a case-by-case basis rather than developing general rules.

| Boundary condition | Effect |
|---|---|
| Supported End | $z=0$<br>$\theta_x=0$<br>$\theta_y=0$ |
| Free End | $F=0$<br>$\tau_x=0$<br>$\tau_y=0$ |
| Turn | left = right<br>$\tau_x = \tau_y$<br>$\theta_x = \theta_y$<br>$F = F$<br>$z = z$ |
| T | left = right<br>$\theta_y = \theta_x$<br>$z = z$<br>$\tau_x = 2\tau_y$<br>$F = 2F$<br>Due to symmetry: $\theta_x=0$, $\theta_y=0$; $\tau_x=0$, $\tau_y=0$ |

*Figure 4.15 - The boundary conditions on the cantilever differential equations.*

In order to simplify the calculations, it is useful to use the symmetry of the structures. Since the device has mirror symmetry, there is no point in keeping track of both arms which reach out in the doubled back cantilever. One arm is simply the mirror opposite of the other. In practice this results in the extra boundary conditions at the T shown in Figure 4.15.

The tilt of the end mirror is solved using the method of section 2.5.1. First, the force is calculated by starting at the tip of the cantilever and integrating towards the base of the cantilever. Next, the torques are calculated, again starting from the tip and integrating towards the base of the cantilever. Finally, the tilt angle is calculated by starting at the base of the cantilever and integrating out to the tip. At each turn or T, we flip the appropriate variables and continue integrating.

The calculation is fairly straightforward, although somewhat messy, so it is useful to use a program such as Mathematica to carry out the integrations. The resulting third order polynomial for the tilt can be made to go to zero at the tip with appropriate choices of dimensions. Figure 4.12 was drawn using the curves calculated from this Mathematica routine, with the aspect ratio adjusted to make the tilt large enough to be seen. The material parameters and thicknesses were known from the growth. The total thickness of the cantilever was taken to be 1.65 μm (2.65 μm of DBR - 1 μm of etching). Figure 4.16 shows the other parameters used in the calculation. The length of the cross beam ($l_2$) was kept constant at 100 μm. Three other parameters ($l_1$, $r$, and $w$) were varied. We then solved for the doubled back length ($l_3$) necessary to set the tilt to zero at the cantilever tip. The results are summarized in Table 4.1.

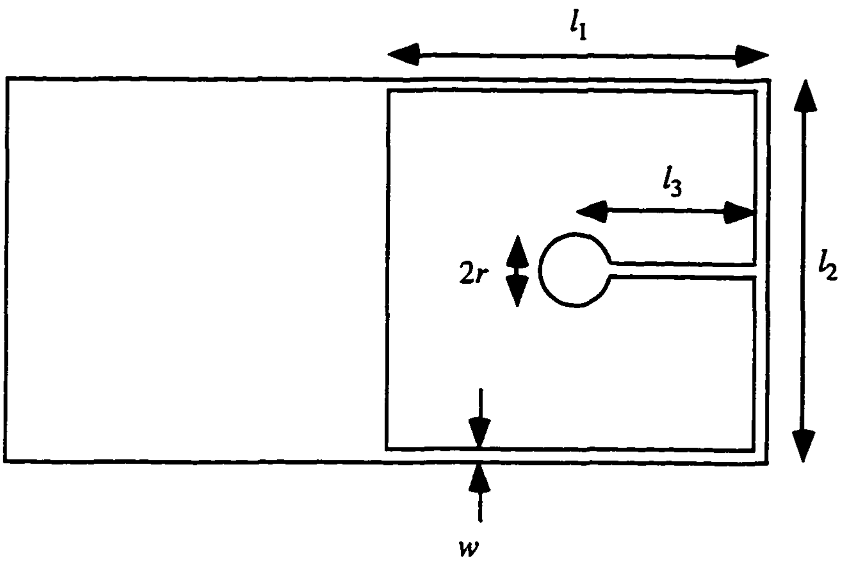


*Figure 4.16 - Top view of doubled back structure with labels of the various dimensions used in the calculation.*

| l1(μm) | r(μm) | w(μm) | l3(μm) |
|---|---|---|---|
| 50 | 5 | 2 | 29.3 |
| <u>50</u> | <u>10</u> | <u>2</u> | <u>24.9</u> |
| 50 | 10 | 4 | 34.9 |
| <u>100</u> | <u>5</u> | <u>2</u> | <u>66.3</u> |
| <u>100</u> | <u>10</u> | <u>2</u> | <u>58.7</u> |
| <u>100</u> | <u>10</u> | <u>4</u> | <u>77.3</u> |
| <u>100</u> | <u>10</u> | <u>6</u> | <u>88.5</u> |
| <u>100</u> | <u>10</u> | <u>8</u> | <u>95.6</u> |
| 200 | 5 | 2 | 150.4 |
| <u>200</u> | <u>10</u> | <u>2</u> | <u>136.7</u> |
| 200 | 10 | 4 | 169.0 |

*Table 4.1 - List calculated structures which have zero tilt in the end circle. Underlined structures were the ones actually used in the mask.*

## 4.4 Fabrication

Figure 4.17 shows the fabrication for the tunable VCSELs which is similar to that of the tunable detector. For the sake of simplicity, the isolation wet etch is not shown. The main difference between the VCSEL fabrication and the detector fabrication is the proton implant process. We take care to stop the anisotropic etch, shown in step 1, at the very top of the GaAs sacrificial layer. The samples are then proton implanted. This is followed by an isotropic wet etch. As shown in section 4.3.3.4 this etch allows the gold evaporated later to "overhang" the proton implanted region, allowing the lateral injection of current. Finally, we do the selective etch and evaporate gold with shadow masking.

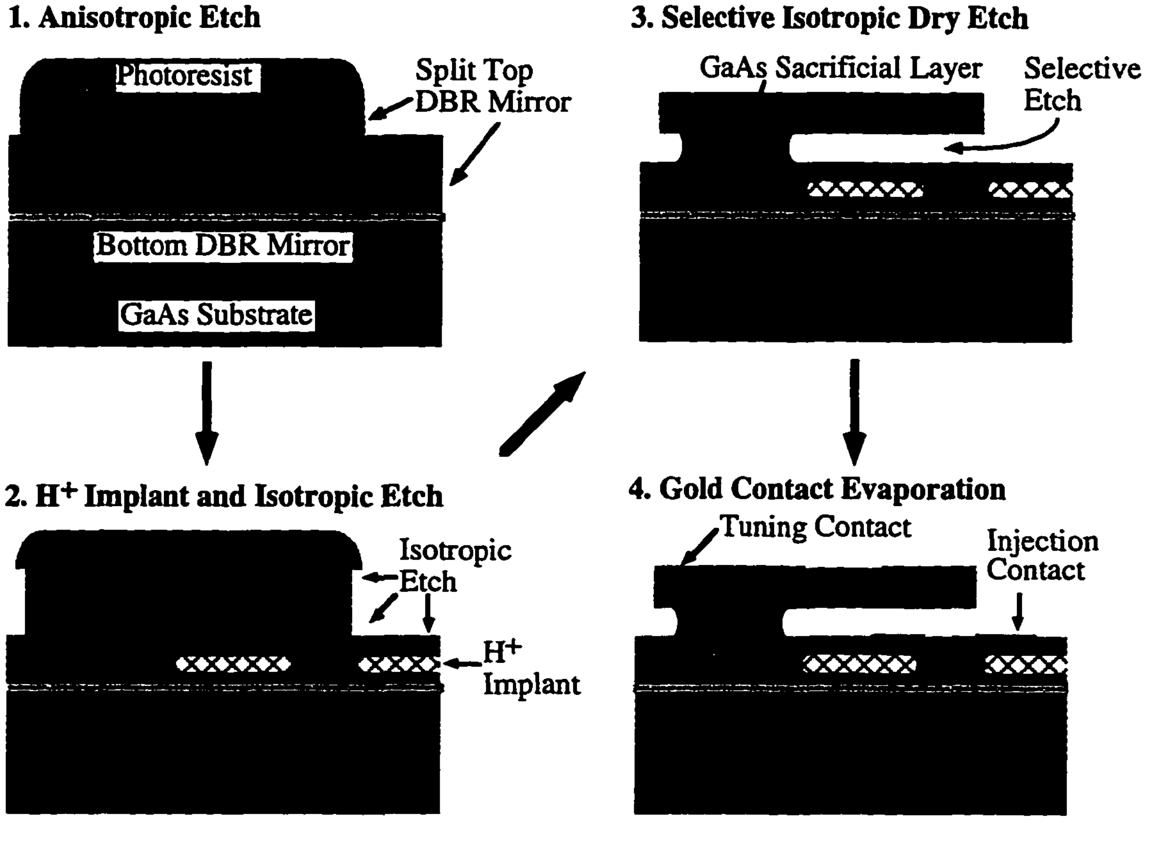


*Figure 4.17 - General fabrication procedure for the proton implanted micromechanical tunable VCSEL*

One difficulty in the processing was caused by the error in the growths described earlier. A 3/4 $\lambda$ GaAs layer which was included right above the active region was accidentally grown as $Al_{0.1}Ga_{0.9}As$. This layer was intended to be undercut to "break" the gold and help isolate the middle contact pad. Since this did not occur, we had to rely on the shadow masking and the proton implant to isolate the devices. This did not work so well and explains the high threshold currents described in the performance section.

Figure 4.18 shows and SEM of a completed device. This doubled back structure extended out 50 μm before doubling back. The end circle diameter was 20 μm and the cantilever widths were approximately 2 μm. The tuning contact is the large, 100 μm by 100 μm, pad. The middle *p* contact is the small pad inside the cantilever structure. For some of the doubled back devices one outgoing arm was broken off, but they still functioned suggesting that loss is not sensitive to cantilever tilt.

*Figure 4.18 - SEM of the completed proton implanted micromechanical tunable VCSEL*

## 4.5 Performance

### 4.5.1 Tuning and Spectra

Figure 4.19 shows the output spectrum of the VCSELs as they are tuned over their 15 nm range. As seen in the figure, the lasing wavelength first tunes from 935 nm to 925 nm as the tuning voltage is changed from 0 to 5 V. The wavelength then jumps to 943 nm as the VCSEL changes Fabry-Perot modes and then tunes down to 938 nm as the tuning voltage is changed form 5.5 V to 5.7 V. In future designs, this jump could be avoided by placing the initial lasing wavelength towards the longer end of the spectrum. The wavelength always blue-shifts with increased applied tuning voltage, confirming that the tuning is due to micromechanical motion and not thermal tuning.

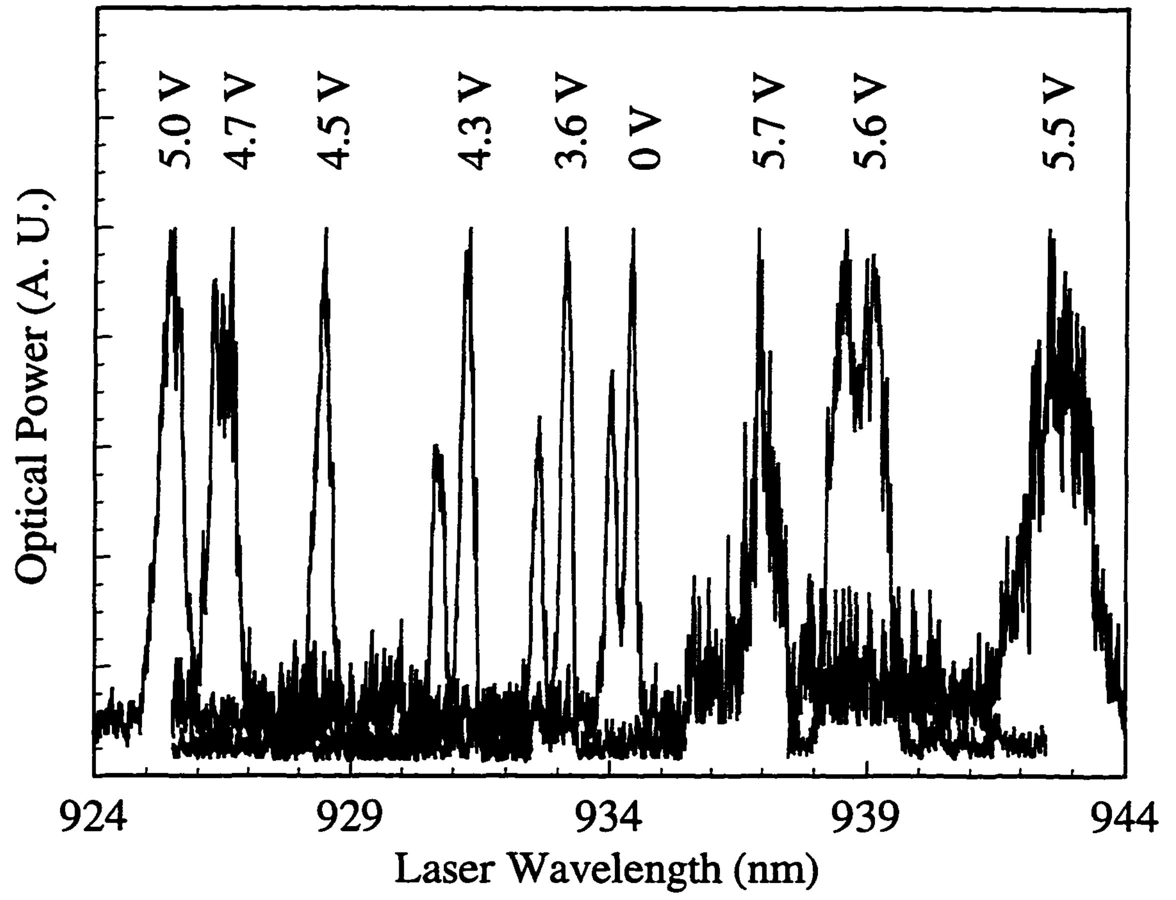


### 4.5.2 Light-Current properties

Figure 4.21 shows the pulsed LI curves of the VCSELs at various wavelengths. The threshold current is fairly insensitive to wavelength. There is a large leakage current most likely due to proton implant isolation problems. The VCSELs were able to lase CW at comparable thresholds to the pulsed, as shown in Figure 4.22. Pulsed powers for the VCSELs were typically 50 to 100 μW.

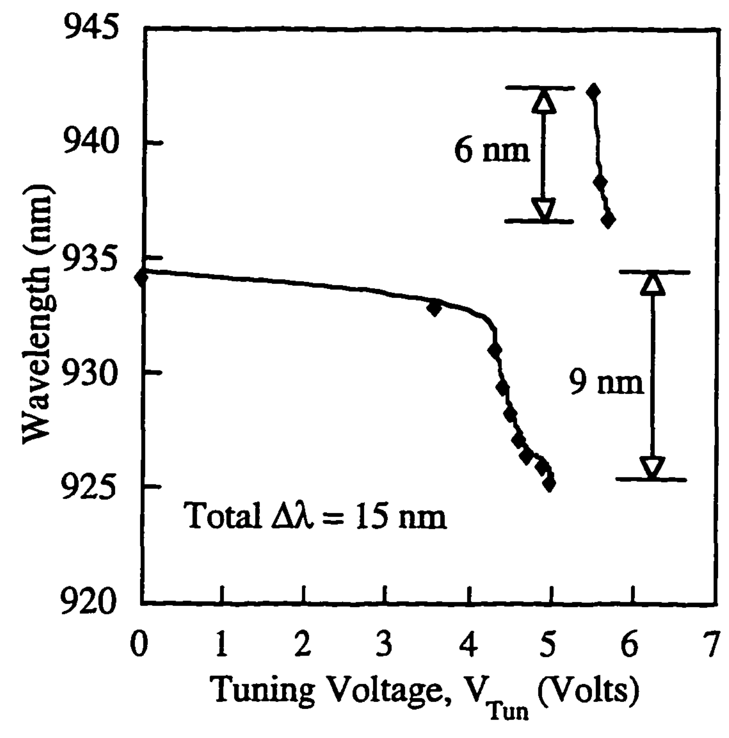


*Figure 4.20 - Plot of wavelength versus tuning voltage for the proton implanted micromechanical tunable VCSEL.*

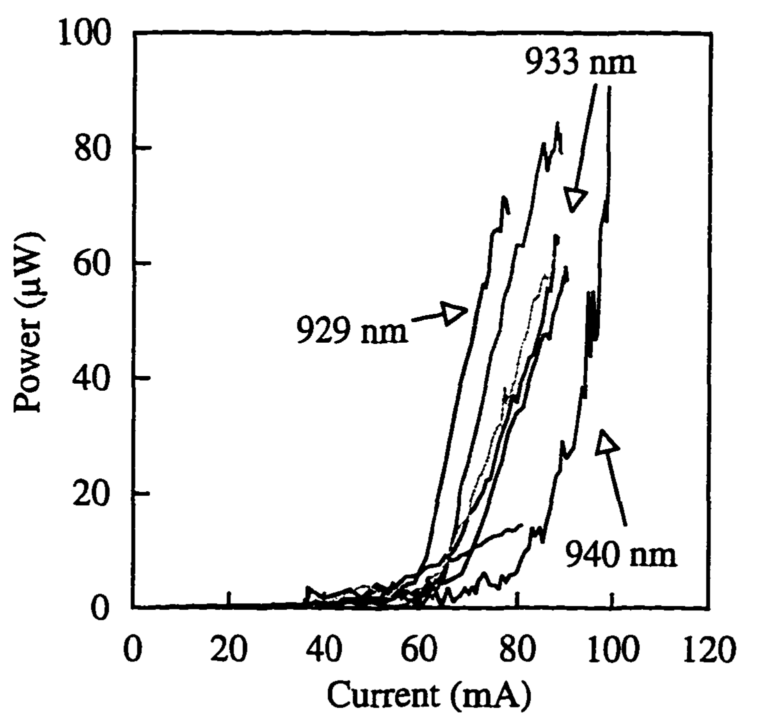

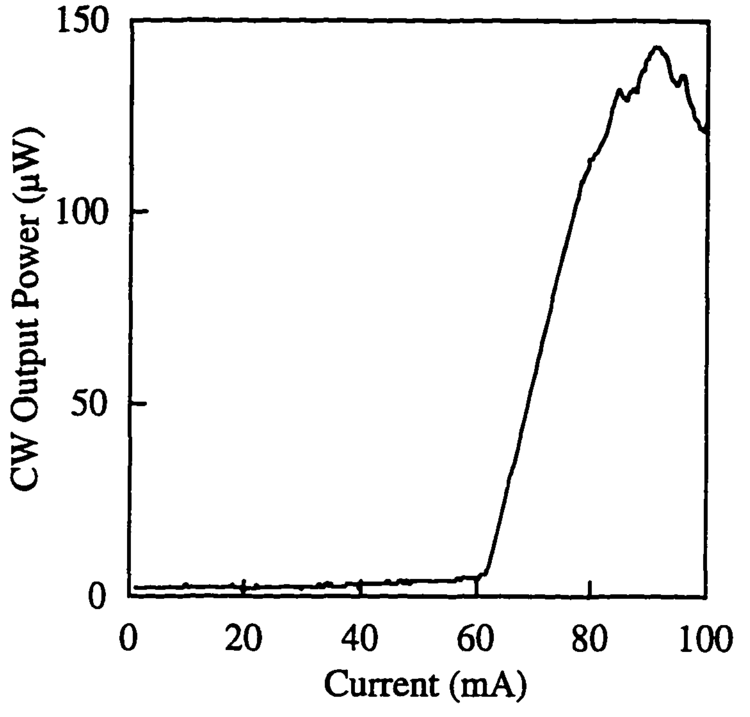


### 4.5.3 Near Field

The near field image (i.e., what the output of the laser looks like) for a tunable device is shown in Figure 4.23. The laser is lasing in a higher order, two lobed, mode. Below threshold, the near field is just an even distribution of light. Above threshold, this two lobed mode pops out with a clear null in the center. While this is undesirable for some applications, it nonetheless is excellent proof that the device is lasing.

One way to get lasers which lase in their circular fundamental mode is to make the devices smaller. This cuts off higher order modes so they do not exist or are so lossy that they cannot lase. The devices discussed above had a 20 µm diameter end circle, but the chip also had some 10 µm diameter end circle devices. These lased in the lowest order fundamental mode shown in Figure 4.24. The threshold currents for these devices were 110 mA, a number unimaginably large for a VCSEL. However, this does show that these devices can lase in the circular mode necessary in many applications.

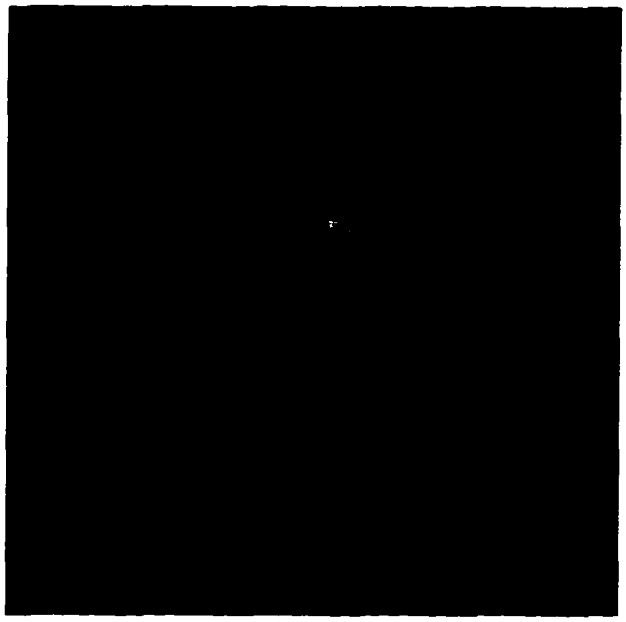

*Figure 4.23 - Near field image of a 20 μm diameter proton implanted micromechanical tunable VCSEL. These lasers preferred to lase in a higher order transverse mode.*

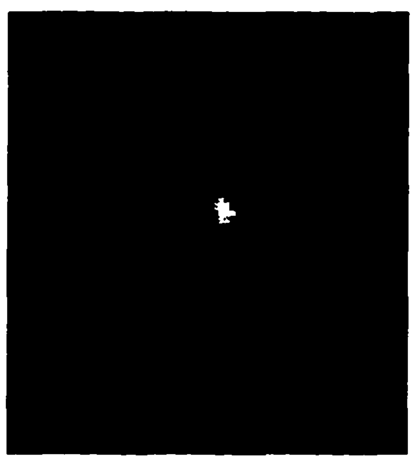

*Figure 4.24 - Near field of a 10 μm diameter proton implanted micromechanical tunable VCSEL. Although, these lased in a circular mode, the threshold current was amazingly high, Ith ~110 mA.*

## 4.6 Conclusion

In this chapter we have discussed the first micromechanical tunable VCSEL structure which broke many records for tuning, increasing the tuning range for VCSELs by 50%. CW, room temperature operation was achieved. These promising early results demonstrated the potential of this tuning technique and served as a proof-of-concept. The next chapter shows some of the improvements that were made on this first device and the record performance that resulted.

## 4.7 References

[1] C. J. Chang-Hasnain, J. P. Harbison, C. E. Zah, L. T. Florez, and N. C. Andreadakis, "Continuous wavelength tuning of two-electrode vertical cavity surface emitting lasers," *Electron. Lett.*, vol. 27, no. 11, p. 1002-1003, 1991.

[2] T. Wipiejewski, B. Weigl, K. Panzlaff, E. Zeeb, and K. J. Ebeling, "Vertical-Cavity Surface-Emitting Laser Diodes for Short Distance Optical Fiber Networks," 1994, Proceedings of the 44th Electronics Components and Technology Conference, Washington, DC, p. 330-4.

[3] L. Fan, M. C. WU, H. C. Lee, and P. Grodzinski, "10.1 nm range continuous wavelength-tunable vertical-cavity surface-emitting lasers," *Electron. Lett.*, vol. 30, no. 17, p. 1409-1410, 1994.

[4] P. R. Berger, N. K. Dutta, K. D. Choquette, G. Hasnain, and N. Chand, "Monolithically Peltier-cooled vertical-cavity surface-emitting lasers," *Appl. Phys. Lett.*, vol. 59, no. 1, p. 117-119, 1991.

[5] C. Gmachi, A. Kock, M. Rosenberger, E. Gornik, M. Micovic, and J. F. Walker, "Frequency tuning of a double-heterojunction AlGaAs/GaAs-vertical-cavity surface-emitting laser by a serial integrated in-cavity modulator diode," *Appl. Phys. Lett.*, vol. 62, no. 3, p. 219-221, 1993.

[6] M. S. Wu, E. C. Vail, G. S. Li, W. Yuen, and C. J. Chang-Hasnain, "Tunable

micromachined vertical cavity surface emitting laser," *Electron. Lett.*, vol. 31, no.4, p. 1671-1672, 1995.

[7] M. Tong, D. G. Ballegeer, A. Ketterson, E. J. Roan, K. Y. Cheng, and I. Adeseda, "A comparative study of wet and dry selective etching processes for GaAs/AlGaAs/InGaAs Pseudomorphic MODFETS," *J. of Electronic Materials*, vol. 21, no. 1, p. 9-15, 1992.

# 5. Oxidized Micromechanical Tunable VCSELs

## 5.1 Introduction

In the previous chapter, micromechanical tunable VCSELs were demonstrated for the first time[1]. However, those devices had considerably higher threshold currents and lower output powers than conventional VCSELs. In this chapter, we present improved tunable VCSELs with tuning ranges as high as 19.1 nm, threshold currents as low as 460 μA, and powers as high as 0.9 mW under room temperature CW operation. This represents a factor of 100 improvement in threshold current and a factor of 10 improvement in power. At the time, this was the widest tuning range, the lowest threshold current, and highest output power ever achieved with a micromechanical tunable VCSEL. This also represented the widest continuous tuning range for any monolithic semiconductor laser, as well as the first time threshold currents and output powers were on par with those of the best VCSELs. The key reason for such a huge improvement was the use of a recently developed oxidation technique.

## 5.2 Principle of Operation

Figure 5.1 shows a schematic of the device. The key difference of this device is an oxidized layer is used for current confinement instead of a proton implant. This oxidation process is a recent discovery[34] which has been used with conventional VCSELs to achieve low threshold currents, high output powers, and high efficiency. In this process, a high Al-concentration AlGaAs layer is oxidized until only a small aperture of unoxidized material is left. The oxide is an insulator and forces current into the aperture. In addition to funneling the current, this oxide has a lower refractive index than unoxidized AlGaAs and guides the light. These two effects keep the light and injected current underneath the cantilever end circle.

Besides this change, this VCSEL is similar to the device of the previous chapter. The structure is an *npn* structure which is tuned by applying a voltage between the top and middle contacts. The active region is pumped by passing a current between the middle contact and the substrate.

## 5.3 Layer Design

Two layer structures were designed, one with 20 nm of tuning and one

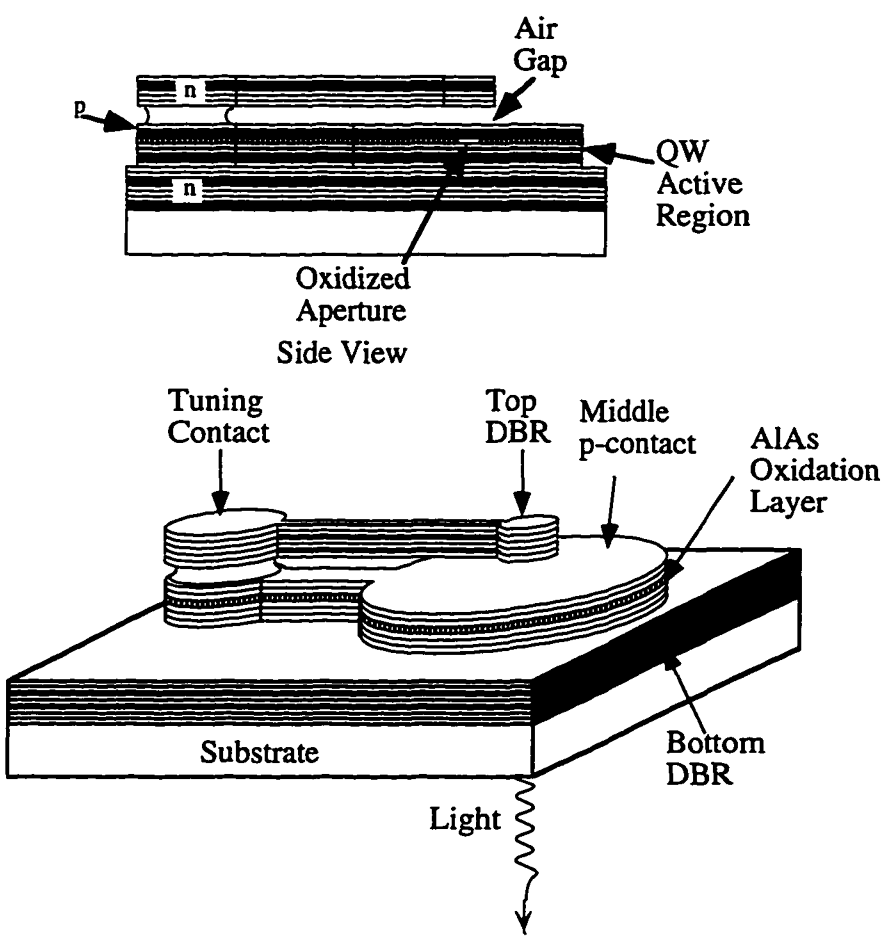


*Figure 5.1 - Schematic of the micromechanical tunable VCSEL showing a side view and a 3-d view. In the side view, note the oxidized aperture which confines the current and the light underneath the tuning head.*

with 30 nm of tuning. This section discusses the layer structures for the two designs and compares their calculated performances.

### 5.3.1 Design 1 - 20 nm Tunable Device

The layer structure is similar to the VCSEL of the previous chapter with two differences: the addition of a 3/4 λ oxidation layer and an increase in the tuning range by removing *p*-layers. The layers are again grown on an *n*+ substrate. First, the *n*-doped bottom mirror is grown, consisting of 19 1/2 graded AlAs/GaAs bottom mirror pairs, followed by 4 graded $Al_{0.6}Ga_{0.4}As$/GaAs mirror pairs. Then the active region is grown, consisting of a λ-cavity of $Al_{0.1}Ga_{0.9}As$ with three 80 Å $In_{0.15}Ga_{0.85}As$ QW's separated by 100 Å barriers in the center. Next, the *p*-layers are grown, starting with the graded 3/4 λ AlAs oxidation layer and followed by 4 graded $Al_{0.6}Ga_{0.4}As$/GaAs mirror pairs. The final *p*-doped layer is a 1/4 λ $Al_{0.1}Ga_{0.9}As$ stop etch layer, which is doped *p*+ for contacting. Next, the i-doped GaAs sacrificial layer is grown. This layer is designed to be 14100 Å thick which is approximately 3/2 λ in air and is 5 1/4 λ in GaAs. Next, the top *n*-DBR layers are grown, which consist of 22 1/2 $Al_{0.6}Ga_{0.4}As$/$Al_{0.1}Ga_{0.9}As$ mirror pairs. This is followed by a 1/2 λ GaAs sacrificial layer. This last sacrificial layer is included so that it can be selectively etched away, leaving a smooth interface for the top gold layer.

Tuning and reflectivity calculations were performed on this new structure. The mode splitting of the device was 24 nm and the device was designed to tune 20 nm before mode-hopping. The bottom mirror reflectivity is illustrated in Figure 5.2. The top mirror reflectivity for various air gap thicknesses is shown in Figure 5.3. The device lases at wavelengths far from the dips in the top mirror reflectivity.

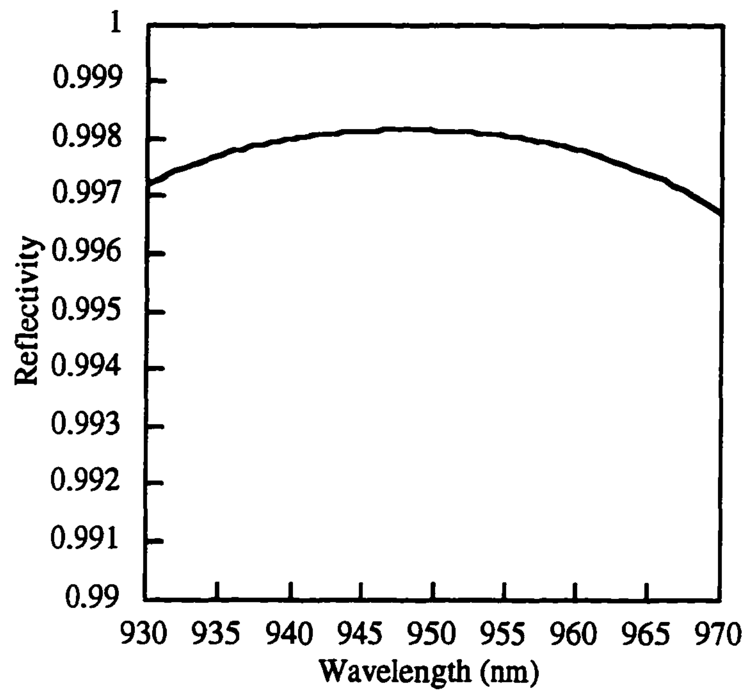


*Figure 5.2 - Reflectivity of the bottom mirror as a function of wavelength.*

The mirror loss as a function of tuning is shown in Figure 5.4. The round-trip loss is fairly constant at around 0.27% over the middle of the tuning range,

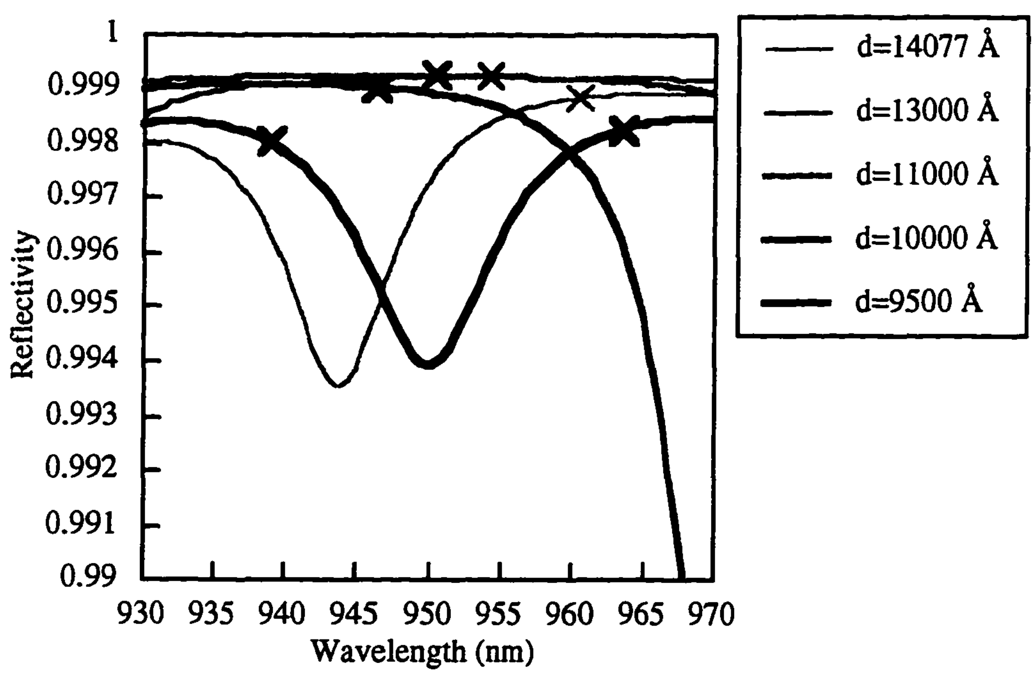


*Figure 5.3 - Top mirror reflectivities as a function of wavelength for various air gap thicknesses. The Fabry-Perot mode positions are denoted by the X's.*

but increases to 0.4% at the edges, which is significant enough to effect device performance.

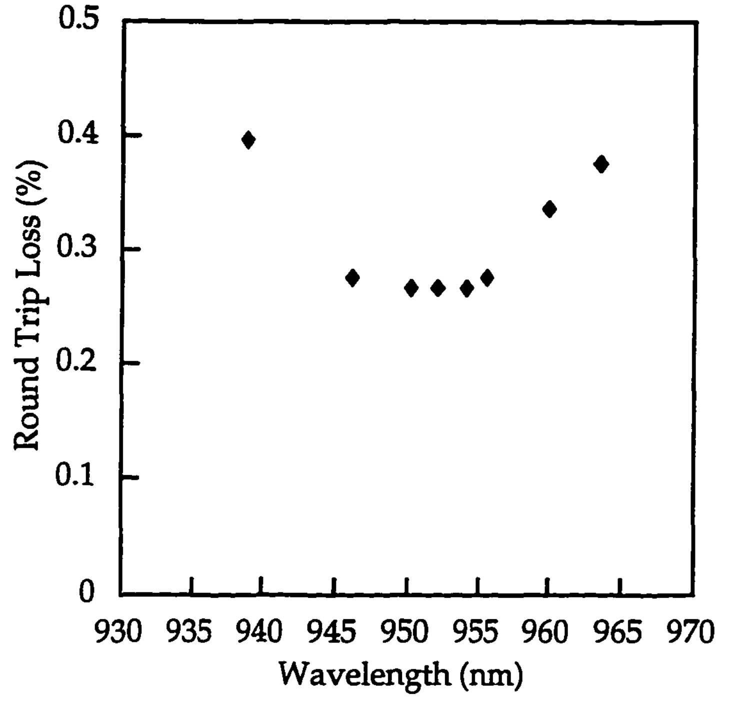


*Figure 5.4 - The change in round-trip loss as the device is tuned.*

### 5.3.2 Design 2 - 30 nm Tunable Device

Another layer structure was designed with approximately 30 nm of tuning. This structure was essentially the same as the 20 nm tuning structure except that 3 of the graded $Al_{0.6}Ga_{0.4}As/GaAs$ mirror pairs in the *p*-layers were moved up to the top *n*-DBR layers. This brings the total number of top *n*-DBRs to 25 1/2 and reduces the *p*-layers to the AlAs oxidation layer and 1 1/2 mirror pairs.

The mode splitting of this device is 36 nm and it is designed to continuously tune over 30 nm. The bottom mirror for this device is the same as in Figure 5.2. The top mirror reflectivity for this device is shown in Figure 5.5. Comparing this to Figure 5.3, several important differences are evident. The overall reflectivity is higher for the 30 nm structure and the dips in reflectivity are less pronounced. The increased reflectivity is due to the reduced numbers of *p*-layers which absorb light due to free carrier absorption. With less of these layers, the overall reflectivity goes up. The reduced reflectivity of the *p*-layers makes the air gap a weaker Fabry-Perot cavity, resulting in the smaller dips. The loss is summarized in Figure 5.6. The loss is similar to the 20 nm tuning device because the loss is dominated by the bottom mirror reflectivity, which is the same for both devices.

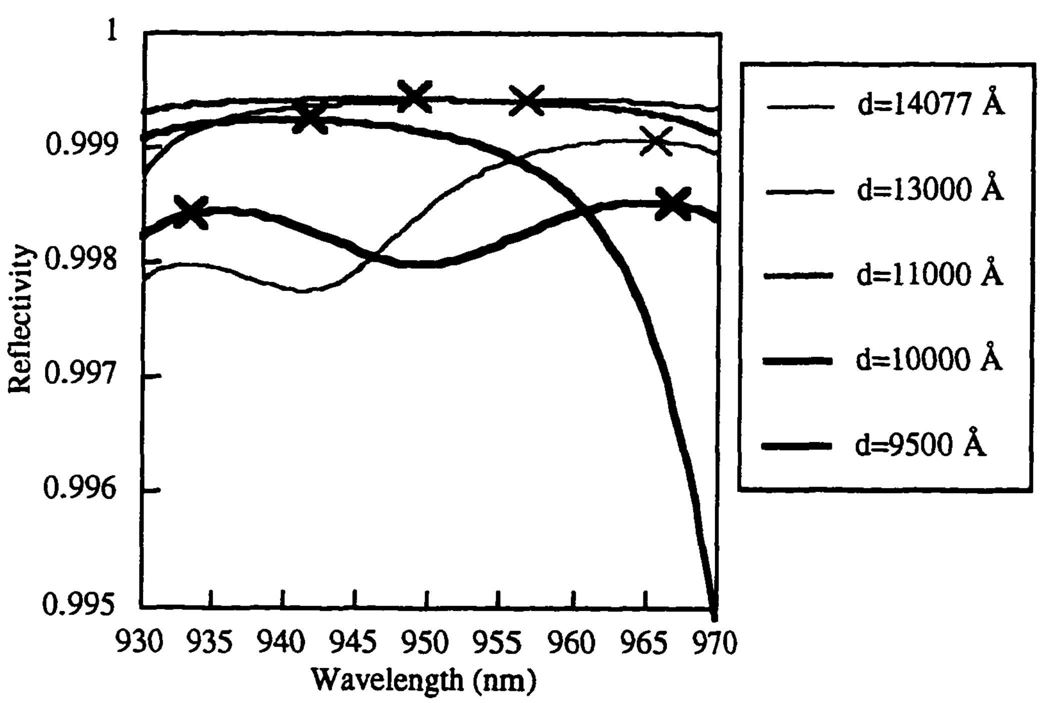


*Figure 5.5 - Top mirror reflectivity as a function of wavelength for the 30 nm tuning structure at various tuning gap thicknesses. X's show the wavelength of lasing for a particular air gap thickness.*

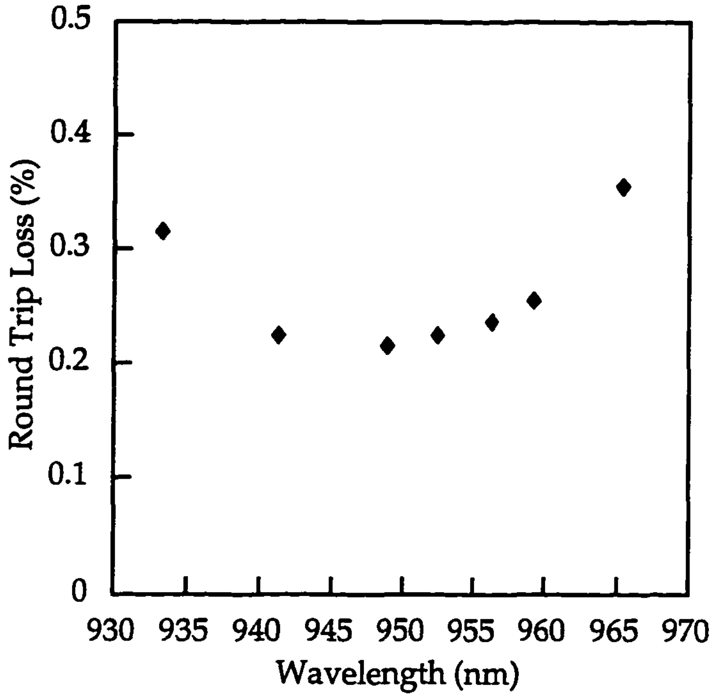


*Figure 5.6 - The change in round-trip loss with wavelength for the 30 nm tuning device.*

### 5.3.3 Discussion

Although the 30 nm tuning device has wider tuning range and less free carrier absorption, the 20 nm device is better because its increased number of *p*-layers decreases the lateral resistance. Since heating limits the output power of VCSELs, this extra power dissipation is significant. The lower power dissipation of the 20 nm tuning structure should allow it to achieve higher powers.

To calculate the approximate resistivity of the *p*-layers, assume a 5 μm aperture underneath a 15 μm end circle. Assume that the gold outside this 15 μm end circle is perfectly conducting. This circular injection region can be approximated by a 30 μm wide, 5 μm long injection strip of the same thickness. These *p*-layers are doped $10^{18}/cm^3$ except for the last 200 Å, which is doped $10^{19}/cm^3$. The hole mobility[5] is 100 $cm^2$/V-s for adoping density of $10^{18}/cm^3$ and 50 $cm^2$/V-s for a doping density of $10^{19}/cm^3$. The resistance of a rectangular layer is given by the formula

$$R = \frac{l}{\mu p w t q} \tag{5-1}$$

where $R$ is the resistance, $l$ is the length, $\mu$ is the mobility, $w$ is the width, $t$ is the thickness, and $q$ is the charge of an electron. Using this formula and combining the different doping resistances in parallel, the total resistance of the layers can be calculated. This calculation gives a resistance of 150 Ω for the 20 nm tuning device and 340 Ω for the 30 nm tuning device. For 1 mA bias current, this means a drop of 0.15 V and 0.34 V and a power dissipation of 0.15 mW and 0.34 mW for the 20 nm and 30 nm tuning devices, respectively. These numbers are fairly small compared to the total voltage drop of the device (~2.5V) and power dissipation (2.5 mW). However, at higher currents of 10 mA, the voltage goes up by a factor of ten and the power by a factor of 100 and becomes a significant fraction of the total voltage and power.

In the future, as more efficient and wider tuning range structures are developed, this effect will become more significant. However, there are ways to reduce the problem. First, the doping level and thickness of the *p*-layers can be increased to increase the conductivity of the layers, but this has the adverse effect of increasing free carrier absorption. The gold could be brought closer to the oxide aperture by reducing the size of the tuning head, but this increases optical loss. Alternatively, a *pnp* structure instead of an *npn* structure could be used. The lateral injection layers would then be *n* doped. Electrons have both a higher mobility (factor of 30 bigger than holes) and a lower free carrier absorption (almost half that of holes). Thus, for the same level of free carrier absorption, the resistance is reduced by a factor of 60.

## 5.4 Growth

Figure 5.7 shows the measured and calculated reflectivity for the 30 nm structure. Two of the Fabry-Perot peaks and DBR stop band line up fairly well. The rest of the dips do not agree as closely, but this is not unusual. There is some amount of inherent ripple in the measurement stage, which can disguise the smaller Fabry-Perot peaks, and the ripples outside the DBR band fluctuate rapidly with small growth errors.

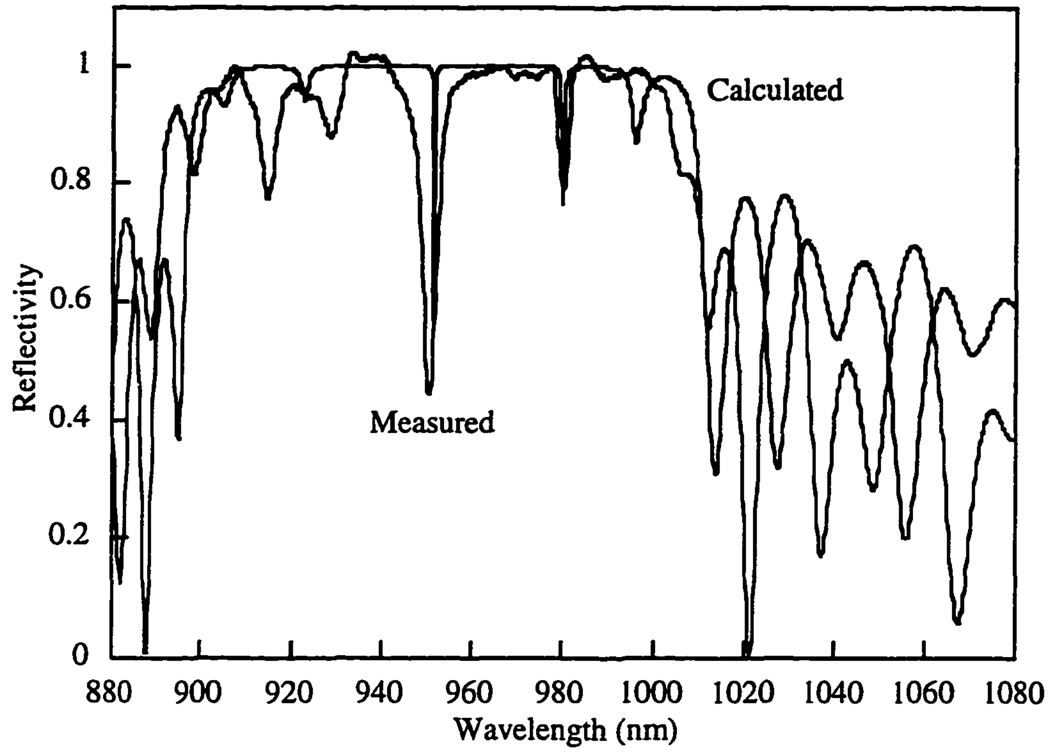


*Figure 5.7 - Measured and calculated reflectivity for the 30 nm tuning structure.*

The 20 nm structure's measured and calculated reflectivities are shown in Figure 5.8. This growth was found to be miscalibrated by 30 nm. This was due to an error where the calibration laser was pointed at the edge of the wafer instead of the center.

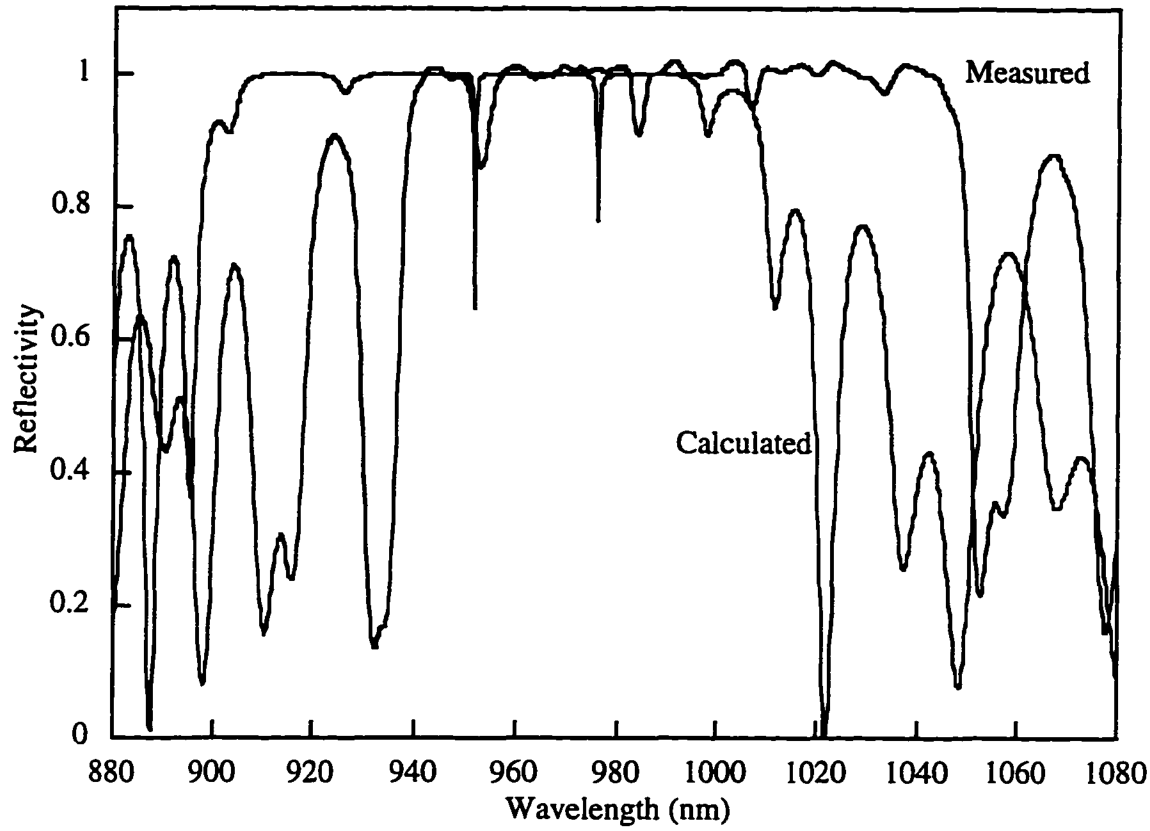


*Figure 5.8 - Calculated and measured reflectivity of the nominal 20 nm tuning wafer (235). Note the growth is shifted approximately 30 nm from the design wavelength.*

Both these wafers were fabricated. Surprisingly, the misaligned 20 nm tuning wafer worked and the 30 nm wafer did not. This was not due to the more aggressive design of the 30 nm wafer. When the 30 nm wafer was tested, it functioned as an LED. However, most of the light was at ~980 nm and did not tune much with voltage. Therefore, the gain peak of the QWs was shifted to longer wavelengths from its design point of 950 nm. Luckily, this shift coincided with the layer thickness growth errors for the 20 nm structure. This device lased with low thresholds and high power as described in the performance section.

## 5.5 Fabrication

The fabrication is summarized in Figure 5.9, the significant addition of the oxidation step. Wet oxidation is a discovery that has recently been attracting a great deal of attention with VCSELs. A VCSEL structure with a high Al concentration AlGaAs layer is etched into large mesas that expose the layer, and placed in a steam atmosphere at approximately 425° C. The high Al concentration layer uniformly oxidizes in from the edges. Layers with less aluminum than $Al_{0.9}Ga_{0.1}As$ oxidize extremely slowly, so the rest of structure is unaffected. The key is to stop the oxidation process, leaving a small unoxidized aperture at the center of the mesa. The oxidized material is insulating and has a much lower refractive index ($n$~1.5) than that for unoxidized material ($n$~2.9). The current and light are thus confined to the oxidized aperture. By placing the tuning head in the center of the large mesa, we can ensure that the oxidized aperture is underneath the tuning head.

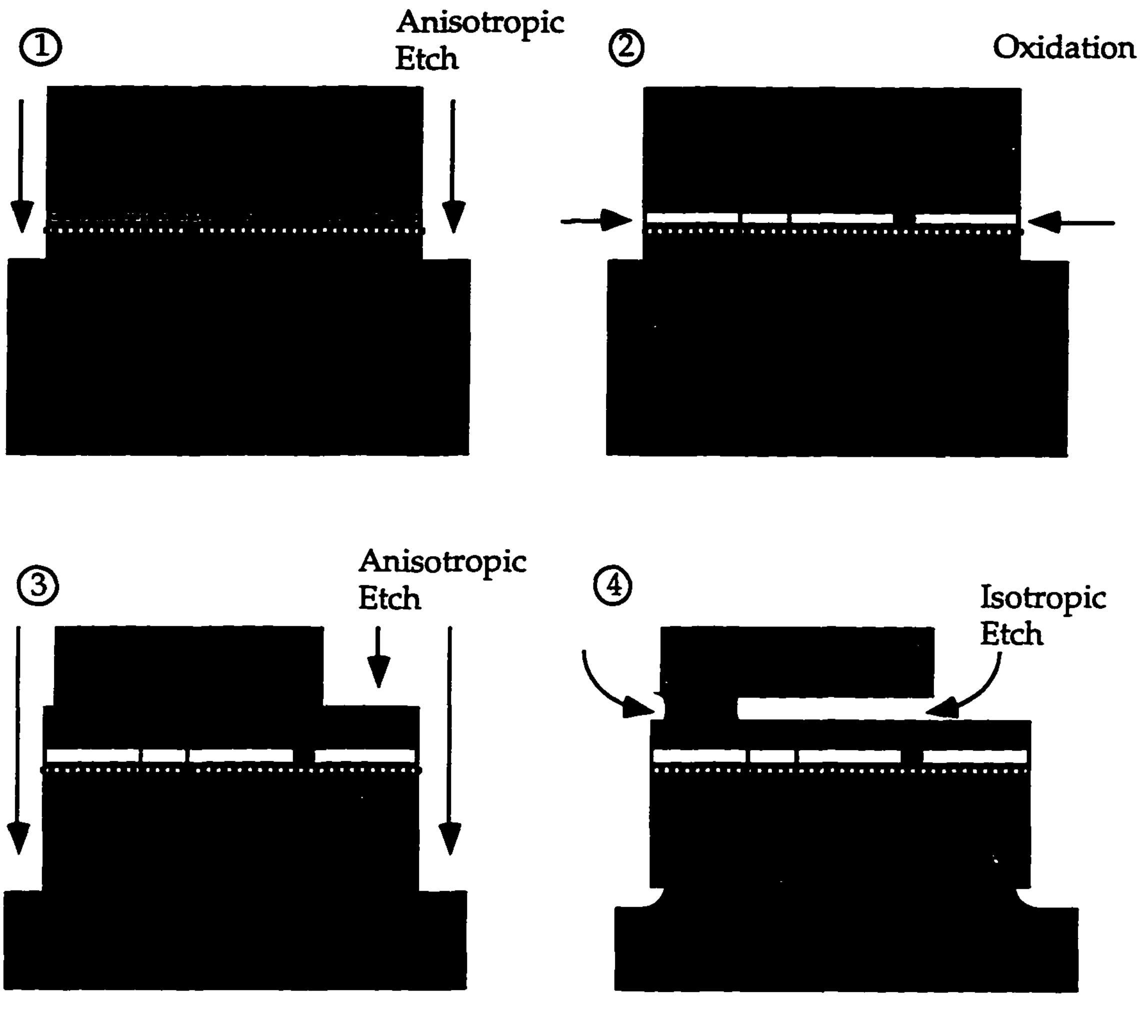


*Figure 5.9 - Major fabrication steps for the oxidized VCSEL.*

Several of the steps have to be rearranged to accommodate the oxidation process. Unlike the proton implant, which is performed towards the end, the oxidation is performed early. This stops the cantilever from being exposed during the oxidation process, so there is no danger of a thin oxide building up on the cantilever and potentially causing strain and bending.

### 5.5.1 Photolithography

The first step in the new process is the photolithography. To perform the oxidation, we must etch down 6 μm to reach the oxidation layer. For isolation reasons, this must be done with a dry etcher to get vertical side walls. Performing lithography on such a non-planar substrate is very challenging.

Typically, photoresist is only 1.4 μm thick and is unlikely to cover a 6 μm vertical drop. Using thicker photoresist is not possible, because the cantilevers are only 2 μm wide which is already difficult with 1.4 μm thick resist. The solution is to use a trick so that all the photolithography can be done in the beginning. First, a 5000 Å thick layer of $SiN_x$ is put on the wafer. Then the $SiN_x$ is patterned with the *cantilever* mask. The $SiN_x$ is selectively etched with BOE 6:1. Then the photoresist is washed off. We then repattern the sample with the mesas for oxidation. Now the cantilever lithography is already done, and later in step 3 of the process, we can use the $SiN_x$ as a mask for the cantilever etch.

Unlike the proton-implanted tunable VCSELs, this VCSEL's cantilever never gets thinned by an etch. It remains 3 μm thick along its full length. Since this is twice as thick as the proton-implanted tunable VCSEL, the cantilever must be twice as long to keep the tuning voltage roughly the same. So the dimensions for the cantilever are now nominally 200 μm long, 2 μm wide, and 3 μm thick.

### 5.5.2 Oxidation

The oxidation process can be blocked if there is some film covering the sidewalls of the mesa. This can occur in two ways. First, during dry etching some material is redeposited on the mesa sidewalls*. Second, high Al concentration layers also oxidize in air at room temperature. Unfortunately, this is not the same oxide that forms in the oxidation furnace, and there is some evidence that this room-temperature oxide blocks the high-temperature oxide from forming.

The usual way around this is to wet etch the mesas immediately prior to sticking the samples into the oxidation furnace. This way, there is no redeposition on the sidewalls (as in dry etching) and there is no time for the room temperature oxide to form (It typically takes minutes to form a room-temperature oxide layer). However, we need to use dry etching for isolation reasons, so we performed a short BOE 6:1 dip before putting them into the

* Indeed, this is one of the mechanisms that ensures vertical sidewalls.

oxidation furnace. This etches only high Al concentration AlGaAs and is used to etch away the room-temperature oxide and any redeposition from the dry etcher. Of course, BOE 6:1 also etches $SiN_x$, which we use as a mask for the cantilever. So, it is important to leave the mesa photoresist on for this step. Then the mesa photoresist is removed with acetone, methanol, and $O_2$ dry etch, and the sample is placed into the oxidation furnace. This method worked well even with a few days in between the dry etch and the oxidation step.

Since the oxidation process is new, some characterization was required before proceeding with real samples. Figure 5.10 shows the oxidation depth as a function of oxidation time for both AlAs and $Al_{0.98}Ga_{0.02}As$ oxidation layers. The mesas used in the devices are large (~200 μm diameter), requiring 100 μm of lateral oxidation. Pure AlAs was used to keep the oxidation times reasonable.

The variation in the oxidation depth shown in Figure 5.10 is not quite as bad as it seems. The data was for many different types of samples and growths, with different thickness layers, and different days. Two consecutive runs with the same processing and growth had an accuracy of about +/- 2.5% in oxidation depth. One of the problems is that the oxidation rate can change rapidly near the edge of the wafer, as shown in Figure 5.11. To achieve good reproducibility, the edges of the wafer must not be used. Sample loading could also be improved. At first it typically took a minute to load the sample, but this time has been improved to less than 10 seconds, causing less variation in the starting temperature of the oxidation. In the future, $Al_{0.98}Ga_{0.02}As$ layers could be used, which, although slower, are more reproducible in oxidation depth.

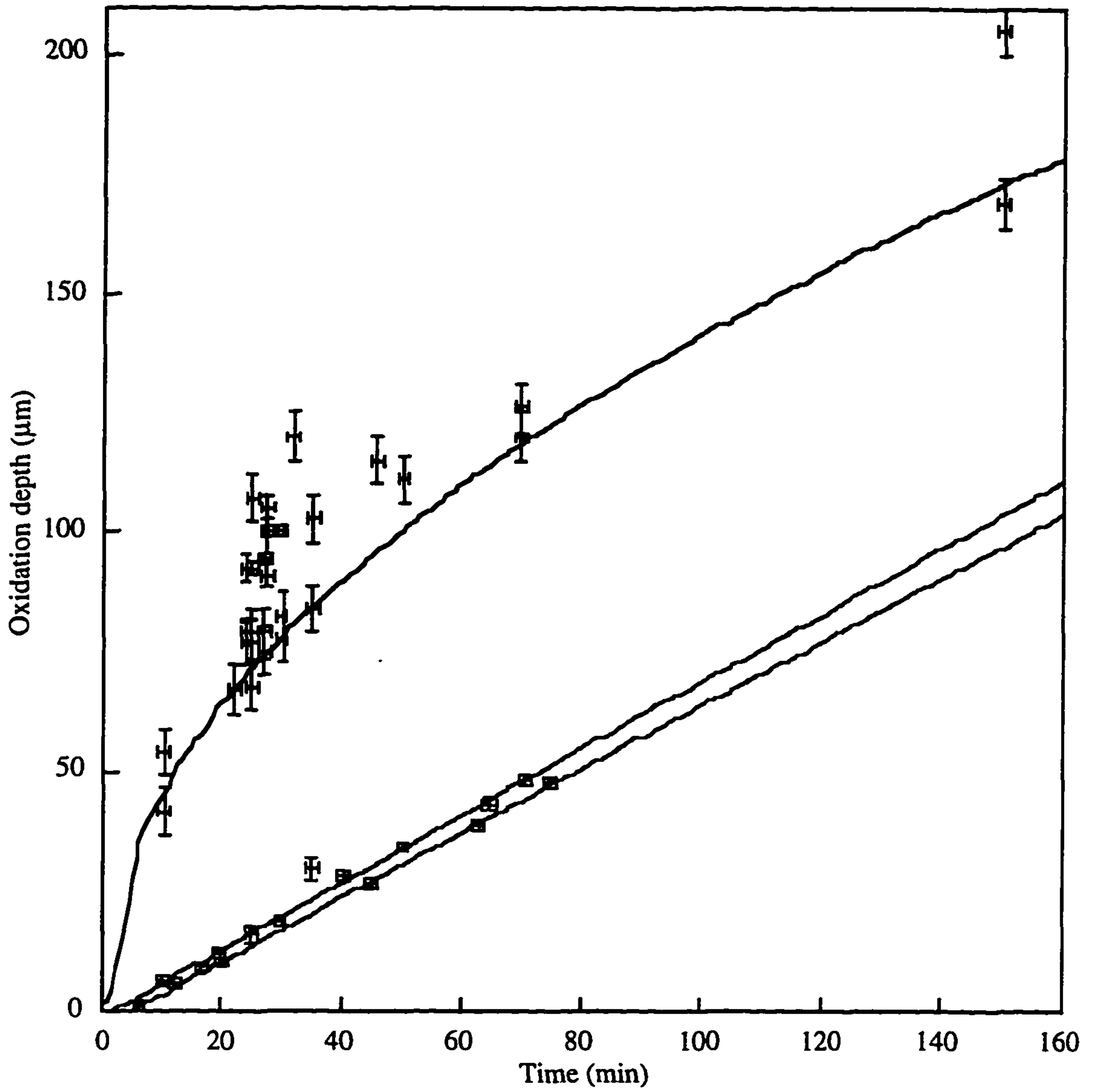


*Figure 5.10 - Plot of oxidation depth versus oxidation time for pure AlAs (black) and $Al_{0.98}Ga_{0.02}As$ (gray). Note that the AlAs follows a square root diffusion limited curve while the $Al_{0.98}Ga_{0.02}As$ follows a straight reaction limited curve.*

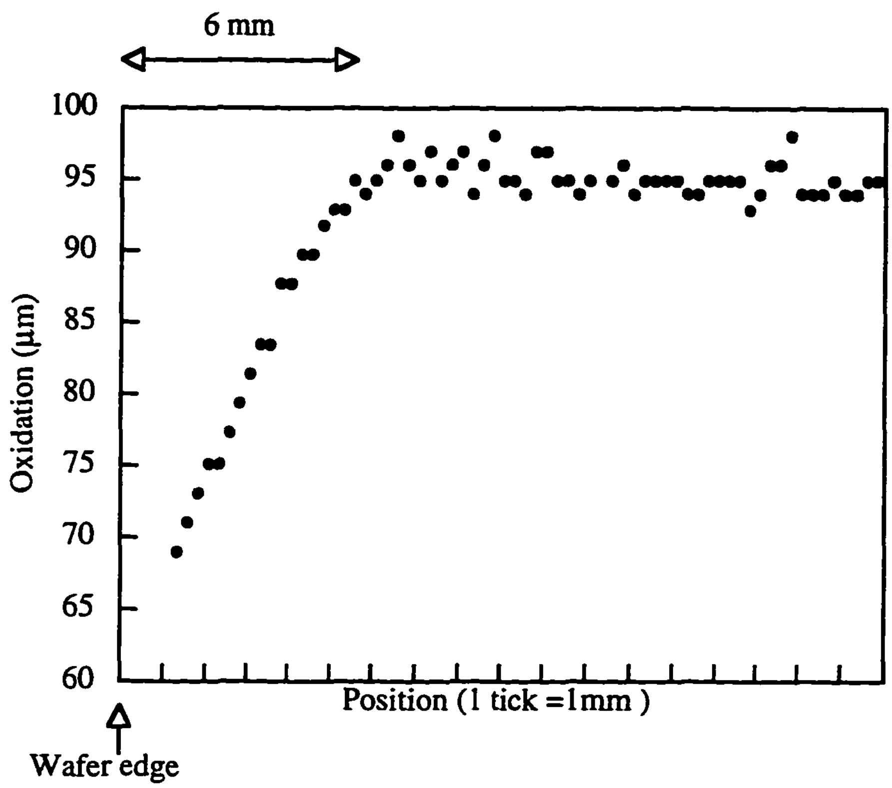


*Figure 5.11 - Plot of oxidation depth as a function of position in the wafer. Note that close to the edge the oxidation rate drops dramatically.*

### 5.5.3 Isolation

When the sample is dipped in BOE 6:1 before being oxidized, the high Al concentration layer is undercut by approximately 1 µm. This can be used to our advantage for isolating the devices as shown in Figure 5.12. If gold is evaporated onto a sample that is undercut, the gold "breaks" across the undercut, provided that the gold is thinner than the undercut layer. This happens already with the top cantilever: it is not connected to the middle *p*-layer by the gold, because the gold is broken across the undercut GaAs sacrificial layer. By doing this across the oxidation layer, the shadow mask step is no longer necessary and gold can be blanket-evaporated. The one problem is that normally the oxidation layer is only 800 Å thick and the gold is 3000 Å thick. To get around this, we use a 3/4 $\lambda$ oxidation layer, which is 2400 Å thick and only 1500 Å of gold. This does not leave a large margin for error. For this method to work reliably, it is necessary to use dry etching to get a vertical sidewall to cleanly break the gold. This is why the first etch must be a dry etch.

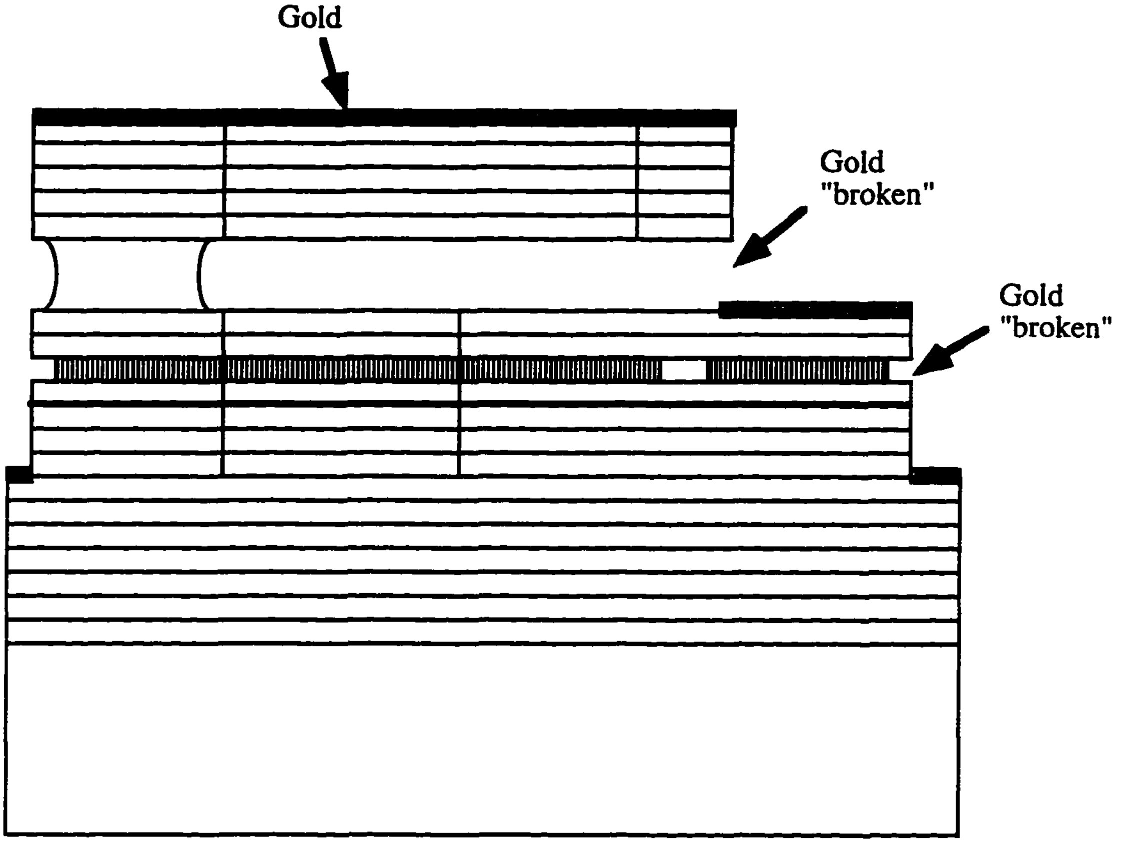


*Figure 5.12 - Schematic showing how the gold can be "broken" by undercutting devices. This self-aligned process automatically isolates devices and contacts without any patterning of the gold.*

### 5.5.4 Final Steps

The rest of the processing is fairly similar to that described in previous chapters. We use the anisotropic dry etch to form the cantilevers, this time using $SiN_x$ as the mask. Then the isotropic selective dry etch is used to free the cantilever from the substrate. Finally, 1500 Å of gold is blanket evaporated to form the contacts.

## 5.6 Performance

Figure 5.13 shows the tuning spectra for a device with an oxidized aperture of ~10 μm. The device continuously tunes over 19.1 nm as the tuning voltage changes from 0 to 14.4 V. At the maximum bias of 14.4 V, the wavelength of the emitted light has completely wrapped around to the original wavelength at 0 V. A single step wavelength discontinuity is seen at ~955 nm due to the growth error discussed in section 5.4, resulting in a Fabry-Perot wavelength at 0 V near the center of the free-spectra range. This could be corrected by growing the 0 V Fabry-Perot resonance at the long wavelength end of the tuning range. The device lases in the lowest order transverse mode and the side mode suppression ratio is more than 12.5 dB over the entire tuning range. The tuning current is less than 0.5 μA at all times.

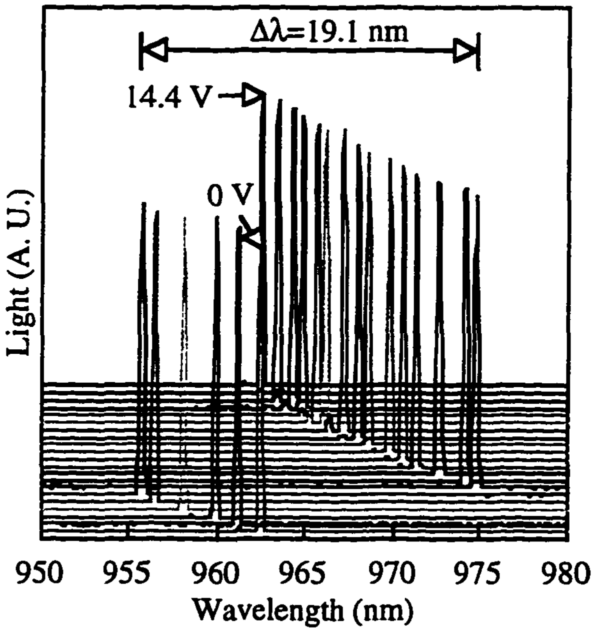


*Figure 5.13- Tuning spectra for a device oxidized to an aperture of approximately 10 μm. The 19.1 nm of tuning achieved for this device is the largest tuning ever achieved with a VCSEL.*

The LI curves for the device are shown in Figure 5.14. The kinks in the LI curve are attributed to the weak external cavity formed by the substrate and could be avoided in the future with a top-emitting device. The threshold current versus wavelength for the device is plotted in Figure 5.15. The threshold current is less than 5.4 mA over 18 nm of the tuning range and less than 8.5 mA over the entire tuning range.

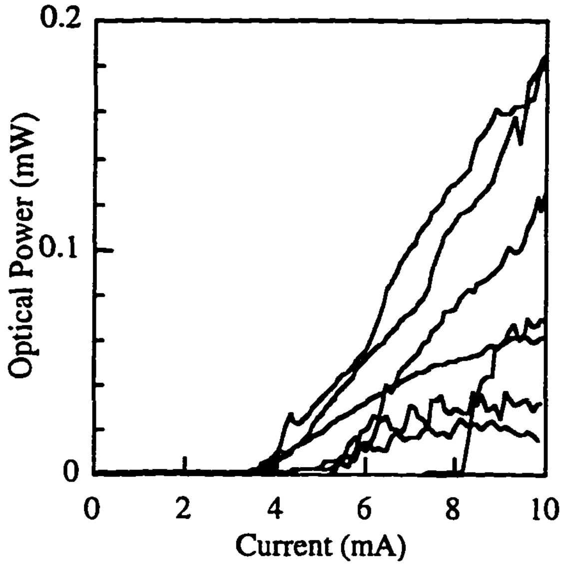


*Figure 5.14 - LI curves for the 10 μm aperture tuning device over the entire tuning range, including the LI curves for the two most extreme wavelengths.*

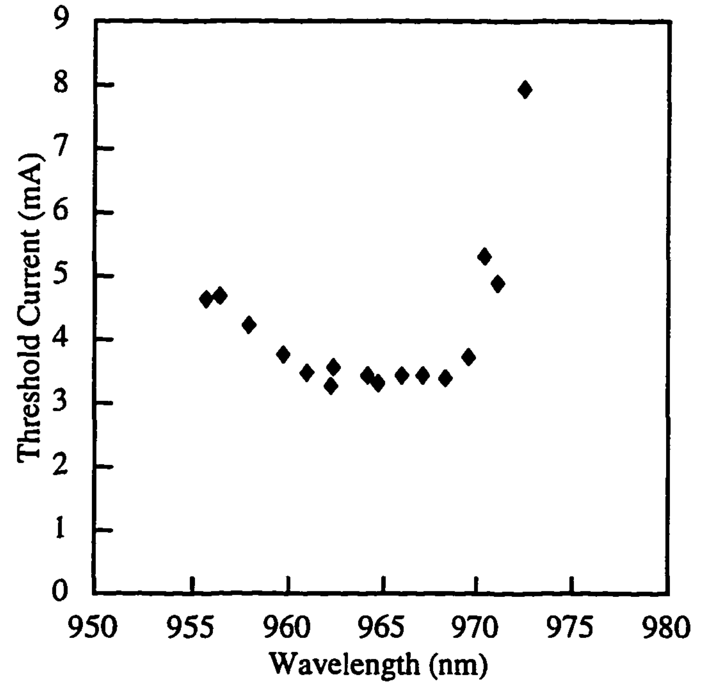


*Figure 5.15 - Plot of threshold current as a function of wavelength for the 10 μm aperture device.*

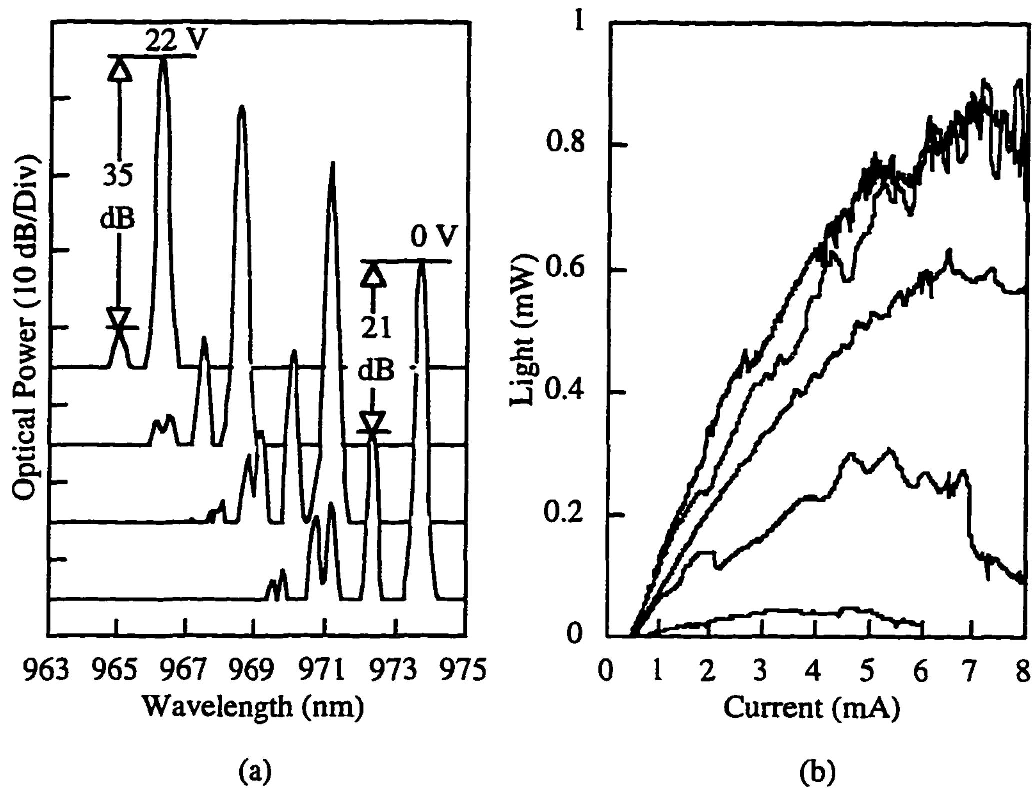


*Figure 5.16 - The spectrum and LI curves for a device with a 5 μm aperture. Once again LI curves over the entire tuning range have been included, including the most extreme wavelengths.*

The spectra for a device oxidized to an aperture of ~5 μm diameter are shown in Figure 5.16(a). The device lases in a single transverse mode and the side mode suppression ratio for this device is greater than 20 dB over the entire tuning range. The same spectra can be replotted on a linear scale and are shown in Figure 5.17. The other modes, which all appear at shorter wavelengths, are higher order transverse modes which are not lasing. The large transverse mode spacing of 1.3 nm indicates significant waveguiding by the oxide. The LI curves for the device are shown in Figure 5.16(b). The threshold current is 460 μA and the peak output power is 0.9 mW. Both the threshold and the output power were the best for a micromechanical tunable VCSEL at the time of publication. The optical power densities on the GaAs/air interface (~0.4 MW/cm$^2$ for a 1 mW, 5 μm by 5 μm device) are well below the damage threshold. Thermal effects limit the output power.

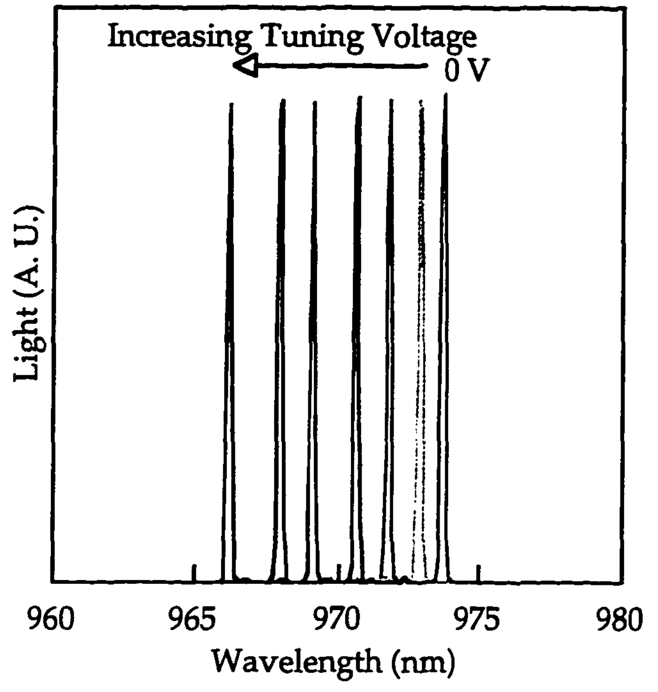


*Figure 5.17 - The same spectrums for the 5 μm device but on a linear scale instead of a log scale.*

The threshold current and peak power as a function of wavelength are plotted in Figure 5.18. The roughly parabolic dependence of threshold current and peak power can be seen with the fits shown in the figure. There is some scatter in the threshold current, which we believe is due to the backside reflection of the substrate. This could be corrected with a top-emitting device. Top-emitting devices are slightly more complicated to fabricate, which is why these first devices were bottom-emitting.

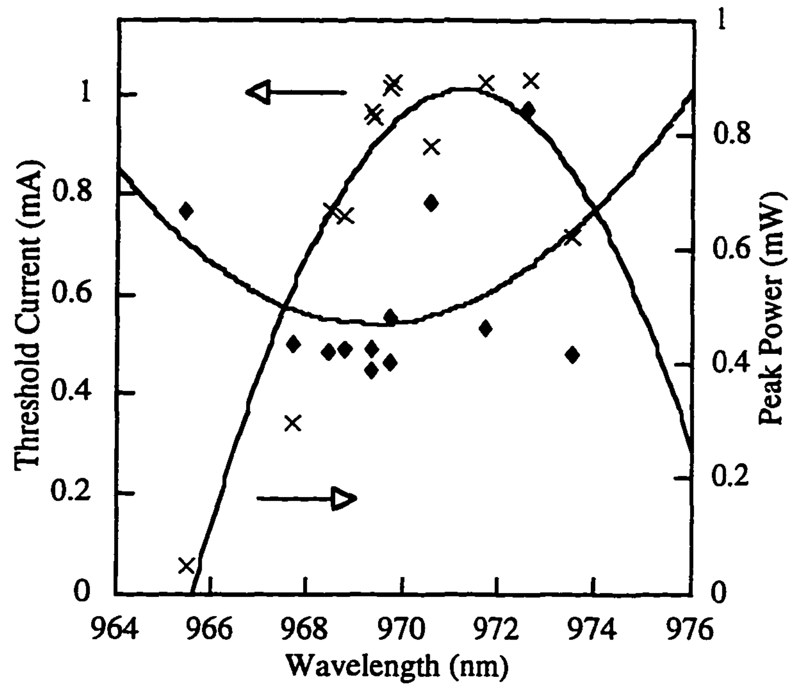


*Figure 5.18 - Plot of threshold current and peak power as a function of wavelength for the 5 μm aperture device.*

The spectrum and near field of the device versus pumping are shown in Figure 5.19. As can be seen from the figure, higher order modes do not come in until 3 times threshold. At higher pumping, the lowest order transverse mode and the first order mode (two lobed) essentially remain equal in power. Another interesting point, which has been studied extensively in our group[6], is the shrinkage of the near field pattern in the transition from below threshold to above threshold.

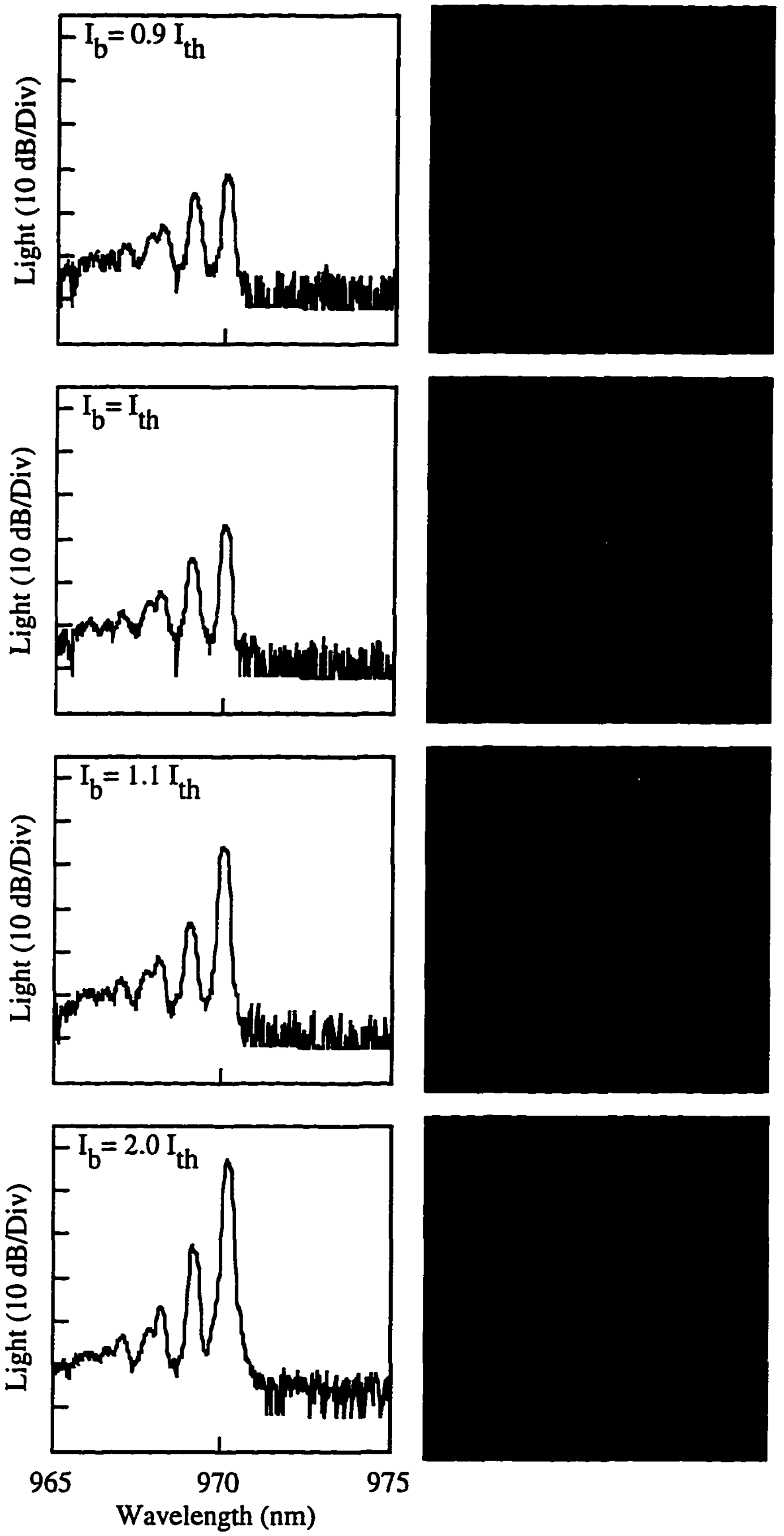


*Figure 5.19 - Spectra and near field of the 5 μm device at various pumping levels. The next highest mode does not come in until 3 times threshold.*

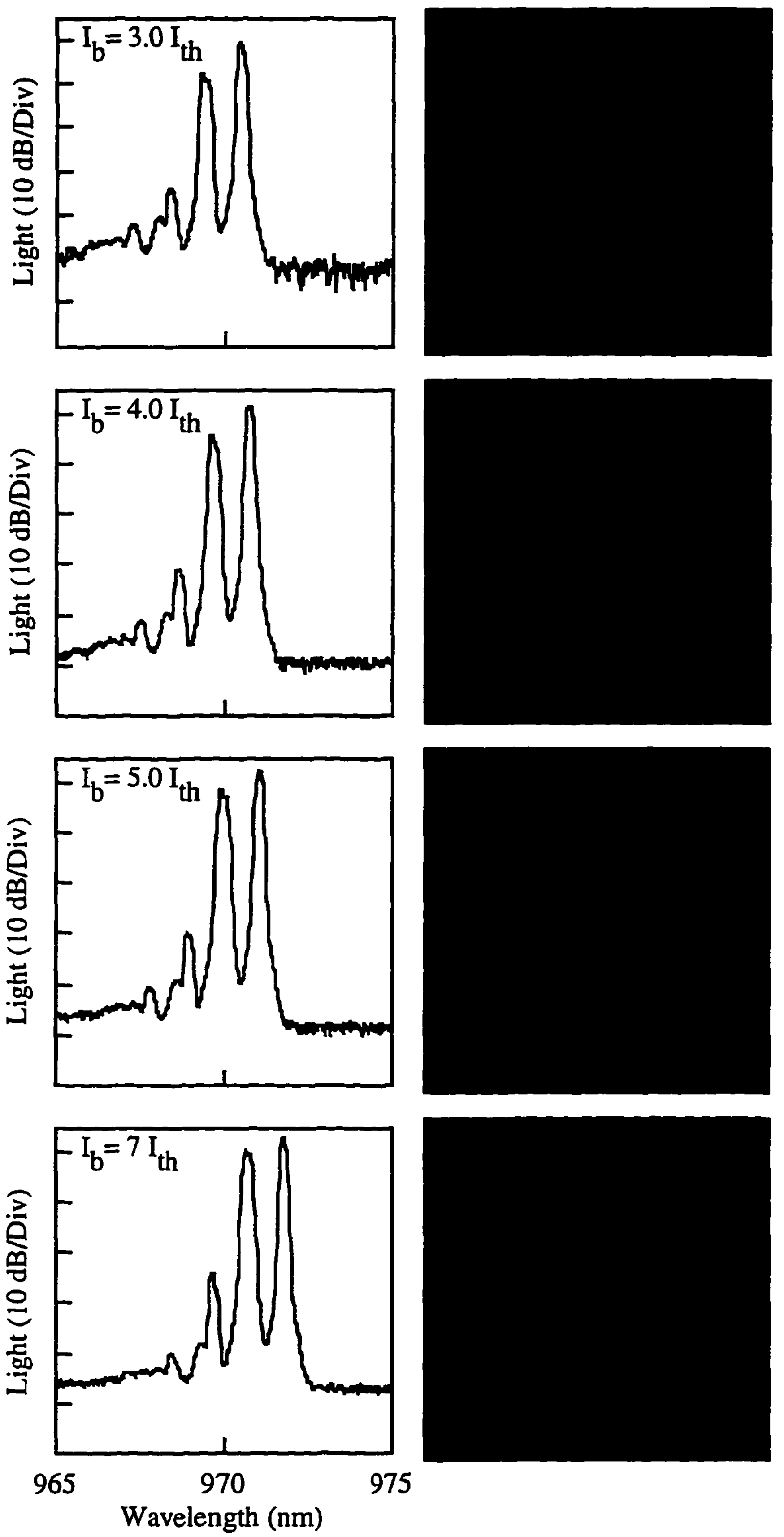
$I_b = 3.0\ I_{th}$
$I_b = 4.0\ I_{th}$
$I_b = 5.0\ I_{th}$
$I_b = 7\ I_{th}$
Light (10 dB/Div)
965
970
975
Wavelength (nm)

## 5.7 Mode Oscillation in Multimode Devices

The larger aperture devices (>10 μm) were observed to lase in a higher order transverse mode when biased several times above threshold. The lasing mode changed with tuning voltage. An example is shown in Figure 5.20, which shows the near field and spectra for a large aperture (>10μm) device biased several times above threshold at various tuning voltages. The near field and spectra show the device is oscillating between the fundamental mode and the next highest mode.

The oscillations are due to the substrate forming an external cavity which causes a ripple in the reflectivity with wavelength[7]. The period of the oscillations (0.28 nm) matches that of the calculated Fabry-Perot resonances of the substrate (0.285 nm). Figure 5.21 shows that as the device is tuned, the modes sweep across this oscillating reflectivity, causing the power in the modes to oscillate. This occurs even though the mode spacing (1.3 nm) is several times larger than the Fabry-Perot mode spacing of the substrate (0.28 nm). For the device in Figure 5.20, it happens that the fundamental mode lines up on a reflectivity maximum when the second order mode lines up on a reflectivity minimum, and vice versa. In devices with different transverse mode spacings, different oscillations were observed. Oscillations between the fundamental mode and a four lobed mode or between two mixtures of modes have also been observed.

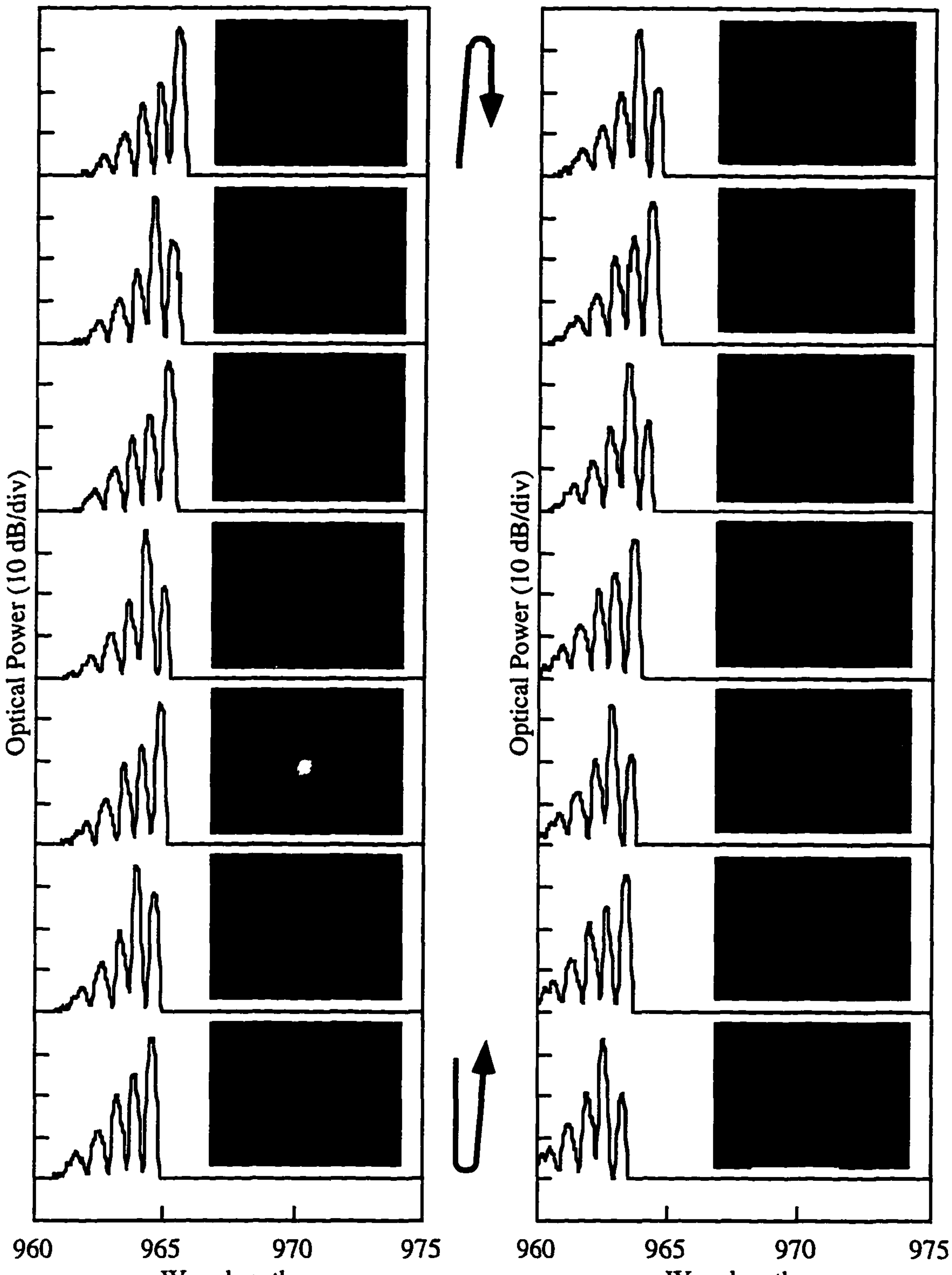


*Figure 5.20 - Oscillations in the near field and spectra caused by tuning a large aperture device when operated far above threshold. The tuning voltage changes from 12.0 V to 15.2 V from the upper left to the lower right.*

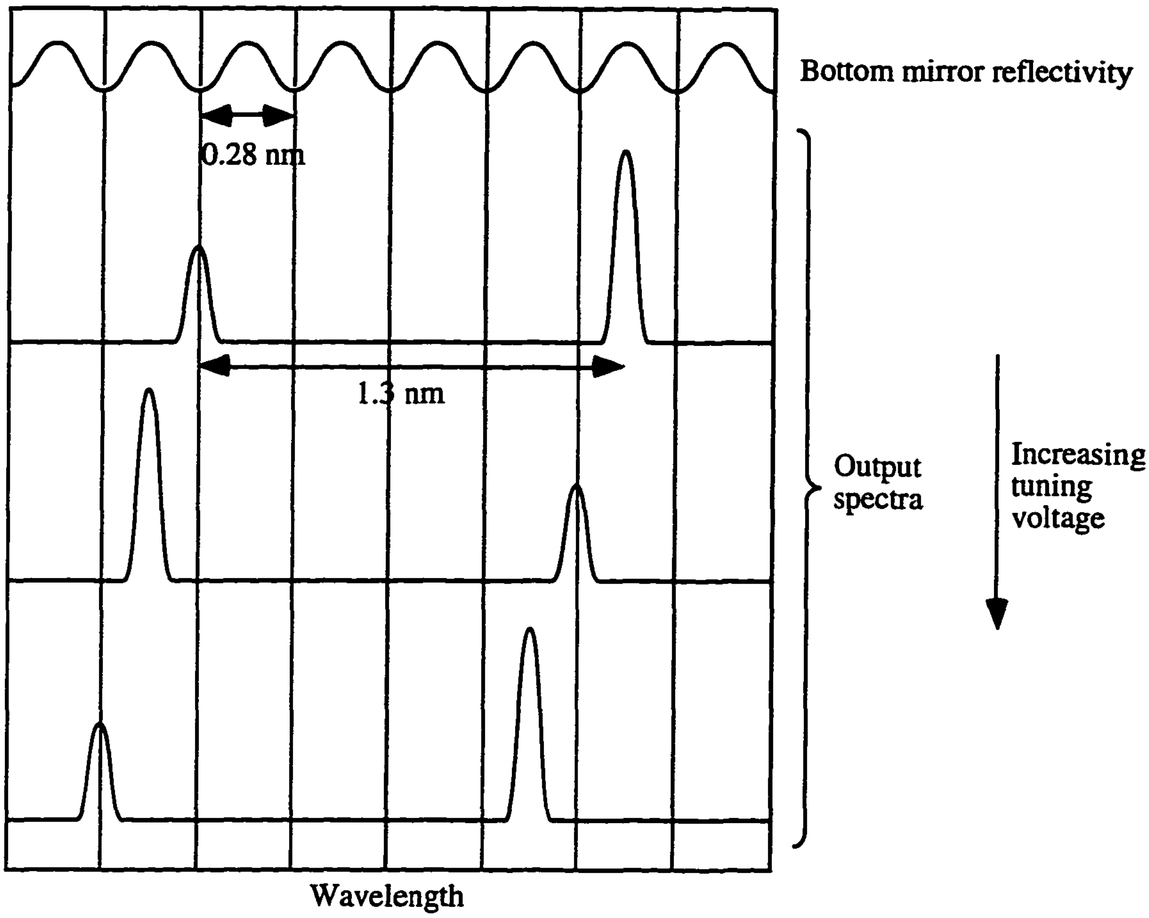


*Figure 5.21 - Schematic showing why mode oscillation occurs. The bottom mirror reflectivity oscillates with wavelength due to the weak Fabry-Perot cavity formed by the substrate. Different transverse modes see different reflectivity due to this effect. The mode which has the highest reflectivity oscillates as the device is tuned.*

## 5.8 Use as a Broadband Source

Although most applications require sources with a single, narrow linewidth that are continuously tunable by an external source, broad bandwidth sources are interesting for sensor applications and for elimination of optical feedback effects. Two applications already use broad bandwidth sources: fiber gyroscopes[8] and optical low coherence reflectometers[9]. Fiber gyroscopes allow rotation rate to be measured with no moving parts and are used in navigation. Optical low coherence reflectometry is a method for measuring the reflectivity of optical systems[10-15] as a function of position. Reflectivities of -146 dB[16] can be measured with micron accuracy[17]. These systems currently use LEDs[18] as their sources. However, LEDs are inefficient both at generating light and coupling the light into a fiber. A source with a broad bandwidth, but the efficiency and spatial coherence of a laser, is needed. Superluminescent diodes[19-22] and superluminescent fiber amplifiers have also been proposed as broad bandwidth sources, but these devices are still inefficient at low powers and produce jagged spectrums which are unsuitable for these applications. Superluminescent fiber amplifiers also require a pump laser.

Tunable lasers can be used as a broad bandwidth source by quickly sweeping the lasing wavelength. Provided that the integration time for a measurement is much longer than the sweep time of the laser, a swept source can be used in all broad bandwidth applications. Tunable lasers have been used as broad bandwidth sources[23]. However, their application has been limited since these tunable lasers are typically bulky, slow tuning, or not continously tunable. Micromechanical tunable VCSELs, on the other hand, can quickly (~μs) and continuously tune much faster than the millisecond integration times of most applications.

### 5.8.1 Theory of a Swept Laser as a Broad Bandwidth Source

This section shows that a swept source can be used in broad bandwidth applications. In both the applications listed above, the output of the broadband source is split into two, sent along two different length paths, recombined, and detected. As one of the path lengths is changed the coherence function of the source is mapped out. We rederive the coherence function[8] here. Assuming the system is single mode, then

$$P(\Delta t) \propto \left\langle \left| E(t) + E(t+\Delta t) \right|^2 \right\rangle \tag{5-2}$$

where $t$ is time, $\Delta t$ is the delay introduced by the path length difference, $P(\Delta t)$ is the average power detected for $\Delta t$ path length difference, and $E(t)$ is the electric field of the broadband source at time $t$. The time average is usually ms or larger to reduce noise. This can be approximated as an infinite time average, since any changes in the broadband source occur at a much faster time scale (typically μs). Equation (5-2) can be expanded to

$$P(\Delta t) \propto \left\langle |E(t)|^2 \right\rangle + \left\langle |E(t+\Delta t)|^2 \right\rangle + 2\left\langle E(t)E^*(t+\Delta t) \right\rangle \qquad (5\text{-}3).$$

The first two terms are constant with $\Delta t$, so we focus on the third term. $E(t)$ can be broken up into its various spectral components as

$$\begin{aligned} E(t) &= \int_{-\infty}^{\infty} \mathrm{Re}\left(f(\omega-\omega_0)e^{i\omega t}\right)d\omega \\ &= \int_{-\infty}^{\infty} f(\omega-\omega_0)e^{i\omega t} + f^*(\omega-\omega_0)e^{-i\omega t}d\omega \\ &= \int_{-\infty}^{\infty} \left[f(\omega-\omega_0) + f^*(-\omega-\omega_0)\right]e^{i\omega t}d\omega \end{aligned} \qquad (5\text{-}4)$$

where $f(\omega-\omega_0)$ describes the lineshape of $E(t)$ around a center frequency, $\omega_0$. Plugging this into the third term of (5-3) and performing some mathematical operations yields

$$\langle E(t)E(t+\Delta t)\rangle = \mathrm{F.T.}[s_e(\omega)](\Delta t)\cos(\omega_0\Delta t) + i\,\mathrm{F.T.}[s_0(\omega)](\Delta t)\sin(\omega_0\Delta t) \qquad (5\text{-}5)$$

where $\mathrm{F.T.}[\;](\Delta t)$ means the Fourier Transform of the enclosed function evaluated at $\Delta t$ and $s_e(\omega)$ and $s_o(\omega)$ are the even and odd part of the spectral power density $s(\omega)$ defined by the equation

$$s(\omega) = f(\omega)f^*(\omega) \qquad (5\text{-}6)$$

The important point here is that equation (5-5) depends only on spectral power density. This means that if a broad spectrum is measured by the spectrometer, it does not matter whether it is a rapidly sweeping tunable source or a true broadband source. Both can be used in broad bandwidth applications.

This can be difficult to grasp at first. A spontaneous emission source $\langle E(t)E(t+\Delta t)\rangle$ must be zero for large $\Delta t$ because $E(t)$ and $E(t+\Delta t)$ are uncorrelated. For a swept tunable source $\langle E(t)E(t+\Delta t)\rangle$ is also zero, but for a different reason. If averaged over short times, the device does not tune much and $\langle E(t)E(t+\Delta t)\rangle$ is nonzero. But as the wavelength is swept, the phase between $E(t)$ and $E(t+\Delta t)$ changes. By averaging over the entire tuning time, the fringes average out to zero, except for the case where $\Delta t$=0. In this case, $E(t)$ and $E(t+\Delta t)$

remain in phase even as the wavelength changes. The net effect is that these two different cases, the spontaneous emission source and the swept tunable source, have exactly the same coherence functions if their spectral power densities look the same.

### 5.8.2 Direct Chirping of Wavelength

The tunable VCSEL can be made into a broadband source by directly modulating the tuning voltage on the device. The spectra for a 100 μm cantilever device driven at resonance is shown in Figure 5.22. The resonance frequency for such a device is 300 kHz. This means the time to sweep across the entire tuning range is only 1.6 μs. The figure shows the spectra as the AC voltage is increased. This device is initially single mode with a side mode suppression ratio >30 dB even when biased at its maximum power of 4.5 mA. As the voltage is increased a square spectrum with "horns" at the end is produced. The horns are caused by the sinusoidal motion of the tuning head. The device spends more time at the ends of the tuning range where it is reversing directions, than in the middle where it is rapidly moving. As the AC voltage amplitude is increased, the

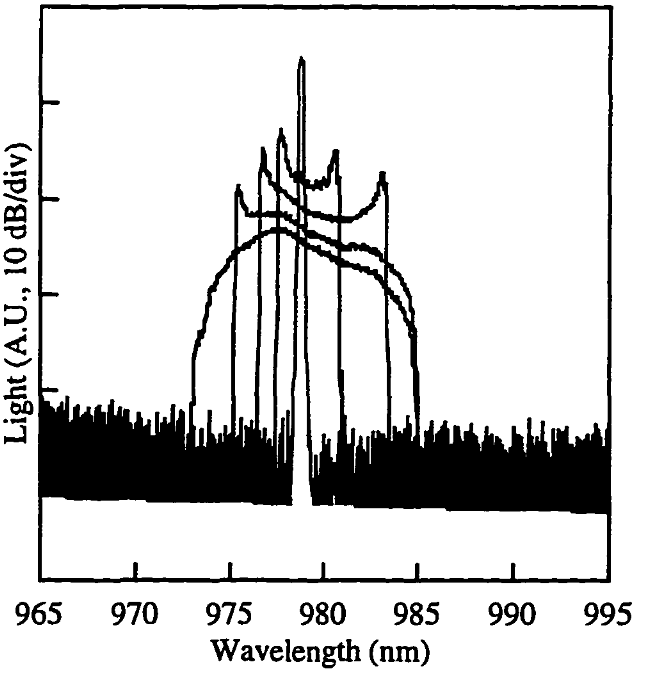


*Figure 5.22 - Spectra of a single mode device with AC tuning voltages*

spectrums get wider, until eventually the horns disappear and the bandwidth no longer increases. This is because the device only lases over a finite wavelength range. Thus beyond a minimum oscillation level, the spectra is not sensitive to the driving signal. The total achievable bandwidth with this device is 12 nm.

The LI curves for this device, while completely broadened and not chirped, are shown in Figure 5.23. For the chirped case, the output power is lower since the laser spends more time, on average, at wavelengths where the device performance is not as good as the center wavelength.

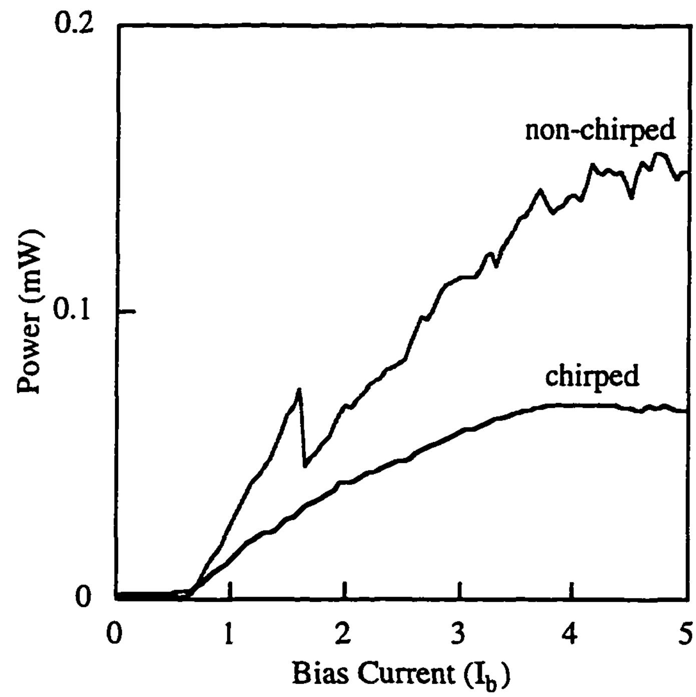


*Figure 5.23 - LI curves for the single mode device for both the chirped and the non-chirped case.*

The chirped and unchirped spectra for a larger area device are shown in Figure 5.24. These devices are multimode, as shown by the unchirped curve, but a much wider chirped spectrum can be obtained, in this case 24 nm. These curves were taken at 8 mA bias current at the point of maximum power.

The LI curves for this device are shown in Figure 5.25. Note that the ripples due to the backside reflection disappear when the device is chirped. This immunity to optical feedback is typical of broad bandwidth sources. Note also that even in the chirp mode the device is able to give off more than a 0.25 mW.

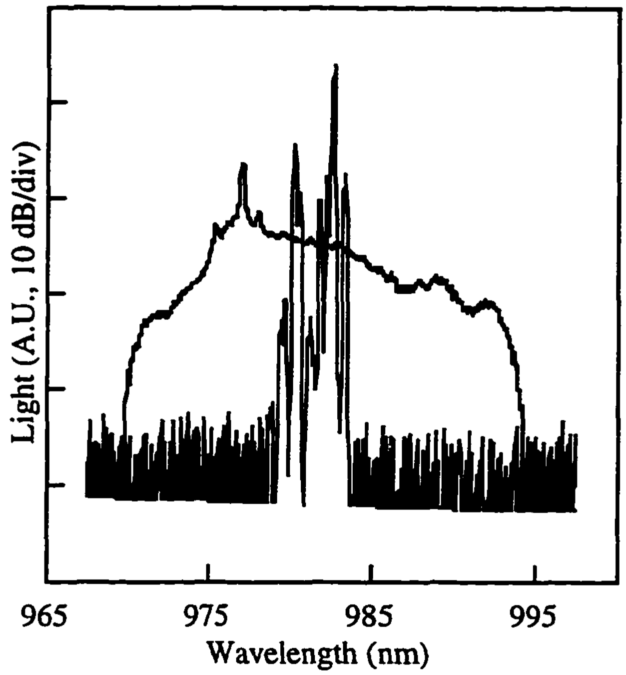


*Figure 5.24 - Broad spectrum achievable with a larger aperture device showing both the chirped and unchirped case.*

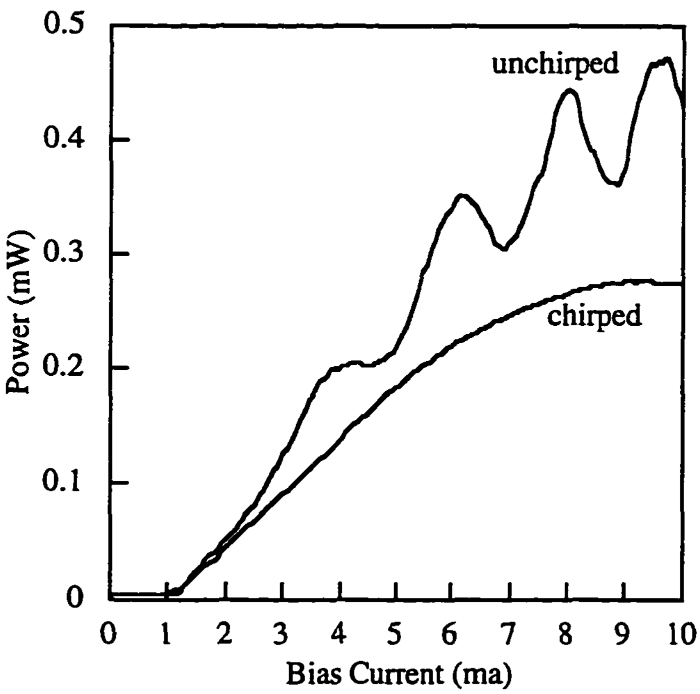


*Figure 5.25 - LI curves for the larger aperture device for both the chirped and unchirped case. Note the absence of ripples for the chirped case.*

Figure 5.26 shows the modulation response of the device. For these measurements, we used devices with stiffer, 100 µm long cantilevers. These devices have faster response times, but also require dc voltages of 100 V to tune. However, if they are driven at resonance, it is possible to sweep them over their entire tuning range using a square wave with a low and a high value of 0 V and 16 V, respectively.

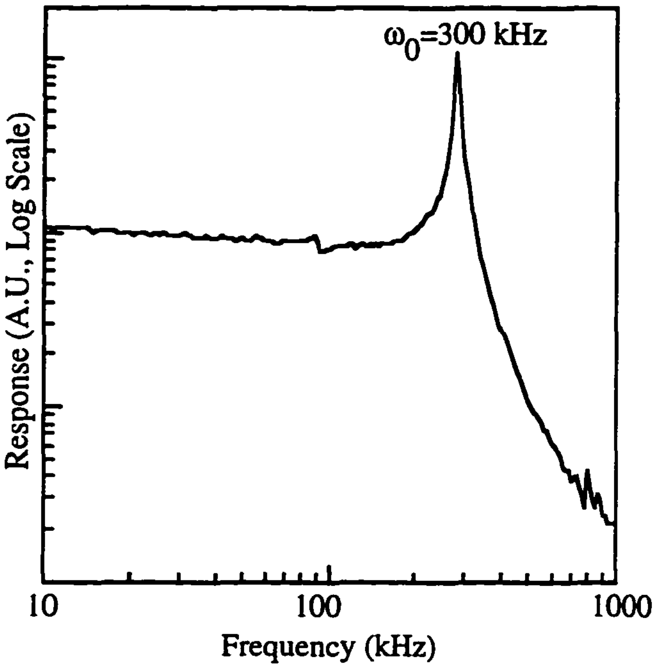


*Figure 5.26 - Modulation response of the 100 µm cantilever device. Note the factor of 10 enhancement in response at the resonant frequency.*

### 5.8.3 Self-Chirping

The above techniques for generating a broad spectrum required an AC voltage source. If a self-chirping device could be made, it could lower costs and increase reliability. We have observed this self-chirping effect in a few of the devices with light *n* doping and abrupt heterojunctions in the top DBR mirror.

When these devices are biased with low tuning voltages, the device functions as a tunable VCSEL. A typical LI for the VCSEL is shown in Figure 5.27. Low threshold currents of 700 µA and high output power of 0.22 mW are achieved. The laser operates in a single transverse mode and has a side mode suppression ratio of >20 dB. The near field confirms that the device is lasing in the fundamental transverse mode.

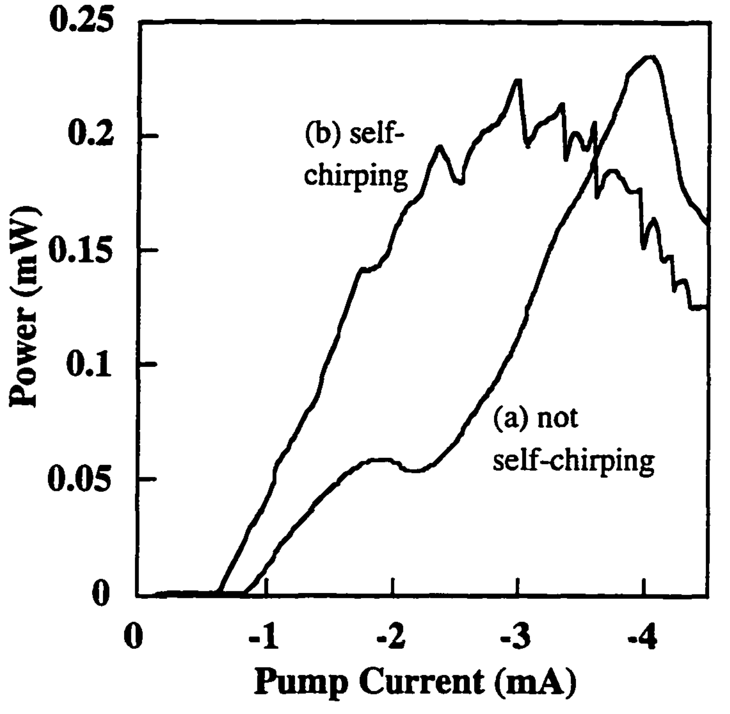


*Figure 5.27 - LI curves for both the (a) not self-chirping and (b) self-chirping cases.*

When the top *pn* junction is reverse biased at voltages > 17 V, the device begins to self-chirp. That is, the cantilever begins to sweep up and down at the mechanical resonance of the cantilever (in this case, longer cantilevers were used with resonance frequencies of 76 kHz), causing the wavelength to oscillate. The spectra of a device when in this mode are shown in Figure 5.28. We again see the "horns" in the spectrum due to the sinusoidal motion of the cantilever and wavelength. Spectral widths as high as 10 nm were observed, even though only DC biases were applied to the device.

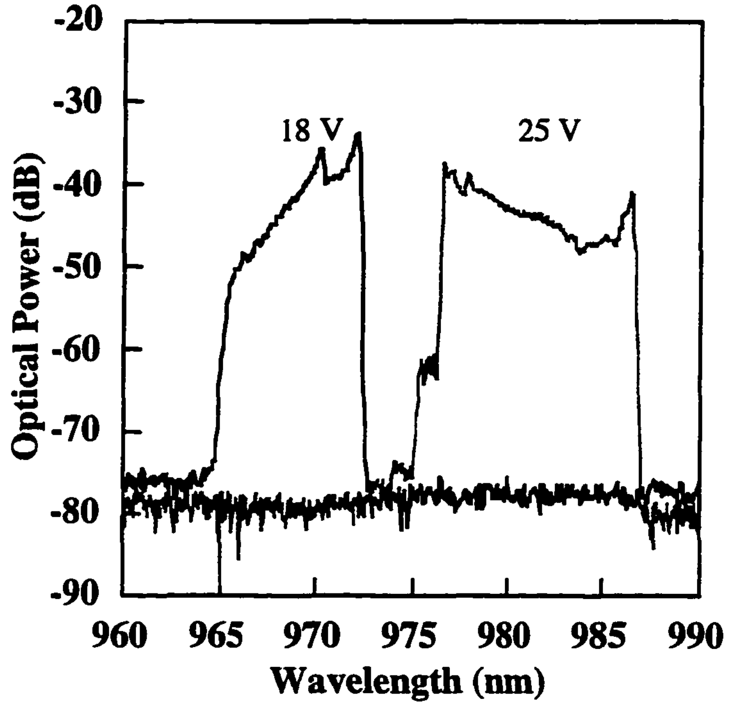


*Figure 5.28 - Spectra of the device while self chirping. Only DC biases are applied but broad spectrums are still obtained.*

Figure 5.29 shows emission from a self-chirping laser after passing through a tunable filter. Note that the peaks shift in time as the filter is tuned. The bottom of the figure shows the wavelength as a function of time. The wavelength oscillates at 76 kHz, matching the mechanical resonance frequency of these devices, as shown in Figure 5.30. Larger cantilevers with lower resonance frequency are used for self-chirping because of their increased voltage sensitivity.

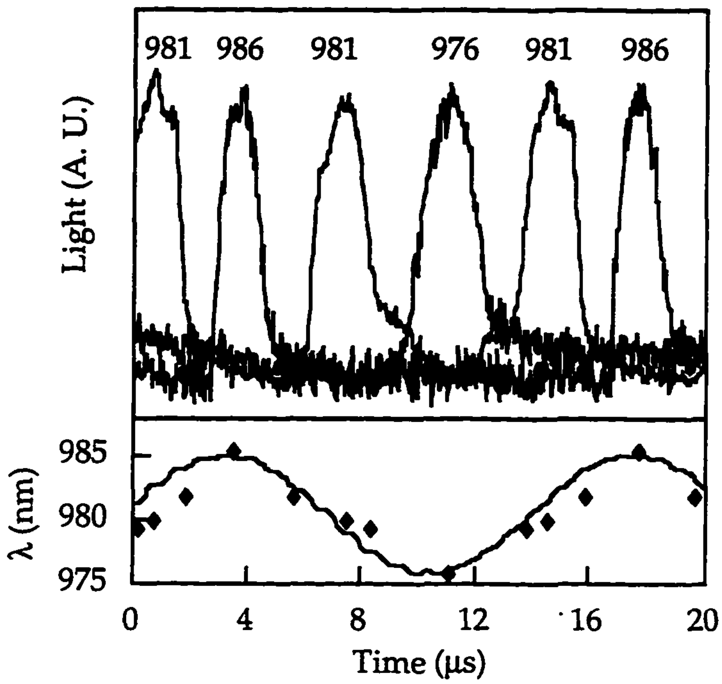


*Figure 5.29 - (top) Emission versus time from a self chirping device after being passed through a tunable filter tuned to different wavelengths. (bottom) Wavelength versus time. The oscillation at 76 kHz matches the resonance frequency of the cantilever.*

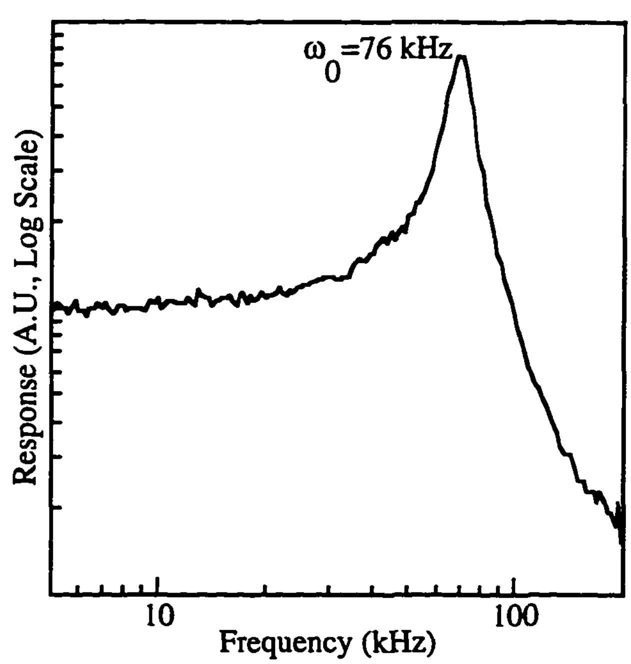


*Figure 5.30 - Modulation response of the 200 μm long cantilever.*

Figure 5.27 also shows the LI curve for a device when in the self-chirping mode. It is still a laser with a definite kink in the LI curve. The power peaks at 0.2 mW. The fluctuations in the LI curve due to backside reflections are averaged out when the device is self-chirping.

The self-chirping is caused by an internal feedback mechanism. The top *n*-mirrors in this device were lightly doped ($10^{16}/cm^3$) and the heterojunctions were not graded. However, at this low doping level the $Al_{0.6}Ga_{0.4}As$ layers in the DBR are fully depleted. In order for current to flow, electrons have to hop over these barriers. This is difficult to do thermally, since the energy barrier (~0.3 eV) is several times larger than *kt*. Photons can help the electrons jump the barrier via free carrier absorption. These extra electrons in the $Al_{0.6}Ga_{0.4}As$ layer help reduce the fields and decrease absorption due to the Franz-Keldish effect. There are two net effects of these mechanisms: (1) The top *n*-DBR acts as a photoconductor and (2) the top *n*-DBR acts as a saturable absorber.

These two effects explain the self-chirping of the device. Because some of the applied tuning voltage can now be dropped in the top DBR mirror, the voltage across the air gap now also depends on the amount of light circulating in the device. This opens up a feed-back mechanism, since the lasing power can now effect the air gap voltage, which in turn can change the lasing wavelength and hence the lasing power. This alone is not enough to cause self-chirping, however. The saturable absorber is also needed to make the device bistable.

To see how this works, look at the 17 V spectrum in Figure 5.28. First, the laser starts out at a long wavelength and is "on." The photocurrent generated in the *n*-DBR causes more voltage to be dropped across the air gap. This causes the laser to shift to shorter wavelengths. At some point, it shifts to such a short wavelength that it can no longer lase. Without the photocurrent, more voltage is dropped across the *n*-DBR and less across the air gap. The device starts to swing back to longer wavelengths, but it can not turn on immediately due to the saturable absorber. Eventually the saturable absorber is overcome and the device turns back on again, and the whole process repeats itself.

## 5.9 Life Tests

Lifetime is an important parameter with mechanical tuning devices. Although section 2.6 showed that long lifetime is expected, it is necessary to verify this experimentally. Some very preliminary lifetime experiments were performed with the improved oxidized VCSEL of this chapter.

First, one of the 100 μm cantilevers devices was biased above threshold and swept at its resonant frequency of 300 kHz over its entire tuning range overnight while lasing. Every 5 minutes the resonant signal was removed and the wavelength at 0 V was measured. The results are shown in Figure 5.31. As can be seen, barely any wavelength shift occurs, even after billions of cycles. So no mechanical deformation of the cantilever takes place.

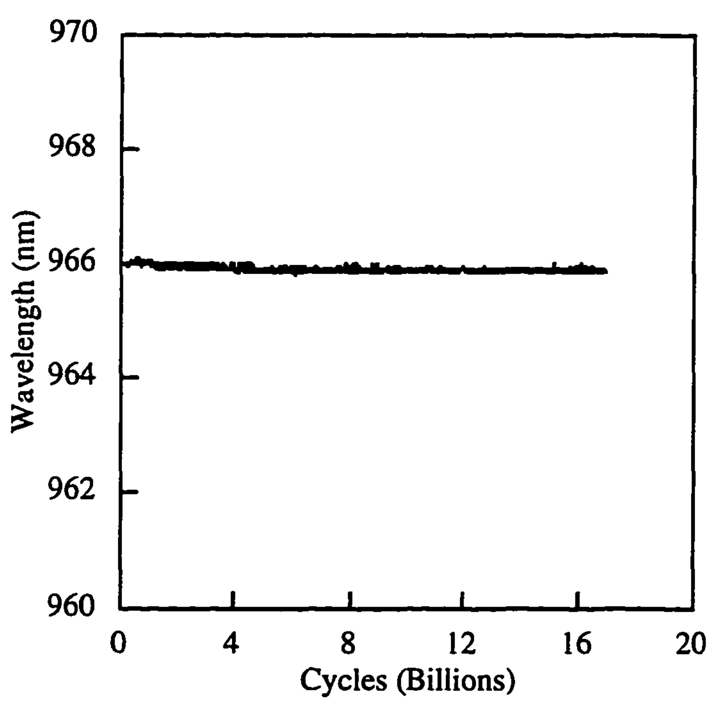


*Figure 5.31 - Wavelength of the 0 V versus complete cycles of resonant pumping of the cantilever. Virtually no drift in wavelength occurs indicating that the cantilever is completely undeformed despite billions of cycles.*

The other possible change with time could be electrical. Figure 5.32 shows the wavelength of a 200 μm long cantilever device left oscillating overnight over its entire tuning range. This time the device was biased at 10 kHz, below the resonant frequency. The wavelength was sampled at the maximum voltage of 16 V. Here, we do see an approximately 1 nm shift in wavelength with number of cycles. This suggests a change in the electrical connection to the tuning contact. To overcome this problem, the doping in the $n$-DBR should be increased and true $n$-contacts (Ni/Au/Ge) instead of just Au should be used.

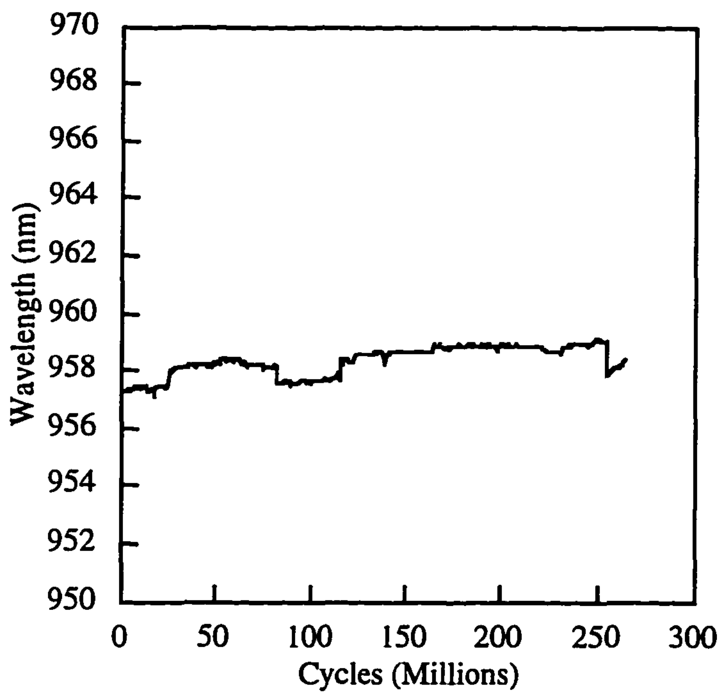


*Figure 5.32 - Plot of wavelength versus number of cycles for a 200 μm long cantilever device with the wavelength sampled at the maximum tuning voltage of 16 V.*

This lifetime testing is still preliminary. Further testing is required before long lifetime can be conclusively established..

## 5.10 Conclusion

Micromechanical tunable VCSELs with performance comparable to normal VCSELs were demonstrated for the first time. Record sub-mA threshold, 0.9 mW power, and 19.1 nm tuning were achieved. Several novel effects were observed, including self chirping and mode oscillation. Even more important than the records, this chapter demonstrates that micromechanical tunable VCSELs are viable devices.

## 5.11 References

[1] M. S. Wu, E. C. Vail, G. S. Li, W. Yuen, and C. J. Chang-Hasnain, "Tunable micromachined vertical cavity surface emitting laser," *Electron. Lett.*, vol. 31, no.4, p. 1671-1672, 1995.

[2] E. C. Vail, G. S. Li, W. Yuen, and C. J. Chang-Hansnain, "High performance micromechanical tunable vertical cavity surface emitting lasers," *Electron. Lett.*, vol. 32, no. 20, p. 1888-1889, 1996.

[3] K. D. Choquette, R. P. Schneider, K. L. Lear, K. L., and K. M. Geib, "Low threshold voltage vertical-cavity lasers fabricated by selective oxidation," *Electron. Lett.*, vol. 30, no. 24, p. 2043-2044, 1994.

[4] K. L. Lear, K. D. Choquette, R. P. Schneider, Jr., S. P. Kilcoyne, and K. M Geib, "Selectively oxidised vertical cavity surface emitting lasers with 50% power conversion efficiency." *Electron. Lett.*, vol. 31, no. 3, p. 208-209, 1995.

[5] S. Adachi, *GaAs and Related Materials*, (Singapore, World Scientific, c1994)

[6] G.Giaretta, M.Y.Li, G.S.Li, M.Yuen and C.Chang-Hasnain, "A novel 4x8 Single-Mode Independently Addressable Oxide-Isolated VCSEL Array",submitted to *IEEE Photon. Technol. Lett.*, 1996.

[7] C. J. Chang-Hasnain, J. P. Harbison, C.-E. Zah, M. W. Maeda, L. T. Florez, N. G. Stoffel, and T. P. Lee, "Multiple wavelength tunable surface-emitting laser arrays," *IEEE Journal of Quantum Electronics* , vol. 27, no. 6, p. 1368-1376, 1991.

[8] H. Lefèvre. *The Fiber-Optic Gyroscope*, (Boston : Artech House, c1993)

[9] W. V. Sorin, and D. M. Baney, "A Simple Intensity Noise Reduction Technique for Optical Low-Coherence Reflectometry," *IEEE Photon. Technol. Lett.*, vol. 4, no. 12, p. 1404-1406, 1992.

[10] A. Küng, and P.-A. Robert, "Measured Integrated Optical Circuits Using a Low Coherence Light Source," *Optical Engineering*, vol. 34, no. 7, p. 2049-54, 1995.

[11] K. Takada, H. Yamada, Y. Hibino, and S. Mitachi, "Range Extension in Optical Low Coherence Reflectometry Achieved by Using a Pair of Retroreflectors," *Electron. Lett.*, vol. 31, no. 18, p. 1565-7, 1995.

[12] K. Takada, A. Himeno, and K. Yukimatsu, "Resolution-Controllable Optical Time Domain Reflectometry Based on Low Coherence Interference," *J. of Lightwave Technol.*, vol 9., no. 11, p. 1534-9.

[13] K. Kasaya, Y. Yoshikuni, and H. Ishii, "Measurements of a Semiconductor Waveguide Using a Low-Coherence Interferometric Reflectometer," *IEEE Photon. Technol. Lett.*, vol. 8, no. 2, p. 251-3, 1996.

[14] X. J. Wang, T. E. Milner, R. P. Dhond, W. V. Sorin, S. A. Newton, and J. S. Nelson, "Characterization of Human Scalp Hairs by Optical Low-Coherence Reflectometry," *Optics Lett.*, vol. 20, no. 6, p. 524-6, 1995.

[15] G. M. Foster, "Measurements of Return Loss on OEIC Structures, Using Optical Low-Coherence Reflectometry," *Optical and Quantum Electronics*, vol. 27, p. 1075-9, 1995.

[16] W. V. Sorin, and D. M. Baney, "A Simple Intensity Noise Reduction Technique for Optical Low-Coherence Reflectometry," *IEEE Photon. Technol. Lett.*, vol. 4, no. 12, p. 1404-6, 1992.

[17] X. Clivaz, F. Marquis-Weible, and R. P. Salathe, "Optical Low-Coherence Reflectometry with 1.9 μm Spatial Resolution," *Electron. Lett.*, vol. 28, no. 16, p. 1553-5, 1992.

[18] J. E. Fouquet, G. R. Trott, W. V. Sorin, M. J. Ludowise, and D. M. Braun, "High-Power Semiconductor Edge-Emitting Light-Emitting Diodes for Optical Low Coherence Reflectometry," vol. 31, no. 8, p. 1494-503, 1995.

[19] B. D. Patterson, J. E. Epler, B. Graf, H. W. Lehmann, and H. C. Sigg, "A Superluminescent Diode at 1.3 μm with Very Low Spectra Modulation," *IEEE J. of Quantum Electron.*, vol. 30, no. 3, p. 703-12, 1994.

[20] G. A. Alphonse, D. B. Gilbert, M. G. Harvey, and M. Ettenberg, "High-Power Superluminescent Diodes," *IEEE J. of Quantum Electron.*, vol. 24, no. 12, p. 2454-7, 1988.

[21] L. Goldberg, and D. Mehuys, "High Power Superluminescent Diode Source," *Electron. Lett.*, vol. 30, no. 20, p. 1682-4, 1994.

[22] Y. Kashima, A. Matoba, and H. Takano, "Performance and Reliability of InGaAsP Superluminescent Diode," *J. of Lightwave Technol.*, vol. 10, no. 11, p. 1644-9, 1992.

[23] K. Takada and H. Yamada, "Narrow-Band Light Source with Acoustooptic Tunable Filter for Optical Low-Coherence Reflectometry," *IEEE Photon. Technol. Lett.*, vol. 8, no. 5, p. 658-60, 1996.

# 6. Conclusion

Micromechanical tuning can be used to achieve wide, continous tuning at a potentially low cost. This thesis has demonstrated tunable filters, detectors and lasers based on this concept. Each of these non-optimized devices achieved record tuning. The tunable filter achieved the widest tuning of a monolithic tunable semiconductor filter, 70 nm. The tunable detector achieved the widest tuning of a monolithic tunable detector, 33 nm. The tunable laser achieved the widest, continous tuning of monolithic laser, 19.1 nm. All of these devices were simple to tune, requiring only a voltage of approximately 10 V. This combination of record performance simple biasing, and potential low cost make this device useful in a wide variety of applications.

This thesis also described the first demonstration of a micromechanical tunable VCSEL. An improved tunable VCSEL was also shown with the first demonstrated performance comparable to that of the best VCSELs (sub mA threshold current, 0.9 mW of output power).

This thesis also discussed the many other advantages of micromechanical tunable VCSELs. Polarization insensitivity, simple fabrication, circular modes, 2-D arrays, lack of cleaved facets, and wafer scale testing all make this technology look attractive compared to competing edge-emitting technology.

We also showed that micromechanical tunable devices did not suffer from the same problems common with bulk mechanical tuning. Tuning speeds were shown to be quite fast, ~μs. The lifetime of the single crystalline cantilever should be long, with billions of cycles already demonstrated with no failure. Alignment and tilt tolerances of the top mirror were shown to be very lenient due to waveguiding. The vibration sensitivity of these devices is shown to be low, with several g's of acceleration required to cause detuning.

These results were shown to agree quite well with calculations developed in this thesis. These calculations can now be used to design new devices in the future. We have also tried to show some simple ways of designing devices without having to go through the full batttery of calculations.

With optimized structures, the tuning range of these devices can be at least doubled and the other characteristics of the devices improved. Filters and detectors with tuning ranges of several hundred nm and tunable lasers with 40 nm tuning ranges should be possible. Devices with better extinction ratios, bandwidths, powers, and thresholds are possible. In addition, this technique can be used to create devices in other wavelength ranges all the way from the visible to the communication wavelengths at 1.55 μm. I believe this thesis just marks the beginning of an exciting and productive time for micromechanical tuning.